# Investigation of the Structure-Mechanical Relationship of the Porcine Thoracic Aorta with a Focus on Glycosaminoglycans and Residual Stress

Noor Ghadie

A doctoral thesis submitted in partial fulfillment of the requirements of the degree of
DOCTORATE IN PHILOSOPHY
Biomedical Engineering

Ottawa-Carleton Institute for Biomedical Engineering
University of Ottawa
Ottawa, Ontario, Canada

السلام عليكم

Peace be with you

Que la paix soit avec vous

# ABSTRACT

The extracellular matrix (ECM) of the aorta is a complex meshwork of elastin, collagen, and glycosaminoglycans (GAG). It also modulates the mechanical properties of the aorta, which in turn dictate lethal ruptures such as those caused by aneurysm and dissection. Amongst other roles, aortic stiffness controls the aorta's ability to expand and recoil, and residual stresses, which are those existing in the absence of load, affect the magnitude and distribution of the mechanical stresses throughout the aortic wall. Mechanical stresses can be predicted via complex computer models, powerful tools that can also provide insight regarding the risk of rupture, given that ruptures occur when the mechanical stresses exceed the strength of the aorta. While this dissertation is primarily focused on the effect of GAG on residual stresses, other ECM (collagen, elastin) and mechanical (stiffness) factors are considered to expand our understanding of the structure-mechanics relationship in the aorta. This is important because the ECM undergoes extensive remodelling during aging and disease, but it is also critically important, as mentioned, in the context of aortic rupture.

We first explored the mechanical roles of GAG in a finite element model by studying both the transmural residual stresses and the opening angle (an indicator of circumferential residual stresses) in ascending (AS) aortic ring models. Both were shown to be modulated by the GAG content, gradient, and the nature of the transmural distribution. While a heterogeneous GAG distribution led to the development of residual stresses which could be released by a radial cut, this was not the case when a homogeneous distribution was prescribed.

Because the GAG distributions used in the first study were based on assumptions, and to get an *in vitro* understanding of the ECM role in modulating residual stresses, biomechanical mechanisms were explored in thoracic aortas from 5- to 6-month-old pigs. In a second study, we

generated new detailed data on the distributions of collagen, elastin and GAG, throughout the aortic wall in the AS, arch (AR), and descending thoracic (DT) regions, and established correlations between the ECM constituents and the opening angle. The strongest correlations were observed between the opening angle and the total collagen:GAG ratio as well as the total GAG content. In line with our first *in silico* work, this *in vitro* investigation revealed that the GAG content and gradient modulate circumferential residual stresses and suggested that the interaction between GAG and the ECM fibers also plays a role in regulating residual stresses.

In a third study, we examined the extent of contribution of GAG to circumferential residual stresses and to the radial compressive stiffness of the aortic wall, as well as the underlying mechanism through which GAG contribute to the mechanical properties using enzymatic GAG depletion. GAG depletion was associated with a decrease in the opening angle, by approximately 25%, 32%, 42% in the AS, AR, and lower DT regions respectively, and an increase in the radial compressive stiffness of the AS aorta. Glycation was also associated with a decrease in the opening angle, in which GAG depletion also had a similar effect. A small loss of water content was detected after GAG depletion, and the AS region was also associated with a significant loss of compressive deformation in the inner layer of the aorta following GAG depletion, suggesting that GAG interact with ECM fibers in their effect on aortic mechanics.

The garnered experimental geometrical data and intramural GAG distributions were finally used to simulate animal-specific aortic rings from the AS, AR, and DT regions. The opening angle response was evaluated in solid matrices assuming one layer, and two layers to capture the different mechanical behaviors of the intima-media and the adventitia. A Holmes-Mow constitutive relationship was used and material parameters were obtained by curve fitting experimental stress-strain curves obtained from biaxial tests. Numerical results were evaluated

by comparing simulated and experimental opening angles, revealing a notable overall agreement between the two.

# ACKNOWLEDGMENTS

This journey owes itself to the presence and support of talented and compassionate individuals. I was fortunate to have been supervised by Dr. Michel Labrosse and Dr. Jean-Philippe St-Pierre and I couldn't have asked for a more enriching experience. Their collaborative efforts provided me with invaluable technical, computational and experimental skills which enabled this multidisciplinary research. Thank you for your wisdom and your patience, your kind and uplifting words, and for your support in and outside the lab. Dr. Labrosse: I am sincerely grateful for your trust and confidence in my work, your encouragement to go beyond my limits, and for teaching me the value of independence in research. Dr. St-Pierre: a heartfelt thank you for your mentorship, the profound life lessons you have shared with me, and for nurturing my critical thinking skills as a researcher.

My experience at the University of Ottawa taught me the value of a supportive group. I'd like to thank the St-Pierre Biomaterials group for their help in the lab and for their friendship: Dayna Zunder, Jordan Nhan, Luisa Metzler, Sietske Barnes, Justin Quan, Nimrah Munir, Abrie Girgis, Michael Mulholland, and all former and new members of the lab. I appreciate the help of my volunteer students, Nadege Uwurukundo Mpore, Aya Al-shawabkeh and Issiaka Traoré. I would like to take this opportunity to thank Dr. Xudong Cao for allowing me to access his lab. I also wish to thank my thesis advisory committee, Dr. Andrew Speirs and Dr. Fabio Variola. Their professional and technical insights had a profound impact in shaping this multidisciplinary research.

The University of Ottawa was a second home to me for the past 9 years. I wish to thank the academic and non-academic staff, especially within the faculty of engineering. I am grateful for all the opportunities and for providing me with an environment to evolve personally and

professionally, as well as for the chances I was given to contribute to the growth and development of future generations.

I dedicate this milestone to my incredible family. To my sister Marwa, the sunshine of our family. To my mother Mounira, my biggest cheerleader, and my father Mohamed, my proudest supporter; their selfless dedication, endless sacrifices, and dream of providing me with an education have been my constant source of motivation. I am also grateful for the support and love of my brothers, Hyder and Ibrahim. Finally, to my husband Mohammad, my partner and my best buddy: this journey would have not been the same without you; thank you for the laughter, the meals, the patience, the love, the friendship, the sacrifices and for cheering me up during my toughest days; thank you for being the funniest and most compassionate distraction I could have asked for; your presence means the world to me.

# PREFACE

This dissertation is structured into three parts (Opening, *In vitro* and *in silico* Investigations, and Closing), each containing multiple chapters, as outlined below:

I. Opening:
    1. Chapter 1: Introduces the dissertation with brief background information and the rationale, and discusses the main objectives of this work.
    2. Chapter 2: Provides the background information and fundamental concepts that apply to the research presented in this dissertation.
    3. Chapter 3: Critically reviews the contribution of glycosaminoglycans (GAG) to aortic mechanics, identifies gaps in the literature and suggests further lines of investigations.

II. *In vitro* and *in silico* Investigations:
    4. Chapter 4: Establishes and validates a numerical framework that facilitates the investigation of the impact of GAG on residual stress.
    5. Chapter 5: Characterizes the intramural distribution of the main extracellular matrix constituents and establishes correlations between these components and the opening angle, an indicator of residual stresses.
    6. Chapter 6: Focuses on gaining a deeper understanding of the mechanical roles of GAG in the aorta, as well as the mechanisms through which they regulate mechanical properties.
    7. Chapter 7: Introduces animal-specific aortic ring computer models, and evaluates their ability to capture the contribution of GAG to the opening angle.

III. Closing:

8. Chapter 8: Provides the key aspects of discussion, concluding remarks and recommendations for future work.

This dissertation is comprised of five original articles for which I was lead author. I led the design of the experimental and numerical protocols, the acquisition of the data experimentally, numerically and/or analytically, and the analysis and interpretation of the data. I also drafted the first version of the articles and was involved in revising them critically and in making the final approval decision of the versions to be considered for submission. At the time of submission of this thesis, one of the articles was published as a conference proceeding, two were published in journals in the field, one was accepted, and one was prepared for submission. In this dissertation, the content of the publications has been reformatted to ensure appropriate presentation and cohesiveness of the document, including and not limited to abbreviations adjustments, referencing style, and figure, table, section and appendix numbering modifications.

# TABLE OF CONTENTS

# LIST OF FIGURES

# LIST OF TABLES

# LIST OF SYMBOLS AND ABBREVIATIONS

| | |
|---|---|
| 2D | Two Dimensional |
| 3D | Three Dimensional |
| $\beta_o$ | Reference Configuration |
| $\beta_t$ | Deformed Configuration |
| $\bar{\bar{C}}$ (**C**) | Cauchy-Green Deformation |
| $\bar{\bar{\bar{\bar{\mathbb{C}}}}}$ | Stiffness |
| det | Determinant |
| $\bar{\bar{E}}$ | Green-Lagrange Strain Tensor |
| $\varepsilon$ | Internal Energy Density |
| $\bar{\bar{F}}$ | Transformation Gradient |
| $\bar{\bar{I}}$ | Identity Tensor |
| $\mathrm{I}_1$ | First Invariant of the Right Cauchy-Green Deformation |
| $\mathrm{I}_2$ | Second Invariant of the Right Cauchy-Green Deformation |
| $J$ | Volume Ratio |
| $k$ | Bulk Modulus |
| $\Lambda_\theta$ | Circumferential Prestretch |
| $\eta$ | Entropy |
| $\bar{\bar{P}}$ | First Piola-Kirchhoff Stress Tensor |
| $\psi$ | Helmholtz Potential |
| $R$ | Radius in Open Configuration |
| $\rho$ | Radius in Unloaded Configuration |
| $\rho_o$ | Mass Density in $\beta_o$ |
| $\bar{\bar{S}}$ | Second Piola-Kirchhoff Stress Tensor |
| $\bar{\bar{\sigma}}$ | Cauchy Stress Tensor |
| $T$ | Temperature |
| $T^S$ | Second Piola-Kirchhoff Membrane Tension |
| $W$ | Strain Energy |
| $\vec{x}$ | Position Vector in $\beta_t$ |
| $\vec{X}$ | Position Vector in $\beta_o$ |

| | |
|---|---|
| AAA | Abdominal Aortic Aneurysm |
| AFM | Atomic Force Microscopy |
| AGE | Advanced Glycation End Product |
| ANOVA | Analysis of Variance |
| AR | Arch |
| AS | Ascending |
| CI | Confidence Interval |
| CML | N$^e$-carboxymethyl-lysine |
| DHLNL | Dehydro-dihydroxylysinonorleucine |

| | |
|---|---|
| DMMB | Dimethylmethylene blue |
| DOLD | Pyrraline deoxyglucasone-lysine dimer |
| ECM | Extracellular Matrix |
| EDTA | Ethylenediaminetetraacetic Acid |
| FCD | Fixed Charge Density |
| FD | Fiber Direction |
| FE | Finite Element |
| GAG | Glycosaminoglycans |
| GOLD | Glyoxal CML glyoxal-lysine dimer |
| HLNL | Dehydro-hydroxylysinonorleucine |
| IEEE | Institute of Electrical and Electronics Engineers |
| LDT | Lower descending throacic |
| MOLD | Methyl glyoxal-lysine dimer |
| PG | Proteoglycans |
| SEM | Standard Error of the Mean |
| sGAG | Sulfated GAG |
| SMC | Smooth Muscle Cells |
| TAA | Thoracic Aortic Aneurysm |
| TAAD | Thoracic Aortic Aneurysms and Dissections |
| TPPS | 5,10,15,20-tetraphenyl-21H,23H-porphine tetra-sulfonate |
| UDT | Upper Descending Thoracic |
| XD | Cross Fiber Direction |
| ZSS | Zero Stress State |

# I

# OPENING

# 1 INTRODUCTION

Background | Rationale

## 1.1 OVERVIEW & RATIONALE

According to the World Health Organization, cardiovascular diseases are the leading cause of death in the world, accounting for approximately 38% of all global mortalities [1]. Particularly, the probability of suffering from an aortic disease continuously increases, carrying a high burden of morbidity and mortality [2–4]. Thoracic aortic aneurysms and aortic dissections cause around 30,000 to 60,000 deaths per year in the U.S. [5], and around 30,000 individuals are diagnosed yearly in Europe [6]. In Canada, nearly 20,000 abdominal aortic aneurysm diagnoses are made yearly [7], and 9,392 cases of thoracic aortic aneurysm were reported between 2002 and 2014 in Ontario alone [3].

An aortic aneurysm is a localised permanent dilatation of the aorta to more than 50% of its original normal diameter. The current gold standard used to assess the risk of rupture of an aortic aneurysm is the aortic diameter, which has been recognized by clinicians as an insufficient metric [8–10]. Indeed, although the thoracic and abdominal aortas differ in size and morphology, the same threshold of approximately 5.0-5.5 cm diameter is being used to evaluate the patient's eligibility for surgery of both aortic regions [8,9,11,12]. This metric also ignores the natural differences in aortic diameters between sex and/or patients with different body sizes [4]. Aside from the methodological challenges associated with the accurate measurement of the aortic diameter from medical imaging, some aortic ruptures occur below the standard threshold, while some larger aneurysms do not rupture [8,9,13]. Because ruptures occur when the mechanical stresses in the aortic wall exceed its local strength, increasingly complex computer models that can predict mechanical stresses in aortic tissues continue to hold promise over the current gold standard and offer hope for more accurate predictions of aortic ruptures [10].

The development of such models requires an in depth understanding of the tissue structure, composition and function under both physiological and pathological states. In particular, to properly assess the total mechanical stresses applied to the aortic wall, one must take into account the stresses originating from external loads as well as the residual stresses, which are those existing in absence of external load [14]. Residual stresses influence the magnitude of the stress distribution within the aortic wall and, therefore, ignoring them leads to biased predictions of the stress experienced by the tissue [14,15]. In addition to contributing to the magnitude of the total mechanical stresses, residual stresses affect their distribution, and are thought to ensure a homogeneous distribution of stresses throughout the aortic wall, hence minimizing stress concentrations [14,16,17]. Residual stresses are also believed to affect tissue stiffness (or its inverse, compliance) [14], a clinically important marker in predicting cardiovascular disease [18,19]. Aortic compliance dictates the ability of the aorta to expand and recoil and is essential to accommodate the deformations caused by the cyclic pumping of the heart. In addition, a compliant aorta is necessary in reducing the cardiac afterload, and controlling blood pressure [20,21]. Residual stresses and aortic stiffness differ between sex [17,22], and increase with age [17,18].

Residual stresses and stiffness are thought to be modulated by both the morphology and composition of the tissue. Particularly, the contribution of the non-cellular component, known as the extracellular matrix (ECM) [23], to the mechanical properties of the aorta remains an active area of investigation. The ECM is heterogeneous along the aortic tree and the aortic wall, facts that are ignored by the current diameter criterion for assessment of risk of rupture. The aortic ECM is mainly comprised of fibrous constituents, elastin and collagen, and ground substance such as glycosaminoglycan (GAG)/proteoglycans (PG). The ECM goes through continuous physiological remodelling which involves the degradation of existing proteins and subsequent synthesis of new protein to maintain its integrity [23]. However, in various pathologies, the ECM undergoes abnormal remodeling, thereby perturbing its homeostasis which is necessary for preserving the tissue’s structure-functional relationships [23–26]. The independent contribution of elastin and collagen to aortic mechanical properties has been an ongoing area of investigation [27–32], while that of GAG/PG only gained attention recently and remains poorly understood [33,34]. In addition, contradicting information has been reported on the contribution of the ECM to the mechanical properties [28,29], and knowledge on how the interaction between the ECM constituents affects the mechanical properties of the aorta is limited.

Interesting phenomena in the ECM are the deposition of enzymatic crosslinks, and non-enzymatic crosslinks which forms advanced glycation end products (AGEs). Although immature enzymatic crosslinks, and AGEs are initially found during the early stages of growth and development [35–37], they are also implicated in aging and disease such as aneurysms [38,39]. Furthermore, while the effect of glycation crosslinks on aortic stiffness has been thoroughly studied, where crosslink accumulation has been shown to be associated with an increase in stiffness [40,41], the direct contribution of glycation crosslinks to residual stresses has not yet been investigated.

Compelling evidence supports the understanding that the quantity, distribution, orientation and interconnection of the ECM constituents modulate the mechanical properties in the aorta [42]; however, our understanding remains incomplete. A thorough comprehension of these relationships is a prerequisite to establishing predictive computational tools for assessing risk of ruptures in clinical settings. Overall, the work presented in this thesis is expected to have far-reaching consequences on the current understanding of aortic mechanics through its contribution of new knowledge of the effect of ECM constituents on aortic mechanics, mainly GAG and residual stresses.

## 1.2 OBJECTIVES

The purpose of this work was to investigate how the aortic ECM modulates residual stresses present in the aortic wall, as well as the mechanical properties of the aorta. The work was governed by the primary hypothesis that GAG regulate residual stress. The primary focus was placed on the study of the contribution of GAG to residual stresses. Our work towards this overarching goal was subdivided into multiple objectives and investigated through combined experimental and computational studies.

### 1.2.1 Objective 1

The first objective was to establish a finite element framework in FEBio [43], an open-source finite element software, to simulate the effect of GAG in a computer model, and to replicate the results reported by Azeloglu et al. [33], who studied the effect of GAG on residual stresses in rodent aortic rings under different external bath osmolarities. Furthermore, our purpose was to modify the existing rodent model to provide insights into the influence of GAG in porcine animals, which are larger and more representative of human physiology, and are readily available for experimental investigations, reflecting the tissue resources accessible to us.

### 1.2.2 Objective 2

The rodent model by Azeloglu et al. [33] and the porcine model we built in Objective 1 were associated with certain limitations. Namely, prescribed GAG distributions were obtained from Leghorn chickens, and were based on qualitative histological observations [44,45]. This facilitated the execution of parametric studies, allowing us to gain initial insights into the influence of GAG on the opening angle and mechanical stress distribution in the porcine aorta.

However, the quantity and distribution of GAG is expected to vary between species and the different regions of the aortic tree. As such, Objective 2 was to characterize the mural distributions of GAG and major ECM molecules, collagen and elastin, in young (5-6 months old) pig aortas and to evaluate the correlations between GAG and the opening angle, in addition to those of collagen and elastin, in order to acquire a better understanding of how the main ECM constituents collectively influence residual stresses in the aorta.

### 1.2.3 Objective 3

The correlations deciphered under Objective 2 provide important insights on possible contributions of distinct ECM constituents to residual stresses and the potential interactions between them. However, to mitigate unwarranted causal assumptions, our Objective 3 was to elucidate the precise influence of GAG on residual stress and compressive properties, which remain to date poorly understood, via enzymatic depletion and to identify other factors that may play a role in modulating residual stresses in the aorta, such AGE accumulation which occurs with age and disease.

### 1.2.4 Objective 4

Objective 4 was to create animal-specific aortic ring models using the experimental anatomical dimensions and mural GAG distributions acquired in Objectives 2 and 3 in order to capture the effect of GAG on residual stress through a computational finite element model using FEBio [43]. Furthermore, our Objective 4 was also to mathematically describe the solid matrix' mechanical behavior from biaxial tensile data. In addition to modelling the matrix as one layer, the distinct elastic properties of the intima-media and the adventitia were considered by modelling the solid matrix as two layers.

## 1.3 OBJECTIVES ORGANIZATION

Chapters 1, 2 and 3 in Section I lay the foundation through a comprehensive literature review, followed by individual chapters dedicated to addressing each of the objectives in-depth, in Section II of this dissertation. Objective 1 is presented in Chapter 4 and was published in the 2020 42nd Annual International Conference of the IEEE Engineering in Medicine & Biology Society (EMBC) [43]. Objective 2 is discussed in detail in Chapter 5 through a published study in Annals on Biomedical Engineering [46]. Objective 3 is presented in Chapter 6, and was accepted by Acta Biomaterialia at the time of submission of this thesis. Finally, Objective 4 is detailed in Chapter 7 as a manuscript that has been prepared for submission. The closing discussion is in Section III.

## 1.4 REFERENCES

[1] World Health Organization, Cardiovascular diseases (CVDs), (2021). https://www.who.int/news-room/fact-sheets/detail/cardiovascular-diseases-(cvds) (accessed March 13, 2023).

[2] J.A. Elefteriades, E.A. Farkas, Thoracic Aortic Aneurysm, Journal of the American College of Cardiology. 55 (2010) 841–857. https://doi.org/10.1016/j.jacc.2009.08.084.

[3] R.S. McClure, S.B. Brogly, K. Lajkosz, D. Payne, S.F. Hall, A.P. Johnson, Epidemiology and management of thoracic aortic dissections and thoracic aortic aneurysms in Ontario, Canada: A population-based study, The Journal of Thoracic and Cardiovascular Surgery. 155 (2018) 2254-2264.e4. https://doi.org/10.1016/j.jtcvs.2017.11.105.

[4] A.M. Booher, K.A. Eagle, Diagnosis and management issues in thoracic aortic aneurysm, American Heart Journal. 162 (2011) 38-46.e1. https://doi.org/10.1016/j.ahj.2011.04.010.

[5] J.A. Elefteriades, E.A. Farkas, Thoracic Aortic Aneurysm, Journal of the American College of Cardiology. 55 (2010) 841–857. https://doi.org/10.1016/j.jacc.2009.08.084.

[6] O. Trabelsi, F.M. Davis, J.F. Rodriguez-Matas, A. Duprey, S. Avril, Patient specific stress and rupture analysis of ascending thoracic aneurysms, Journal of Biomechanics. 48 (2015) 1836–1843. https://doi.org/10.1016/j.jbiomech.2015.04.035.

[7] Canadian Task Force on Preventive Health Care, Abdominal Aortic Aneurysm—Clinician Summary – Canadian Task Force on Preventive Health Care, (n.d.).

https://canadiantaskforce.ca/abdominal-aortic-aneurysm-clinician-summary/ (accessed March 13, 2023).

[8] J.A. Elefteriades, E.A. Farkas, Thoracic Aortic Aneurysm: Clinically Pertinent Controversies and Uncertainties, Journal of the American College of Cardiology. 55 (2010) 841–857. https://doi.org/10.1016/j.jacc.2009.08.084.

[9] M. Fillinger, Who Should We Operate On and How Do We Decide: Predicting Rupture and Survival in Patients with Aortic Aneurysm, Seminars in Vascular Surgery. 20 (2007) 121–127. https://doi.org/10.1053/j.semvascsurg.2007.04.001.

[10] M.F. Fillinger, M.L. Raghavan, S.P. Marra, J.L. Cronenwett, F.E. Kennedy, In vivo analysis of mechanical wall stress and abdominal aortic aneurysm rupture risk, Journal of Vascular Surgery. 36 (2002) 589–597. https://doi.org/10.1067/mva.2002.125478.

[11] J.Z. Goldfinger, J.L. Halperin, M.L. Marin, A.S. Stewart, K.A. Eagle, V. Fuster, Thoracic Aortic Aneurysm and Dissection, Journal of the American College of Cardiology. 64 (2014) 1725–1739. https://doi.org/10.1016/j.jacc.2014.08.025.

[12] F.A. Lederle, S.E. Wilson, G.R. Johnson, D.B. Reinke, F.N. Littooy, C.W. Acher, D.J. Ballard, L.M. Messina, I.L. Gordon, E.P. Chute, W.C. Krupski, S.J. Busuttil, G.W. Barone, S. Sparks, L.M. Graham, J.H. Rapp, M.S. Makaroun, G.L. Moneta, R.A. Cambria, R.G. Makhoul, D. Eton, H.J. Ansel, J.A. Freischlag, D. Bandyk, Immediate repair compared with surveillance of small abdominal aortic aneurysms, The New England Journal of Medicine. 346 (2002) 1437–44.

[13] D. Rc, M. Cr, B. Dc, O. Lw, Autopsy study of unoperated abdominal aortic aneurysms. The case for early resection., Circulation. 56 (1977) II161-4.

[14] Y. Lanir, Mechanisms of Residual Stress in Soft Tissues, Journal of Biomechanical Engineering. 131 (2009) 044506. https://doi.org/10.1115/1.3049863.

[15] J.A. Peña, M.A. Martínez, E. Peña, Layer-specific residual deformations and uniaxial and biaxial mechanical properties of thoracic porcine aorta, Journal of the Mechanical Behavior of Biomedical Materials. 50 (2015) 55–69. https://doi.org/10.1016/j.jmbbm.2015.05.024.

[16] C.J. Chuong, Y.C. Fung, On Residual Stresses in Arteries, Journal of Biomechanical Engineering. 108 (1986) 189–192. https://doi.org/10.1115/1.3138600.

[17] A. Saini, C. Berry, S. Greenwald, Effect of Age and Sex on Residual Stress in the Aorta, JVR. 32 (1995) 398–405. https://doi.org/10.1159/000159115.

[18] G.L. Pierce, T.A. Coutinho, L.E. DuBose, A.J. Donato, Is It Good to Have a Stiff Aorta with Aging? Causes and Consequences, Physiology. 37 (2022) 154–173. https://doi.org/10.1152/physiol.00035.2021.

[19] J.J. DuPont, R.M. Kenney, A.R. Patel, I.Z. Jaffe, Sex differences in mechanisms of arterial stiffness, Br J Pharmacol. 176 (2019) 4208–4225. https://doi.org/10.1111/bph.14624.

[20] S.Z. Pagoulatou, M. Ferraro, B. Trachet, V. Bikia, G. Rovas, L.A. Crowe, J.-P. Vallée, D. Adamopoulos, N. Stergiopulos, The effect of the elongation of the proximal aorta on the estimation of the aortic wall distensibility, Biomech Model Mechanobiol. (2020). https://doi.org/10.1007/s10237-020-01371-y.

[21] S.S. DeLoach, R.R. Townsend, Vascular Stiffness: Its Measurement and Significance for Epidemiologic and Outcome Studies, CJASN. 3 (2008) 184–192. https://doi.org/10.2215/CJN.03340807.

[22] J.J. DuPont, R.M. Kenney, A.R. Patel, I.Z. Jaffe, Sex differences in mechanisms of arterial stiffness, Br J Pharmacol. 176 (2019) 4208–4225. https://doi.org/10.1111/bph.14624.

[23] S. Jana, M. Hu, M. Shen, Z. Kassiri, Extracellular matrix, regional heterogeneity of the aorta, and aortic aneurysm, Experimental & Molecular Medicine. 51 (2019) 1–15. https://doi.org/10.1038/s12276-019-0286-3.

[24] A. Mammoto, K. Matus, T. Mammoto, Extracellular Matrix in Aging Aorta, Front Cell Dev Biol. 10 (2022) 822561. https://doi.org/10.3389/fcell.2022.822561.

[25] F.S. Cikach, C.D. Koch, T.J. Mead, J. Galatioto, B.B. Willard, K.B. Emerton, M.J. Eagleton, E.H. Blackstone, F. Ramirez, E.E. Roselli, S.S. Apte, Massive aggrecan and versican accumulation in thoracic aortic aneurysm and dissection, JCI Insight. 3 (2018). https://doi.org/10.1172/jci.insight.97167.

[26] A. Didangelos, X. Yin, K. Mandal, A. Saje, A. Smith, Q. Xu, M. Jahangiri, M. Mayr, Extracellular Matrix Composition and Remodeling in Human Abdominal Aortic Aneurysms: A Proteomics Approach, Mol Cell Proteomics. 10 (2011) M111.008128. https://doi.org/10.1074/mcp.M111.008128.

[27] V. Alastrué, E. Peña, M.Á. Martínez, M. Doblaré, Assessing the Use of the “Opening Angle Method” to Enforce Residual Stresses in Patient-Specific Arteries, Ann Biomed Eng. 35 (2007) 1821–1837. https://doi.org/10.1007/s10439-007-9352-4.

[28] S.E. Greenwald, J.E. Moore, A. Rachev, T.P.C. Kane, J.-J. Meister, Experimental Investigation of the Distribution of Residual Strains in the Artery Wall, Journal of Biomechanical Engineering. 119 (1997) 438–444. https://doi.org/10.1115/1.2798291.

[29] P.J. Zeller, T.C. Skalak, Contribution of individual structural components in determining the zero-stress state in small arteries, J Vasc Res. 35 (1998) 8–17. https://doi.org/10.1159/000025560.

[30] J.-W.M. Beenakker, B.A. Ashcroft, J.H.N. Lindeman, T.H. Oosterkamp, Mechanical Properties of the Extracellular Matrix of the Aorta Studied by Enzymatic Treatments, Biophysical Journal. 102 (2012) 1731–1737. https://doi.org/10.1016/j.bpj.2012.03.041.

[31] H. Åstrand, J. Stålhand, J. Karlsson, M. Karlsson, B. Sonesson, T. Länne, In vivo estimation of the contribution of elastin and collagen to the mechanical properties in the human abdominal aorta: effect of age and sex, Journal of Applied Physiology. 110 (2010) 176–187. https://doi.org/10.1152/japplphysiol.00579.2010.

[32] E. Fonck, G. Prod'hom, S. Roy, L. Augsburger, D.A. Rüfenacht, N. Stergiopulos, Effect of elastin degradation on carotid wall mechanics as assessed by a constituent-based biomechanical model, 292 (2007) 10.

[33] E.U. Azeloglu, M.B. Albro, V.A. Thimmappa, G.A. Ateshian, K.D. Costa, Heterogeneous transmural proteoglycan distribution provides a mechanism for regulating residual stresses in the aorta, American Journal of Physiology-Heart and Circulatory Physiology. 294 (2008) H1197–H1205. https://doi.org/10.1152/ajpheart.01027.2007.

[34] J.M. Mattson, R. Turcotte, Y. Zhang, Glycosaminoglycans contribute to extracellular matrix fiber recruitment and arterial wall mechanics, Biomech Model Mechanobiol. 16 (2017) 213–225. https://doi.org/10.1007/s10237-016-0811-4.

[35] A. Brüel, G. Ørtoft, H. Oxlund, Inhibition of cross-links in collagen is associated with reduced stiffness of the aorta in young rats, Atherosclerosis. 140 (1998) 135–145. https://doi.org/10.1016/S0021-9150(98)00130-0.

[36] F. Chiarelli, M. de Martino, A. Mezzetti, M. Catino, G. Morgese, F. Cuccurullo, A. Verrotti, Advanced glycation end products in children and adolescents with diabetes: Relation to glycemic control and early microvascular complications, The Journal of Pediatrics. 134 (1999) 486–491. https://doi.org/10.1016/S0022-3476(99)70208-8.

[37] D. Fujimoto, Aging and cross-linking in human aorta, Biochemical and Biophysical Research Communications. 109 (1982) 1264–1269. https://doi.org/10.1016/0006-291X(82)91913-1.

[38] A. Prasad, P. Bekker, S. Tsimikas, Advanced Glycation End Products and Diabetic Cardiovascular Disease, Cardiology in Review. 20 (2012) 177–183. https://doi.org/10.1097/CRD.0b013e318244e57c.

[39] D. Koole, J.A. van Herwaarden, C.G. Schalkwijk, F.P.J.G. Lafeber, A. Vink, M.B. Smeets, G. Pasterkamp, F.L. Moll, A potential role for glycated cross-links in abdominal aortic aneurysm disease, Journal of Vascular Surgery. 65 (2017) 1493-1503.e3. https://doi.org/10.1016/j.jvs.2016.04.028.

[40] E. Konova, S. Baydanoff, M. Atanasova, A. Velkova, Age-related changes in the glycation of human aortic elastin, Experimental Gerontology. 39 (2004) 249–254. https://doi.org/10.1016/j.exger.2003.10.003.

[41] D. Aronson, Cross-linking of glycated collagen in the pathogenesis of arterial and myocardial stiffening of aging and diabetes:, Journal of Hypertension. 21 (2003) 3–12. https://doi.org/10.1097/00004872-200301000-00002.

[42] J.D. Humphrey, Cardiovascular Solid Mechanics: Cells, Tissues, and Organs, Springer Science & Business Media, 2002.

[43] S.A. Maas, B.J. Ellis, G.A. Ateshian, J.A. Weiss, FEBio: Finite Elements for Biomechanics, J Biomech Eng. 134 (2012) 11005-NaN. https://doi.org/10.1115/1.4005694.

[44] E.U. Azeloglu, M.B. Albro, V.A. Thimmappa, G.A. Ateshian, K.D. Costa, Heterogeneous transmural proteoglycan distribution provides a mechanism for regulating residual stresses in the aorta, American Journal of Physiology-Heart and Circulatory Physiology. 294 (2008) H1197–H1205. https://doi.org/10.1152/ajpheart.01027.2007.

[45] S. Porterfield, T. Calhoon, H. Weiss, Changes in connective tissue colloidal charge density with atherosclerosis and age, American Journal of Physiology-Legacy Content. 215 (1968) 324–329. https://doi.org/10.1152/ajplegacy.1968.215.2.324.

[46] N.M. Ghadie, J.-P. St-Pierre, M.R. Labrosse, Intramural Distributions of GAGs and Collagen vs. Opening Angle of the Intact Porcine Aortic Wall, Ann Biomed Eng. 50 (2022) 157–168. https://doi.org/10.1007/s10439-022-02901-8.

# 2 LITERATURE REVIEW

Background

## 2.1 INTRODUCTION

The purpose of this chapter is to provide the background information and fundamental concepts that apply to the research presented in the subsequent chapters. As our focus centers around the aorta, we start with a description of its anatomy, followed by an examination of its key extracellular matrix (ECM) constituents. Additionally, we delve into the mechanical behavior of soft tissues, like the aorta, which differs significantly from traditional engineering materials. As such, we present a concise overview of the essential concepts in continuum mechanics for soft tissues. The understanding of these concepts is necessary for developing accurate mathematical models that characterize the mechanical behavior of soft tissues. In this work, this was required to conduct studies on aortic models, which are crucial for analyzing their physical behavior through finite element analysis.

## 2.2 AORTIC STRUCTURE

### 2.2.1 Anatomy of the Aorta

The aorta is the main systemic elastic artery that transports oxygen-rich blood to the rest of the body. It consists of the aortic root, the ascending (or tubular ascending) region, the aortic arch, the descending thoracic region, which lie above the diaphragm, and the abdominal region, below the diaphragm [1,2]. An illustration is provided in Figure 3.1. The aorta tapers in diameter from its beginning in the ascending region to its end, and increases in size with age [1,3], height, and weight [4]. The normal aortic diameter depends on the reference population, given that the aortic size varies between individuals. As an example, for a group of individuals of ages ranging between 17 and 92 years (61% male), the mean normal aortic diameter was approximately 3.4 and 2.8 cm in the ascending and arch portions, and 2.4 - 2.5 cm in the descending thoracic aorta [5].

The aorta originates from the left ventricle via the aortic root, which is a composite structure that consists of the annulus, the aortic sinuses (or sinuses of Valsalva), the leaflets of the aortic valve, and the sinotubular junction which interfaces with the ascending aorta, in addition to the origins of the coronary arteries [2,6]. The ascending aorta does not feature any branches, and gives rise to the aortic arch, which ascends diagonally to the left of the fourth thoracic vertebrae, and forms a caned-shape curve. Three arterial trunks arise from the upper convex portion of the arch in human, which are the brachiocephalic artery, the left common carotid artery, and the left subclavian artery [2]. These supply blood to the neck, head and arms [4]. The descending thoracic aorta then begins near the fourth/fifth thoracic vertebra and reaches the diaphragm at the twelfth thoracic vertebra where the abdominal aorta begins [2,4,7]. Numerous small branches initiate from the descending thoracic aorta, mainly the intercostal arteries, in addition to the spinal, esophageal, and bronchial arteries, which supply blood to the spine, diaphragm, chest wall, pericardium, lungs and esophagus [7]. The abdominal aorta runs from the diaphragm and branches into several arteries including the celiac artery, the superior and inferior mesenteric arteries, the renal arteries. The abdominal aorta ends above the pelvis where it bifurcates into the iliac arteries which supply blood to the legs and the organs of the pelvis [8,9].

### 2.2.2 The Normal Aortic Wall

The aortic wall is non homogeneous comprised of three main layers: the intima, the media and the adventitia, which are illustrated in Figure 3.1. The intima is the innermost layer that lines the lumen, and occupies the smallest proportion of the normal aortic wall [10]. The intima is believed to consists of a single layer in the early stages of life, but can remodel into a thicker proportion with age [11–13], or due to chronic diseases, such as atherosclerosis [14] or aneurysm [10]. In a healthy, young subject, the intima mainly consists of a single layer of endothelial cells and an underlying basement membrane (also referred to as basal lamina) [1,15]. In the aorta, the intima could also contain a subendothelial layer of connective tissue and smooth muscle cells [1]. Endothelial cells are thought to be elongated longitudinally in the direction of blood flow [1,12], with a length of approximately 25 to 50 µm. The width and thickness of endothelial cells are about 10 to 15 µm, and 0.2 to 0.5 µm respectively [1]. Endothelial cells secrete and allow for exchange of bioactive substances. They also contribute to the maintenance of physiological equilibrium with respect to thrombosis, and act as barriers to blood to maintain a smooth intimal surface [16]. Endothelial cells may also communicate with the smooth muscle cells via the basement membrane [1]. The basement membrane serves as an extracellular matrix network on which endothelial cells can grow, and is made of primarily laminin, collagen type IV, and proteoglycans [1,15].

The intima and media are interfaced by the internal elastic lamina which consists of a sheet of elastin. The media occupies the largest proportion of the thoracic aortic wall, and its thickness varies with age and position along the aortic tree [11]. The most abundant cell types in the media are smooth muscle cells (SMCs), which are embedded in an ECM. Generally, SMCs possess a spindle shape, and are oriented circumferentially with an approximate length of 100 µm – 200 µm [1,15,17], except in minor cases like near bifurcations [1]. They possess different roles and configurations in small and large vessels, and in elastic and muscular arteries, and also vary between species. In the aorta, an elastic artery, SMCs are mainly arranged side by side and sandwiched between sheets of elastin, into concentric layers, providing a highly organized medial layer [1,16]. Especially in muscular arteries, and also to some extent in elastic arteries, SMCs contribute to regulating blood flow through their ability to relax and contract and are able to respond to mechanical stimuli. They also synthesize the ECM, mainly comprised of elastin, collagen, mainly type I, III, and V, in addition to ground substance such as GAG [1]. Their proliferation is normally slow except in the case of pathogenesis, during which their phenotype and ECM production rate become impaired [12,18].

The external elastic lamina separates the media from the adventitia, the outermost layer of the aortic wall. Similar to the intima and media, the thickness of the adventitia depends on several factors and occupies different proportions in the aortic tree [1,19]. Particularly, in the abdominal aorta the adventitia is considerably thicker than in the thoracic aorta [15]. The adventitia is rich in fibroblasts, collagen namely type I, elastin, nerves and vasa vasorum [1,16]. The adventitia is thought to act as a physical barrier mainly to limit overdistension in the aorta [1], but also plays roles in coordinating the progression of aortic disease [16].

## 2.3 THE EXTRACELLULAR MATRIX

The ECM is a complex meshwork that makes up a key component of the aortic wall, and is synthesized by SMCs, endothelial cells in the intima and fibroblasts in the adventitia. The ECM possesses various functions such as providing tissue with strength, extensibility, resilience and shape, providing cells with a scaffold on which they can adhere and migrate [1]. The ECM of the aorta is primarily comprised of collagen, elastin and GAG. The fibrous constituents, collagen and elastic fibers, are the dominant ECM components of the aortic wall, accounting for approximately 50% by dry weight [15,20].

### 2.3.1 Collagen

Collagen are long, fibrous structural proteins, and are a family of the most abundant type of proteins in the human body, accounting for around 25-30% of human mass protein [21]. Collagen possesses a high rate of turnover, allowing for damaged collagen to be quickly replaced by newly synthesized fibers. The mean turnover rate is thought to be around 3 to 5%/day, and could exceed 10%/day in certain tissues [22]. Collagen fibers are synthesized hierarchically by cells. At the molecular lever, they comprise three polypeptide $\alpha$ chains, which can be identical or different, depending on each collagen type. The three polypeptide $\alpha$ chains are wrapped into a tight collagen triple helix and are made of repeated patterns of Gly-X-Y [23]. Here, “Gly” refers to glycine, and X and Y refer to any other amino acid of the remaining 19 types [1]. The most common type of sequences however involve proline, with glycine being at every third residue [24,1,23]. The collagen triple helices are on the order of 285-300 nm long, and 1.4-2.0 nm in diameters [1,25]. At this stage, they are referred to as procollagen [25] or tropocollagen [21], and can polymerize into microfibrils and subfibrils, which are on the order of 4 to 25 nm in diameter [1,21]. These are further organized in packs, side by side with a periodicity of 67 nm called D-period, to form a collagen fibril [1,21,23,25]. Collagen fibrils have lengths and diameters on the order of 1 µm [21] and 10-500 nm respectively [1]. Fibrils are further bundled together to form collagen fibers that vary in length and diameter (1 – 500 µm). Fibrils and fibers are further stabilized by crosslinks, and form a disordered collagen matrix [21].

At least 28 different types of collagen have been identified so far, with collagen type I being the most abundant [21,25]. Collagen types are mediated by the differences in assembly at the level of the hierarchy, including the $\alpha$ chains as mentioned earlier. As an example, collagen type I possesses two $\alpha_1(I)$ and one $\alpha_2(I)$ chains. In the cardiovascular system, existing collagen types include collagen type I, III, and IV, in addition to type V, VI, and VIII [1]. In the aorta, the type I and type III collagen are dominant, accounting for 80-90% of the total collagen present in the aortic wall [20,26]. Although understanding the biomechanical roles of collagen remains an area of investigation, one of the main functions of collagen in the aorta is to provide tensile strength. Under physiological load, collagen fibers are undulated in the aorta, and therefore exhibit their true stiffness only once straightened [1].

### 2.3.2 Elastin

Elastic fibers are macromolecules primarily composed of elastin, a highly hydrophobic ECM protein that provides elasticity to the aorta and other arteries in the cardiovascular system [27,28]. Elastin is stable with a half life of 40-70 years [27,29], but has a very low rate of turnover [30], limiting its ability to repair when damaged. This is an unusual characteristic of an ECM constituent, because generally ECM production is dynamic throughout the lifespan of an individual [27]. Elastic fibers are composite structures formed of a core that is made of mature elastin, which makes up more than 90% of the fiber, and an outer layer of fibrillin and microfibrils [31], mostly composed of fibrillin -1 and -2 [27]. Mature elastin is an insoluble polymer and consists of tropoelastin molecules that are covalently bound to each other by crosslinks [32]. Elastin is synthesized through a complex process called elastogenesis [32], which is still under study and has been a matter of debate for several decades [27,33]. The process starts from the cells, which synthesize the tropoelastin molecule [32], known for its ability to expand to more than 8 times of its original length, making it one of the most extensible and elastic monomer proteins [28]. After secretion, tropoelastin is released into the extracellular space, and undergoes crosslinking through enzymes from the lysyl-oxidase family, and coacervation, a thermodynamic process through which troposelastin assembles into aggregates [27]. Elastin plays major roles in modulating the mechanical properties of the cardiovascular system including the aorta, as well as in disease. Elastic fibers' main mechanical characteristic is to provide reversible stretchability (compliance), given their ability to stretch when loaded and revert back to their original size when unloaded [25]. In the aorta, the amounts of elastin are highest in the proximal aorta, and decreases distally from the heart. Their elastic contribution to the aorta is recognized and modelled as the Windkessel effect [27].

### 2.3.3 Glycosaminoglycans/Proteoglycans

Briefly, GAG are negatively-charged polysaccharide compounds that are composed of repeating disaccharide units. Most GAG are covalently bound to protein cores to form a category of modified proteins known as PG. A detailed review on GAG/PG, central to this dissertation, is provided in Chapter 3.

### 2.3.4 Crosslinks & Advanced Glycation End Products

Crosslinking is the process of joining molecules through intermolecular covalent bonds [34]. Generally speaking, there are two major types of crosslinks: enzymatic and non-enzymatic [34–36]. Enzymatic crosslinking is mediated by lysyl-oxidase, and provides elastin and collagen with stability, which is crucial to their normal function [34,35,37]. In collagen, the biosynthesis of enzymatic crosslinks starts with the reduction of lysyl- or hydroxylysyl- residues by lysyl-oxidase into aldehydes [34]. These aldehydes (lysyl- or hydroxylysyl- aldehydes) then undergo a series of condensation reactions to first form the dehydro-hydroxylysinonorleucine (HLNL) and dehydro-dihydroxylysinonorleucine (DHLNL) divalent cross-links [36,37]. These then further react with lysyl- or hydroxylysyl- residues to form multivalent mature crosslinks, which are mainly pyridinoline and deoxy-pyridinoline [34,37]. Although still elusive, elastin crosslinks are synthesised through a similar process, mainly via the reduction of lysyl- or hydroxylysyl- residues, to form elastin crosslinks which are primarily desmosine and isodesmosine [34,36,37].

Non-enzymatic crosslinking is mediated by glycated lysyl- residues to form advanced glycation end products (AGEs) [34]. AGEs are sugar crosslinks and are also known as glycotoxins [38]. AGEs are heterogeneous and complex structures, and their characterization remains elusive [39]. In general, AGEs are produced from non-enzymatic reactions between a sugar and free amino acid groups in proteins [39,40]. This reaction was first described by Louis Camille Maillard in the early 1900s [41]. The common driving force for the creation of AGEs is oxidative stress, leading to the formation of glycoxidation products. Examples of glycoxidation products include pentodisine, $N^e$-carboxymethyl-lysine (CML), and glyoxal CML glyoxal-lysine dimer (GOLD) [39,40]. Pentosidine is the most well known and studied AGE, with fluorescent properties [34]. Other types of AGEs that can be produced via non-oxidative rearrangement include methyl glyoxal-lysine dimer (MOLD) and pyrraline deoxyglucasone-lysine dimer (DOLD) [39,40]. Even though AGEs are complex and exist in different types, they are known to produce the same chemical outcome, being the formation of covalent crosslinks between the proximate amino acid groups of proteins [39,42].

Although immature enzymatic crosslinks, like HLNL and DHLNL, and AGEs are present during the early stages of growth and development [37,43,44], they are also implicated in disease and aging. For instance, AGEs accumulation contributes to age-related connective tissue deficit [45], neurological conditions such as Alzheimer's [39], and are implicated in a wide range of pathologies such as rheumatoid arthritis [39], diabetes and cardiovascular diseases [40]. Similarly, with age, mature crosslinks such as pyridinoline, and AGEs such as pentosidine and CML, are thought to accumulate [40,44,46,47].

In the aorta, extensive crosslinking of collagen and elastin alters their physical properties, which reduces the aortic compliance (or causes aortic stiffening) [48–50]. For instance, experimental studies performed on rats aged 4.5, 14 and 27 months demonstrated that collagen and elastin AGE markers (collagen and elastin fluorescence) were increased in aortas from the older rats compared to the adult rats by 42% and 17% respectively, and that the AGE markers positively correlated with the aortic stiffness [47]. Additionally, breaking AGEs in rat subjects with alagebrium chloride (ALT-711), a non-enzymatic breaker of AGE crosslinks, increased the aortic compliance, distensibility and diameter [51]. Similarly, in a clinical study the total arterial compliance increased in human subjects treated with ALT-711 [52].

AGEs have also been found to be implicated in many other cardiovascular diseases such as hypertension [53], atherosclerosis [54] and aneurysms [55,56], and have been shown to play a role in the development of diabetic cardiovascular complications [40]. McNulty et al. demonstrated that the concentration of plasma AGEs is significantly higher in hypertensive patients compared to normotensive subjects, and also showed that it relates to aortic stiffness [53]. Kume et al. performed a study on 22 atherosclerotic aortic wall samples from autopsies, and showed AGE accumulation in the intimal lesions in more than 50% of the aortic atherosclerosis samples in addition to intracellular accumulation in the atherosclerotic plaques and fatty streaks [57]. Glycation has also been shown to be accelerated in the human aorta with age and diabetes [57]. Additionally, AGEs have been shown to be involved in TAA and have been proposed as a new risk factor, as AGE levels have been found to be increased in patients suffering from TAA [127].

## 2.4 SOFT TISSUE BEHAVIOR

Blood vessels, skin, tendons and ligaments are examples of soft biological tissues which are typically fiber reinforced composite structures, generally consisting of collagen and elastin. Because of their compositions, soft tissues are heterogeneous at the microscopic scale. Soft tissues generally have high flexibility and are distinct from hard mineralized tissue such as bone [58]. Their biomechanical behavior is dictated by the integrated manifestation and interaction of its constituents such as collagen, elastin and the hydrated matrix of GAG/PG [1,58]. Biological soft tissues share common characteristics even though each of them possesses a unique behavior [1].

The aorta amongst other soft tissues displays a J-shaped non-linear tensile stress-strain relationship, as shown in Figure 2.1A. This significantly differs from stress-strain relationships of hard tissue or engineering materials such as steel, which are characterized by a linear curve in the elastic phase and are therefore characterized by an intrinsic stiffness or Young's modulus, defined as the (constant) slope of the curve. By contrast, the slope of a non-linear material stress-strain behavior varies along the curve. Additionally, consistent with a J-shape, the curve for soft tissue typically begins with a compliant toe region, and exhibits much stiffer responses over finite stretches [1].

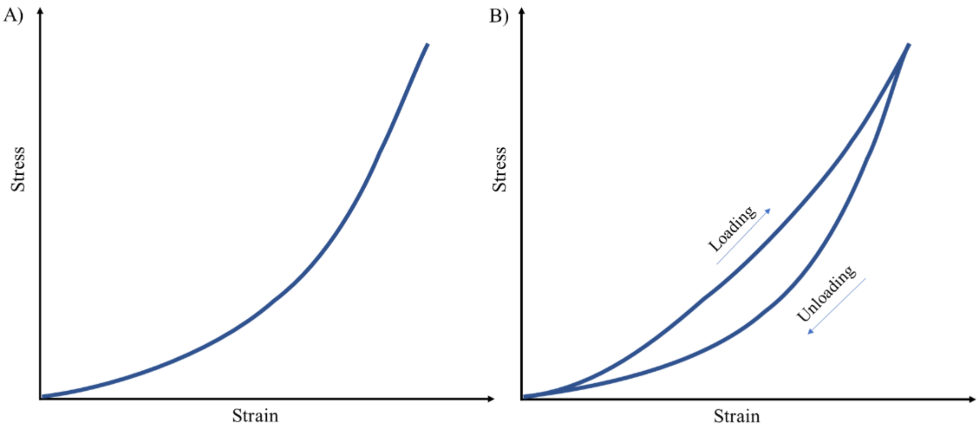

*Figure 2.1:(A) Schematic of typical stress-strain relationship of soft biological tissue. (B) Representative figure of a hysteresis loop showing the loading and unloading paths.*

Many soft biological tissues also exhibit anisotropy which refers to the dependency of the mechanical response on the material or loading direction. This is due to the organization of the ECM fibers, which tend to possess a preferred orientation [1,58]. However, based on experimentations conducted on porcine and human samples, both isotropic (or quasi-isotropic)

[59,60] and anisotropic behaviors of the aorta, namely displaying a stiffer response in the fiber (circumferential) direction [61,62], have been reported. Many soft tissues also experience hysteresis, a process through which the loading and unloading cycles of the stress-strain response do not coincide, indicating loss of energy and representing an inelastic response. This is illustrated in Figure 2.1B and the material is said to have no memory of motion. To reach repeatable loading and unloading curves, samples can be preconditioned. The process of preconditioning involves applying a number of loading cycles until the loading and unloading paths coincide [1,63]. Because soft biological tissue contain water, they are nearly incompressible and also exhibit viscoelastic properties. Viscoelasticity combines elastic (stress proportional to instantaneous magnitude of strain) and viscous (stress proportional to time rate of change of strain) behaviors. Viscoelastic materials are sensitive to the rate of applied loading and exhibit creep and stress relaxation. Creep is the process through which the strain varies with time under constant load, and stress-relaxation is the process through which stress decreases over time when material is held at constant strain [23,64]. Nevertheless, in the context of quasi-static loading that can be set in *in vitro* experiments, viscoelastic effects may be neglected, as done in the present work. Finally, the characteristics of a material define the theoretical framework adopted for analysing how tissues behave in health and disease. A concise overview on continuum mechanics relevant to soft tissues is therefore provided next.

## 2.5 PRELIMINARIES IN CONTINUUM MECHANICS

Generally speaking, mechanics is the branch of applied mathematics and physics that studies the behavior of bodies under the action of applied forces. Continuum mechanics in turn, is the branch of mechanics that is based on the continuum hypothesis. The continuum hypothesis approximates the mechanical behavior of a body by assuming average properties, rather than taking into account its discrete nature especially at the microscopic level, and therefore the macroscopic behavior of a body can be modelled assuming that matter is continuous. In this section, we provide a brief overview on basic concepts and notations in continuum mechanics. The understanding of these concepts is fundamental to the development of mathematical models, called constitutive models, that can model the mechanical behavior of tissues and that are requisites to conducting finite element analysis. The notions provided in this section are from "Nonlinear continuum mechanics for finite element analysis" [65] and "Cardiovascular solid mechanics: cells, tissues, and organs" [1].

### 2.5.1 The Deformation Gradient

Consider the deformation of an object from a reference configuration ($\beta_o$) at time t = 0, to a current (or deformed) configuration ($\beta_t$) at time t. The position vector of a given particle in $\beta_o$ is $\vec{X}$, and in $\beta_t$ is $\vec{x}$, where the coordinate systems are {O, $\overrightarrow{E_A}$} and {o, $\overrightarrow{e_\iota}$} respectively. Here, $\overrightarrow{E_A}$ and $\overrightarrow{e_\iota}$ are orthonormal bases, with indices 1,2,3 to describe the 3-D space. The position vectors can therefore be represented as $\vec{X} = X_A \overrightarrow{E_A}$ and $\vec{x} = x_\iota \overrightarrow{e_\iota}$, using the Einstein summation convention where entities with repeated indices are summed, and $\vec{X}$ and $\vec{x}$ are known as the material and spatial coordinates respectively. Without loss of generality, the origins O and o are set to coincide. The displacement vector from $\beta_o$ to $\beta_t$ is therefore $\vec{u} = \vec{x} - \vec{X}$.

Because we are interested in describing the motion of material particles, differential line segments $d\vec{X}$ and $d\vec{x}$ in $\beta_o$ and $\beta_t$ are introduced. Knowing that a second order tensor transforms a vector into another vector, the transformation gradient $\bar{\bar{F}}$ that relates the infinitesimal vector in the reference configuration $d\vec{X}$ into the corresponding vector in the current configuration $d\vec{x}$ is defined using the dot product, such that:

$$d\vec{x} = \bar{\bar{F}} \cdot d\vec{X}$$

The determinant of the transformation gradient is the volume ratio $J = \frac{dv}{dV} = \det \bar{\bar{F}}$, where $dV$ and $dv$ are the differential volumes in $\beta_o$ and $\beta_t$ respectively. Therefore, $\det \bar{\bar{F}}$ maps the original differential volumes to the current ones. Note that, if the material is isochronic, meaning that its volume is preserved, the material is incompressible and $\frac{dv}{dV} = \det \bar{\bar{F}} = J = 1$.

Although the non-symmetric tensor $\bar{\bar{F}}$, which may contain rigid body contributions, is a useful measure of deformation, there is at least one more convenient measure of deformation, the right Cauchy-Green deformation tensor $\bar{\bar{C}}$ , which can be defined in terms of the deformation gradient tensor $\bar{\bar{F}}$ as follows:

$$\bar{\bar{C}} = \bar{\bar{F}}^T \cdot \bar{\bar{F}}$$

Tensor $\bar{\bar{C}}$ is symmetric and independent of rigid body motion. $\bar{\bar{C}}$ is a material tensor in the reference configuration and can typically be expressed as a function of the material coordinate $\vec{X}$.

### 2.5.2 Strain

When there is no motion ($\vec{X} \equiv \vec{x}$), the transformation gradient $\bar{\bar{F}} = \frac{d\vec{x}}{d\vec{X}}$ reduces to the identity tensor $\bar{\bar{I}}$, and therefore the left Cauchy-Green tensors $\bar{\bar{C}}$ also reduces to $\bar{\bar{I}}$. Similarly, when the motion is a rigid body motion, $\bar{\bar{C}}$ also reduces to the identity tensor. This does not make $\bar{\bar{C}}$ a good candidate to describe strain, and there is therefore a need to define a strain tensor that reduces to $\bar{\bar{0}}$ in the absence of deformation. $\bar{\bar{C}}$ can be used to define the Green-Lagrange strain tensor (or St. Venant) $\bar{\bar{E}}$ as:

$$\bar{\bar{E}} = \frac{1}{2}\left(\bar{\bar{C}} - \bar{\bar{I}}\right)$$

$\bar{\bar{E}}$ is symmetric and independent of rigid body motion.

### 2.5.3 Traction and Stress

Consider the differential force $d\vec{f}$ acting on a differential area $da$, with $da$ having an orientation given by an outward normal vector $\vec{n}$, in the current configuration $\beta_t$. The traction vector $\vec{T}^{(n)}$ can be introduced as:

$$\vec{T}^{(n)} = \frac{d\vec{f}}{da}$$

The standard definition of a stress in the current configuration, and as introduced in engineering education, is as a force per unit area. However, because stress measures a force over an oriented area, where the force and the area have different orientations, a second order tensor that transforms the orientation vector $\vec{n}$ in $\beta_t$ ($|\vec{n}| = 1$) to the traction vector $\vec{T}^{(n)}$ is introduced as the Cauchy stress tensor $\bar{\bar{\sigma}}$, as well known in linear elasticity, such that

$$\vec{T}^{(n)} = \vec{n} \cdot \bar{\bar{\sigma}}$$

The Cauchy stress tensor is a symmetric tensor, and is the actual physical stress felt by the body (force/area), often called true stress. Because $\bar{\bar{\sigma}}$ is a spatial tensor (in $\beta_t$) and because it can often be difficult to predict the deformed configuration of a body, it could be difficult to assess $\bar{\bar{\sigma}}$. Alternatively, the first Piola-Kirchhoff stress tensor $\bar{\bar{P}}$ is a measure of stress that is defined with respect to the reference configuration. Let us translate the actual force $d\vec{f}$ acting on $da$ in the deformed configuration $\beta_t$ from its position $\vec{x}$, to its corresponding position $\vec{X}$ in the reference configuration $\beta_o$, such that it acts on $dA$ with a normal vector $\vec{N}$. The new traction vector in the reference configuration is $\vec{T}^{(N)} = \frac{d\vec{f}}{dA}$, and the new stress tensor is $\bar{\bar{P}}$ such that:

$$\vec{T}^{(N)} = \vec{N} \cdot \bar{\bar{P}}$$

Note that $\bar{\bar{P}}$ is defined in terms of the actual force over the reference area and is also a (non-symmetric) two-point tensor, like $\bar{\bar{F}}$, because is relates $d\vec{f}$ in the current configuration and $\vec{N}dA$ in the reference configuration.

To define the second Piola-Kirchhoff stress tensor $\bar{\bar{S}}$ in the reference configuration $\beta_o$, one must define a fictitious force $d\tilde{f} = \bar{\bar{F}}^{-1} \cdot df$ acting on $\vec{N}dA$ in $\beta_o$. The new traction vector is $\vec{\tilde{T}}^{(N)} = \frac{d\tilde{f}}{dA}$, and $\bar{\bar{S}}$ is the second order tensor that transforms the orientation vector $\vec{N}$ in $\beta_o$ to the traction vector $\vec{\tilde{T}}^{(N)}$ such that:

$$\vec{\tilde{T}}^{(N)} = \vec{N} \cdot \bar{\bar{S}}$$

The first and second Piola-Kirchhoff stress tensors relate to the Cauchy stress tensor, and therefore these stress measures and the deformation gradient are interrelated.

$$\bar{\bar{\sigma}} = \frac{1}{J}\bar{\bar{F}} \cdot \bar{\bar{P}} \;\; \bar{\bar{\sigma}} = \frac{1}{J}\bar{\bar{F}} \cdot \bar{\bar{S}} \cdot \bar{\bar{F}}^{T}$$

$$\bar{\bar{P}} = \bar{\bar{S}} \cdot \bar{\bar{F}}^{T}.$$

### 2.5.4 Constitutive Formulation

Constitutive formulations are equations that characterize the macroscopic behavior of a material, which results from its internal constitution, in response to load. The simplest constitutive law is the widely known Hooke’s law which describes linear material behavior, and therefore relates the stress and strain linearly via the Young’s modulus. However, many materials are nonlinear and have complex behaviors, and their response depends on various parameters like strain rate, temperature, etc. It is therefore usually not possible to use just one constitutive relationship to describe the material’s behavior under all conditions; rather, a set of separate constitutive equations are formulated to describe various material responses under specific conditions. In this section, we will focus on deriving constitutive formulations for an isothermal hyperelastic material, a special case of elastic material, where the work done by the stresses during deformation is dependent only on the initial and final states. Hyperelasticity is a useful theory that establishes constitutive formulations for nonlinear material such as rubber-like material, elastomers, polymers and biological materials, and will be used for the characterization of the aortic mechanical properties in this dissertation. The behavior of a hyperelastic material is defined via a strain energy function per unit undeformed volume, as detailed next.

Continuum mechanics is based on five main principles: conservation of mass, conservation on linear momentum, conservation of angular momentum, conservation of energy and entropy inequality. Let us consider the entropy inequality given its usefulness in deriving the existence of constitutive relations. The entropy inequality is the 2nd law of thermodynamics and can be written in various forms, and the Clausius-Duhem equation is written as follows:

$$-\rho_o\left(\frac{d\psi}{dt}+\eta\frac{dT}{dt}\right)+\bar{\bar{P}}^T:\frac{d\bar{\bar{F}}}{dt}-\frac{1}{T}\overrightarrow{q_o}\cdot\nabla_o T\geq 0$$

In this equation, $\rho_o$ is the mass density in the reference configuration, $\psi$ is the Helmholtz potential which is a thermodynamic potential that measures the useful work in a system at constant temperature, $\eta$ is the entropy such that $\psi=\varepsilon-\eta T$, where $\varepsilon$ is the internal energy density, $T$ is the temperature, $\overrightarrow{q_o}$ is the referential heat flux vector, and $\nabla_o$ is the referential del operator $\frac{\partial()}{\partial\vec{X}}$. The Clausius-Duhem equation suggests that for a given thermoelastic process, one must define four constitutive functions: Helmholtz potential, entropy, stress, and heat flux. For an isothermal process ($T$ = constant) with no heat transfer ($\overrightarrow{q_o}$ = 0), this equation reduces to:

$$-\rho_o \frac{d\psi}{dt} + \bar{\bar{P}}^T : \frac{d\bar{\bar{F}}}{dt} \geq 0$$

By definition, (hyper)elastic responses are reversible and therefore the inequality can be replaced by an equality. Additionally, with $\psi = \psi(\bar{\bar{F}})$, $\frac{d\psi}{dt} = \frac{\partial\psi}{\partial\bar{\bar{F}}} : \frac{\partial\bar{\bar{F}}}{\partial t}$, the equation becomes:

$$\left(-\rho_o \frac{d\psi}{d\bar{\bar{F}}} + \bar{\bar{P}}^T\right) : \frac{d\bar{\bar{F}}}{dt} = 0$$

A sufficient condition to satisfy this equation is $-\rho_o \frac{d\psi}{d\bar{\bar{F}}} + \bar{\bar{P}}^T = \bar{\bar{0}}$, and therefore the stress (1st Piola-Kirchhoff tensor $\bar{\bar{P}}$) and the Helmholtz potential $\psi$ are not independent constitutive functions, and are related via:

$$\bar{\bar{P}} = \rho_o \frac{d\psi}{d\bar{\bar{F}}^T}$$

For isothermal hyperelastic processes, it can be shown that $\rho_o\psi(\bar{\bar{F}}) = W(\bar{\bar{F}})$, where the Helmholtz potential $\psi$ is defined per unit mass and the strain, and $W$ is the strain energy and can be defined per unit volume. It can also be shown that $\frac{d\psi}{d\bar{\bar{F}}^T} = 2\frac{d\psi}{d\bar{\bar{C}}}\bar{\bar{F}}^T$. Therefore, we can also write:

$$\bar{\bar{P}} = 2\frac{dW}{d\bar{\bar{C}}}\bar{\bar{F}}^T$$

The second Piola-Kichhoff stress tensor can therefore be expressed as:

$$\bar{\bar{S}} = 2\frac{dW}{d\bar{\bar{C}}}$$

Although $\bar{\bar{S}}$ is a physically non-interpretable measure of stress, it provides an easy descriptor for hyperelastic materials, and is very convenient in constitutive formulation. Since $\bar{\bar{E}} = \frac{1}{2}\left(\bar{\bar{C}} - \bar{\bar{I}}\right)$, we can manipulate constitutive equations in the form of $W(\bar{\bar{E}})$, such that:

$$\bar{\bar{S}} = \frac{dW}{d\bar{\bar{E}}}$$

This constitutive approach is widely used in describing biological tissues and is convenient in its simplicity in defining the stiffness of the material, which is defined as the change in stress with respect to the change in strain.

$$\bar{\bar{\bar{\bar{\mathbb{C}}}}} = \frac{d\bar{\bar{S}}}{d\bar{\bar{E}}}$$

Alternatively, expressing deformation in terms of the right Cauchy-Green deformation tensor $\bar{\bar{C}}$ instead of the Green-Lagrange strain tensor $\bar{\bar{E}}$ can also often be convenient. This allows for the utilization of constitutive laws in the form of $W(\bar{\bar{C}})$ as an alternative approach. Here, $W$ can depend on $\bar{\bar{C}}$ through its invariants, the roots of the characteristic equation $\det\left(\bar{\bar{C}} - \mu\bar{\bar{I}}\right) = 0$.

Constitutive equations are necessary to perform finite element analysis, as will be discussed in Section 2.6. While various specific forms of hyperelastic constitutive equations have been developed, for illustrative purposes, three specific forms are introduced. These forms are utilized in the implementation of finite element analysis within the scope of this dissertation.

#### *2.5.4.1 Neo-Hookean*

One of the simplest hyperelastic models is the Neo-Hookean constitutive model which can be used for both compressible and incompressible materials. It depends on two material parameters: shear modulus $\mu$ and bulk modulus $k$ [66]. The Neo-Hookean model is commonly used to describe incompressible hyperelastic materials [67,68]. The strain energy density function is given in the equation below [67]:

$$\mathrm{W} = \frac{\mu}{2}(\mathrm{I}_1 - 3) + \frac{k}{2}(J - 1)^2$$

In this equation, $\mathrm{I}_1$ is the first invariant of the right Cauchy-Green deformation and $\mathrm{I}_1 = 2(E_{11} + E_{22} + E_{33}) + 3$. It can be noticed that this equation is a linear function of the 1st invariant and therefore the Neo-Hookean model does not provide the best predictive capacity for large strains. In summary, the Neo-Hookean model is robust and efficient when it comes to finite element modelling but becomes less accurate for larger strains and is limited to isotropic materials.

#### ***2.5.4.2 Holzapfel-Gasser-Ogden***

With the purpose of modeling the mechanical behavior of anisotropic arterial tissue, the Holzapfel-Gasser-Ogden model, known as the HGO model was developed in 2000 [68]. The constitutive equation consists of two main components: 1) a Neo-Hookean [67] model to represent the isotropic solid matrix and, 2) a family of fibers to capture the anisotropic behavior of the material [68]. The motivation behind this formulation was to implement a composite-like constitutive law that would allow to characterize arterial tissue as reinforced with a family of collagen fibers [68]. Initially, the model was introduced with a family of two fibers, which capture the strain energy stored in the collagen fibers within the arterial wall, as follows:

$$\bar{W} = c(\bar{\mathrm{I}_1} - 3) + \frac{k_1}{2k_2}\sum_{n=4,6}\left[e^{k_2(\bar{\mathrm{I}_n}-1)^2} - 1\right]$$

Recalling the Neo-Hookean constitutive law, $\bar{\mathrm{I}_1} = \bar{\mathrm{I}}_1(\bar{\bar{\bar{C}}})$ is the first invariant of the right Cauchy-Green deformation $\bar{\bar{\bar{C}}}$, c is a stress-like material constant and $k$ is the bulk modulus. In the second component describing the fibers, $k_1$ is a positive stress-like material constant and $k_2$ is a dimensionless material parameter [68]. Furthermore, $\overline{\mathrm{I}_4}$ and $\overline{\mathrm{I}_6}$ are the fourth and sixth invariants of the the right Cauchy-Green deformation: $\overline{\mathrm{I}_4} = \overrightarrow{N_1} \cdot \bar{\bar{\bar{C}}} \cdot \overrightarrow{N_1}$ and $\overline{\mathrm{I}_6} = \overrightarrow{N_2} \cdot \bar{\bar{\bar{C}}} \cdot \overrightarrow{N_2}$, where $\overrightarrow{N_1}$ and $\overrightarrow{N_2}$ are directional vectors of the two-fiber family. Note that $\bar{\bar{\bar{C}}} = J^{-2/3}\bar{\bar{C}}$.

#### *2.5.4.3 Holmes-Mow*

The Holmes-Mow constitutive law that was introduced in the 1990s [69]. The motivation for this formulation was to model hydrated tissue such as cartilage and intervertebral disks. The constitutive equation is given by:

$$W = \frac{1}{2}c(e^{Q} - 1)$$

$$c = \frac{\lambda + 2\mu}{2\beta}$$

$$Q = \frac{\beta}{\lambda + 2\mu}[(2\mu - \lambda)(I_1 - 3) + \lambda(I_2 - 3) - (\lambda + 2\mu)\ln J^2]$$

In these equations, $I_1$ and $I_2$ are the first and second invariants of the right Cauchy-Green tensor, where $I_2 = (2E_{11} + 1)(2E_{22} + 1) + (2E_{11} + 1)(2E_{33} + 1) + (2E_{22} + 1)(2E_{33} + 1)$, $\lambda$ and $\mu$ are the Lamé parameters, $\beta$ is an exponential stiffening coefficient, and $J$ is the Jacobian of the deformation gradient.

## 2.6 FINITE ELEMENT ANALYSIS

The finite element method is one of the most powerful numerical techniques to solve partial differential and integral equations that gained large interest in engineering applications. It has been proven to be valuable in tackling intricate challenges across a range of fields, including structural, fluid and heat transfer applications, and became a valuable tool for industrial applications including automotive and aerospace [70]. In fact, the development of finite element methods was also one of the key contributors to the emergence of biomechanics [1], and offers the potential to advance various domains of medicine and biology [71]. Numerous software packages have been developed to facilitate the use of finite element analysis, including widely used platforms like ANSYS and NASTRAN. More recently, the development of suites tailored specifically to biological applications, such as FEBio (platform used in this dissertation), have become available [71]. These platforms facilitate the development of computer models that can help simulate and analyse complex structures.

Running a finite element analysis includes three main steps: pre-processing, solution, and post-processing [72]. The first step in pre-processing involves creating a geometry, which can be imported or constructed within the finite element software. It also entails assigning boundary and loading conditions to model the environmental interactions, such as defining forces and constraints on displacements. Initial conditions may also be specified in dynamic or time-dependent problems, and may include temperature, velocity, acceleration or initial state of stress. The material behavior is described using constitutive equations and is one of the most crucial factors in dictating the reliability of the outcome of the analysis. The selection of the proper constitutive formulation depends on the material type (linear vs. non linear, isotropic vs anisotropic) [70–72]. Hyperelastic constitutive models (discussed in Section 2.5.4) are most commonly used to describe the behavior of biological tissues, and many of them are available in current finite element software. Furthermore, when working with biological problems, it is also possible to create biphasic or triphasic mixtures, which allows one to incorporate a fluid phase to the solid structure, and account for solutes that can either be neutral or carry ionic charges [73,74]. The pre-processing step also requires one to discretize the domain via a process called meshing. This involves dividing a domain into a finite number of non-overlapping subdomains called elements connected at nodes. Hexahedral (brick) and tetrahedral (pyramid) elements are common types of solid (i.e. three-dimensional) elements that consist of a minimum of eight and four nodes respectively. Although nodes may exist within the volume of an element, those located at their corners, edges and faces allow to connect the elements throughout the continuum. Shell elements (two-dimensional) also exist for applications where the continuum's thickness is much smaller than its size. Numerous meshing techniques are available and the accuracy of the finite element solution highly depends on the nature, density and type of mesh employed [70,71,75,76].

The pre-processing step allows one to reduce a complex problem into a series of simpler subproblems. The finite element solver then assembles the governing equations and seeks approximate solutions within the domain [1,72]. The two primary analysis methods are linear and non-linear finite element methods. Linear finite element analysis is well established and is used when the relationships between loads, stresses, strains, and displacements are linear. In most cases it is a relatively simple process as it deals with linear equations. However, many engineering problems cannot be modeled as linear systems: if one of the relationships between loads, stress, strains and displacements is not linear, the system becomes nonlinear. While nonlinear methods provide a more accurate representation of real-world phenomena and account for the nonlinear characteristics of structures, their implementation is much more complex. Nonlinearities can be categorized in different ways, but the four main categories are: 1) Geometric nonlinearity: when the relationship between kinematic quantities is nonlinear; 2) material nonlinearity: when the relationship between stress and strain is nonlinear; 3) boundary nonlinearity: when the boundary condition change as a function of deformation; 4) force nonlinearity: when forces depend on deformation. Finite element formulations are generally founded on a weak (integral form) of a physical law. The simplest and most common formulations are based on the principle of virtual work and the principle of minimum potential energy [77]. As the focus of this dissertation does not include the formulation of new finite element theory, it will not be discussed in detail, and the reader is referred for example to "*Introduction to Nonlinear Finite Element Analysis*" [77] for a comprehensive coverage of this topic.

One of the most popular methods in finite element analysis to solve nonlinear equations, also being one of the methods employed by FEBio, is the Newton Raphson method. Most numerical methods for solving a system of nonlinear equations consist of initializing the problem by assuming an initial estimate for nodal displacements (or other variables of interest). The process then involves finding increments of the initial estimate. The goal is to find a new estimate that is closer to the solution, by locally approximating the nonlinear equations to linear ones. This process in then iteratively repeated until the solution satisfies the equations, and convergence is reached [77].

In addition, in order to handle constraints in finite element analysis (such as boundary conditions, physical laws, prescribed limits to stresses or displacements, etc.), several techniques have been developed, which differ in their approach, precision, and flexibility. The Lagrange multiplier method involves introducing a Lagrange multiplier as a new variable and creates a new system of equations that are solved simultaneously with the original system of equations, by solving for the Lagrange multiplier along the other variables. As such, the Lagrange multiplier method ensures that the constraints are precisely satisfied in the solution. Alternatively, the penalty method adds a penalty factor that multiples a measure of violation of the constraints to the system of equations. The measure of the violation increases if the constraints are violated, and is zero if the constraints are respected. As such, the penalty method does not ensure that constraints are satisfied precisely, but is it easier and faster to implement that the Lagrange method. The choice between the methods depends on the problem in place. As an example, to solve a finite element problem with an incompressible material, the Lagrange multiplier method would be required, however, for a nearly-incompressible material, the penalty method would be suitable. Other methods exist, such as the augmented Lagrangian method, which combines aspects from both the Lagrange multipliers method and the penalty method, and is often used when both equality and inequality constraints are required. The augmented Lagrangian method introduces a set of Lagrange multipliers -for each constraint- to the objective function required to be minimized. This newly created function is known as the so-called augmented Lagrangian function. Additionally, the augmented Lagrangian method adds a penalty term to the augmented Lagrangian function [78]. Depending on the solver, different methods could be adopted. In FEBio, the penalty method and augmented Lagrangian method are employed.

Post-processing finally allows one to visualize and analyse results, most commonly in a graphical form. Numerous visualization techniques are available and range from color plots, to vector and streamline plots, as well as plotting of specific variables [75].

## 2.7 REFERENCES

[1] J.D. Humphrey, Cardiovascular Solid Mechanics: Cells, Tissues, and Organs, Springer Science & Business Media, 2002.

[2] F. Dagenais, Anatomy of the Thoracic Aorta and of Its Branches, Thoracic Surgery Clinics. 21 (2011) 219–227. https://doi.org/10.1016/j.thorsurg.2010.12.004.

[3] R. Erbel, H. Eggebrecht, Aortic dimensions and the risk of dissection, Heart. 92 (2006) 137. https://doi.org/10.1136/hrt.2004.055111.

[4] J.A. Collins, J.-V. Munoz, T.R. Patel, M. Loukas, R.S. Tubbs, The anatomy of the aging aorta, Clinical Anatomy. 27 (2014) 463–466. https://doi.org/10.1002/ca.22384.

[5] H.W. Chang, S.H. Kim, A.R. Hakim, S. Chung, D.J. Kim, J.H. Lee, J.S. Kim, C. Lim, K.-H. Park, Diameter and growth rate of the thoracic aorta—analysis based on serial computed tomography scans, Journal of Thoracic Disease. 12 (2020). https://doi.org/10.21037/jtd-20-1275.

[6] P. Nagpal, M.D. Agrawal, S.S. Saboo, S. Hedgire, S. Priya, M.L. Steigner, Imaging of the aortic root on high-pitch non-gated and ECG-gated CT: awareness is the key!, Insights into Imaging. 11 (2020) 51. https://doi.org/10.1186/s13244-020-00855-w.

[7] R. Das, Walton Antony S., R.A. Morgan, 50 - Vascular Anatomy of the Thorax, Including the Heart, in: M.A. Mauro, K.P. Murphy, K.R. Thomson, A.C. Venbrux, R.A. Morgan (Eds.), Image-Guided Interventions (Third Edition), Elsevier, Boston, 2020: pp. 392-404.e1. https://doi.org/10.1016/B978-0-323-61204-3.00050-6.

[8] C.T. Tran, C.Y. Wu, S.J. Bordes, F. Lui, Anatomy, Abdomen and Pelvis: Abdominal Aorta, in: StatPearls, StatPearls Publishing, Treasure Island (FL), 2023. http://www.ncbi.nlm.nih.gov/books/NBK525964/ (accessed May 20, 2023).

[9] Prakash, V. Mokhasi, T. Rajini, M. Shashirekha, The abdominal aorta and its branches: anatomical variations and clinical implications, Folia Morphologica. 70 (2011) 282–286.

[10] D.C. Iliopoulos, E.P. Kritharis, A.T. Giagini, S.A. Papadodima, D.P. Sokolis, Ascending thoracic aortic aneurysms are associated with compositional remodeling and vessel stiffening but not weakening in age-matched subjects, The Journal of Thoracic and Cardiovascular Surgery. 137 (2009) 101–109. https://doi.org/10.1016/j.jtcvs.2008.07.023.

[11] P. Komutrattananont, P. Mahakkanukrauh, S. Das, Morphology of the human aorta and age-related changes: anatomical facts, Anat Cell Biol. 52 (2019) 109–114. https://doi.org/10.5115/acb.2019.52.2.109.

[12] A. Milutinović, D. Šuput, R. Zorc-Pleskovič, Pathogenesis of atherosclerosis in the tunica intima, media, and adventitia of coronary arteries: An updated review, Bosn J Basic Med Sci. 20 (2020) 21–30. https://doi.org/10.17305/bjbms.2019.4320.

[13] V.M. Subbotin, Excessive intimal hyperplasia in human coronary arteries before intimal lipid depositions is the initiation of coronary atherosclerosis and constitutes a therapeutic target, Drug Discovery Today. 21 (2016) 1578–1595. https://doi.org/10.1016/j.drudis.2016.05.017.

[14] Y. Nakashima, T.N. Wight, K. Sueishi, Early atherosclerosis in humans: role of diffuse intimal thickening and extracellular matrix proteoglycans, Cardiovascular Research. 79 (2008) 14–23. https://doi.org/10.1093/cvr/cvn099.

[15] S. Jana, M. Hu, M. Shen, Z. Kassiri, Extracellular matrix, regional heterogeneity of the aorta, and aortic aneurysm, Experimental & Molecular Medicine. 51 (2019) 1–15. https://doi.org/10.1038/s12276-019-0286-3.

[16] D. Wang, Z. Wang, L. Zhang, Y. Wang, Roles of Cells from the Arterial Vessel Wall in Atherosclerosis, Mediators of Inflammation. 2017 (2017) e8135934. https://doi.org/10.1155/2017/8135934.

[17] D.P. Wilson, Vascular Smooth Muscle Structure and Function, in: R. Fitridge, M. Thompson (Eds.), Mechanisms of Vascular Disease: A Reference Book for Vascular Specialists, University of Adelaide Press, Adelaide (AU), 2011. http://www.ncbi.nlm.nih.gov/books/NBK534250/ (accessed March 16, 2023).

[18] K.B. Rombouts, T.A.R. van Merrienboer, J.C.F. Ket, N. Bogunovic, J. van der Velden, K.K. Yeung, The role of vascular smooth muscle cells in the development of aortic aneurysms and dissections, Eur J Clin Invest. 52 (2022) e13697. https://doi.org/10.1111/eci.13697.

[19] J.A. Peña, M.A. Martínez, E. Peña, Layer-specific residual deformations and uniaxial and biaxial mechanical properties of thoracic porcine aorta, Journal of the Mechanical Behavior of Biomedical Materials. 50 (2015) 55–69. https://doi.org/10.1016/j.jmbbm.2015.05.024.

[20] A.G. Vouyouka, B.J. Pfeiffer, T.K. Liem, T.A. Taylor, J. Mudaliar, C.L. Phillips, The role of type I collagen in aortic wall strength with a homotrimeric [α1(I)]3 collagen mouse model, Journal of Vascular Surgery. 33 (2001) 1263–1270. https://doi.org/10.1067/mva.2001.113579.

[21] B. Sun, The mechanics of fibrillar collagen extracellular matrix, Cell Rep Phys Sci. 2 (2021) 100515. https://doi.org/10.1016/j.xcrp.2021.100515.

[22] G.J. Laurent, Dynamic state of collagen: pathways of collagen degradation in vivo and their possible role in regulation of collagen mass, American Journal of Physiology-Cell Physiology. 252 (1987) C1–C9. https://doi.org/10.1152/ajpcell.1987.252.1.C1.

[23] V.C. Mow, R. Huiskes, Basic Orthopaedic Biomechanics & Mechano-biology, Lippincott Williams & Wilkins, 2005.

[24] M.L. Colgrave, P.G. Allingham, K. Tyrrell, A. Jones, Multiple Reaction Monitoring for the Accurate Quantification of Amino Acids: Using Hydroxyproline to Estimate Collagen Content, in: M.A. Alterman (Ed.), Amino Acid Analysis: Methods and Protocols, Springer, New York, NY, 2019: pp. 33–45. https://doi.org/10.1007/978-1-4939-9639-1_4.

[25] M.R. Labrosse, Cardiovascular Mechanics, CRC Press, 2018.

[26] P. Berillis, The Role of Collagen in the Aorta’s Structure, TOCVJ. 6 (2013) 1–8. https://doi.org/10.2174/1877382601306010001.

[27] A.J. Cocciolone, J.Z. Hawes, M.C. Staiculescu, E.O. Johnson, M. Murshed, J.E. Wagenseil, Elastin, arterial mechanics, and cardiovascular disease, American Journal of Physiology-Heart and Circulatory Physiology. 315 (2018) H189–H205. https://doi.org/10.1152/ajpheart.00087.2018.

[28] K. Wang, X. Meng, Z. Guo, Elastin Structure, Synthesis, Regulatory Mechanism and Relationship With Cardiovascular Diseases, Frontiers in Cell and Developmental Biology. 9 (2021). https://www.frontiersin.org/articles/10.3389/fcell.2021.596702 (accessed May 9, 2023).

[29] S.M. Arribas, A. Hinek, M.C. González, Elastic fibres and vascular structure in hypertension, Pharmacology & Therapeutics. 111 (2006) 771–791. https://doi.org/10.1016/j.pharmthera.2005.12.003.

[30] L. Baumann, E.F. Bernstein, A.S. Weiss, D. Bates, S. Humphrey, M. Silberberg, R. Daniels, Clinical Relevance of Elastin in the Structure and Function of Skin, Aesthet Surg J Open Forum. 3 (2021) ojab019. https://doi.org/10.1093/asjof/ojab019.

[31] M.J. Sherratt, Tissue elasticity and the ageing elastic fibre, Age (Dordr). 31 (2009) 305–325. https://doi.org/10.1007/s11357-009-9103-6.

[32] L. Debelle, A.M. Tamburro, Elastin: molecular description and function, The International Journal of Biochemistry & Cell Biology. 31 (1999) 261–272. https://doi.org/10.1016/S1357-2725(98)00098-3.

[33] H. Trębacz, A. Barzycka, Mechanical Properties and Functions of Elastin: An Overview, Biomolecules. 13 (2023) 574. https://doi.org/10.3390/biom13030574.

[34] J. Gaar, R. Naffa, M. Brimble, Enzymatic and non-enzymatic crosslinks found in collagen and elastin and their chemical synthesis, Org. Chem. Front. 7 (2020) 2789–2814. https://doi.org/10.1039/D0QO00624F.

[35] B. Sun, The mechanics of fibrillar collagen extracellular matrix, Cell Rep Phys Sci. 2 (2021) 100515. https://doi.org/10.1016/j.xcrp.2021.100515.

[36] K. Reiser, R.J. McCormick, R.B. Rucker, Enzymatic and nonenzymatic cross-linking of collagen and elastin, The FASEB Journal. 6 (1992) 2439–2449. https://doi.org/10.1096/fasebj.6.7.1348714.

[37] A. Brüel, G. Ørtoft, H. Oxlund, Inhibition of cross-links in collagen is associated with reduced stiffness of the aorta in young rats, Atherosclerosis. 140 (1998) 135–145. https://doi.org/10.1016/S0021-9150(98)00130-0.

[38] J. URIBARRI, S. WOODRUFF, S. GOODMAN, W. CAI, X. CHEN, R. PYZIK, A. YONG, G.E. STRIKER, H. VLASSARA, Advanced Glycation End Products in Foods and a Practical Guide to Their Reduction in the Diet, J Am Diet Assoc. 110 (2010) 911–16.e12. https://doi.org/10.1016/j.jada.2010.03.018.

[39] R. Singh, A. Barden, T. Mori, L. Beilin, Advanced glycation end-products: a review, Diabetologia. 44 (2001) 129–146. https://doi.org/10.1007/s001250051591.

[40] A. Prasad, P. Bekker, S. Tsimikas, Advanced Glycation End Products and Diabetic Cardiovascular Disease, Cardiology in Review. 20 (2012) 177–183. https://doi.org/10.1097/CRD.0b013e318244e57c.

[41] W.G. John, E.J. Lamb, The maillard or browning reaction in diabetes, Eye. 7 (1993) 230–237. https://doi.org/10.1038/eye.1993.55.

[42] R. Bucala, Lipoprotein Modification by Advanced Glycosylation Endproducts (AGEs): Role in Atherosclerosis, Trends in Cardiovascular Medicine. 7 (1997) 39–47. https://doi.org/10.1016/S1050-1738(96)00137-5.

[43] F. Chiarelli, M. de Martino, A. Mezzetti, M. Catino, G. Morgese, F. Cuccurullo, A. Verrotti, Advanced glycation end products in children and adolescents with diabetes: Relation to glycemic control and early microvascular complications, The Journal of Pediatrics. 134 (1999) 486–491. https://doi.org/10.1016/S0022-3476(99)70208-8.

[44] D. Fujimoto, Aging and cross-linking in human aorta, Biochemical and Biophysical Research Communications. 109 (1982) 1264–1269. https://doi.org/10.1016/0006-291X(82)91913-1.

[45] L. Karim, S.Y. Tang, G.E. Sroga, D. Vashishth, Differences in non-enzymatic glycation and collagen cross-links between human cortical and cancellous bone, Osteoporos Int. 24 (2013) 2441–2447. https://doi.org/10.1007/s00198-013-2319-4.

[46] B.P. Shapiro, T.E. Owan, S.F. Mohammed, D.M. Meyer, L.D. Mills, C.G. Schalkwijk, M.M. Redfield, Advanced Glycation End Products Accumulate in Vascular Smooth Muscle and Modify Vascular but Not Ventricular Properties in Elderly Hypertensive Canines, Circulation. 118 (2008) 1002–1010. https://doi.org/10.1161/CIRCULATIONAHA.108.777326.

[47] A. Brüel, H. Oxlund, Changes in biomechanical properties, composition of collagen and elastin, and advanced glycation endproducts of the rat aorta in relation to age, Atherosclerosis. 127 (1996) 155–165. https://doi.org/10.1016/S0021-9150(96)05947-3.

[48] F. Mac-Way, V. Couture, M.S. Utescu, S. Ignace, S.A. De Serres, R.-C. Loignon, K. Marquis, R. Larivière, M. Agharazii, Advanced glycation end products, aortic stiffness, and wave reflection in peritoneal dialysis as compared to hemodialysis, Int Urol Nephrol. 46 (2014) 817–824. https://doi.org/10.1007/s11255-013-0597-6.

[49] E. Konova, S. Baydanoff, M. Atanasova, A. Velkova, Age-related changes in the glycation of human aortic elastin, Experimental Gerontology. 39 (2004) 249–254. https://doi.org/10.1016/j.exger.2003.10.003.

[50] D. Aronson, Cross-linking of glycated collagen in the pathogenesis of arterial and myocardial stiffening of aging and diabetes:, Journal of Hypertension. 21 (2003) 3–12. https://doi.org/10.1097/00004872-200301000-00002.

[51] B.H. Wolffenbuttel, C.M. Boulanger, F.R. Crijns, M.S. Huijberts, P. Poitevin, G.N. Swennen, S. Vasan, J.J. Egan, P. Ulrich, A. Cerami, B.I. Lévy, Breakers of advanced glycation end products restore large artery properties in experimental diabetes, Proc Natl Acad Sci U S A. 95 (1998) 4630–4634. https://doi.org/10.1073/pnas.95.8.4630.

[52] D.A. Kass, E.P. Shapiro, M. Kawaguchi, A.R. Capriotti, A. Scuteri, R.C. deGroof, E.G. Lakatta, Improved Arterial Compliance by a Novel Advanced Glycation End-Product Crosslink Breaker, Circulation. 104 (2001) 1464–1470. https://doi.org/10.1161/hc3801.097806.

[53] M. McNulty, A. Mahmud, J. Feely, Advanced Glycation End-Products and Arterial Stiffness in Hypertension*:, American Journal of Hypertension. 20 (2007) 242–247. https://doi.org/10.1016/j.amjhyper.2006.08.009.

[54] S. Kume, M. Takeya, T. Mori, N. Araki, H. Suzuki, S. Horiuchi, T. Kodama, Y. Miyauchi, K. Takahashi, Immunohistochemical and ultrastructural detection of advanced glycation end products in atherosclerotic lesions of human aorta with a novel specific monoclonal antibody., Am J Pathol. 147 (1995) 654–667.

[55] K. Prasad, A. Sarkar, M.A. Zafar, A. Shoker, H.E. Moselhi, M. Tranquilli, B.A. Ziganshin, J.A. Elefteriades, Advanced Glycation End Products and its Soluble Receptors in the Pathogenesis of Thoracic Aortic Aneurysm, Aorta (Stamford). 04 (2016) 1–10. https://doi.org/10.12945/j.aorta.2015.15.018.

[56] D. Koole, J.A. van Herwaarden, C.G. Schalkwijk, F.P.J.G. Lafeber, A. Vink, M.B. Smeets, G. Pasterkamp, F.L. Moll, A potential role for glycated cross-links in abdominal aortic aneurysm disease, Journal of Vascular Surgery. 65 (2017) 1493-1503.e3. https://doi.org/10.1016/j.jvs.2016.04.028.

[57] M. Oimomi, N. Igaki, F. Hata, Y. Kitamura, S. Nishimoto, S. Baba, S. Maeda, Age- and diabetes-accelerated glycation in the human aorta, Archives of Gerontology and Geriatrics. 8 (1989) 123–127. https://doi.org/10.1016/0167-4943(89)90056-3.

[58] G.A. Holzapfel, Biomechanics of Soft Tissue, The Handbook of Materials Behavior Models. 3 (2001) 1049–1063.

[59] J.A. Peña, M.A. Martínez, E. Peña, Layer-specific residual deformations and uniaxial and biaxial mechanical properties of thoracic porcine aorta, Journal of the Mechanical Behavior of Biomedical Materials. 50 (2015) 55–69. https://doi.org/10.1016/j.jmbbm.2015.05.024.

[60] D. Haskett, G. Johnson, A. Zhou, U. Utzinger, J. Vande Geest, Microstructural and biomechanical alterations of the human aorta as a function of age and location, Biomech Model Mechanobiol. 9 (2010) 725–736. https://doi.org/10.1007/s10237-010-0209-7.

[61] V. Deplano, M. Boufi, O. Boiron, C. Guivier-Curien, Y. Alimi, E. Bertrand, Biaxial tensile tests of the porcine ascending aorta, Journal of Biomechanics. 49 (2016) 2031–2037. https://doi.org/10.1016/j.jbiomech.2016.05.005.

[62] C. Martin, T. Pham, W. Sun, Significant differences in the material properties between aged human and porcine aortic tissues, Eur J Cardiothorac Surg. 40 (2011) 28–34. https://doi.org/10.1016/j.ejcts.2010.08.056.

[63] M.M. Safadi, M.B. Rubin, Modeling rate-independent hysteresis in large deformations of preconditioned soft tissues, International Journal of Solids and Structures. 51 (2014) 3265–3272. https://doi.org/10.1016/j.ijsolstr.2014.05.025.

[64] P.P. Purslow, T.J. Wess, D.W.L. Hukins, Collagen Orientation and Molecular Spacing During Creep and Stress-Relaxation in Soft Connective Tissues, Journal of Experimental Biology. 201 (1998) 135–142. https://doi.org/10.1242/jeb.201.1.135.

[65] J. Bonet, R.D. Wood, Nonlinear Continuum Mechanics for Finite Element Analysis, Cambridge University Press, 1997.

[66] Z. Yang, Material Modeling in Finite Element Analysis, CRC Press, 2019. https://doi.org/10.1201/9780367353216.

[67] J. Bergström, Elasticity/Hyperelasticity, in: Mechanics of Solid Polymers, Elsevier, 2015: pp. 209–307. https://doi.org/10.1016/B978-0-323-31150-2.00005-4.

[68] G.A. Holzapfel, T.C. Gasser, R.W. Ogden, A new Constitutive Framework for Arterial Wall Mechanics and a Comparative Study of Material Models, in: S.C. Cowin, J.D. Humphrey (Eds.), Cardiovascular Soft Tissue Mechanics, Kluwer Academic Publishers, Dordrecht, 2000: pp. 1–48. https://doi.org/10.1007/0-306-48389-0_1.

[69] M.H. Holmes, V.C. Mow, The nonlinear characteristics of soft gels and hydrated connective tissues in ultrafiltration, Journal of Biomechanics. 23 (1990) 1145–1156. https://doi.org/10.1016/0021-9290(90)90007-P.

[70] K.-J. Bathe, Finite Element Method, in: Wiley Encyclopedia of Computer Science and Engineering, John Wiley & Sons, Ltd, 2008: pp. 1–12. https://doi.org/10.1002/9780470050118.ecse159.

[71] S.A. Maas, B.J. Ellis, G.A. Ateshian, J.A. Weiss, FEBio: Finite Elements for Biomechanics, J Biomech Eng. 134 (2012) 11005-NaN. https://doi.org/10.1115/1.4005694.

[72] D.V. Hutton, Fundamentals of finite element analysis, The McGraw Hill Companies, 2004.

[73] V.C. Mow, S.C. Kuei, W.M. Lai, C.G. Armstrong, Biphasic Creep and Stress Relaxation of Articular Cartilage in Compression: Theory and Experiments, Journal of Biomechanical Engineering. 102 (1980) 73–84. https://doi.org/10.1115/1.3138202.

[74] D.N. Sun, W.Y. Gu, X.E. Guo, W.M. Lai, V.C. Mow, A mixed finite element formulation of triphasic mechano-electrochemical theory for charged, hydrated biological soft tissues, International Journal for Numerical Methods in Engineering. 45 (1999) 1375–1402. https://doi.org/10.1002/(SICI)1097-0207(19990810)45:10<1375::AID-NME635>3.0.CO;2-7.

[75] S.E. Benzley, K. Merkley, T.D. Blacker, L. Schoof, Pre- and post-processing for the finite element method, Finite Elements in Analysis and Design. 19 (1995) 243–260. https://doi.org/10.1016/0168-874X(94)00072-N.

[76] S. Maas, M. Herron, W. Jeffrey, A. Gerard, FEBio Theory Manual, FEBio Documentation. (n.d.). https://help.febio.org/ (accessed June 1, 2023).

[77] N. Kim, Introduction to Nonlinear Finite Element Analysis, Springer, New York, NY, 2014. https://doi.org/10.1007/978-1-4419-1746-1.

[78] J. Nocedal, S.J. Wright, eds., Numerical Optimization, Springer-Verlag, New York, 1999. https://doi.org/10.1007/b98874.

# 3

# THE CONTRIBUTION OF GLYCOSAMINOGLYCANS/PROTEOGLYCANS TO AORTIC MECHANICS IN HEALTH AND DISEASE: A CRITICAL REVIEW

Noor Ghadie [a], Jean-Philippe St-Pierre [b], Michel R. Labrosse [a,c]

[a] Mechanical Engineering Department, University of Ottawa, Ottawa, ON. Canada K1N6N5

[b] Chemical and Biological Engineering Department, University of Ottawa, Ottawa, ON. Canada K1N6N5

[c] Department of Cardiac Surgery, University of Ottawa Heart Institute, Ottawa, ON. Canada K1Y4W7

Content of this chapter published in IEEE Transactions on Biomedical Engineering | April 2021

Ghadie, N. M., St-Pierre, J. P., & Labrosse, M. R. (2021). The contribution of glycosaminoglycans/proteoglycans to aortic mechanics in health and disease: a critical review. *IEEE Transactions on Biomedical Engineering*, *68*(12), 3491-3500.

## 3.1 FOREWORD

In Chapter 2, basic concepts were reviewed to provide background information related to the work carried out in this dissertation. This chapter in turn provides a comprehensive review of scholarly articles to synthesize the current knowledge regarding the mechanobiological functions of glycosaminoglycans in the normal aortic wall, as well as their role in the pathogenesis of aortic diseases, focusing on aneurysms and dissections. Throughout this investigation, we identified existing gaps in our understanding and proposed avenues for further research, with the goal of advancing our knowledge in this important area of study.

## 3.2 ABSTRACT

While elastin and collagen have received a lot of attention as major contributors to aortic biomechanics, glycosaminoglycans (GAG) and proteoglycans (PG) recently emerged as additional key players whose roles must be better elucidated if one hopes to predict aortic ruptures caused by aneurysms and dissections more reliably. GAG are highly negatively charged polysaccharide molecules that exist in the extracellular matrix (ECM) of the arterial wall. In this critical review, we summarize the current understanding of the contributions of GAG/PG to the biomechanics of the normal aortic wall, as well as in the case of aortic diseases such as aneurysms and dissections. Specifically, we describe the fundamental swelling behavior of GAG/PG and discuss their contributions to residual stresses and aortic stiffness, thereby highlighting the importance of taking these polyanionic molecules into account in mathematical and numerical models of the aorta. We suggest specific lines of investigation to further the acquisition of experimental data to complement simulations and solidify our current understanding. We underscore different potential roles of GAG/PG in thoracic aortic aneurysm (TAAD) and abdominal aortic aneurysm (AAA). Namely, we report findings according to which the accumulation of GAG/PG in TAAD causes stress concentrations which may be sufficient to initiate and propagate delamination. On the other hand, there seems to be no clear indication of a relationship between the marked reduction in GAG/PG content and the stiffening and weakening of the aortic wall in AAA.

Index Terms—Aneurysm, Aorta, Biomaterials, Biomechanics, Glycosaminoglycans, Proteoglycans, Vascular Mechanobiology

## 3.3 INTRODUCTION

The aorta carries blood away from the heart to the rest of the body. The main segments of the aorta are the ascending thoracic aorta, the aortic arch, the descending thoracic aorta and the abdominal aorta (Figure 3.1) [1]. The aorta is a layered structure comprised primarily of smooth muscle cells embedded in an extracellular matrix (ECM) of elastin and collagen fibers, as well as ground substance, which primarily consists of water and glycosaminoglycans/proteoglycans (GAG/PG), with varying compositions and organizations across the tissue depth [2]. The three main layers of the aortic wall are shown in Figure 3.1: the intima, media, and the adventitia. The intima is the innermost layer of the aorta made of endothelial cells and their basement membrane (i.e., ECM), as well as sub-endothelium loose connective tissue, and typically occupies approximately 5% of the aortic wall thickness [3,4]. It is believed to contribute minimally to the load-bearing capacity of the aorta [5,6], except in the case of atherosclerotic disease [7,8]. However, it does possess an array of chemical functions [9]. The intima and the media are interfaced by the internal elastic lamina, which is the first of the many elastic concentric lamellae that compose the media [4,10]. The media is the middle layer of the aorta, and features multiple units of smooth muscle cells sandwiched between concentric elastin sheets reinforced with collagen fibers [10,11]. The media occupies approximately 77-80% of the aortic wall thickness

[3] and is separated from the outermost layer by the external elastic lamina [4,10]. The outermost layer of the aorta is the adventitia, which occupies the remainder of the wall thickness, namely 15-18% [3], and consists of a densely woven network of collagen fibers [11]. While collagen fibers possess high tensile strength, which allows the aorta to maintain its structural integrity, elastin provides the aortic wall with expansion and recoil abilities to accommodate and enhance the cyclic pumping of the heart (the so-called Windkessel effect) [12].

More specifically, since the pioneering work of Burton and Roach on arteries, it has been well established that elastin and collagen are load bearing at low and high stress, respectively [13]. Because elastin is much more distensible than collagen, this bimodal sharing of stress explains the classical nonlinear stress-strain behavior exhibited by soft tissues when they are tested *ex vivo*. Over the years, detailed investigations have revealed that, even in unloaded configurations as they can exist *ex vivo*, elastin is stretched, while undulated collagen fibers are under compression, and are only progressively recruited (i.e., become load bearing) as stretch or stress is increased [2,14–17]. Consistent with these observations, selective degradation of elastin has been demonstrated to cause a major loss of axial pre-stretch, as well as a significant increase in vessel diameter under pressurization compared to the same intact vessel [15,18–20]. Also noteworthy is the increasing rightward shift of the stress-strain curve of tissues whose elastin was degraded at each new loading cycle, suggesting that collagen fibers are disconnected from the non-collagenous matrix, while they still ensure stiffening under high stress [21].

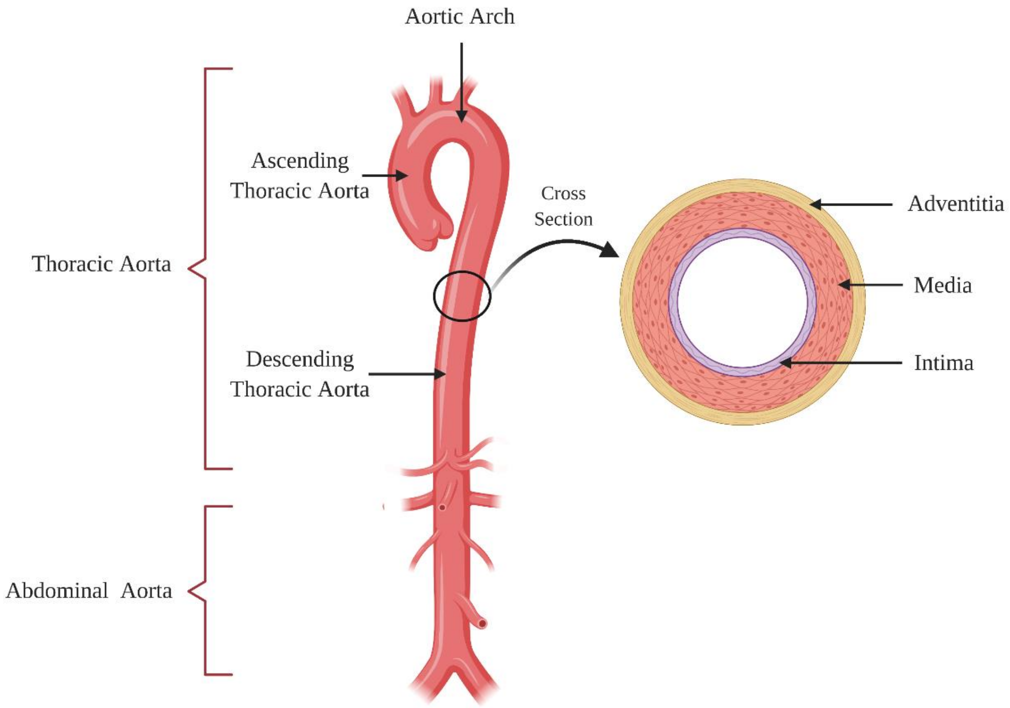

*Figure 3.1:Segments of the normal aorta (left), and layers of the aortic wall (right).*

Building on these important findings, various microstructural analytical and numerical models have been proposed. They typically describe arterial tissue according to the theory of constrained mixtures, and account, through the introduction of so-called deposition stretches, for the individual configurations of elastin and collagen in the unloaded tissue, as well as for the microstructural configuration of collagen fibers [22–27]. These models are especially notable as they allow one to determine the intramural mechanical stresses in the *in vivo* geometry with unprecedented accuracy, and predict the effects of altering the individual contributions of the wall constituents, via elastin degradation or variations in collagen pre-stretch, whether in bulk homogenous distributions or according to an intramural compositional gradient [17,23]. When the intramural heterogeneity of the tissue is represented, typically through two (e.g. medial and adventitial) layers with distinct material properties, the models can also be used to evaluate the residual stresses and strains in the unloaded (unpressurized, unstretched) *ex vivo* geometry, such as exhibited by the opening angle of a ring, or the longitudinal bend of an axial strip taken from the artery after a radial cut [28].

Residual stresses (strains) are defined as stresses (strains) that exist in the aortic wall in the absence of load. Experimental findings have connected residual stresses and strains in large arteries to the existence of functional (i.e., not fragmented) elastin, whereas collagen and smooth muscle cells were explicitly shown not to be involved [20,29]. GAG and PG have also been demonstrated to contribute to residual stresses and strains, depending on the osmolarity of the bathing fluid [30,31] and the intramural distribution of GAG/PG [32,33]. In addition, it has been suggested that the compressive behavior of GAG/PG-supported collagen fibers plays an important role in the unloaded dimensions of arterial tissue [23]. In a recent study, hypotheses in this regard were further distilled down to two scenarios: either the inflation of GAG/PG could cause and fill in collagen waviness, or tensile elastin could compress collagen to make the fibers wavy and GAG/PG fill in the existing waviness [2].

Microstructural, constrained-mixture-based analytical and numerical models are also noteworthy because they can replicate the stress-strain response of *in vivo* tissues, thereby enabling the analysis of aortic stiffness, a clinically important parameter in aortic biomechanics. Indeed, arterial compliance is what controls the cardiac afterload and, as a result, the pressure and flow resulting from the interaction of the heart with the arterial system. The compliance of the proximal aorta accounts for approximately half of the total arterial compliance [34], and stems from the Windkessel effect already mentioned. Therefore, a compliant aortic wall is essential in reducing cardiac afterload and in regulating blood pressure [35,36]. Conversely, increased aortic stiffness, which generally results from disease or aging, plays a major role in hypertension and could be a strong clinical marker for the detection of cardiovascular disease-associated mortality risks [37]. This is why the accurate estimation of aortic compliance is a chief objective toward improved risk stratification and optimized patient management.

Outside of the cardiovascular literature, it is well established that GAG/PG along with collagen, are the ECM's main components that modulate the mechanical behavior of cartilage [38,39]. Collagen confers tensile strength to articular cartilage, while GAG/PG play fundamental mechanical roles due to their lubricating properties, hydraulic permeability, and osmotic swelling, which contribute to cartilage's compressive and shear strengths [38–42]. By contrast, GAG/PG in aortic tissues have not garnered nearly as much attention. Yet, GAG/PG's mechanical and structural roles in normal and pathological aortic tissues have clearly emerged as areas of research deserving further investigation [2,5,6,32,43,44].

This thrust of GAG/PG into the cardiovascular spotlight has also been motivated in large part by clinical issues such as ruptures of the aorta, due to aortic aneurysms or dissections, and that are still eluding predictions [5,45–49]. On the one hand, aortic aneurysms are permanent dilatations by 50% or more of the aortic diameter [4] and are known to rupture suddenly [5]; although threshold values for diameter and/or yearly expansion rates have been set beyond which surgical intervention is mandated by clinical guidelines, many ruptures unfortunately take place below these thresholds [47]. On the other hand, dissections typically initiate from a tear in the intima and may lead to the separation of the intimal and medial layers, with potentially fatal outcomes when the tear expands, bifurcates and breaches the adventitia [51]. There is currently no way for clinicians to predict the occurrence and outcome of aortic dissections, and this puts such patients at a significant disadvantage. Overall, aortic ruptures, whether from aortic aneurysms or dissections, are associated with significant morbidity, as well as devastating and costly complications [47,52,53]. According to the Centers of Disease Control and Prevention, aortic aneurysm is the 19th [54,55] leading cause of mortality in the United States and in 2017, aortic aneurysms caused approximately 10,000 deaths in the United States alone [56].

These instances of aortic ruptures essentially reveal holes in our fundamental understanding of aortic tissue mechanics and properties. Hence a current focus on increasingly detailed analyses of the layer-specific material properties, deformations and mechanical stresses experienced by the aorta. In addition, inclusion of residual stresses in mathematical and computational models has been shown to have a significant impact on our understanding of the distribution and magnitude of stresses across the aortic wall under physiological pressure [28,57–59]. This is highly relevant to the mechanistic framework adopted in this review, whereby rupture takes place when the deformations or mechanical stresses imposed on a specific region of the aorta exceed the strength of said region.

The accumulation of new findings prompted the present focused review on GAG/PG in the aorta. GAG are highly negatively charged polysaccharides that are made up of repeating disaccharides composed of uronic acid and hexosamine units [60]. GAG are classified primarily based on the chemical structure of their repeating disaccharide units [61]. Essentially, there are six types of GAG families: hyaluronic acid (also called hyaluronan), dermatan sulfate, keratan sulfate, chondroitin sulfate, heparan sulfate, and heparin [62]. Heparin is the mostly sulfated heparan sulfate [63] and hyaluronan is the only non-sulfated GAG that does not bond to a protein core [6].

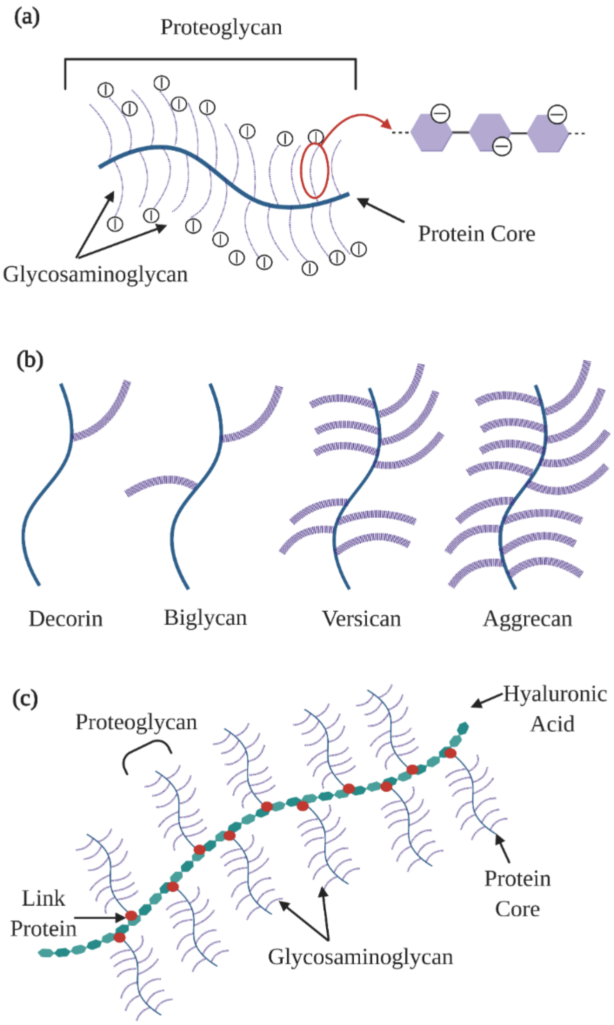

*Figure 3.2: (a) Glycosaminoglycans covalently bound to a protein core to form a proteoglycan;(b) Examples of small (decorin, biglycan) and large (versican, aggrecan) proteoglycans; (c) Aggregate.*

Usually, GAG do not exist alone in the body, of course with the exception of hyaluronan. Rather, they are covalently associated with protein cores to form a category of modified proteins, known as proteoglycans (PG) [61], [64] (Figure 3.2a). The classification process of PG is more complex than for GAG, and is based on 3 criteria: cellular location, protein homology, and the protein modules that are present within their protein cores [61]. PGs in ECM typically contain chondroitin sulfate and dermatan sulfate GAG chains [64]. In general, the ECM encloses small interstitial proteoglycans as well as large proteoglycans. Small PG include decorin, biglycan and fibromodulin, whereas large PG include aggregan, versican, neucoran and brevican [64,65]. For example, decorin contains only one GAG chain, while larger PG like aggrecan contains over 100 chains [64]. Figure 3.2b illustrates small molecular sized PG such as decorin and biglycan bound to one and two GAG chains respectively, and large PG such as versican and aggrecan containing many GAG chains. Large PG share structural similarities and are capable of binding to hyaluronan, the only non-sulfated GAG, to form large aggregates as shown in Figure 3.2c [65–67].

In this critical review, we aim to summarize the current understanding of the mechanobiological functions of GAG/PG in the normal aortic wall, as well as the impact of GAG/PG on aortic diseases such as aneurysms and dissections. All the while, we will identify knowledge gaps and propose paths of inquiry in hopes of ultimately enhancing the accuracy of mathematical models of aortic mechanics, and furthering clinical guidelines and standard of care.

## 3.4 GAG AND PG IN THE NORMAL AORTA

### 3.4.1 Observations from Tissue Analysis

In addition to hyaluronan [68], at least three types of sulphated GAG are present in blood vessels: chondroitin sulfate, heparan sulfate, and dermatan sulfate [69,70]. By isolating different types of GAG in human, porcine, canine, rat, hen and rabbit tissues, it has been demonstrated that GAG proportions, as well as their dominant types, vary between species, with chondroitin sulfate being predominant in both porcine and human tissues [71,72]. In mammals such as porcine, canine, rabbit and humans, the intima and media of the aorta is composed of 40-56% chondroitin sulfate (percentage of total GAG), 4–30% dermatan sulfate, 9–32% heparan sulfate and 4–24% hyaluronan [68,71]. Furthermore, it has been noted, through histological observations [32] and electrophoresis and chromatography [72], that the distribution of GAG is not homogeneous across the aortic wall, with higher levels towards the media and the intima.

Most recently, 20 types of PG have been identified in the human thoracic aorta's ECM [73]. The main large PG in the human aorta appears to be versican, which is covalently bound to chondroitin sulfate. It constitutes 53.5% of total PG and is mostly present in the intima [74,75]. Small PG, such as biglycan and decorin, are rich in dermatan sulfate and/or chondroitin sulfate and have been found to account for 40% of total PG in arteries [74,75]. Biglycan is localized in the intimal, outer medial and adventitial layers, while decorin is restricted to the adventitia of normal aortas [76]. In general, the majority of PG are believed to reside in the media and can exist in its interstitial space or associated with elastin and collagen [77].

Together, GAG/PG represent only 2-5% of the thoracic aortic wall in dry mass [78], which may account for the little attention they have received compared to collagen and elastin. However, an increasing number of studies have shown that GAG/PG also contribute to the arterial wall mechanobiological functions. The following sub-sections discuss the most relevant findings relative to aortic mechanics in normal tissues. Of particular importance, GAG/PG have been found to contribute to the mechanics of normal arteries through their ability to swell [32,79].

### 3.4.2 A Fundamental Behavior Associated with GAG/PG: Swelling

GAG are highly negatively charged molecules that are fixed within the ECM of the arterial wall. To maintain electroneutrality, they attract cations such as $Na^+$ from the interstitial fluid and cause an influx of water molecules into the tissue. This creates an osmotic pressure in the regions containing GAG, a phenomenon called Gibbs-Donnan swelling [66,80]. An illustration of this phenomenon is presented in Figure 3.3. In-vitro experiments demonstrate that swelling in the arterial wall increases when decreasing the osmolarity of the external solution in which the arterial samples are bathing [30,79]. Indeed, when the osmolarity of the external solution decreases, an osmotic gradient arises and water flows into the tissue to balance this gradient, increasing tissue volume [81]. Importantly, while similar amounts of swelling occur at a given osmolarity, the distribution of swelling across the aortic thickness may vary. For instance, two types of swelling distributions were detected in murine carotids: a sigmoid distribution where the swelling was nearly uniform in the medial layer, and a peak distribution where the swelling was concentrated in one intra-lamellar space in the media [79].

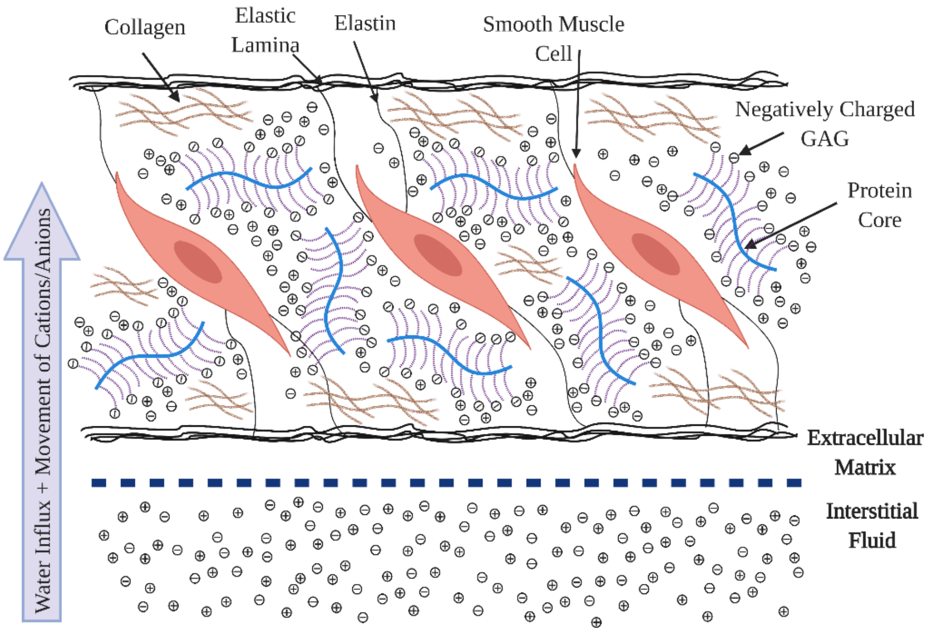

*Figure 3.3: Osmotic swelling mechanism caused by the presence of GAG/PG in the ECM of normal vascular tissue. Only one lamellar unit of the aortic wall is represented.*

The swelling distribution has not yet been deciphered in the aorta, where GAG/PG are heterogeneously distributed with higher levels towards the inner layers of its wall [72]. Thus, a possible correlation between the transmural GAG/PG and swelling distributions has yet to be investigated and, if established, could constitute a key contribution to better understanding the residual stresses discussed next. Furthermore, while uniform swelling may put the arterial wall network composed of collagen and elastin under tension [11], highly localized swelling, on the other hand, induces elevated pressures at specific locations in the aortic wall, and might separate the medial lamellae and initiate a delamination process that could propagate and lead to a dissection [82]. This will be discussed in relation to the diseased aorta in Section 3.5.

### 3.4.3 Residual Stresses

Residual stresses in the aorta manifest themselves when a short excised (i.e. unpressurized, and untethered) aortic segment or ring is sliced open: the ring typically opens up as an arc, demonstrating the release of circumferential residual stresses (Figure 3.4). In addition, an initially straight narrow longitudinal strip cut along an aortic segment takes on a bent shape, demonstrating the release of longitudinal residual stresses [28]. Although the magnitude of the residual stresses is typically much less than that of *in vivo* stresses, inclusion of residual stresses into detailed single- or multi- layered mathematical models of the aorta has been found to have a profound impact on the values and distributions of intramural *in vivo* stresses [28,57–59,83]. Therefore, these stresses are of prime relevance when one aims to refine the current understanding of aortic mechanics.

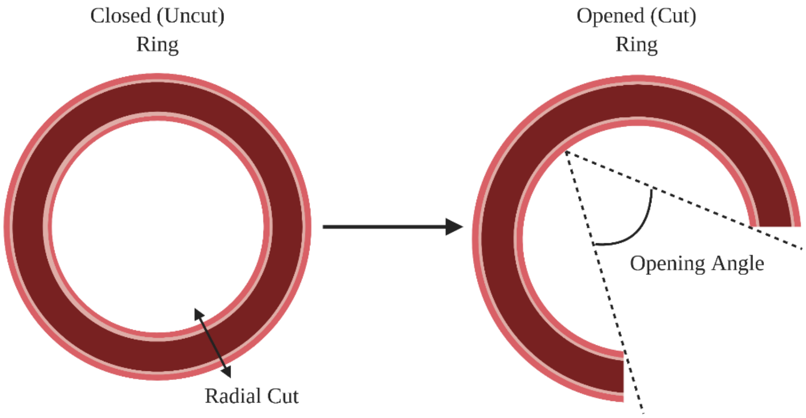

*Figure 3.4: Opening angle in an aortic ring sample caused by the presence of circumferential residual stresses in the unpressurized, untethered aortic wall.*

The origin of residual stresses in arteries has been attributed to tissue growth and adaptation to the mechanical environment during development [23,84]. Residual stresses have been shown to be dependent on location and may be affected by several factors including tissue composition [23,85]. Azeloglu et al. investigated the mechanical role of PG in the thoracic aorta in rats, and established that an inhomogeneous intramural distribution of PG induced an inhomogeneous swelling in the tissue due to a variation in the osmotic pressure across the wall thickness. In turn, this resulted in variations in the opening angle as a tell-tale sign of variations in circumferential residual stresses. Azeloglu et al.'s findings highlighted the swelling properties of GAG/PG, combined with their inhomogeneous transmural distribution, as contributing factors to residual stresses in arteries. Lanir [86] also proposed that osmotic swelling, as induced by the presence of GAG/PG, is key to determining residual stresses in all cardiovascular tissues and organs.

Azeloglu et al. also showed that the opening angle increased with increased GAG/PG fixed charge densities (FCDs) [32]. Indeed, the negatively charged GAG/PG can be expected to cause charge-to-charge repulsive forces, which serve as a mechanism for resisting compression and shear [66,80], as well as contribute to residual stresses. In a follow-up numerical study carried out in our laboratory (*please refer to Chapter 4*), we observed that FCD levels, as well as GAG transmural gradients [33], modulated the circumferential residual stresses and opening angles in porcine ascending aortic rings. It is important to note that Azeloglu's observations and ours were based on qualitative measurements and assumptions of FCD levels and GAG transmural distributions. This underlines the pressing need for quantitative measurements of GAG/PG in both porcine and human aortic tissues to further corroborate these findings.

To complete the description of the connection between GAG/PG and residual stresses, it is important to mention that the opening angle has also been found to be affected by the osmolarity of the bathing solution [30]. Azeloglu et al. reported from simulations of a rat thoracic aortic ring that the opening angle increased from 5°, to 37° to 206° when decreasing the external bath osmolarity from 2,000 mosM, to 300 mosM to 2 mosM [32]. This phenomenon was confirmed in murine thoracic aortic samples in other reports [30,79]. By contrast, a 143% overall decrease in opening angle was reported in murine carotids when the osmolarity was decreased [79]. These seemingly contradictory results may suggest different contents and distributions of GAG/PG between the thoracic and carotid vessels [87]. While higher levels of GAG/PG have been found towards the medial and intimal layers in the murine thoracic aorta [32], the intramural distribution of GAG/PG is still unknown in murine carotids, where their small size is a significant obstacle to investigation [88]. It would therefore be valuable to explore the transmural GAG/PG distributions in aortas and arteries of larger animal models, so that analyses would not only be facilitated by the larger sizes of the vessels, but also the findings might be more relevant to human health.

### 3.4.4 Tissue Stiffness

Another mechanical factor that has been found to be influenced by GAG/PG is tissue stiffness. Let us recall that a stress-strain curve can be obtained using a uniaxial or biaxial testing machine for *ex vivo* testing to measure the force (converted to stress) as a function of displacement or elongation (converted to strain) on a given tissue sample (see Figure 3.5). As mentioned before, for soft tissues, the stress-strain curve is typically highly nonlinear, and tissue stiffness (or elastic modulus) is defined as the slope of the curve at a given point. As expected in soft tissues, the stiffness of aortic tissues is low under small strains/stresses (indicative of the uncoiling of wavy collagen fibers embedded in easily stretched elastin components), goes through a transition zone (indicative of the progressive recruitment of reinforcing fibers under increasing stretch/load), and increases at larger strains/stresses (indicative of a progressive straightening out of the collagen fibers). Interestingly, a leftward shift has been observed at larger strains in the stress-strain curves of rodent arterial tissues digested to remove 65% of chondroitin and dermatan sulfate

[89]. This corresponded to a decrease in the stretchability (compliance) of the tissue after removal of GAG, or in other words, an increase in stiffness at a given strain value. These results were obtained by deriving the elastic moduli of treated and untreated samples, showing higher elastic moduli for samples depleted of GAG/PG [89]. Such findings underscore the fact that, although collagen and elastin are known as the main contributors to the arterial wall stiffness [90–93], GAG/PG may also play a role. In another study, Mattson et al. showed, through equibiaxial and non-equibiaxial testing of porcine thoracic aortas, that the transition points of the stress-strain curves in both the longitudinal and circumferential directions took place at lower strains after removal of GAG [2], suggesting earlier stiffening of GAG depleted tissues [2,66]. Moreover, a leftward shift in the stress-strain curve was detected after removal of GAG. The absence of GAGs was also reported to cause an earlier recruitment and mechanical engagement of collagen and elastin fibers, and straighter adventitial collagen fibers [2]. The stress-strain response of GAG depleted tissues was successfully predicted, opening the possibility to develop new constitutive models that could include the contribution of GAG to aortic mechanics [66]. Interestingly, using atomic force microscopy (AFM), Beenakker et al. [11] found that depletion of GAG/PG reduced the compressive stiffness of the medial and adventitial layers in porcine tissue.

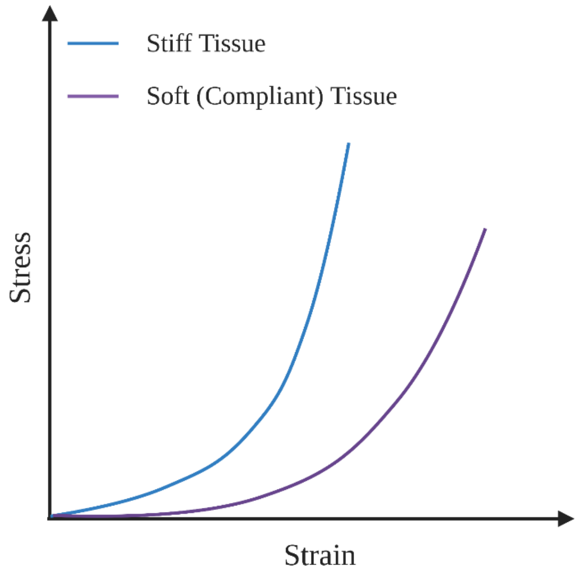

*Figure 3.5: Stress-strain curves of stiffer vs. softer tissues. The same plot can also illustrate the leftward shift in the stress-strain response of aortic tissues subjected to GAG depletion, as observed partially in [2], [89].*

In addition, it is worth pointing out that mathematical models of the aorta have shown that, while the inclusion of layer-specific information about the opening angle (or a corollary, such as a deposition stretch) allowed for more accurate predictions of the intramural stress distribution under physiological pressure [28,83], a stiffer aortic behavior under pressurization was also predicted when the residual stresses were not included in the calculations [59]. Because of the high clinical relevance of aortic compliance, as mentioned in the introduction, one could envision the development of mathematical models that predict aortic compliance and include residual stresses. In such models, one could imagine that residual stresses could further be predicated by GAG/PG contents and distributions.

## 3.5 GAG/PG IN THE DISEASED AORTA

The discussion this far has remained focused on normal aortic tissues; however, there have been many findings related to GAG/PG in the diseased aorta, as detailed below.

### 3.5.1 Observations from Tissue Analyses

Alterations in the structure, quantity and distribution of GAG/PG have been reported in aortic diseases such as atherosclerosis [94], progeria [95,96], thoracic aortic aneurysms and dissections (TAAD) and abdominal aortic aneurysms (AAA). These modifications have been correlated with the degradation of the aortic wall in such pathologies, and have been thought to influence the mechanobiological functions of the tissue. The specific modifications that GAG/PG undergo in TAAD and AAA are described next, leading to a discussion of the potential mechanical roles of GAG/PG in aortic ruptures.

### 3.5.2 Thoracic Aortic Aneurysms and Dissections

Qualitative observations from patients have confirmed alterations in GAG/PG amounts in TAAD. Overall, the GAG content tends to increase in TAAD, with evidence of the formation of GAG-rich pools, which may drive this accumulation [97]. Abnormal GAG deposition, along with medial degeneration of the aortic wall occur in patients with ascending aortic aneurysms with Loeys-Dietz Syndrome and Marfan Syndrome [98], as well as in children and young adult patients with ascending aneurysm and dissection [99]. In addition, accumulation occurs in dissected aortas, mainly in the dissected regions of the affected aorta [46].

PG have also been observed to accumulate in TAAD [67,73,100]. Furthermore, in familial TAAD patients, PG deposition is associated with an important loss of smooth muscle cells but minimal elastin degradation [101]. Specifically, there is an increase in large molecular sized PG in TAAD. For instance, there is evidence of versican and aggrecan accumulation in human TAAD aortic samples [73]. Accumulation of aggrecan has also been confirmed in Fbn1mgR/mgR mice, which are animal models that usually die from TAAD. In addition, aggrecan was observed to accumulate more in mice that died from dissection/ruptures than in mice that were euthanized, with higher concentrations near the dissected or ruptured areas [73].

Although biglycan deficiency has been shown to lead to also aortic rupture, more work is required before a better understanding of the possible contribution of small molecular sized PG to TAAD emerges [102]. One current hypothesis is that small PG exhibit a decrease in TAAD even though, overall, PG accumulate. There is therefore a need for better quantitative and configurational analyses of PG in TAAD.

### 3.5.3 Abdominal Aortic Aneurysms

In contrast to TAAD, there has been no evidence of pooled GAG accumulations in AAAs. AAAs exhibit a decrease in GAG quantities, with an overall 60% reduction in GAG content observed in human AAA samples compared to normal abdominal aortic tissues, along with a fragmentation and decrease in elastin, and a decrease in number of viable smooth muscle cells. Specifically, heparan sulfate has been shown to decrease by 90%, hyaluronan by 73%, chondroitin sulfate by 65%, with a smaller 8% decrease in dermatan sulfate content [45].

AAAs are also associated with a decrease in overall PG quantities. Theocharis and Karamanos [76] showed a reduction from 5.14 ± 0.45 mg of uronic acid per gram of dry defatted tissue in normal aortas, to 2.03 ± 0.14 in aortas with AAA. Studies have been consistent in reporting decreased quantities of large PG in AAA. Specifically, through quantitative proteomics methods, Didangelos et al. showed a decrease in spectral counts of aggrecan, versican, and perlecan in AAA. Versican's mean spectral counts decreased from 190 ± 5 in normal subjects to 84 ± 18 in subjects with AAA, and aggrecan's counts decreased from 154 ± 23 to 28 ± 11. This accounted for ~55% and ~82% decreases in versican and aggrecan, respectively [74]. In another study, AAAs were associated with an 89% decrease in versican concentration [75]. Although AAAs have been clearly associated with a decrease in large PG concentration, more work is needed to understand the quantitative changes related to small molecular sized PG in AAAs.

Indeed, while similar concentrations in decorin have been reported in normal and aneurysmal aortas [33], there have been conflicting results reported for the small PG biglycan. Specifically, in [76], biglycan concentration was reduced from 1.12 ± 0.10 mg uronic acid per gram of dry defatted tissue in normal aortas to 0.478 ± 0.04 mg uronic acid per gram of dry defatted tissue in aneurysmal aortas, which accounted for a 57% overall decrease. However, in [74], spectral counts of biglycan showed no differences between normal and aneurysmal aortas, as the mean spectral count in control subject was 74 ± 4 compared to 78 ± 10 in AAA from male patients. Furthermore, spatial distribution changes in GAG content remain to be established.

When evaluating modifications to GAG/PG during AAA pathogenesis, the distribution and proportion of large vs. small molecular size PG have also been investigated. For instance, versican concentration decreased from 53.5% of total amounts of PG in normal aortas to 16% of total PG in AAAs [75]. In addition, while small chondroitin sulfate and dermatan sulfate PG occupied 40% of total PGs in normal aortas, their proportion was found to be increased to 84% in aneurysmal aortas [75]. In another study, biglycan and decorin accounted for 22% of total PG in normal aortas, but 25% and 60% of total PG in aneurysmal tissue respectively [76]. Therefore, it appears that the overall proportion of small PG in reference to the total amount of PG is altered in AAAs. GAG/PG have also been shown to exhibit structural modifications in AAAs. For example, not only have AAAs been associated with a decrease in versican concentration, but they have also been found to possess decreased molecular sizes compared to normal aortas [103].

## 3.6 MECHANISMS AT PLAY IN TAAD AND AAA

There are likely different ways by which alterations in GAG/PG contents and distributions in aortic tissues impact the biomechanical behavior of aortas, and might even contribute to the induction of rupture. For instance, it is well established in structural engineering that local discontinuities  in material properties (such as stiffness variations) and/or geometry (such as local cavities) within loaded components give rise to mechanical stress concentrations that can increase local stresses by 2 to 3 fold [5]. It is therefore no surprise that simulations have shown that discontinuities in the arterial wall caused by GAG/PG pooling in the media can give rise to stress concentrations at these sites [6]. The magnitude of these stress concentrations depended on the configuration of the GAG pools. For example, in [43], stress concentrations depended on whether GAG/PG existed as a single pool, two unmerged pools, or two merged pools, where the coalescence of GAG/PG pools gave rise to higher stress concentrations. This significantly increased the stress experienced by the neighboring units, making them prone to failure [43]. In addition, GAG/PG pooling increased the tensile radial stresses, as well as the circumferential/hoop stresses and the axial stresses in the surrounding areas of the pools [82], [6]. Such analyses clearly make the case for GAG/PG pooling to be able to give rise to stress concentrations that may be sufficient to initiate and propagate rupture, and damage the aortic wall. Indeed, increased radial stresses can specifically lead to intra-lamellar delamination when their magnitude surpasses a certain threshold [82,104]. Specifically, radial stresses of ~61 kPa have been established to cause separation of elastic lamellae and failure of medial healthy aortas [105].

It is also important to note that increasing the fixed charge density from −50 to −160 mEq/l was also found to increase the peak radial stress from ∼50 to ∼100 kPa, which surpasses the separation threshold of 61 kPa and might be sufficient to initiate delamination in the aortic wall [6]. A natural question then arises as to what fixed charge densities can be reached in the aorta from GAG accumulation, under normal and pathological conditions? This is another aspect that requires further investigation, especially as modelling also suggests that damage in the media could lead to growth of GAG pools along the circumference of the aorta [43]. This would in turn allow GAG pools to merge with other pools when existent, thereby leading to further increased stress concentrations and higher potential for mechanical disruption and rupture propagation [82]. Overall, because GAG pools are hallmarks of TAAD, and not withstanding other phenomena and changes in the aortic wall, it stands to reason that micro-to-meso scale stress concentrations around such pools could indeed initiate tears and facilitate their propagations in hardly predictable bifurcated paths. This is indeed consistent with clinical observations.

Like TAAD, AAA also features increased aortic stiffness [3,106,107], which may eventually lead to aortic rupture [108–113]. However, unlike TAAD, AAA does not typically feature GAG pools, but a marked decrease in GAG content instead, and is also associated with a decrease in aortic wall strength [106]. Therefore, the underlying rupture mechanism in AAA might not be stress-concentration-related as in TAAD [5,73]. The macro-scale compliance loss observed in AAA is arguably a consequence of the reduction in elastin amounts in these pathological tissues [114]. In turn, compliance loss is known to exacerbate the systolic blood pressure increase experienced in aortic locations near bifurcations, such as in the abdominal aorta [115,116]. This pressure increase is due to the partial reflection of the incident systolic pressure wave due to changing flow conditions. Increased blood pressure (in a stiffer material) brings about excessive stresses in an AAA wall that is also weakened as the disease progresses. While the AAA patho-mechanism might not directly involve GAG or PG, it would seem important to explore whether or not the specific decrease in GAG content noted in AAA might be associated with the progression of the disease and eventual rupture of the aorta. This is another avenue for future investigation, and might help in delineating the possible differences in pathogenesis between TAAD and AAA, in complement to other current biochemical and genetic avenues [26,117,118].

## 3.7 CONCLUSION

The limitations and risks associated with the current clinical assessment of aortic ruptures call for a deeper understanding of aortic biomechanics, and GAG/PG have emerged as influencing constituents. This review highlighted the swelling of GAG/PG as a likely contributor to residual stresses in the aorta. GAG/PG are inhomogeneously distributed in the aortic wall, and the relationship between their intramural distribution and that of swelling has yet to be fully elucidated. We submit that such investigation is vital to better understand residual stresses, which in turn is fundamental for the accurate evaluation of mechanical mural stresses. The realization that GAG/PG quantities and gradients have been suggested to modulate the magnitude of residual stresses based on simulations fed with qualitative experimental data calls for enhanced quantitative layer specific measurements of GAG/PG in the aortic wall. Furthermore, the underlying reasons for the distinct opening angle response to external bath osmolarity between aortas and carotids requires further investigation. Aortic stiffness is also affected by GAG/PG; however, the current experimental data needs solidification to clarify whether GAG/PG' depletion causes an increase or a decrease in aortic stiffness. GAG/PG are also important components to monitor in aortic disease. While overall GAG/PG accumulate in TAAD and diminish in AAA, questions remain regarding the behavior of small PG. Moreover, because GAG/PG pooling in TAAD could potentially lead to stress concentrations that surpass the rupture threshold, causing a delamination to initiate and propagate, there is a need to understand under which FCDs GAG/PG exist in physiological and pathological aortas. In AAA, it is still unclear whether there might be any relationship between the marked reduction in

GAG/PG content and the ongoing stiffening and weakening of the aortic wall.

## 3.8 REFERENCES

[1] E.M. Isselbacher, Diseases of the Aorta, in: C. Rosendorff (Ed.), Essent. Cardiol. Princ. Pract., Humana Press, Totowa, NJ, 2006: pp. 681–690. https://doi.org/10.1007/978-1-59259-918-9_37.

[2] J.M. Mattson, R. Turcotte, Y. Zhang, Glycosaminoglycans contribute to extracellular matrix fiber recruitment and arterial wall mechanics, Biomech. Model. Mechanobiol. 16 (2017) 213–225. https://doi.org/10.1007/s10237-016-0811-4.

[3] D.C. Iliopoulos, E.P. Kritharis, A.T. Giagini, S.A. Papadodima, D.P. Sokolis, Ascending thoracic aortic aneurysms are associated with compositional remodeling and vessel stiffening but not weakening in age-matched subjects, J. Thorac. Cardiovasc. Surg. 137 (2009) 101–109. https://doi.org/10.1016/j.jtcvs.2008.07.023.

[4] M.-J. Chow, R. Turcotte, C.P. Lin, Y. Zhang, Arterial Extracellular Matrix: A Mechanobiological Study of the Contributions and Interactions of Elastin and Collagen, Biophys. J. 106 (2014) 2684–2692. https://doi.org/10.1016/j.bpj.2014.05.014.

[5] J.D. Humphrey, Possible Mechanical Roles of Glycosaminoglycans in Thoracic Aortic Dissection and Associations with Dysregulated TGF-β, J. Vasc. Res. 50 (2013) 1–10. https://doi.org/10.1159/000342436.

[6] S. Roccabianca, G.A. Ateshian, J.D. Humphrey, Biomechanical roles of medial pooling of glycosaminoglycans in thoracic aortic dissection, Biomech. Model. Mechanobiol. 13 (2014) 13–25. https://doi.org/10.1007/s10237-013-0482-3.

[7] G.A. Holzapfel, G. Sommer, C.T. Gasser, P. Regitnig, Determination of layer-specific mechanical properties of human coronary arteries with nonatherosclerotic intimal thickening and related constitutive modeling, Am. J. Physiol.-Heart Circ. Physiol. 289 (2005) H2048–H2058. https://doi.org/10.1152/ajpheart.00934.2004.

[8] M. Kobielarz, M. Kozuń, A. Kuzan, K. Maksymowicz, W. Witkiewicz, C. Pezowicz, The intima with early atherosclerotic lesions is load-bearing component of human thoracic aorta, Biocybern. Biomed. Eng. 37 (2017) 35–43. https://doi.org/10.1016/j.bbe.2016.10.008.

[9] E.B. Smith, Transport, interactions and retention of plasma proteins in the intima: the barrier function of the internal elastic lamina, Eur. Heart J. 11 (1990) 72–81. https://doi.org/10.1093/eurheartj/11.suppl_E.72.

[10] S. Jana, M. Hu, M. Shen, Z. Kassiri, Extracellular matrix, regional heterogeneity of the aorta, and aortic aneurysm, Exp. Mol. Med. 51 (2019) 1–15. https://doi.org/10.1038/s12276-019-0286-3.

[11] J.-W.M. Beenakker, B.A. Ashcroft, J.H.N. Lindeman, T.H. Oosterkamp, Mechanical Properties of the Extracellular Matrix of the Aorta Studied by Enzymatic Treatments, Biophys. J. 102 (2012) 1731–1737. https://doi.org/10.1016/j.bpj.2012.03.041.

[12] J.E. WAGENSEIL, R.P. MECHAM, Vascular Extracellular Matrix and Arterial Mechanics, Physiol. Rev. 89 (2009) 957–989. https://doi.org/10.1152/physrev.00041.2008.

[13] M.R. Roach, A.C. Burton, THE REASON FOR THE SHAPE OF THE DISTENSIBILITY CURVES OF ARTERIES, (n.d.) 11.

[14] P.J. Zeller, T.C. Skalak, Contribution of individual structural components in determining the zero-stress state in small arteries, J. Vasc. Res. 35 (1998) 8–17. https://doi.org/10.1159/000025560.

[15] J. Ferruzzi, M.J. Collins, A.T. Yeh, J.D. Humphrey, Mechanical assessment of elastin integrity in fibrillin-1-deficient carotid arteries: implications for Marfan syndrome, Cardiovasc. Res. 92 (2011) 287–295. https://doi.org/10.1093/cvr/cvr195.

[16] S. Zeinali-Davarani, M.-J. Chow, R. Turcotte, Y. Zhang, Characterization of biaxial mechanical behavior of porcine aorta under gradual elastin degradation, Ann. Biomed. Eng. 41 (2013) 1528–1538. https://doi.org/10.1007/s10439-012-0733-y.

[17] A. Rachev, T. Shazly, A structure-based constitutive model of arterial tissue considering individual natural configurations of elastin and collagen, J. Mech. Behav. Biomed. Mater. 90 (2019) 61–72. https://doi.org/10.1016/j.jmbbm.2018.09.047.

[18] P.B. Dobrin, T.H. Schwarcz, R. Mrkvicka, Longitudinal retractive force in pressurized dog and human arteries, J. Surg. Res. 48 (1990) 116–120. https://doi.org/10.1016/0022-4804(90)90202-d.

[19] P.B. Dobrin, Elastolytic and Collagenolytic Studies of Arteries: Implications for the Mechanical Properties of Aneurysms, Arch. Surg. 119 (1984) 405. https://doi.org/10.1001/archsurg.1984.01390160041009.

[20] E. Fonck, G. Prod'hom, S. Roy, L. Augsburger, D.A. Rüfenacht, N. Stergiopulos, Effect of elastin degradation on carotid wall mechanics as assessed by a constituent-based biomechanical model, 292 (2007) 10.

[21] H. Weisbecker, C. Viertler, D.M. Pierce, G.A. Holzapfel, The role of elastin and collagen in the softening behavior of the human thoracic aortic media, J. Biomech. 46 (2013) 1859–1865. https://doi.org/10.1016/j.jbiomech.2013.04.025.

[22] J.D. HUMPHREY, K.R. RAJAGOPAL, A CONSTRAINED MIXTURE MODEL FOR GROWTH AND REMODELING OF SOFT TISSUES, Math. Models Methods Appl. Sci. (2011). https://doi.org/10.1142/S0218202502001714.

[23] L. Cardamone, A. Valentin, J.F. Eberth, J.D. Humphrey, Origin of Axial Prestretch and Residual Stress in Arteries, Biomech. Model. Mechanobiol. 8 (2009) 431–446. https://doi.org/10.1007/s10237-008-0146-x.

[24] Y. Hollander, D. Durban, X. Lu, G.S. Kassab, Y. Lanir, Experimentally Validated Microstructural 3D Constitutive Model of Coronary Arterial Media, J. Biomech. Eng. 133 (2011) 031007. https://doi.org/10.1115/1.4003324.

[25] A. Valentín, J.D. Humphrey, G.A. Holzapfel, A finite element-based constrained mixture implementation for arterial growth, remodeling, and adaptation: Theory and numerical verification, Int. J. Numer. Methods Biomed. Eng. 29 (2013) 822–849. https://doi.org/10.1002/cnm.2555.

[26] C. Bellini, N.J. Kristofik, M.R. Bersi, T.R. Kyriakides, J.D. Humphrey, A hidden structural vulnerability in the thrombospondin-2 deficient aorta increases the propensity to intramural delamination, J. Mech. Behav. Biomed. Mater. 71 (2017) 397–406. https://doi.org/10.1016/j.jmbbm.2017.01.045.

[27] S.J. Mousavi, Patient-specific stress analyses in the ascending thoracic aorta using a finite-element implementation of the constrained mixture theory, Biomechanics and modeling in mechanobiology. (2017) 13.

[28] T. Sigaeva, G. Sommer, G.A. Holzapfel, E.S.D. Martino, Anisotropic residual stresses in arteries, (n.d.) 12.

[29] S.E. Greenwald, J.E. Moore, A. Rachev, T.P.C. Kane, J.-J. Meister, Experimental Investigation of the Distribution of Residual Strains in the Artery Wall, J. Biomech. Eng. 119 (1997) 438–444. https://doi.org/10.1115/1.2798291.

[30] X. Guo, Y. Lanir, G.S. Kassab, Effect of osmolarity on the zero-stress state and mechanical properties of aorta, Am. J. Physiol.-Heart Circ. Physiol. 293 (2007) H2328–H2334. https://doi.org/10.1152/ajpheart.00402.2007.

[31] Y. Lanir, Mechanisms of Residual Stress in Soft Tissues, J. Biomech. Eng. 131 (2009) 044506. https://doi.org/10.1115/1.3049863.

[32] E.U. Azeloglu, M.B. Albro, V.A. Thimmappa, G.A. Ateshian, K.D. Costa, Heterogeneous transmural proteoglycan distribution provides a mechanism for regulating residual stresses in the aorta, Am. J. Physiol.-Heart Circ. Physiol. 294 (2008) H1197–H1205. https://doi.org/10.1152/ajpheart.01027.2007.

[33] N. Ghadie, J.-P. St-Pierre, M.R. Labrosse, Intramural Glycosaminoglycans Distribution vs. Residual Stress in Porcine Ascending Aorta: a Computational Study*, in: 2020 42nd Annu. Int. Conf. IEEE Eng. Med. Biol. Soc. EMBC, 2020: pp. 2816–2819. https://doi.org/10.1109/EMBC44109.2020.9176381.

[34] C.V. Ioannou, N. Stergiopulos, A.N. Katsamouris, I. Startchik, A. Kalangos, M.J. Licker, N. Westerhof, D.R. Morel, Hemodynamics induced after acute reduction of proximal thoracic

aorta compliance, Eur. J. Vasc. Endovasc. Surg. 26 (2003) 195–204. https://doi.org/10.1053/ejvs.2002.1917.

[35] S.S. DeLoach, R.R. Townsend, Vascular Stiffness: Its Measurement and Significance for Epidemiologic and Outcome Studies, Clin. J. Am. Soc. Nephrol. 3 (2008) 184–192. https://doi.org/10.2215/CJN.03340807.

[36] S.Z. Pagoulatou, M. Ferraro, B. Trachet, V. Bikia, G. Rovas, L.A. Crowe, J.-P. Vallée, D. Adamopoulos, N. Stergiopulos, The effect of the elongation of the proximal aorta on the estimation of the aortic wall distensibility, Biomech. Model. Mechanobiol. (2020). https://doi.org/10.1007/s10237-020-01371-y.

[37] C. Vlachopoulos, K. Aznaouridis, C. Stefanadis, Prediction of Cardiovascular Events and All-Cause Mortality With Arterial Stiffness: A Systematic Review and Meta-Analysis, J. Am. Coll. Cardiol. 55 (2010) 1318–1327. https://doi.org/10.1016/j.jacc.2009.10.061.

[38] L. Han, A.J. Grodzinsky, C. Ortiz, Nanomechanics of the Cartilage Extracellular Matrix, Annu. Rev. Mater. Res. 41 (2011) 133–168. https://doi.org/10.1146/annurev-matsci-062910-100431.

[39] A. Maroudas, J. Mizrahi, E. Ben Haim, I. Ziv, Swelling pressure in cartilage, Adv Microcirc. 13 (1987) 203–212.

[40] M. Jin, A.J. Grodzinsky, Effect of Electrostatic Interactions between Glycosaminoglycans on the Shear Stiffness of Cartilage: A Molecular Model and Experiments, Macromolecules. 34 (2001) 8330–8339. https://doi.org/10.1021/ma0106604.

[41] A.K. Williamson, A.C. Chen, R.L. Sah, Compressive properties and function—composition relationships of developing bovine articular cartilage, J. Orthop. Res. 19 (2001) 1113–1121. https://doi.org/10.1016/S0736-0266(01)00052-3.

[42] W. Zhu, V.C. Mow, T.J. Koob, D.R. Eyre, Viscoelastic shear properties of articular cartilage and the effects of glycosidase treatments, J. Orthop. Res. 11 (1993) 771–781. https://doi.org/10.1002/jor.1100110602.

[43] H. Ahmadzadeh, M.K. Rausch, J.D. Humphrey, Modeling lamellar disruption within the aortic wall using a particle-based approach, Sci. Rep. 9 (2019) 15320. https://doi.org/10.1038/s41598-019-51558-2.

[44] T.N. Wight, A role for proteoglycans in vascular disease, Matrix Biol. 71–72 (2018) 396–420. https://doi.org/10.1016/j.matbio.2018.02.019.

[45] A.D. Theocharis, I. Tsolakis, T. Tsegenidis, N.K. Karamanos, Human abdominal aortic aneurysm is closely associated with compositional and specific structural modifications at the glycosaminoglycan level, Atherosclerosis. 145 (1999) 359–368. https://doi.org/10.1016/S0021-9150(99)00117-3.

[46] M.A. Cattell, P.S. Hasleton, J.C. Anderson, Glycosaminoglycan content is increased in dissecting aneurysms of human thoracic aorta, Clin. Chim. Acta. 226 (1994) 29–46. https://doi.org/10.1016/0009-8981(94)90100-7.

[47] J.A. Elefteriades, E.A. Farkas, Thoracic Aortic Aneurysm, J. Am. Coll. Cardiol. 55 (2010) 841–857. https://doi.org/10.1016/j.jacc.2009.08.084.

[48] S.W. Rabkin, Accentuating and Opposing Factors Leading to Development of Thoracic Aortic Aneurysms Not Due to Genetic or Inherited Conditions, Front. Cardiovasc. Med. 2 (2015) 21. https://doi.org/10.3389/fcvm.2015.00021.

[49] Shen Ying H., LeMaire Scott A., Webb Nancy R., Cassis Lisa A., Daugherty Alan, Lu Hong S., Aortic Aneurysms and Dissections Series: Part II, Arterioscler. Thromb. Vasc. Biol. 40 (2020) e78–e86. https://doi.org/10.1161/ATVBAHA.120.313804.

[50] T.M. Gunn, V.A. Gupta, V. Nadig, V.L. Sorrell, S.P. Saha, Ascending Aortic Aneurysm, in: R.S. Dieter, R.A. Dieter Jr., R.A. Dieter III (Eds.), Dis. Aorta, Springer International Publishing, Cham, 2019: pp. 161–173. https://doi.org/10.1007/978-3-030-11322-3_11.

[51] E.S. Crawford, The Diagnosis and Management of Aortic Dissection, JAMA. 264 (1990) 2537–2541. https://doi.org/10.1001/jama.1990.03450190069031.

[52] M.H. Guo, J.J. Appoo, R. Saczkowski, H.N. Smith, M. Ouzounian, A.J. Gregory, E.J. Herget, M. Boodhwani, Association of Mortality and Acute Aortic Events With Ascending Aortic Aneurysm, JAMA Netw. Open. 1 (2018). https://doi.org/10.1001/jamanetworkopen.2018.1281.

[53] O. Trabelsi, F.M. Davis, J.F. Rodriguez-Matas, A. Duprey, S. Avril, Patient specific stress and rupture analysis of ascending thoracic aneurysms, J. Biomech. 48 (2015) 1836–1843. https://doi.org/10.1016/j.jbiomech.2015.04.035.

[54] G.A. Kuzmik, A.X. Sang, J.A. Elefteriades, Natural history of thoracic aortic aneurysms, J. Vasc. Surg. 56 (2012) 565–571. https://doi.org/10.1016/j.jvs.2012.04.053.

[55] National Center for Injury Prevention and Control-blank template, (n.d.). https://webappa.cdc.gov/cgi-bin/broker.exe (accessed November 17, 2020).

[56] CDC, Aortic Aneurysm | cdc.gov, Cent. Dis. Control Prev. (2019). https://www.cdc.gov/heartdisease/aortic_aneurysm.htm (accessed August 26, 2020).

[57] R.N. Vaishnav, J. Vossoughi, ESTIMATION OF RESIDUAL STRAINS IN AORTIC SEGMENTS, in: C.W. Hall (Ed.), Biomed. Eng. II, Pergamon, 1983: pp. 330–333. https://doi.org/10.1016/B978-0-08-030145-7.50078-7.

[58] R.N. Vaishnav, J. Vossoughi, Residual stress and strain in aortic segments, J. Biomech. 20 (1987) 235–239. https://doi.org/10.1016/0021-9290(87)90290-9.

[59] M. Zhang, H. Liu, Z. Cai, C. Sun, W. Sun, An improved analytical method to estimate three-dimensional residual stresses of the aorta, Appl. Math. Model. 90 (2021) 351–365. https://doi.org/10.1016/j.apm.2020.08.063.

[60] N. Taniguchi, ed., Glycochemistry, Springer, Tokyo, 2008.

[61] R.V. Iozzo, L. Schaefer, Proteoglycan form and function: A comprehensive nomenclature of proteoglycans, Matrix Biol. J. Int. Soc. Matrix Biol. 42 (2015) 11–55. https://doi.org/10.1016/j.matbio.2015.02.003.

[62] K. Balagurunathan, H. Nakato, U.R. Desai, Glycosaminoglycans: Chemistry and biology, Humana Press, 2015.

[63] L. Zhang, Glycosaminoglycans in development, health and disease, Academic Press, 2010.

[64] A. Varki, R. Cummings, J. Esko, H. Freeze, G. Hart, J. Marth, Proteoglycans and Glycosaminoglycans, Cold Spring Harbor Laboratory Press, 1999. https://www.ncbi.nlm.nih.gov/books/NBK20693/ (accessed May 27, 2020).

[65] B. Bode-Lesniewska, M.T. Dours-Zimmermann, B.F. Odermatt, J. Briner, P.U. Heitz, D.R. Zimmermann, Distribution of the large aggregating proteoglycan versican in adult human tissues., J. Histochem. Cytochem. 44 (1996) 303–312. https://doi.org/10.1177/44.4.8601689.

[66] J.M. Mattson, Y. Wang, Y. Zhang, Contributions of Glycosaminoglycans to Collagen Fiber Recruitment in Constitutive Modeling of Arterial Mechanics, J. Biomech. 82 (2019) 211–219. https://doi.org/10.1016/j.jbiomech.2018.10.031.

[67] Shen Ying H., Lu Hong S., LeMaire Scott A., Daugherty Alan, Unfolding the Story of Proteoglycan Accumulation in Thoracic Aortic Aneurysm and Dissection, Arterioscler. Thromb. Vasc. Biol. 39 (2019) 1899–1901. https://doi.org/10.1161/ATVBAHA.119.313279.

[68] B.G. Salisbury, W.D. Wagner, Isolation and preliminary characterization of proteoglycans dissociatively extracted from human aorta., J. Biol. Chem. 256 (1981) 8050–8057.

[69] M.W. Lark, T.K. Yeo, H. Mar, S. Lara, I. Hellström, K.E. Hellström, T.N. Wight, Arterial chondroitin sulfate proteoglycan: localization with a monoclonal antibody., J. Histochem. Cytochem. 36 (1988) 1211–1221. https://doi.org/10.1177/36.10.3047228.

[70] T.N. Wight, M.W. Lark, M.G. Kinsella, Blood vessel proteoglycans, Biol. Proteoglycans. (1987) 267–295.

[71] J. Aikawa, H. Munakata, M. Isemura, N. Ototani, Z. Yosizawa, Comparison of glycosaminoglycans from thoracic aortas of several mammals., Tohoku J. Exp. Med. 143 (1984) 107–112. https://doi.org/10.1620/tjem.143.107.

[72] A. Gardais, J. Picard, B. Hermelin, Glycosaminoglycan (GAG) distribution in aortic wall from five species, Comp. Biochem. Physiol. Part B Comp. Biochem. 44 (1973) 507–515. https://doi.org/10.1016/0305-0491(73)90025-4.

[73] F.S. Cikach, C.D. Koch, T.J. Mead, J. Galatioto, B.B. Willard, K.B. Emerton, M.J. Eagleton, E.H. Blackstone, F. Ramirez, E.E. Roselli, S.S. Apte, Massive aggrecan and versican accumulation in thoracic aortic aneurysm and dissection, JCI Insight. 3 (2018). https://doi.org/10.1172/jci.insight.97167.

[74] A. Didangelos, X. Yin, K. Mandal, A. Saje, A. Smith, Q. Xu, M. Jahangiri, M. Mayr, Extracellular Matrix Composition and Remodeling in Human Abdominal Aortic Aneurysms: A Proteomics Approach, Mol. Cell. Proteomics. 10 (2011) M111.008128. https://doi.org/10.1074/mcp.M111.008128.

[75] A.D. Theocharis, I. Tsolakis, A. Hjerpe, N.K. Karamanos, Human abdominal aortic aneurysm is characterized by decreased versican concentration and specific downregulation of versican isoform V0, Atherosclerosis. 154 (2001) 367–376. https://doi.org/10.1016/S0021-9150(00)00504-9.

[76] A.D. Theocharis, N.K. Karamanos, Decreased biglycan expression and differential decorin localization in human abdominal aortic aneurysms, Atherosclerosis. 165 (2002) 221–230. https://doi.org/10.1016/S0021-9150(02)00231-9.

[77] J. Halper, Proteoglycans and diseases of soft tissues, in: Prog. Heritable Soft Connect. Tissue Dis., Springer, 2014: pp. 49–58.

[78] Wight T N, Cell biology of arterial proteoglycans., Arterioscler. Off. J. Am. Heart Assoc. Inc. 9 (1989) 1–20. https://doi.org/10.1161/01.ATV.9.1.1.

[79] T.A. Sorrentino, L. Fourman, J. Ferruzzi, K.S. Miller, J.D. Humphrey, S. Roccabianca, Local Versus Global Mechanical Effects of Intramural Swelling in Carotid Arteries, J. Biomech. Eng. 137 (2015). https://doi.org/10.1115/1.4029303.

[80] W.M. Lai, J.S. Hou, V.C. Mow, A Triphasic Theory for the Swelling and Deformation Behaviors of Articular Cartilage, J. Biomech. Eng. 113 (1991) 245–258. https://doi.org/10.1115/1.2894880.

[81] A. Tobias, B.D. Ballard, S.S. Mohiuddin, Physiology, Water Balance, in: StatPearls, StatPearls Publishing, Treasure Island (FL), 2020. http://www.ncbi.nlm.nih.gov/books/NBK541059/ (accessed November 17, 2020).

[82] H. Ahmadzadeh, M.K. Rausch, J.D. Humphrey, Particle-based computational modelling of arterial disease, J. R. Soc. Interface. 15 (2018) 20180616. https://doi.org/10.1098/rsif.2018.0616.

[83] G.A. Holzapfel, R.W. Ogden, Modelling the layer-specific three-dimensional residual stresses in arteries, with an application to the human aorta, J. R. Soc. Interface. 7 (2010) 787–799. https://doi.org/10.1098/rsif.2009.0357.

[84] T. Matsumoto, K. Hayashi, K. Ide, Residual strain and local strain distributions in the rabbit atherosclerotic aorta, J. Biomech. 28 (1995) 1207–1217. https://doi.org/10.1016/0021-9290(94)00179-8.

[85] D.P. Sokolis, Regional distribution of layer-specific circumferential residual deformations and opening angles in the porcine aorta, J. Biomech. 96 (2019) 109335. https://doi.org/10.1016/j.jbiomech.2019.109335.

[86] Y. Lanir, Osmotic swelling and residual stress in cardiovascular tissues, J. Biomech. 45 (2012) 780–789. https://doi.org/10.1016/j.jbiomech.2011.11.018.

[87] M. Rafuse, X. Xu, K. Stenmark, C.P. Neu, X. Yin, W. Tan, Layer-specific arterial micromechanics and microstructure: Influences of age, anatomical location, and processing technique, J. Biomech. 88 (2019) 113–121. https://doi.org/10.1016/j.jbiomech.2019.03.026.

[88] M.J. Merrilees, K.M. Tiang, L. Scott, Changes in Collagen Fibril Diameters Across Artery Walls Including a Correlation with Glycosaminoglycan Content, Connect. Tissue Res. 16 (1987) 237–257. https://doi.org/10.3109/03008208709006979.

[89] R.E. Gandley, M.K. McLaughlin, T.J. Koob, S.A. Little, L.J. McGuffee, Contribution of chondroitin-dermatan sulfate-containing proteoglycans to the function of rat mesenteric arteries, Am. J. Physiol.-Heart Circ. Physiol. 273 (1997) H952–H960. https://doi.org/10.1152/ajpheart.1997.273.2.H952.

[90] J.E. Wagenseil, R.P. Mecham, Elastin in large artery stiffness and hypertension, J Cardiovasc. Transl. Res. 5 (2012) 264–273. https://doi.org/10.1007/s12265-012-9349-8.

[91] A.J. Cocciolone, J.Z. Hawes, M.C. Staiculescu, E.O. Johnson, M. Murshed, J.E. Wagenseil, Elastin, arterial mechanics, and cardiovascular disease, Am. J. Physiol.-Heart Circ. Physiol. 315 (2018) H189–H205. https://doi.org/10.1152/ajpheart.00087.2018.

[92] D.A. Stakos, D.N. Tziakas, G.K. Chalikias, K. Mitrousi, C. Tsigalou, H. Boudoulas, Associations Between Collagen Synthesis and Degradation and Aortic Function in Arterial Hypertension, Am. J. Hypertens. 23 (2010) 488–494. https://doi.org/10.1038/ajh.2010.2.

[93] S. Zeinali-Davarani, Y. Wang, M. Chow, R. Turcotte, Y. Zhang, Contribution of collagen fiber undulation to regional biomechanical properties along porcine thoracic aorta., J. Biomech. Eng. 137 (2015) 051001–051001. https://doi.org/10.1115/1.4029637.

[94] Wight Thomas N., Merrilees Mervyn J., Proteoglycans in Atherosclerosis and Restenosis, Circ. Res. 94 (2004) 1158–1167. https://doi.org/10.1161/01.RES.0000126921.29919.51.

[95] M. Lewis, PRELP, collagen, and a theory of Hutchinson–Gilford progeria, Ageing Res. Rev. 2 (2003) 95–105. https://doi.org/10.1016/S1568-1637(02)00044-2.

[96] S.-I. Murtada, Y. Kawamura, A.W. Caulk, H. Ahmadzadeh, N. Mikush, K. Zimmerman, D. Kavanagh, D. Weiss, M. Latorre, Z.W. Zhuang, G.S. Shadel, D.T. Braddock, J.D. Humphrey,

Paradoxical aortic stiffening and subsequent cardiac dysfunction in Hutchinson–Gilford progeria syndrome, J. R. Soc. Interface. 17 (2020) 20200066. https://doi.org/10.1098/rsif.2020.0066.

[97] L.F. Borges, Z. Touat, A. Leclercq, A. Al Haj Zen, G. Jondeau', B. Franc, M. Philippe, O. Meilhac, P.S. Gutierrez, J.-B. Michel, Tissue diffusion and retention of metalloproteinases in ascending aortic aneurysms and dissections, Hum. Pathol. 40 (2009) 306–313. https://doi.org/10.1016/j.humpath.2008.08.002.

[98] J.J. Maleszewski, D.V. Miller, J. Lu, H.C. Dietz, M.K. Halushka, Histopathologic Findings in Ascending Aortas From Individuals With Loeys-Dietz Syndrome (LDS), Am. J. Surg. Pathol. 33 (2009) 194–201. https://doi.org/10.1097/PAS.0b013e31817f3661.

[99] D. Jain, H.C. Dietz, G.L. Oswald, J.J. Maleszewski, M.K. Halushka, Causes and histopathology of ascending aortic disease in children and young adults, Cardiovasc. Pathol. 20 (2011) 15–25. https://doi.org/10.1016/j.carpath.2009.09.008.

[100] C.D. Koch, C.M. Lee, S.S. Apte, Aggrecan in Cardiovascular Development and Disease, J. Histochem. Cytochem. 68 (2020) 777–795. https://doi.org/10.1369/0022155420952902.

[101] Guo Dong-Chuan, Regalado Ellen S., Minn Charles, Tran-Fadulu Van, Coney Joshua, Cao Jiumei, Wang Min, Yu Robert K., Estrera Anthony L., Safi Hazim J., Shete Sanjay S., Milewicz Dianna M., Familial Thoracic Aortic Aneurysms and Dissections, Circ. Cardiovasc. Genet. 4 (2011) 36–42. https://doi.org/10.1161/CIRCGENETICS.110.958066.

[102] A.-M. Heegaard, A. Corsi, C.C. Danielsen, K.L. Nielsen, H.L. Jorgensen, M. Riminucci, M.F. Young, P. Bianco, Biglycan Deficiency Causes Spontaneous Aortic Dissection and Rupture in Mice, Circulation. 115 (2007) 2731–2738. https://doi.org/10.1161/CIRCULATIONAHA.106.653980.

[103] A.D. Theocharis, I. Tsolakis, A. Hjerpe, N.K. Karamanos, Versican undergoes specific alterations in the fine molecular structure and organization in human aneurysmal abdominal aortas, Biomed. Chromatogr. 17 (2003) 411–416. https://doi.org/10.1002/bmc.263.

[104] S. Roccabianca, C. Bellini, J.D. Humphrey, Computational modelling suggests good, bad and ugly roles of glycosaminoglycans in arterial wall mechanics and mechanobiology, J. R. Soc. Interface. 11 (2014) 20140397. https://doi.org/10.1098/rsif.2014.0397.

[105] N.F. MacLean, N.L. Dudek, M.R. Roach, The role of radial elastic properties in the development of aortic dissections, J. Vasc. Surg. 29 (1999) 703–710. https://doi.org/10.1016/S0741-5214(99)70317-4.

[106] D.A. Vorp, Biomechanics of abdominal aortic aneurysm, J. Biomech. 40 (2007) 1887–1902. https://doi.org/10.1016/j.jbiomech.2006.09.003.

[107] R.J. Okamoto, J.E. Wagenseil, W.R. DeLong, S.J. Peterson, N.T. Kouchoukos, T.M. Sundt, Mechanical Properties of Dilated Human Ascending Aorta, Ann. Biomed. Eng. 30 (2002) 624–635. https://doi.org/10.1114/1.1484220.

[108] M.E. DeBakey, G.M. Lawrie, Dissecting Aneurysms of the Aorta, in: Y. Wu, R.M. Peters (Eds.), Int. Pract. Cardiothorac. Surg., Springer Netherlands, Dordrecht, 1986: pp. 1237–1242. https://doi.org/10.1007/978-94-009-4259-2_104.

[109] T.N.P. Johns, Dissecting Aneurysm of the Abdominal Aorta: Report of a case with repair of Perforation, Ann. Surg. 137 (1953) 232–235.

[110] B. Steckmeier, Epidemiologie der Aortenerkrankung: Aneurysma, Dissektion, Verschluss, Radiol. 41 (2001) 624–632. https://doi.org/10.1007/s001170170111.

[111] S. Weimann, G. Flora, Primary abdominal aortic dissection, Eur. J. Vasc. Surg. 3 (1989) 369–371. https://doi.org/10.1016/S0950-821X(89)80077-5.

[112] R.A.P. Scott, P.V. Tisi, H.A. Ashton, D.R. Allen, Abdominal aortic aneurysm rupture rates: A 7-year follow-up of the entire abdominal aortic aneurysm population detected by screening, J. Vasc. Surg. 28 (1998) 124–128. https://doi.org/10.1016/S0741-5214(98)70207-1.

[113] Vorp David A., Geest Jonathan P. Vande, Biomechanical Determinants of Abdominal Aortic Aneurysm Rupture, Arterioscler. Thromb. Vasc. Biol. 25 (2005) 1558–1566. https://doi.org/10.1161/01.ATV.0000174129.77391.55.

[114] C.M. He, M.R. Roach, The composition and mechanical properties of abdominal aortic aneurysms, J. Vasc. Surg. 20 (1994) 6–13. https://doi.org/10.1016/0741-5214(94)90169-4.

[115] T. Länne, B. Sonesson, D. Bergqvist, H. Bengtsson, D. Gustafsson, Diameter and compliance in the male human abdominal aorta: Influence of age and aortic aneurysm, Eur. J. Vasc. Surg. 6 (1992) 178–184. https://doi.org/10.1016/S0950-821X(05)80237-3.

[116] S.J. Marchais, A.P. Guerin, B. Pannier, G. Delavaud, G. London, Arterial Compliance and Blood Pressure, Drugs. 46 (1993) 82–87. https://doi.org/10.2165/00003495-199300462-00015.

[117] P. Lacolley, V. Regnault, P. Segers, S. Laurent, Vascular Smooth Muscle Cells and Arterial Stiffening: Relevance in Development, Aging, and Disease, Physiol. Rev. 97 (2017) 1555–1617. https://doi.org/10.1152/physrev.00003.2017.

[118] Sénémaud Jean, Caligiuri Giuseppina, Etienne Harry, Delbosc Sandrine, Michel Jean-Baptiste, Coscas Raphaël, Translational Relevance and Recent Advances of Animal Models of Abdominal Aortic Aneurysm, Arterioscler. Thromb. Vasc. Biol. 37 (2017) 401–410. https://doi.org/10.1161/ATVBAHA.116.308534.

# II

# *IN VITRO* AND *IN SILICO* INVESTIGATIONS

# 4

# INTRAMURAL GLYCOSAMINOGLYCANS DISTRIBUTION VS. RESIDUAL STRESS IN PORCINE ASCENDING AORTA: A COMPUTATIONAL STUDY*

---

Noor Ghadie [a], Jean-Philippe St-Pierre [b], Michel R. Labrosse [a,c]

[a] Mechanical Engineering Department, University of Ottawa, Ottawa, ON. Canada K1N6N5

[b] Chemical and Biological Engineering Department, University of Ottawa, Ottawa, ON. Canada K1N6N5

[c] Department of Cardiac Surgery, University of Ottawa Heart Institute, Ottawa, ON. Canada K1Y4W7

Content of this chapter published in the 42nd Annual International Conference of the IEEE Engineering in Medicine & Biology Society (EMBC) | July 2020

Ghadie, N., St-Pierre, J. P., & Labrosse, M. R. (2020, July). Intramural glycosaminoglycans distribution vs. residual stress in porcine ascending aorta: a computational study. In *2020 42nd Annual International Conference of the IEEE Engineering in Medicine & Biology Society (EMBC)* (pp. 2816-2819). IEEE.

## 4.1 FOREWORD

In this chapter, we established the computational framework needed to simulate the effect of glycosaminoglycans (GAG) on residual stresses. We first validated the implementation of the framework against previously published scenarios. A preliminary investigation of the effect of GAG on the opening angle and residual stresses was conducted through parametric studies. These studies involved evaluating the opening angle under various GAG distributions. These studies served as an initial investigation into the roles of GAG, offering a preliminary understanding until the necessary parameters were obtained to construct a more precise computer model. In this section, the Von Mises stress has been referred to as "effective stress", as per the terminology adopted by FEBio.

## 4.2 ABSTRACT

In this computational modelling work, we explored the mechanical roles that various glycosaminoglycans (GAG) distributions may play in the porcine ascending aortic wall, by studying both the transmural residual stress as well as the opening angle in aortic ring samples. A finite element (FE) model was first constructed and validated against published data generated from rodent aortic rings. The FE model was then used to simulate the response of porcine ascending aortic rings with different GAG distributions prescribed through the wall of the aorta. The results indicated that a uniform GAG distribution within the aortic wall did not induce residual stresses, allowing the aortic ring to remain closed when subjected to a radial cut. By contrast, a heterogeneous GAG distribution led to the development of residual stresses which could be released by a radial cut, causing the ring to open. The residual stresses and opening angle were shown to be modulated by the GAG content, gradient, and the nature of the transmural distribution.

## 4.3 INTRODUCTION

Glycosaminoglycans (GAG), the fundamental building blocks of proteoglycans (PG), are highly negatively charged molecules that compose, by dry weight, 2-5% of the wall of normal arteries [1]. Their mechanical role has emerged as an active area of research in mechanobiology and arterial biomechanics [2-6]. Through theoretical, experimental and computational analyses, Azeloglu et al. showed that the existence of GAG in the arterial wall induced Donnan swelling pressure that depends on the osmolarity of the external environment, and suggested that the heterogeneous transmural GAG distribution provided a mechanism for regulating residual stresses [2]. Residual stresses are those existing in the absence of external loads; they have been extensively studied due to their significant impact on the stress distribution within the pressurized aortic wall [2,7,8]. Residual stresses may be evaluated *ex vivo* by measuring the opening angle obtained after a radial cut has been made in an arterial ring sample [2,9]. Roccabianca et al. also showed that localized pooling of GAG could lead to stress concentrations that may be able to disrupt the extracellular matrix of the arterial wall [4,5]. Since ruptures that occur in the ascending region of the aorta can be lethal [10], and also to develop a better understanding of the roles GAG may play in the arterial wall mechanics, we aimed to examine the effects of GAG content and distribution on both residual stresses and opening angle in porcine ascending aortas.

## 4.4 METHODS

### 4.4.1 General Framework

A structural mechanics computational analysis was set up based on the equilibrium swelling theory introduced by Azeloglu et al. [2]. This consisted in analyzing a solid mixture-based tissue that combined an elastic porous solid matrix with a Donnan equilibrium swelling material that described the swelling induced by the presence of fixed charged densities (FCDs). The tissue was assumed to be charged with FCDs and bathing in an external solution of monovalent counter ions

[2]. The FCDs characterize the presence of negatively charged GAG in the aortic tissue, whereas the external bath describes a NaCl solution normally used to reproduce the physiological environment during experimental studies. The model was developed using open source software FEBio version 2.9.1 (https://febio.org/). Before proceeding with the development of the porcine ascending aortic model, aortic rings from rodents were modeled and the results were validated against data obtained in previously published scenarios, using parameters from Azeloglu et al. [2].

### 4.4.2 Reproducing the Rodent Model

One quarter of an aortic ring was created with an outer diameter of 1.92 mm, a wall thickness of 0.137 mm and a slice thickness of 1.09 mm [2]. To exactly reproduce the work done in Azeloglu et al., the ring was meshed using 20-node quadratic hexahedral elements, with 5 elements across the wall thickness, 12 elements along the circumference, and 4 elements along the slice thickness of the one-quarter model. A neo-Hookean constitutive relation was used to describe the solid matrix with a Young's modulus of 0.28 MPa and a Poisson's ratio of 0 [2]. The fluid volume fraction in the reference configuration was set to 0.7, with an osmotic coefficient of 1 [2]. Due to the scarcity of experimental data, Azeloglu et al. used published records of GAG FCD ($c_0^F$) in Leghorn chickens [3], namely: -40 meq/L in the first and second layers (intima and media), -20 meq/L in the third layer (transition), and 0 meq/L in the fourth and fifth layers (adventitia). The effective (Von Mises) stress distributions in both the uncut and cut geometries were generated and opening angles were evaluated under external bath osmolarities of 2 mosM, 300 mosM and 2,000 mosM [2].

### 4.4.3 Porcine Model

To explore the behavior of aortas more similar to humans', the previous model was modified to build a three dimensional finite element model of a porcine ascending aortic ring using an outer diameter of 18.58 mm, a wall thickness of 2.26 mm [11] and a slice thickness of 10.55 mm (preserving the same length/thickness ratio as in Azeloglu et. al). One-quarter of a ring was modeled with the same mesh density as in the analysis of rodent rings, which yielded converged solutions. The response of the porcine model was evaluated using a physiological external bath osmolarity of 300 mosM. To describe the solid matrix, we used a 2-fiber family model with a strain energy density function described by the following equations:

$$\psi=\frac{\mu}{2}(I_1-3)+\sum_{n=4,6}\frac{\xi}{\beta\alpha}\left(e^{\alpha(I_n-1)^{\beta}}-1\right)$$

$$I_n = \mathbf{N}.\mathbf{C}.\mathbf{N}$$

$$\mathbf{N} = \sin\varphi\cos\theta\,\mathbf{e_1} + \sin\varphi\sin\theta\,\mathbf{e_2} + \cos\varphi\,\mathbf{e_3}$$

In these equations, $\mu$ is a stress-like material parameter equal to 0.0491 MPa [12] and $I_1$ is the first invariant of the right Cauchy-Green deformation tensor **C**; $\xi$ represents the fiber modulus and is equal to 0.0014 MPa, $\beta$ is the power of exponential argument with a value of 2, and $\alpha$ is the coefficient of exponential argument equal to 13.311 [12]; $I_n$ is the square of the fiber stretch and **N** describes the fiber orientation, where $\theta$ and $\varphi$ are the spherical angles for fiber orientation in the local coordinate system, and are equal to $90^0$ and $51.45^0$ respectively [12]. These material parameters were obtained by Pena et al. through biaxial testing performed on porcine ascending aortic samples [12].

The FCD distribution provided in Azeloglu et al. was used as a baseline distribution, where -40 meq/L was prescribed in the medial and intimal layers, -20 meq/L in the transition layer, and 0 meq/L in the adventitial layer [2]. The analysis was then performed on both the uncut and radially cut aortic ring geometries. The peak wall effective (Von Mises) stresses were obtained for both geometries, as well as the opening angle for the cut geometry [9]. To better explore the influence of the FCD distribution and content on the residual stresses in the porcine aortic ring, three parametric studies were carried out as follows: in Parametric Study 1, the aortic wall was assigned a constant FCD distribution ranging between 0 and -80 meq/L in increments of -20 meq/L; in Parametric Study 2, the baseline transmural FCD distribution (i.e. $c_0^F$ = -40, -20, 0 meq/L in the intima/media, transition layer, and adventitia respectively) was prescribed and offset in increments of -5 meq/L or iteratively multiplied by a factor of 1.15; and in Parametric Study 3, the baseline FCD distribution was inverted (i.e. $c_0^F$ = 0, -20, -40 meq/L in the intima/media, transition layer, and adventitia respectively) and offset in increments of -5 meq/L or iteratively multiplied by a factor of 1.15.

## 4.5 RESULTS

### 4.5.1 Rodent Model

Our model was able to reproduce the opening angle results of rodent aortic rings in Azeloglu et al. at external bath solutions of 2, 300 and 2,000 mosM with an average error of 6%. The results are shown in Table 4.1. The effective (Von Mises) stress distributions in both closed and open rodents' rings are presented in Figures 4.1a and 4.1e respectively. Note that these rings were not subjected to any external loads, and as such, the presence of FCDs induced a transmural residual stress distribution in the aortic wall, as shown in Figure 4.1a.

When the ring was radially cut, it opened to relieve the internal residual stress. Indeed, the effective stresses decreased in Figure 4.1e compared to Figure 4.1a.

*Table 4.1: Opening Angle Comparison*

| **External Bath Osmolarity (mosM)** | **Opening Angle (degrees)** | |
|---|---|---|
| | ***Azeloglu's Model*** | ***Our Model (reproduced)*** |
| 2 | 206 | 206.2 |
| 300 | 37 | 36.1 |
| 2,000 | 5 | 5.8 |

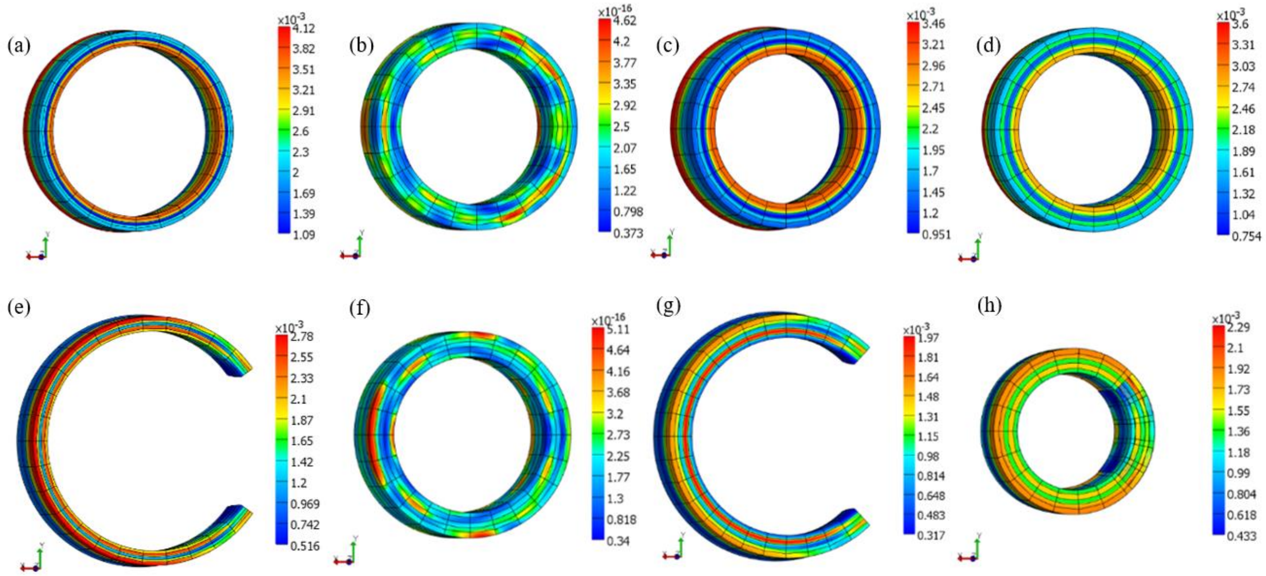

*Figure 4.1: Effective (Von Mises) stress distribution (MPa) in (a) closed geometry of the reproduced rodent aortic ring from [2]; (b) closed ascending porcine aortic ring assigned a constant FCD distribution ($c_0^F$ = -40 meq/L in all layers); (c) closed ascending porcine aortic ring assigned the same baseline FCD distribution as in [2] ($c_0^F$ = -40 meq/L in the intimal and medial layers, $c_0^F$ = -20 meq/L in the transition layer and $c_0^F$ = 0 meq/L in the adventitia); (d) closed ascending porcine aortic ring assigned an inverted FCD distribution compared to [2] ($c_0^F$ = 0 meq/L in the intimal and medial layers, $c_0^F$ = -20 meq/L in the transition layer and $c_0^F$ = -40 meq/L in the adventitia); (e) open geometry of the reproduced rodent aortic ring from [2]; (f) radially cut ascending porcine aortic ring assigned the same FCD distribution as in (b); (g) open ascending porcine aortic ring assigned the same FCD distribution as in (c) ; (h) open ascending porcine aortic ring assigned the same FCD distribution as in (d).*

### 4.5.2 Porcine Model

For qualitative comparison purposes, we presented the effective (Von Mises) stress distributions in representative cases of the uncut (Figures 4.1b,c,d) and radially cut geometries (Figure 4.1f,g,h) for the porcine ascending aortic rings. Rings with a uniform transmural FCD distribution at -40 meq/L are shown in Figures 4.1b and 4.1f. Both figures show nearly zero effective stresses within the aortic wall. In addition, no opening angle was observed in the cut ring (Figure 4.1f). In Parametric Study 1, similar results were obtained for all the cases analyzed by varying $c_0^F$ from 0 to -80 meq/L in increments of -20 meq/L.

Figures 4.1c and 4.1g respectively illustrate uncut and radially cut porcine aortic rings from the ascending region, when assigned the baseline FCD distribution obtained from Azeloglu et al. [2]. When the ring was uncut, this distribution induced the development of effective residual stresses within the ring's wall: Figure 4.1c shows higher effective stresses towards the intimal and medial layers which contained the highest GAG quantities, and lower stresses towards the adventitia with lower GAG quantities. When the ring was radially cut, the FCD distribution induced an opening angle, shown in Figure 4.1g. By contrast, inverting the FCD distribution (Figures 4.1d and 4.1h) caused the cut ring to fold over itself ("closing angle", Figure 4.1h).

Figures 4.2a and 4.2b illustrate the results from Parametric Study 2 when the FCD distribution varied from of $c_0^F$ = -40, -20, 0 meq/L (baseline) to $c_0^F$ = -100, -80, -60 meq/L in the intimal/medial, transition and adventitial layers respectively, in -5 meq/L offsets. The peak effective stresses in the radially cut porcine aortic rings increased with increased offset, but always stayed lower than the peak effective stresses in the uncut porcine aortic rings. Both the peak effective stresses in the uncut porcine aortic rings (Figure 4.2a) and the opening angle (Figure 4.2b) increased to a maximum value with increased offset and then slightly decreased.

Figures 4.2c and 4.2d illustrate the results from Parametric Study 2 when the FCD distribution varied from a distribution of $c_0^F$ = -40 meq/L, -20 meq/L and 0 meq/L to a distribution of $c_0^F$ = -214 meq/L, -107 meq/L, 0 meq/L in the intimal/medial, transition and adventitial layers respectively, in successive multiplications by 1.15 (15% increases). The peak effective stresses in the radially cut and uncut porcine aortic rings increased exponentially with successive multiplications, with the former always staying below the latter. As shown in Figure 4.2d, the opening angle increased linearly with successive multiplications.

For lack of space, results from Parametric Study 3 for the inverse FCD distributions are not included; they yielded similar increasing variations in peak effective stress as those shown for Parametric Study 2, and increasing closing angles.

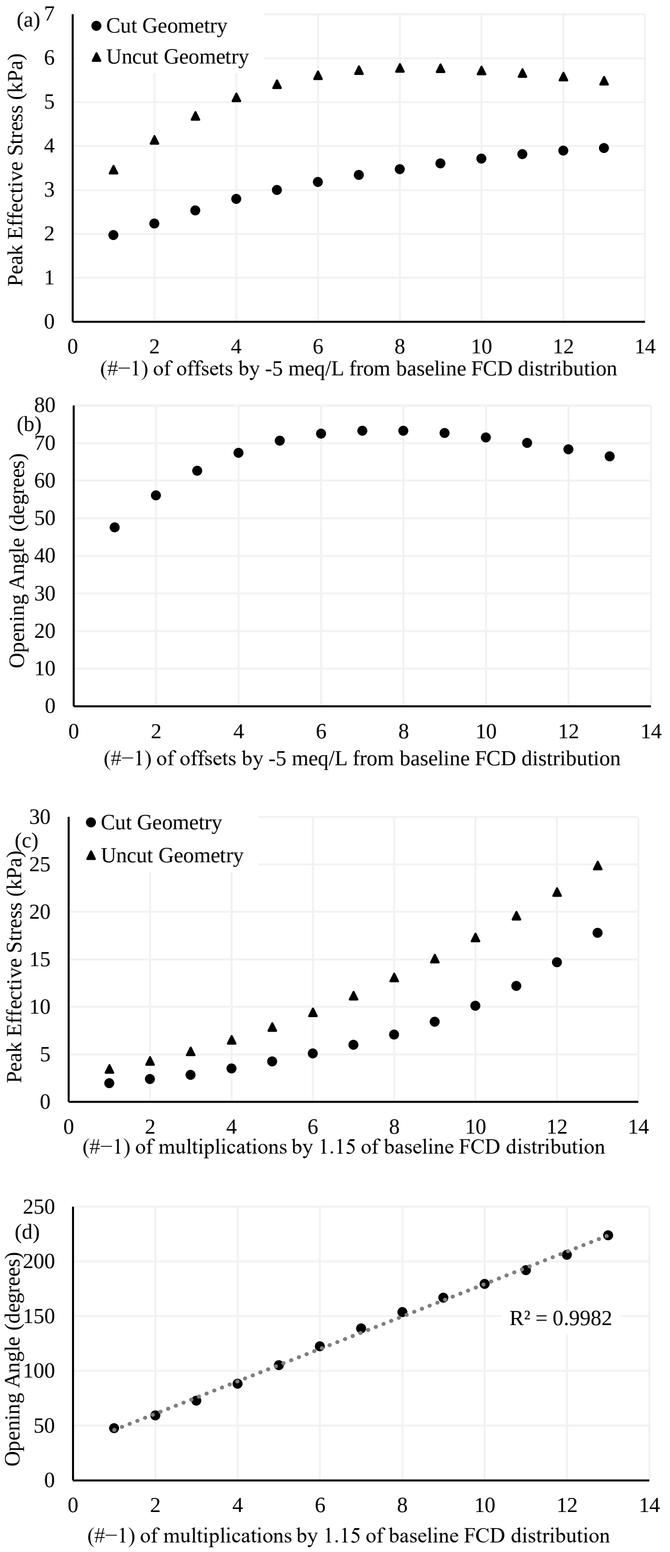

*Figure 4.2: Results from porcine aortic ring model. Variation of the peak effective (Von Mises) stress (a) and opening angle (b) when increasing the baseline GAG distribution by -5 meq/L increments. Variation of the peak effective (Von Mises) stress (c) and opening angle (d) when multiplying the baseline GAG distribution by 1.15 multiple times.*

## 4.6 DISCUSSION

The response of radially cut rodent aortic rings due to change in external bath osmolarities has been studied previously, and higher opening angles at lower osmolarities were reported [2]. Our main interest in this work was to evaluate the change in residual stresses and opening angles in both closed and open rings due to variation in GAG content and distribution in the porcine ascending aorta. None of the rings in this study were subjected to any external loads and, as such, the developed stresses were indeed residual stresses. We showed that a uniform FCD distribution did not lead to the development of any stresses in closed rings (Figure 4.1b), and did not induce any opening in radially cut rings (Figure 4.1f). This suggested that a heterogeneous transmural distribution is essential for the development of residual stresses, which was confirmed in both Figures 4.1c and 4.1d. PG/GAG have been reported to exist in higher contents towards the intima and media, with lower levels towards the adventitia of the arterial wall [2,13]. When studying closed rings using the baseline distribution given in [2], we observed higher effective stresses in the intimal and medial layers which featured higher FCDs, and lower effective stress values towards the adventitia which featured lower FCDs (Figures 4.1c).

In addition, the FCD distribution was found to be an important factor affecting the opening/closing response of aortic rings subjected to radial cuts. Herein, the porcine ascending aortic ring was found to open under baseline FCD distribution (Figure 4.1g), which featured higher FCD contents towards the intimal and medial layers. By contrast, the ring curled over itself ("closing angle") when assigned an inverse FCD distribution (Figure 4.1h).

Moreover, Figure 4.2 suggests that not only the FCD content quantity and distribution affects the stresses and opening angles, but that, more specifically, the intramural gradient of FCD content could also have an impact. When the FCD content increased but the gradients between the intimal/medial and the transition layers as well as between the transition and adventitial layers stayed constant, the peak effective stresses in both closed and cut geometries increased until it reached a plateau (Figure 4.2a) and the opening angle increased to a maximum value of approximately $73^0$ and then slightly decreased (Figure 4.2b). When the FCD content and the gradients between the intimal/medial and the transition layers as well as between the transition and adventitial layers increased, the peak effective stress increased sharply, following an exponential profile (Figure 4.2c), and the opening angle increased linearly to reach a maximum value of $223^0$ in the extreme evaluated FCD distribution of $c_0^F$ = -214 meq/L, -107 meq/L, 0 meq/L in the intimal/medial, transition and adventitial layers respectively. Figure 4.2 also supports the evaluation of residual stresses through the measurement of the opening angle. Indeed, subjecting the porcine ascending aortic ring to a radial cut was associated with a stress relief where the effective stresses were reduced by an average 40%.

Given that, in this study, we set FCD contents and distributions based on qualitative measurements and assumptions [2,3,12], and knowing that in most experimental studies, aortic rings have been reported to open when subject to a radial cut [2,7,8], a natural follow-up question arises as to whether the contents and distributions used herein exist in porcine or human tissues. As such, the quantitative measurement of physiochemical properties of GAG in both porcine and human aortic tissues should now be investigated for better predictive modelling of aortic stresses.

## 4.7 CONCLUSION

In summary, building on findings established by others in the rodent aorta, this study allowed us to develop a better understanding of the behavior of the porcine ascending aorta, as a reasonable model for the human aorta. We confirmed that the existence of GAG contributes to the presence of residual stresses, which can be at least partially relieved after a radial cut is performed through the aortic ring. In addition, we showed that the GAG content impacts the intensity of residual stresses, and we were able, for the first time, to predict from computational modeling that the transmural GAG gradient distribution, is expected to modulate the residual stress and opening angle in porcine ascending aortic rings.

## 4.8 REFERENCES

[1] Wight, T. N. Cell biology of arterial proteoglycans. *Arteriosclerosis* 9.1 (1989): 1-20.

[2] Azeloglu, E. U., et al. Heterogeneous transmural proteoglycan distribution provides a mechanism for regulating residual stresses in the aorta. *American Journal of Physiology-Heart and Circulatory Physiology* 294.3 (2008): H1197-H1205.

[3] Porterfield, S. P., Calhoon, T. B. and Weiss H. S. Changes in connective tissue colloidal charge density with atherosclerosis and age. *American Journal of Physiology-Legacy Content* 215.2 (1968): 324-329."

[4] Roccabianca, S., Bellini, C., and Humphrey, J. D. Computational modelling suggests good, bad and ugly roles of glycosaminoglycans in arterial wall mechanics and mechanobiology. *Journal of The Royal Society Interface* 11.97 (2014): 20140397.

[5] Roccabianca, S., Ateshian, G. A. and Humphrey, J. D. Biomechanical roles of medial pooling of glycosaminoglycans in thoracic aortic dissection. *Biomechanics and modeling in mechanobiology* 13.1 (2014): 13-25.

[6] Mattson, J. M., Turcotte, R., and Zhang, Y. Glycosaminoglycans contribute to extracellular matrix fiber recruitment and arterial wall mechanics. *Biomechanics and modeling in mechanobiology* 16.1 (2017): 213-225.

[7] Lanir, Y. Mechanisms of residual stress in soft tissues. *Journal of biomechanical engineering*, 131.4 (2009):044506.

[8] Peña, J. A., Martínez, M. A., and Peña, E. Layer-specific residual deformations and uniaxial and biaxial mechanical properties of thoracic porcine aorta. *Journal of the Mechanical Behavior of Biomedical Materials* 50 (2015):55-69.

[9] Labrosse, M. R., Gerson, E. R., Veinot, J. P., and Beller, C. J. Mechanical characterization of human aortas from pressurization testing and a paradigm shift for circumferential residual stress. *Journal of the mechanical behavior of biomedical materials* 17 (2013): 44-55.

[10] Martin, C., Sun, W., Pham, T., and Elefteriades, J. Predictive biomechanical analysis of ascending aortic aneurysm rupture potential. *Acta biomaterialia* 9.12 (2013): 9392-9400.

[11] Rastgar Agah, M., et al. "Mechanical behavior of porcine thoracic aorta in physiological and supra-physiological intraluminal pressures." *Proceedings of the Institution of Mechanical Engineers, Part H: Journal of Engineering in Medicine* 231.4 (2017): 326-336.

[12] Pena, J. A., et al. "Over length quantification of the multiaxial mechanical properties of the ascending, descending and abdominal aorta using Digital Image Correlation." *Journal of the mechanical behavior of biomedical materials* 77 (2018): 434-445.

[13] Gardais, A., Picard, J., and Hermelin, B. (1973). Glycosaminoglycan (GAG) distribution in aortic wall from five species. *Comparative Biochemistry and Physiology Part B: Comparative Biochemistry* 44.2 (1973) 507-515.

## 4.9 SUPPLEMENTARY INFORMATION

Note that the material provided in the Supplementary Information section of Chapter 4 was generated using FEBioStudio Version 1.7, while the data provided in the body of Chapter 4 was generated using FEBio version 2.9.1, which may have led to slight discrepancies.

### 4.9.1 Principal Stress Figures

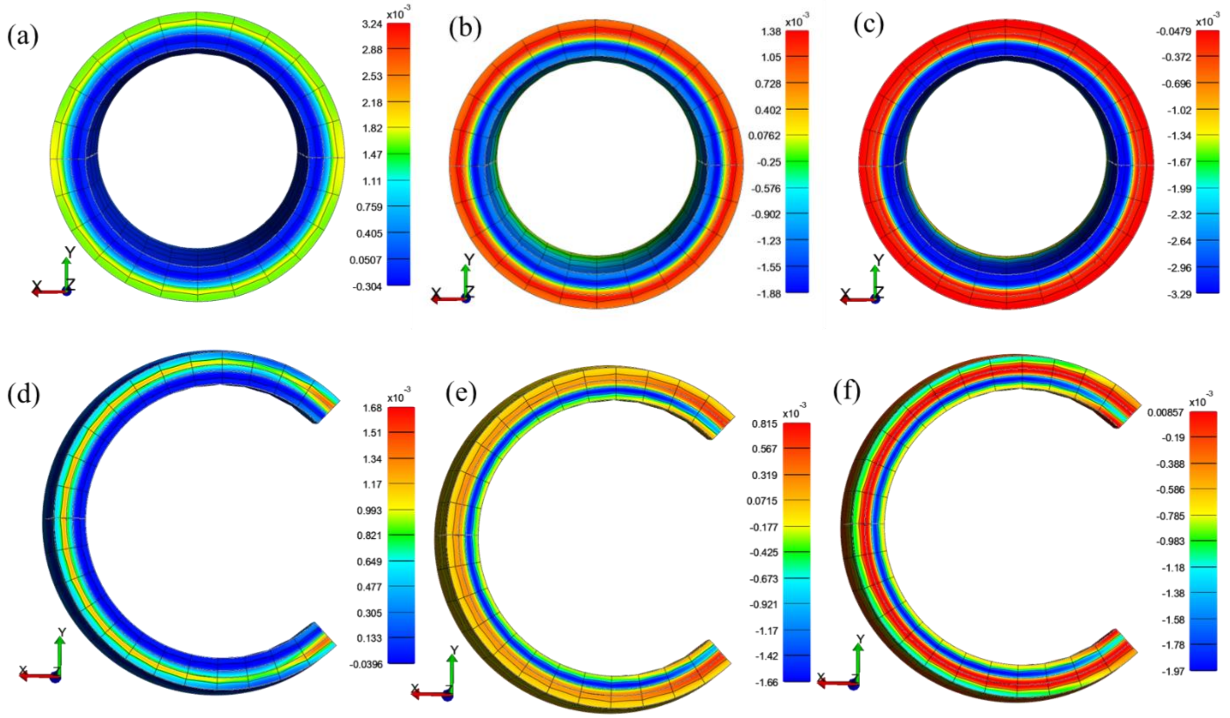

*Figure S4.1:Principal Stress (a,d) 1, (b,e) 2 and (c,f) 3 in closed (a,b,c) and open (d,e,f) porcine aortic rings assigned the same baseline FCD distribution as in [2] ($c_0^F$ = -40 meq/L in the intimal and medial layers, $c_0^F$ = -20 meq/L in the transition layer and $c_0^F$ = 0 meq/L in the adventitia).*

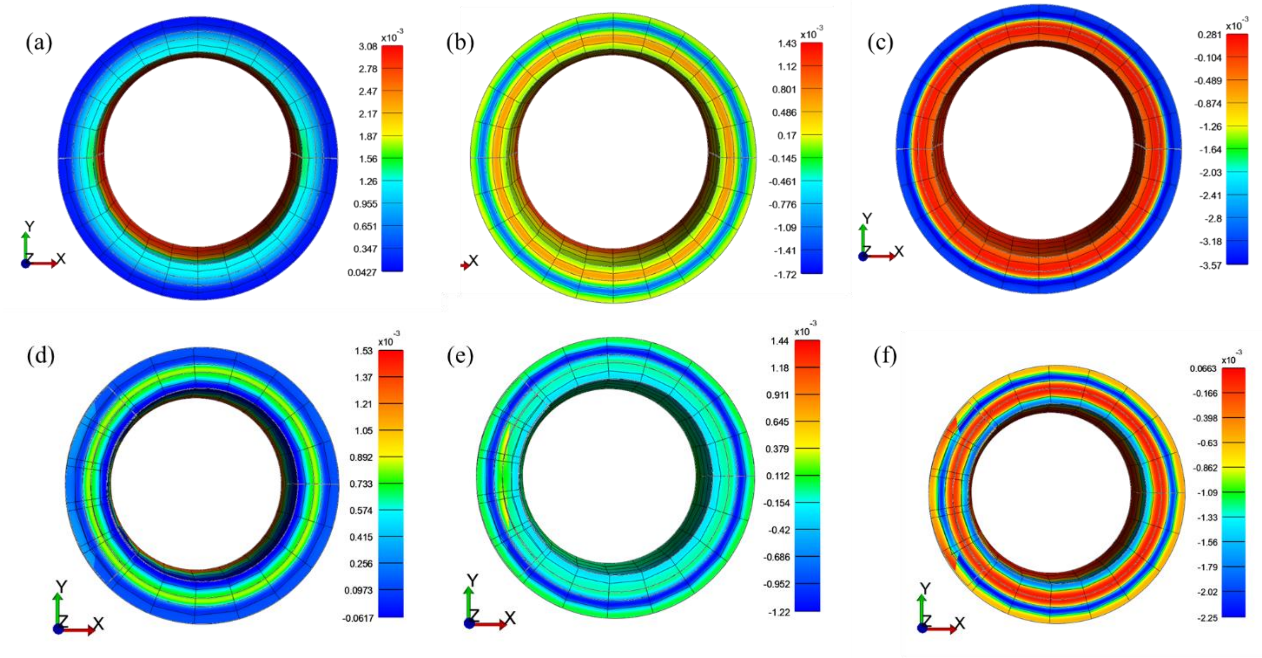

*Figure S4.2: Principal Stress (a,d) 1, (b,e) 2 and (c,f) 3 in closed (a,b,c) and open (d,e,f) porcine aortic rings assigned an inverted FCD distribution compared to [2] ($c_0^F$ = 0 meq/L in the intimal and medial layers, $c_0^F$ = -20 meq/L in the transition layer and $c_0^F$ = -40 meq/L in the adventitia)*

### 4.9.2 Mesh Sensitivity Analysis

*Table S4.1: Mesh sensitivity analysis of open porcine aortic ring model prescribed with -70 mEq/L in the first and second layers (intima and media), -50 mEq/L in the third (transition) layer, and -30 mEq/L in the fourth and fifth layers (adventitia). Parameters are provided for a quarter model*

| Number of elements in thickness | Number of elements in length | Number of elements in circumference | Number of elements | Number of nodes | Opening Angle (deg) | Effective Stress in Outer Element at Free End (kPa) |
|---|---|---|---|---|---|---|
| 5 | 4 | 8 | 160 | 951 | 71.5 | 0.52 |
| 5 | 4 | 10 | 200 | 1169 | 72.04 | 0.51 |
| **5** | **4** | **12** | **240** | **1387** | **72.51** | **0.51** |
| 5 | 4 | 14 | 280 | 1605 | 72.51 | 0.51 |
| 5 | 4 | 20 | 400 | 2259 | 72.82 | 0.51 |
| 5 | 4 | 25 | 500 | 2804 | 72.96 | 0.51 |
| 5 | 4 | 30 | 600 | 3349 | 73.04 | 0.50 |
| 5 | 4 | 35 | 700 | 3894 | 73.09 | 0.49 |
| 5 | 4 | 40 | 800 | 4439 | 73.13 | 0.48 |

### 4.9.3 Additional Information

In Chapter 4, the direction of the fibers was defined using the global coordinate system (x,y,z) as illustrated in Figure 4.1. As a follow up to the publication, in this section, we report results for models in which fibers were redefined using element local coordinate system, in order to ensure that fibers are at an angle $\pm 51.45^{o}$ along the circumference in all elements. The conclusions reported in the chapter are not affected, however, there were slight changes to the absolute values for the opening angles and stresses, which is the reason why we report them in this appendix section. Appropriate changes have been made to Figure 4.2, which are now presented in Figure S4.3. There were no changes to the results associated with the baseline distribution, and as such, Figure 4.1 was not affected, nor rectified.

For parametric Study 2 when the FCD distribution varied from of $c_0^F$ = -40, -20, 0 meq/L (baseline) to $c_0^F$ = -100, -80, -60 meq/L in the intimal/medial, transition and adventitial layers respectively, in -5 meq/L offsets, the trends for both the stresses in the cut and uncut geometries as well as the opening angles remained similar. While there were no major changes in the values for the opening angle, slight changes were detected for the stress results. The corresponding data is in Figure S4.3a and b.

Similarly, for parametric Study 2 when the FCD distribution varied from a distribution of $c_0^F$ = -40 meq/L, -20 meq/L and 0 meq/L to a distribution of $c_0^F$ = -214 meq/L, -107 meq/L, 0 meq/L in the intimal/medial, transition and adventitial layers respectively, in successive multiplications by 1.15 (15% increases), the trend for the stresses remained similar, such that the peak effective stresses in the radially cut and uncut porcine aortic rings increased exponentially with successive multiplications, with the former always staying below the latter. The absolute values slightly differed after redefining fiber axis, and are presented in Figure S4.3c. However, the opening angle no longer increased linearly, as shown in Figure S4.3d, and reached a maximum value of 172$^o$, which was still much larger than opening angles when the FCD distribution was varied in offsets of -5 mEq/L.

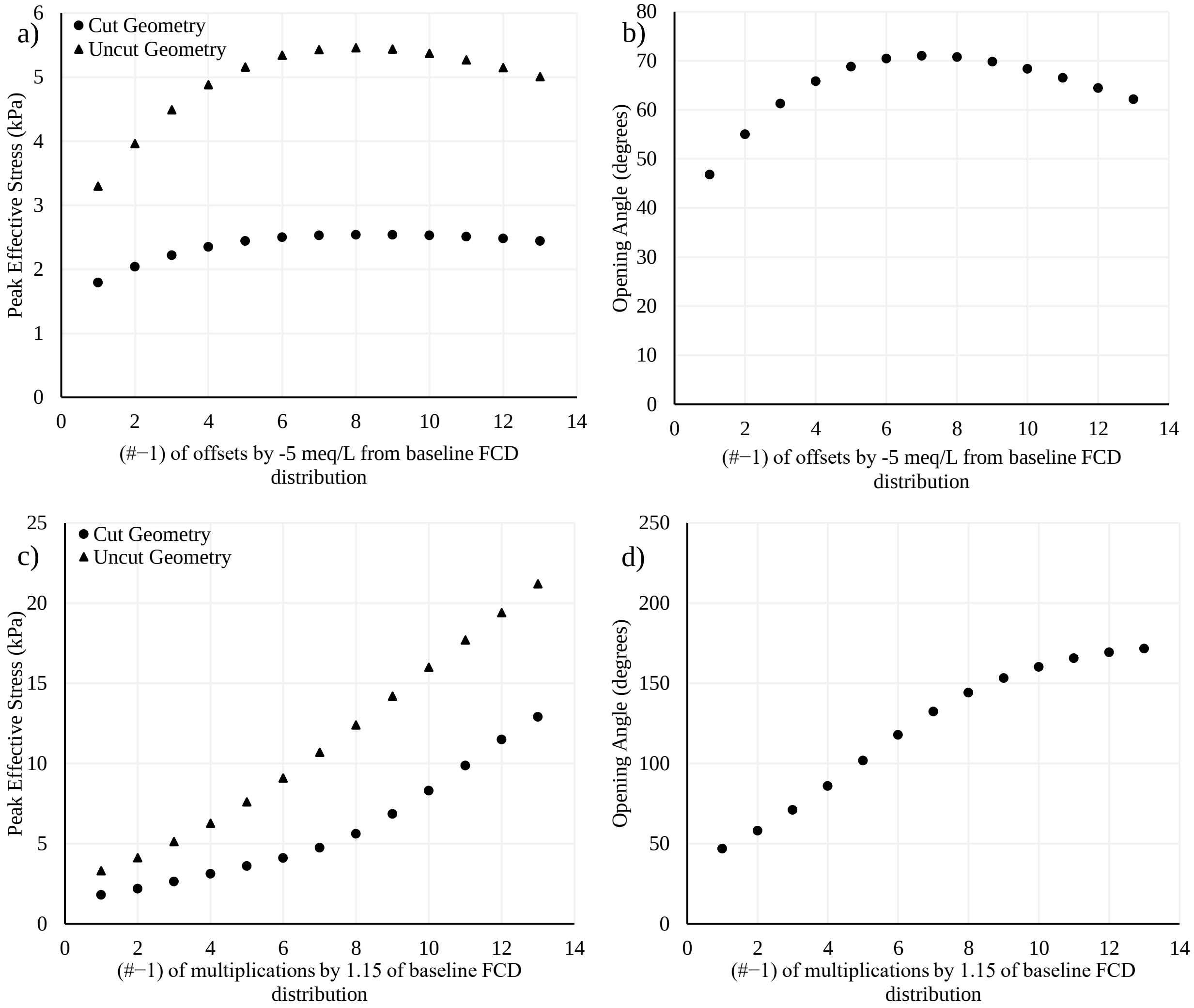

*Figure S4.3: Results from porcine aortic ring model with fibers redefined in the element local coordinate system (ensuring an orientation of ±51,45$^o$ along the circumference in all elements). Variation of the peak effective* (Von Mises) *stress (a) and opening angle (b) when increasing the baseline GAG distribution by -5 meq/L increments. Variation of the peak effective* (Von Mises) *stress (c) and opening angle (d) when multiplying the baseline GAG distribution by 1.15 multiple times.*

# 5

# INTRAMURAL DISTRIBUTIONS OF GAGS AND COLLAGEN VS. OPENING ANGLE OF THE INTACT PORCINE AORTIC WALL

---

Noor Ghadie [a], Jean-Philippe St-Pierre [b], Michel R. Labrosse [a,c]

[a] Mechanical Engineering Department, University of Ottawa, Ottawa, ON. Canada K1N6N5

[b] Chemical and Biological Engineering Department, University of Ottawa, Ottawa, ON. Canada K1N6N5

[c] Department of Cardiac Surgery, University of Ottawa Heart Institute, Ottawa, ON. Canada K1Y4W7

Content of this chapter published in Annals of Biomedical Engineering | February 2022

Ghadie, N. M., St-Pierre, J. P., & Labrosse, M. R. (2022). Intramural Distributions of GAGs and Collagen vs. Opening Angle of the Intact Porcine Aortic Wall. Annals of Biomedical Engineering, 50(2), 157-168.

## 5.1 FOREWORD

The numerical investigation carried out in Chapter 4 provided important first insights into the effect of glycosaminoglycan (GAG) on residual stresses, but was associated with a number of limitations. First, while the distributions of GAG throughout the aortic wall is expected to vary between species, the baseline distribution was built based on observations from Leghorn chickens. Second, these distributions were approximated from qualitative histological observations, which may introduce inaccuracies in their quantity estimations. For these reasons, and as also discussed in Chapter 3, we aimed to characterize the distribution of sulfated GAG (sGAG) throughout the wall of porcine aortas. To offer a comprehensive characterization of the extracellular matrix, collagen and elastin were also investigated. Furthermore, to experimentally investigate the impact of sGAG on residual stresses and, consequently, validate the fidelity of the simulation results, correlations between sGAG content and gradient and the opening angle were established from *in vitro* results. This aimed to provide experiential evidence and support to the simulation outcomes, ensuring their reliability and confirming the influence of sGAG distribution on residual stress. In an attempt to achieve a comprehensive understanding of how the primary ECM constituents collectively impact residual stresses in the aorta, correlations between collagen, elastin and the collagen:sGAG ratio with the opening angle were established.

## 5.2 ABSTRACT

The heterogeneity and contribution of collagen and elastin to residual stresses has been thoroughly studied, but more recently, glycosaminoglycans (GAG) also emerged as potential regulators. In this study, the opening angle of aortic rings (an indicator of circumferential residual stresses) and the mural distributions of sulfated GAG (sGAG), collagen, and elastin were quantified in the ascending, aortic arch and descending thoracic regions of 5- to 6-month-old pigs. The opening angle correlated positively with the aortic ring’s mean radius and thickness, with good and moderate correlations respectively. The correlations between the sGAG, collagen, elastin, and collagen:sGAG ratio and the opening angle were evaluated to identify aortic compositional factors that could play roles in regulating circumferential residual stresses. The total collagen:sGAG ratio displayed the strongest correlation with the opening angle ($r = -0.715$, $p < 0.001$), followed by the total sGAG content which demonstrated a good correlation ($r = 0.623$, $p < 0.001$). Additionally, the intramural gradients of collagen, sGAG and collagen:sGAG correlated moderately with the opening angle. We propose that, in addition to the individual role sGAG play through their content and intramural gradient, the interaction between collagen and sGAG should be considered when evaluating circumferential residual stresses in the aorta.

**Keywords**: Residual Stress, Opening angle, Aorta, Glycosaminoglycans, Collagen.

## 5.3 INTRODUCTION

Current state-of-the-art mathematical and computational biomechanical models of large arteries, such as those that might be used to predict aortic ruptures, include elastin, collagen fibers and possibly smooth muscle cells (SMCs) as microstructural constituents [1–7]. The high water content is typically accounted for by isochoric deformations (local incompressibility [8]). The models consider one, two or three load-bearing layers, corresponding to the intima, media and adventitia, or groups thereof. There is overwhelming agreement that residual stresses (i.e. all the stresses existing in the unloaded configuration after removal of in-situ longitudinal stretch and luminal pressure) play a crucial role in homogenizing the *in vivo* stresses experienced by the arterial wall and, therefore, require inclusion for meaningful biomechanical predictions [1,9].

The circumferential and longitudinal residual stresses manifest *ex vivo* via the opening angle of a ring of the artery after a radial cut, and the bending of a strip cut longitudinally, respectively [5,10,11]. Such experiments on the intact wall only reveal an approximate zero stress state (ZSS), a crucial reference configuration in continuum mechanics [1]. Indeed, when the layers of the arterial wall are mechanically separated, they exhibit ZSSs that are different from that of the intact wall [3,10–12].

Focusing on circumferential residual stresses and strains, the opening angle of the intact wall can be recovered in models either via a top-down approach based on phenomenological information about layer-dependent opening angle values [1,13], or via a bottom-up approach using models featuring pre-stretches obtained from microstructural information about elastin and collagen [4,7]. Indeed, if one knows the ZSS of the individual, or group of, aortic layers, putting them back into a closed cylindrical tubular segment allows one to determine the load-free configuration (i.e. un-stretched and unpressurized) with residual stresses and strains, onto which in-situ longitudinal stretch and luminal pressure can be applied to assess *in vivo* stresses [13–15]. Alternatively, if one doesn't know the opening angles of the individual, or group of, aortic layers, and therefore, if the ZSS is unknown, residual stress fields in the load-free configuration can be induced via the inclusion of longitudinal and circumferential pre-stretches, which account for the existence of different microstructural constituents, such as collagen and elastin, in the extracellular matrix (ECM) [1,7,16]. For instance, it is well established that elastin is deposited and cross-linked during the perinatal period and features a half-life on the order of decades. Therefore, it experiences extensive elastic deformations during normal biological growth until maturity [17–19]. By contrast, collagen turns over continuously and is assumed to be deposited at a preferred stretch value at maturity [14,18]. However, determination of all the relevant prestretch values remains elusive, and as a result, most biomechanical models, even those microstructurally-inspired, still require the identification of at least some parameters through a phenomenological approach (top-down) based on the overall response of the artery, rather than knowledge of its individual constituents (bottom-up) [1,20]. Therefore, a more comprehensive understanding of residual stresses is still needed.

Experimental findings have connected residual stresses and strains in large arteries to the existence of functional elastin [21]. As to the role of collagen, contradicting results have been reported, as it was shown to have no effect [22], and to play a role [23], in residual stresses. Similarly, while some reports have shown that SMCs are not involved [22,23] in regulating residual stresses, others have shown that their state of activation may play a role [24]. Simulations have also shown that less elastin in arteries would induce a reduction in opening angle, and that collagen plays a complementary role [18]. However, the dependence of the opening angle on the osmolarity of the bathing fluid [9,25] and the intramural distribution of glycosaminoglycans (GAG) and proteoglycans (PG), which are constituents of the ground substance in the aortic ECM, has suggested that GAG/PG are involved in residual stresses and strains as well [26–28]. It can therefore be hypothesized that intramural differential concentration of GAG/PG may influence, at least in part, the elastin and collagen pre-stretches mentioned above, and may provide a complementary pathway for regulating residual stresses in the arterial wall.

For lack of comprehensive data, the distributions of the ECM's components in most models including swelling through osmotic pressure have been based on an array of assumptions and histological observations [26,27,29,30], the latter remaining qualitative or semi-quantitative in nature, as they can be impacted by the use of labelling molecules and sectioning nonuniformities [31,32]. To advance basic knowledge with relevance to the human aorta, the purpose of this study was to investigate the ECM's main constituents, namely elastin, collagen and GAG, and their correlation to circumferential residual stresses in 5-6 months old porcine aorta. Special attention was paid to the intramural distributions of these constituents in different locations of the aortic tree. This study represents an early step of an ongoing program to elucidate the role of GAG/PG in the dynamic evolution of aortic residual stresses with aging and pathologies.

## 5.4 MATERIALS AND METHODS

### 5.4.1 Tissue Harvesting

Seven excised aortas from 5- to 6-month-old pigs weighing approximately 90-100 kg were obtained from a local abattoir and were cleaned from adjacent fatty and connective tissue. Samples were preserved at $4^0$C and were subsequently tested within 24 hours of slaughter. Three main regions of the aortic tree were studied: the ascending region, the aortic arch region, and the descending thoracic region, as detailed in Figure 5.1a. Samples from the descending thoracic region were excised from between the sixth and eighth intercostal arteries [33]. Three aortic rings of 4-5 mm in axial length were excised from each of the three regions of interest. The front and right quadrants of the rings were identified using fine surgical stitches (Figure 5.1b). This allowed tracking of the location of the back and left regions subsequent to radially cutting each ring for opening angle measurements. Following measurement of the opening angle, each ring was processed for evaluation of the ECM content as described below. Aortas 1 to 5 were tested for sulfated GAG (sGAG) and collagen contents (n = 45). For completeness, elastin content was also investigated; one ring per region was obtained and tested for this purpose from Aortas 3 to 7 (n = 15). Samples obtained from Aortas 6 and 7 were used for elastin evaluation only.

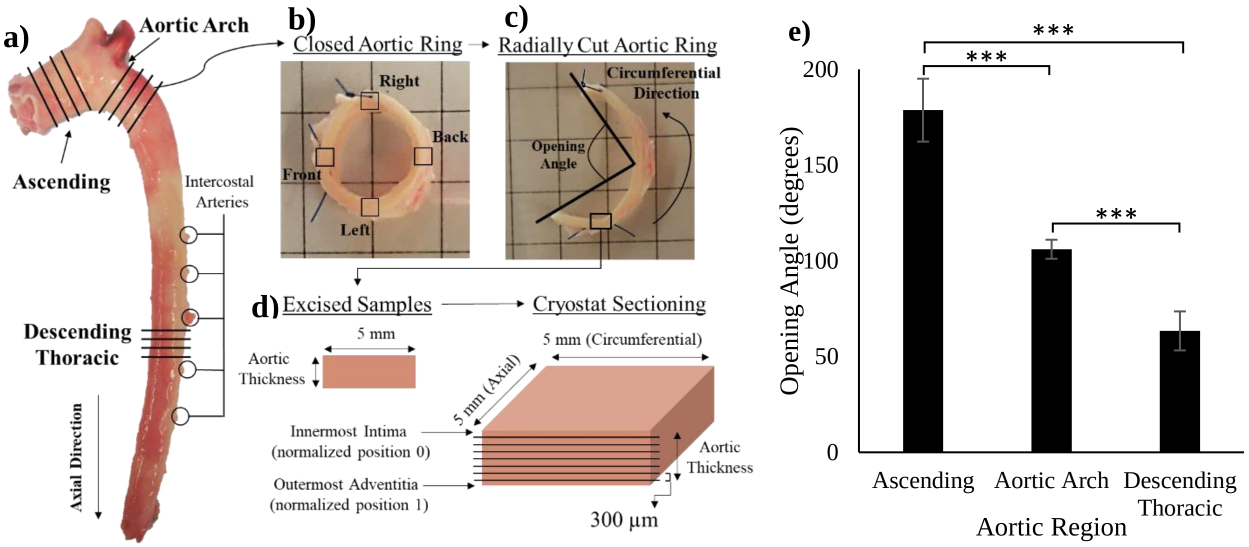

*Figure 5.1: (a) Image of an excised thoracic aorta with key anatomical features and location of rings excised for investigation. (b) Image of an aortic ring after excision from the aorta including the sutures added for quadrant localization. Insets show the different quadrants. (c) Image of a cut aortic ring for opening angle measurement. (d) Illustration of an excised aortic sample stored for microstructural analysis, and direction of cryostat sectioning (e) Opening angles of aortic rings obtained from different anatomical regions presented as mean ± standard error of the mean (SEM) (n=17 rings per region obtained from 7 animals, 3 anatomical regions per animal). *** indicates p < 0.001 (Welch with Games-Howell Post-Hoc test).*

To explore potential differences in tissue composition within a single ring, we analyzed the differences in mural contents and distributions of sGAG and collagen between the back, front, left and right quadrants. This was investigated in Aortas 1 and 2 for sGAG (n = 18 rings) and in Aorta 1 for collagen (n = 9 rings). Because no statistical difference was observed between the quadrants (Supplemental Figures S5.6 and S5.7), only one location per ring was investigated in the remainder of the study. Similarly, the content and mural distribution of elastin was assumed to be similar for all quadrants, and only one location was investigated (1 ring per region of a single aorta).

### 5.4.2 Opening Angle Measurement

Rings were left to float in transparent petri dishes containing 300 mosM of phosphate buffered solution at room temperature, positioned over a calibration grid. A digital picture of each closed ring was taken (Figure 5.1b). Each ring was then subjected to a radial cut, which allowed to relieve most of the circumferential residual stresses. The rings were left to stabilize for approximately 20 min [11,22,34] and a second digital picture was taken (Figure 5.1c). We then calculated the opening angle using a previously published custom-written MATLAB code [34]. Briefly, the method involved measuring the opening angle from the inner and outer arc lengths in the load-free and stress-free configurations, as described in [34,35]. For reference, in the present study, the opening angle is considered null when the ring is closed, in the load-free configuration. Samples approximately 5 mm by 5 mm in the axial and circumferential directions of the aortic rings were then excised from each ring (Figure 5.1d) and either kept frozen at -$20^0$C for further testing (microstructural analysis) or processed immediately (histological analysis), as explained in the following Sections.

### 5.4.3 Microstructural Analysis

To quantify the aortic intramural distributions of sGAG, collagen and elastin, aortic tissue samples were frozen in water and 300 µm-thick sections across the aortic wall thickness from the stored 5x5 mm samples (Figure 5.1d) were obtained by serial sectioning using cryostat (CM3050 S; LEICA). Wet weights for each section were obtained for normalization of the ECM contents. Due to variability in tissue thickness, the number of cryostat sections varied between samples, and normalized positions of the tissue sections were used through the thickness of the aortic wall (normalized position = $\frac{i-1}{n-1}$, “i” being the index of the corresponding cryosection sample, and “n” being the total number of cryosections). The innermost intima was always section i = 1, thereby having a normalized position of 0, and the outermost adventitia was always section i = n, thereby having a normalized position of 0 (Figure 5.1d).

The sGAG and collagen contents in each section were quantified from papain digested samples. Briefly, sections were incubated with 40 µg/ml of papain from papaya latex in 5 mM of cysteine and 5 mM of ethylenediaminetetraacetic acid (EDTA) at $60^o$C for 48 hours. The sGAG content was determined using a dimethylmethylene blue (DMMB) spectrophotometric assay [36]. The standard curve was generated using chondroitin sulfate A sodium salt and the color change was quantified spectrophotometrically by measuring the absorbance at 525 and 590 nm wavelengths and calculating the ratio A525/A590. The collagen content was estimated by quantifying hydroxyproline in acid hydrolyzed papain digests. Papain digest aliquots were hydrolyzed using an equal volume of 6 N HCl at $100^0$C for 18 hours, after which they were neutralized with an equal volume to the papain digest aliquot of 5.7 N NaOH. Hydroxyproline was quantified using the Ehrlich's reagent assay [37]. L-Hydroxyproline was used as a standard, and the color change was quantified spectrophotometrically at 560 nm. It was assumed that hydroxyproline contains 10% of the collagen weight. The elastin content was quantified using a Fastin$^{TM}$ elastin colorimetric assay kit (Biovendor R&D), according to the manufacturer's instructions. Briefly, tissue sections were immersed in 750 µL of 0.25 M oxalic acid placed in Pyrex tubes and incubated at $100^0$C for 2 hours to extract water soluble α-elastin. The supernatant was collected, and the extraction step was repeated with fresh oxalic acid solution. Two extractions were sufficient to ensure that most of the tissue elastin was solubilized. Precipitated elastin was then incubated with 5,10,15,20-tetraphenyl-21H,23H-porphine tetra-sulfonate (TPPS) in citrate buffer, after which the elastin-bound dye was released using the manufacturer's dye dissociating reagent. The color change was quantified spectrophotometrically at 513 nm. Standards were prepared from bovine α-elastin.

### 5.4.4 Histological Analysis

In addition to the quantitative analyses described above, histological analyses were carried out as follows. Tissue samples from the three anatomical regions investigated were procured from two aortas and fixed in 10% formalin solution for 72 hours, then transferred to 70% ethanol. Samples were dehydrated in a water-ethanol series with increasing ethanol concentration. Samples were then cleared with xylene, after which the tissues were infiltrated with molten paraffin wax. Samples were then cut into 4 µm-thick sections and stained with Alcian blue, Masson Trichrome, and Verhoeff's -VanGieson elastic stains. Alcian blue was used to highlight GAG within the aortic tissue in blue; Masson's trichrome allowed visualization of cells in red and collagen in blue and Verhoeff-VanGieson's stained elastin within the tissue in black.

### 5.4.5 Statistical Analysis

Results are presented as mean ± standard error of the mean (SEM) and statistical analyses were performed using IBM SPSS Statistics 26.0. One-way ANOVA was used to evaluate the significance in differences between groups (regions or quadrants). Levene's test was used to verify equal variance between groups. Tukey HSD was used as a Post Hoc test when Levene's test was not significant, while Games-Howell was used as a Post Hoc test for cases when significance was found in Levene's test.

Correlation between tissue opening angle and contents of ECM components was evaluated by calculating the total, average (per section) amounts of sGAG, collagen, collagen:sGAG ratio and elastin, as well as their intramural gradients. The gradient was calculated as the difference between the values from the first and last sections of the aortic wall. Pearson's correlation "r" was calculated to evaluate the strength and significance of the correlations. The correlations were classified as strong correlations when the r value was higher than 0.7, good when the r value was between 0.5 and 0.7, moderate when the r value was between 0.3 and 0.5, and poor when the r value was lower than 0.3 [38]. Significance was accepted at the 95% confidence level (2-tailed).

## 5.5 RESULTS

### 5.5.1 Opening Angle and Aortic Dimensions

The opening angle decreased in aortic rings extracted from distal regions compared to those extracted from more proximal regions to the heart, with statistical difference between the ascending, arch and descending thoracic regions (Figure 5.1e). A distal decrease in the aortic ring's radius and thickness measured in the load-free configuration was also observed (Supplemental Figure S5.1). Animal-specific results for the opening angle, radius and thickness in the load-free configuration are provided in Supplemental Figures S5.2-S5.4. These figures show that the extent of the variations in the opening angle, radius and thickness between regions were animal-dependent; however, their overall values decreased from the ascending to the descending thoracic regions. In addition, the opening angle was found to correlate with the mean radius and thickness of the aortic ring as shown in Figure 5.2; a good correlation was detected with the radius ($r = 0.544$, $p < 0.001$), and a moderate correlation was found with the thickness ($r = 0.396$, $p = 0.004$).

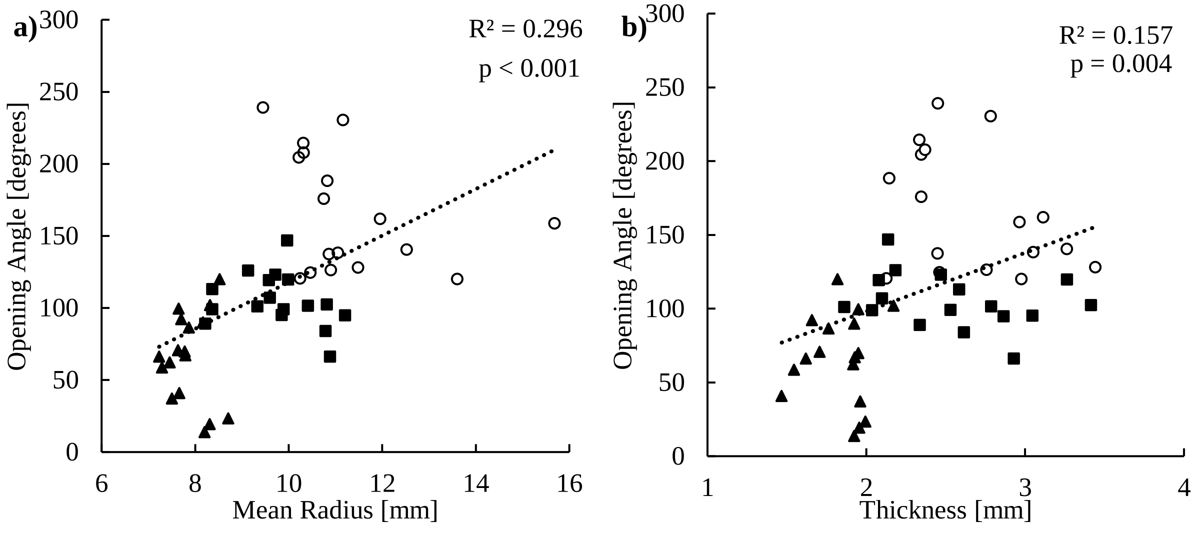

*Figure 5.2: Variation of the opening angle as a function of (a) mean radius of the aortic ring (r=0.544; N=51 from 7 animals, 3 anatomical regions per animal), and (b) aortic thickness (r=0.396; N=51 from 7 animals, 3 anatomical regions per animal). The radius and thickness are measured in the load-free configuration. Samples from the ascending, aortic arch and descending thoracic regions are represented by hollow circles, solid squares and solid triangles, respectively.*

### 5.5.2 Dry Weight Contents of ECM Components

Figure 5.3a displays the overall dry weight (dw) normalized composition of the aortic wall's ECM. The sGAG content decreased significantly from 1.03±0.04 %dw in the ascending aorta to 0.83±0.03 %dw and 0.78±0.02 %dw in the aortic arch and descending thoracic regions, respectively. Compositions in collagen and elastin did not display significant differences between regions, and varied from 19 to 21 %dw, and 21 to 28 %dw, respectively (Figure 5.3a).

### 5.5.3 Intramural Distributions of ECM Components

The intramural distributions of sGAG, collagen and elastin are shown in Figure 5.3b, Figure 5.3c, and Supplemental Figure S5.5, respectively. The intramural distribution of the collagen:sGAG ratio is shown in Figure 5.3d. The results show that sGAG decreased in content from the innermost intima to the outermost adventitia, in accordance with qualitative observations from histological staining (Figure 5.4). An inverse profile was observed in the case of the collagen and collagen:sGAG ratio distributions, with higher contents found towards the adventitia. The elastin distribution showed higher content in the media.

The total (Tukey HSD, $p < 0.001$) and average (Tukey HSD, $p < 0.01$) amounts calculated from the sGAG distribution in the ascending region were found to be significantly different from those in the aortic arch and descending thoracic regions (Aortas 1-5, Figure 5.3b), with higher sGAG amounts in the ascending region. The average collagen (Tukey HSD, $p < 0.001$) and collagen:sGAG (Tukey HSD, $p < 0.01$) in the ascending region were found to be significantly different from the descending thoracic region, but not from the aortic arch region. In particular, lower levels were observed in the ascending region, with visible differences localized in the adventitia (Figure 5.3c, 5.3d). While no significant difference was found in the total amount of collagen between the regions, the total collagen:sGAG in the ascending region was found to be significantly different from the aortic arch and descending thoracic regions (Tukey HSD, $p < 0.001$).

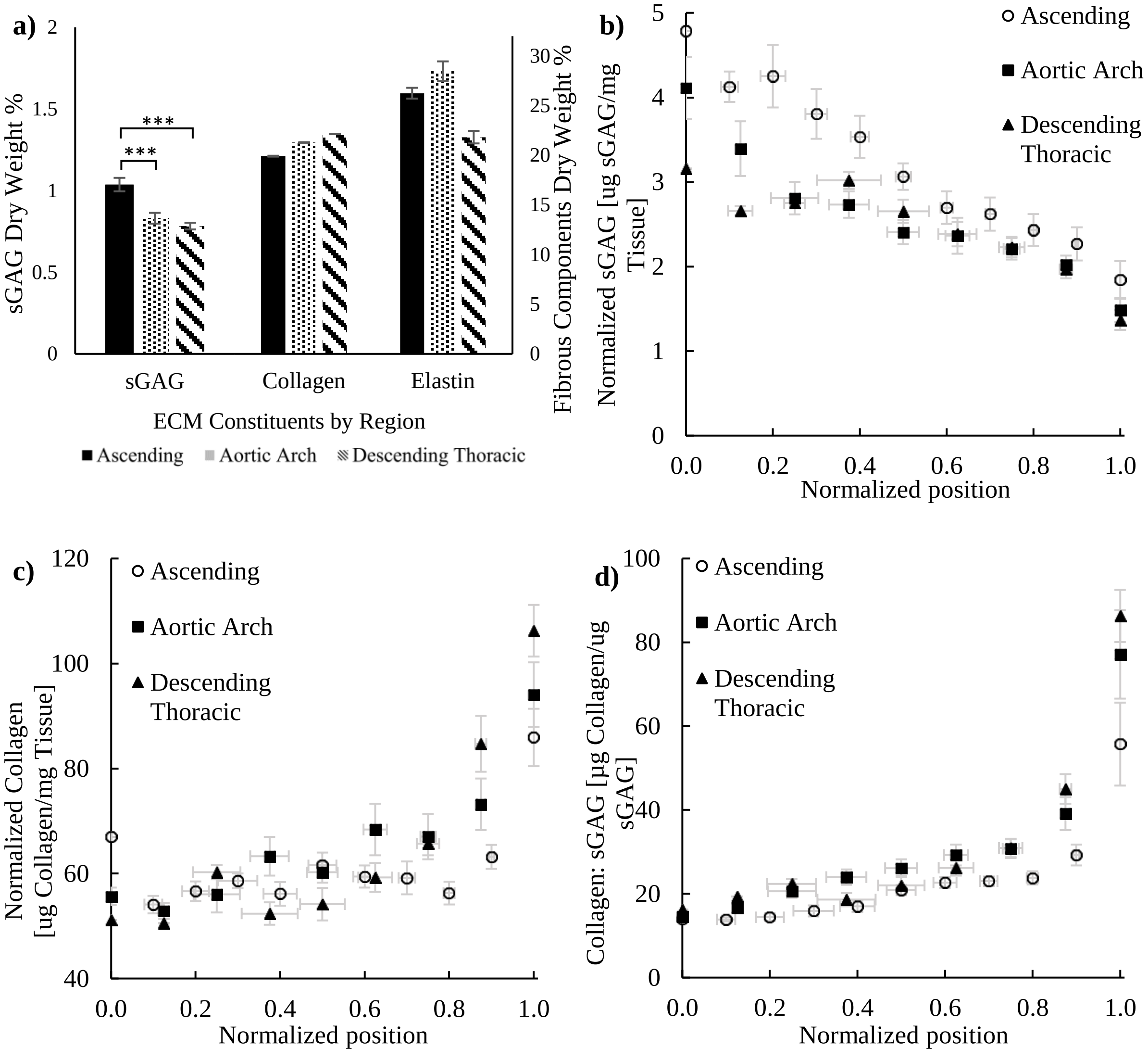

*Figure 5.3: (a) Overall composition of the main ECM components, sGAG (N=15 from 5 animals), collagen (N=15 from 5 animals), and elastin (N=5 from 5 animals) normalized by dry weight in the ascending, aortic arch and descending thoracic regions of porcine aortas (mean ± SEM). *** indicates $p < 0.001$ (ANOVA with Tukey HSD Post-Hoc test). (b) Intramural distribution of sGAG (N=15 from 5 animals) (c) collagen (N=15 from 5 animals) and (d) collagen:sGAG (N=15 from 5 animals), in the ascending, aortic arch and descending thoracic regions. Position 0.0 along the x-axis refers to the innermost intima while position 1.0 refers to the outermost adventitia. Error bars along x-axis represent the SEM for section position to account for the fact that samples produced different numbers of sections because of variations in thicknesses.*

The differences in gradients for sGAG, collagen and collagen:sGAG ratio between the regions were also investigated (Supplemental Figure S5.8). The sGAG and collagen gradients in the ascending region were significantly different from those in the descending thoracic region (Tukey HSD, p = 0.008 and p = 0.017 respectively) but not from those in the aortic arch region. Elastin did not display any significant differences between the regions of interest.

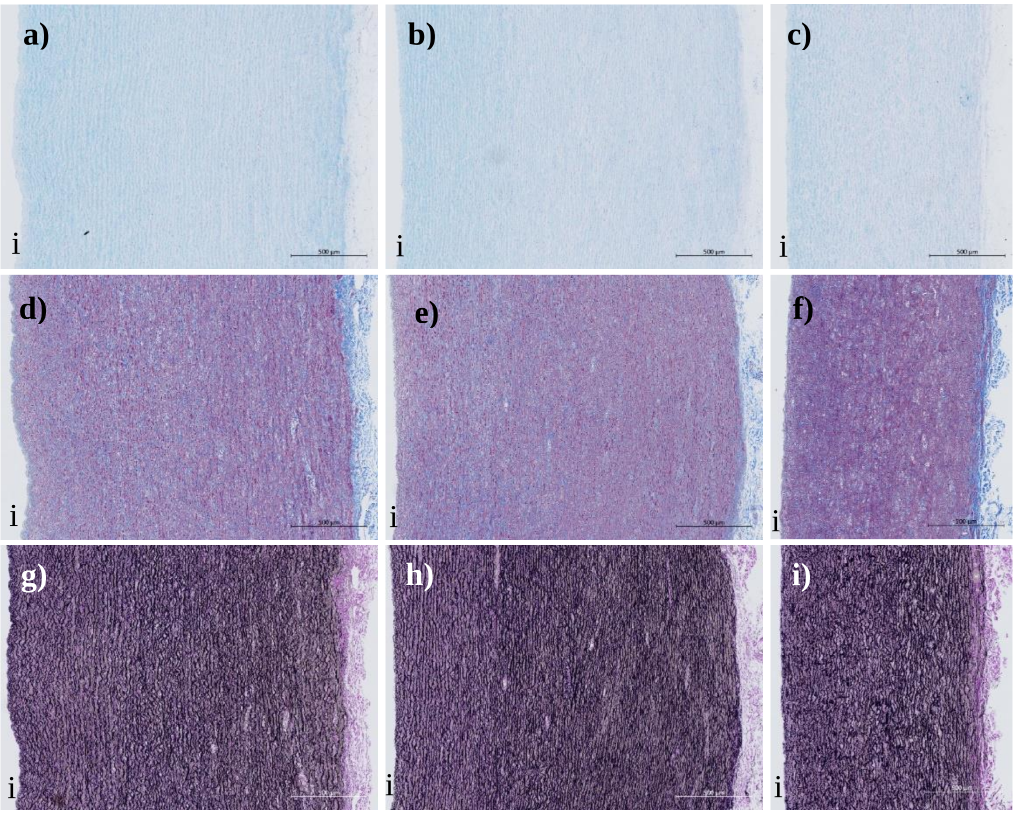

*Figure 5.4: Representative histology sections of aortic tissues from (a,d,g) the ascending, (b,e,h) aortic arch, and (c,f,i) descending thoracic aorta, stained with (a-c) Alcian blue, (d-f) Masson's trichrome, and (g-i) Verhoeff's - VanGieson's. Intimal layers are aligned with the left side of each panel, marked with the letter "i".*

For details on the variability between animals, we included examples of the sGAG, collagen and collagen:sGAG ratio distributions from Aortas 2 and 4 in Supplemental Figure S5.9. In Aorta 2, for which the opening angle displayed a significant difference between the 3 regions (Supplemental Figure S5.2), there was a visible shift between the sGAG distribution in the ascending region compared to that in the abdominal and aortic arch regions. The differences in distributions were more subtle in Aorta 4 (Supplemental Figure S5.9d), where no significant difference in opening angle was detected between the regions.

### 5.5.4 Correlations with Opening Angle

The correlations between the opening angle and the total and gradient of sGAG, collagen and collagen:sGAG ratio are presented in Figure 5.5.

Results for the average sGAG, collagen and collagen:sGAG ratio and for elastin are provided in Supplemental Figures S5.10 and S5.11, respectively. It can be observed that sGAG contents correlated positively with the opening angle, while collagen contents and collagen:sGAG ratio correlated negatively with the opening angle. The strongest correlations were associated with collagen:sGAG ratio and the sGAG contents. In particular, collagen:sGAG ratio calculated from the total amounts of collagen and sGAG (Figure 5.5e) displayed the strongest correlation with the opening angle (strong correlation, $r = -0.715$, $p < 0.001$). Good correlations were also found between the total sGAG content (Figure 5.5a) and the opening angle ($r = 0.667$, $p < 0.001$), as well as the average content of sGAG ($r = 0.623$, $p < 0.001$) and collagen:sGAG ratio ($r = -0.54$, $p < 0.001$), and the opening angle (Supplemental Figures S5.10a and S5.10c, respectively).

Moderate correlations were detected between the opening angle and the gradients of sGAG ($r = -0.320$, $p = 0.032$), collagen ($r = -0.367$, $p = 0.045$), and the collagen:sGAG ratio ($r = -0.348$, $p = 0.019$) (Figures 5.5b, 5.5d and 5.5f, respectively). While the total collagen content in the aortic wall did not display any significant correlation with the opening angle (Figure 5.5c), the average collagen amount across the aortic wall demonstrated a moderate correlation with the opening angle, as shown in Supplemental Figure S5.10b ($r = -0.410$, $p = 0.005$). Elastin did not display any correlations with the opening angle (Supplemental Figure S5.11).

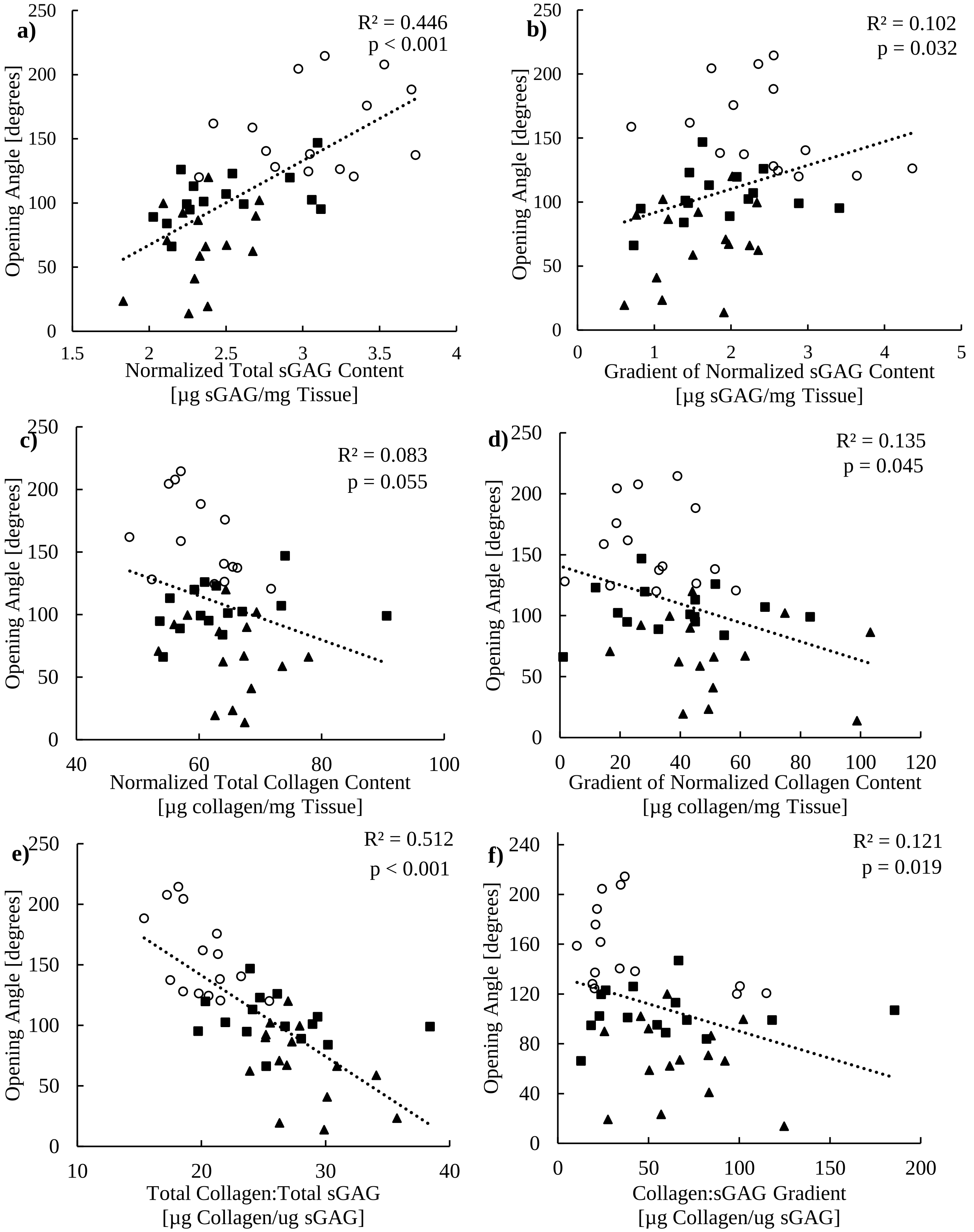

*Figure 5.5: Variation of the (a) total sGAG content (r=0.667;N=45), (b) sGAG gradient (r=0.320;N=45), (c) total collagen contents (r=-0.288;N=45), (d) collagen gradient (r=-0.367;N=45), (e) collagen:sGAG ratio (r=-0.715;N=45) calculated from the total amounts of collagen and sGAG, and (f) gradient of the collagen:sGAG ratio (r=-0.348;N=45), with respect to the opening angle. Samples from the ascending, aortic arch and descending thoracic regions are represented by hollow circles, solid squares and solid triangles, respectively.*

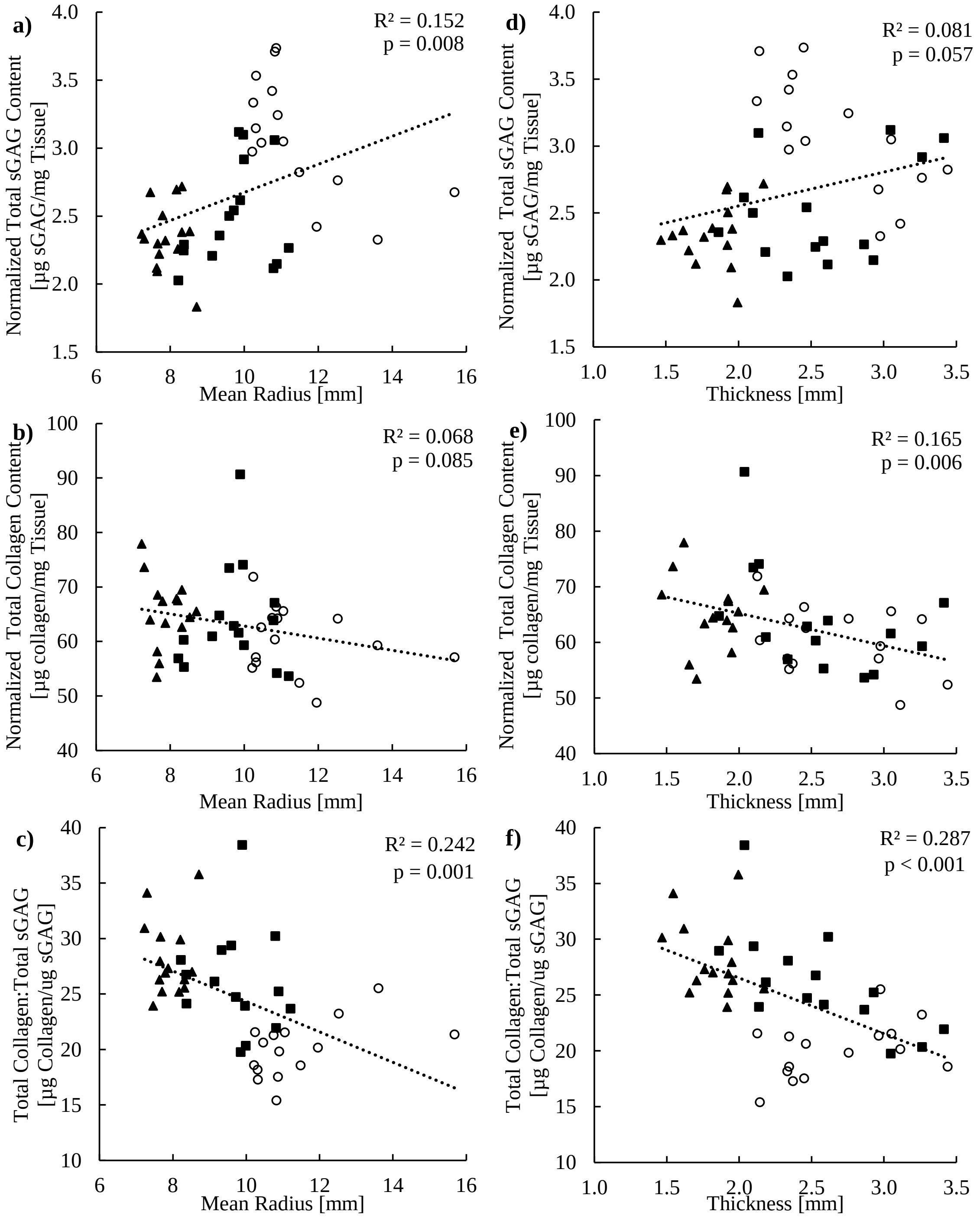

*Figure 5.6: Variation of the (a) total sGAG contents (r=0.390;N=45 from 5 animals), (b) total Collagen contents (r=-0.26;N=45 from 5 animals), (c) collagen:sGAG (r=-0.492;N=45 from 5 animals) calculated from the total amounts of collagen and sGAG, with respect to the aortic ring's mean radius; (d) total sGAG contents (r=0.285;N=45 from 5 animals), (e) total collagen contents (r=-0.406;N=45 from 5 animals), (f) collagen:sGAG (r=0.535;N=45 from 5 animals) calculated from the total amounts of collagen and sGAG, with respect to the aortic ring's thickness. Samples from the ascending, aortic arch and descending thoracic regions are represented by hollow circles, solid squares and solid triangles, respectively.*

### 5.5.5 Influence of Aortic Dimensions

The variation of the total amounts of sGAG, collagen, and their ratio with respect to the aortic ring's mean radius and thickness were investigated (Figure 5.6). The total sGAG content ($r = 0.390$, $p = 0.008$) and the collagen:sGAG ratio ($r = -0.492$, $p = 0.001$) correlated moderately with the mean aortic ring's radius. While the total sGAG content did not display any correlation with the aorta's thickness, the total collagen content displayed a moderate correlation ($r = -0.406$, $p = 0.006$), and the collagen:sGAG ratio showed a good correlation with the aortic thickness ($r = 0.535$, $p < 0.001$).

## 5.6 DISCUSSION

In an effort to better understand and predict aortic biomechanics, the need to quantify the intramural distribution of elastin and collagen, and more recently GAG, in the aortic wall, has been emphasized in a number of recent studies [39–41]. In the present work, we acquired data from porcine aortas isolated from 5- to 6-month old animals. With collagen content highest in the adventitia, and elastin content highest in the media, quantification of collagen and elastin confirmed our qualitative histological observations, and information available from the literature [42,43]. Our quantitative results show that pigs, like rodents [26], display higher sGAG contents towards the intimal and medial layers of the aortic wall. Detailed spatial quantification underscored that sGAG also exist in the adventitia, but in lower quantities, in accordance with qualitative histological observations in Figure 5.4 and [42,39,44]. Along the aortic tree, while sGAG content significantly decreased from the ascending to the descending thoracic regions, collagen tended to increase in content, in agreement with findings from the ovine aorta [41]. While the elastin content in the aorta was expected to decrease away from the heart [41], the higher variability of elastin content between aortas in comparison to collagen and sGAG may be the cause of lack of significance.

The mass fractions of elastin and collagen determined herein will be useful to inform future constrained mixture models of the porcine aorta [14]. The quantified sGAG mass distributions can be used to evaluate experimentally-based intramural distributions of fixed charged densities (FCDs), which in turn may improve the representative and predictive capabilities of the mathematical models that include Donnan osmotic swelling [26,27,29,30]. Based on plausible, but unverified distributions, such models have previously suggested that higher GAG amounts may give rise to larger opening angles [26,27], and that a heterogeneous distribution of GAG may be a factor in the development of residual stresses within the tissue [26]. Conversely, simulations have suggested that a homogeneous transmural GAG distribution would result in the absence of circumferential residual stresses [27]. Our measurements do show a good correlation between the opening angle of the intact wall with the total sGAG content, and a moderate correlation with the gradient of sGAG through the aortic wall, and this effect spanned the three regions considered along the aortic tree. As mentioned in the Introduction, the opening angle of the intact wall relates to the approximate circumferential residual stress field in the load-free configuration.

In studies using elastase and collagenase to selectively remove different components of the arterial ECM, collagen alone has been reported to not contribute to residual stresses [22], or to play a complementary role in them [18,23]. Indeed, when evaluating collagen alone, we found that the total collagen content in the aortic wall did not correlate with the opening angle, while the average collagen content correlated moderately negatively with the opening angle. However, because collagen fibers are assembled by PG cross-linked collagen fibrils [39,45,46], there exists a strong microstructural coupling between collagen and GAG, and this may justify our finding that, among all parameters studied, the opening angle enjoyed the best correlation with the total collagen:sGAG ratio.

In addition, according to [28,29], the swelling stress of the GAG present in the arterial wall puts the network composed of elastin and collagen fibers, under tension. It was also noted that collagen fibers can be assumed to resist against the recoil of the stretched elastin network, as treatment with collagenase resulted in reduced dimensions of arteries [47]. Because GAG are the only microstructural ECM constituents that can sustain the compression needed to balance the tension present in the elastin and collagen network, in view of our findings, we further suggest that the inhomogeneous distribution of GAG across the vessel wall could affect the elastin pre-stretch levels, but even more so the collagen pre-stretch levels present in the load-free configuration, and in turn influence the opening angle of the wall after radial cut. Therefore, our findings are compatible with the current understanding of circumferential residual stresses in arteries, but also provide new insights into how pre-stretches may be partially mediated.

Additional experimental findings herein include the effect of geometry on circumferential residual stresses. Specifically, our data suggest an increase in opening angle with increased diameter, in accordance with previous computer simulations [26]. However, our data show a moderate positive correlation between the aortic thickness and the opening angle, whereas the latter simulations showed a decrease in opening angles for thicker aortas [26]. More work is needed for definitive answers -- while the radius and thickness of the thoracic aorta were reported to increase with age [44], the opening angle remained unchanged in [44], and increased in [48].

While our data suggest that the distributions of GAG and collagen may play a complementary role in the development of circumferential residual stress, other features, such as the role of fiber crosslinks GAG to fibers crosslinks should also be evaluated. It should be noted too, that this study has focused on the evaluation of animal aortic tissues from a single species with a narrow range of ages and no signs of vascular pathologies. Employing the methods presented in this study to evaluate changes in the intramural distribution of ECM components with age and disease will be critical to gaining a more complete understanding of the composition-function relationships in aortic tissues. Furthermore, investigating a broader range of tissue compositions is likely to provide a clearer appreciation of the correlations between the contents of ECM components and the development of residual stresses. It is also important to note that in this study, SMCs were neither passivated nor activated and therefore, a limitation of this work is that the state of contractility of the SMCs was unknown. Finally, layer-dependent information about the opening angle would help in developing a comprehensive model of the porcine aorta to further clarify the contribution of Donnan osmotic pressure on circumferential residual stresses.

For the first time, detailed quantification of sGAG, along with collagen and elastin, was carried out through the porcine aortic wall thickness. Collagen and sGAG displayed inverse profiles such that collagen increases in content from the innermost intima to the outermost adventitia, while the sGAG content decreases. In addition, we were able to show for the first time through experimental studies that the sGAG content and the sGAG intramural gradient may play a role in modulating residual circumferential stresses, by demonstrating good and moderate correlations with the opening angle, respectively. Furthermore, we were able to show, and for the first time, that the collagen:sGAG ratio may be an important parameter when evaluating residual stresses, suggesting that the interaction between sGAG and collagen could be a central feature that deserves to be taken into account when studying the residual stresses in the aorta.

## 5.7 REFERENCES

[1] C. Díaz, J.A. Peña, M.A. Martínez, E. Peña, Unraveling the multilayer mechanical response of aorta using layer-specific residual stresses and experimental properties, Journal of the Mechanical Behavior of Biomedical Materials. 113 (2021) 104070. https://doi.org/10.1016/j.jmbbm.2020.104070.

[2] T. Sigaeva, G. Sommer, G.A. Holzapfel, E.S. Di Martino, Anisotropic residual stresses in arteries, Journal of The Royal Society Interface. 16 (2019) 20190029. https://doi.org/10.1098/rsif.2019.0029.

[3] D.P. Sokolis, Regional distribution of layer-specific circumferential residual deformations and opening angles in the porcine aorta, Journal of Biomechanics. 96 (2019) 109335. https://doi.org/10.1016/j.jbiomech.2019.109335.

[4] A. Rachev, T. Shazly, A structure-based constitutive model of arterial tissue considering individual natural configurations of elastin and collagen, Journal of the Mechanical Behavior of Biomedical Materials. 90 (2019) 61–72. https://doi.org/10.1016/j.jmbbm.2018.09.047.

[5] M. Amabili, P. Balasubramanian, I. Bozzo, I.D. Breslavsky, G. Ferrari, Layer-specific hyperelastic and viscoelastic characterization of human descending thoracic aortas, Journal of the Mechanical Behavior of Biomedical Materials. 99 (2019) 27–46. https://doi.org/10.1016/j.jmbbm.2019.07.008.

[6] S.G. Sassani, S. Tsangaris, D.P. Sokolis, Layer- and region-specific material characterization of ascending thoracic aortic aneurysms by microstructure-based models, Journal of Biomechanics. 48 (2015) 3757–3765. https://doi.org/10.1016/j.jbiomech.2015.08.028.

[7] C. Bellini, J. Ferruzzi, S. Roccabianca, E.S. Di Martino, J.D. Humphrey, A Microstructurally Motivated Model of Arterial Wall Mechanics with Mechanobiological Implications, Ann Biomed Eng. 42 (2014) 488–502. https://doi.org/10.1007/s10439-013-0928-x.

[8] K.Y. Volokh, Compressibility of Arterial Wall in Ring-cutting Experiments, (2006) 8.

[9] Y. Lanir, Mechanisms of Residual Stress in Soft Tissues, Journal of Biomechanical Engineering. 131 (2009) 044506. https://doi.org/10.1115/1.3049863.

[10] G.A. Holzapfel, G. Sommer, M. Auer, P. Regitnig, R.W. Ogden, Layer-Specific 3D Residual Deformations of Human Aortas with Non-Atherosclerotic Intimal Thickening, Ann Biomed Eng. 35 (2007) 530–545. https://doi.org/10.1007/s10439-006-9252-z.

[11] J.A. Peña, M.A. Martínez, E. Peña, Layer-specific residual deformations and uniaxial and biaxial mechanical properties of thoracic porcine aorta, Journal of the Mechanical Behavior of Biomedical Materials. 50 (2015) 55–69. https://doi.org/10.1016/j.jmbbm.2015.05.024.

[12] G. Sommer, P. Regitnig, L. Költringer, G.A. Holzapfel, Biaxial mechanical properties of intact and layer-dissected human carotid arteries at physiological and supraphysiological loadings, American Journal of Physiology-Heart and Circulatory Physiology. 298 (2010) H898–H912. https://doi.org/10.1152/ajpheart.00378.2009.

[13] V. Alastrué, E. Peña, M.Á. Martínez, M. Doblaré, Assessing the Use of the “Opening Angle Method” to Enforce Residual Stresses in Patient-Specific Arteries, Ann Biomed Eng. 35 (2007) 1821–1837. https://doi.org/10.1007/s10439-007-9352-4.

[14] J.D. Humphrey, K.R. Rajagopal, A constrained mixture model for growth and remodeling of soft tissues, Math. Models Methods Appl. Sci. 12 (2002) 407–430. https://doi.org/10.1142/S0218202502001714.

[15] G.A. Holzapfel, R.W. Ogden, Modelling the layer-specific three-dimensional residual stresses in arteries, with an application to the human aorta, Journal of The Royal Society Interface. 7 (2010) 787–799. https://doi.org/10.1098/rsif.2009.0357.

[16] S.J. Mousavi, S. Avril, Patient-specific stress analyses in the ascending thoracic aorta using a finite-element implementation of the constrained mixture theory, Biomech Model Mechanobiol. 16 (2017) 1765–1777. https://doi.org/10.1007/s10237-017-0918-2.

[17] E.C. Davis, Elastic lamina growth in the developing mouse aorta., J Histochem Cytochem. 43 (1995) 1115–1123. https://doi.org/10.1177/43.11.7560894.

[18] L. Cardamone, A. Valentín, J.F. Eberth, J.D. Humphrey, Origin of axial prestretch and residual stress in arteries, Biomech Model Mechanobiol. 8 (2009) 431. https://doi.org/10.1007/s10237-008-0146-x.

[19] J.E. Wagenseil, R.P. Mecham, Vascular Extracellular Matrix and Arterial Mechanics, Physiological Reviews. 89 (2009) 957–989. https://doi.org/10.1152/physrev.00041.2008.

[20] L. Maes, H. Fehervary, J. Vastmans, S.J. Mousavi, S. Avril, N. Famaey, Constrained mixture modeling affects material parameter identification from planar biaxial tests, J Mech Behav Biomed Mater. 95 (2019) 124–135. https://doi.org/10.1016/j.jmbbm.2019.03.029.

[21] E. Fonck, G. Prod’hom, S. Roy, L. Augsburger, D.A. Rüfenacht, N. Stergiopulos, Effect of elastin degradation on carotid wall mechanics as assessed by a constituent-based biomechanical model, American Journal of Physiology-Heart and Circulatory Physiology. 292 (2007) H2754–H2763. https://doi.org/10.1152/ajpheart.01108.2006.

[22] S.E. Greenwald, J.E. Moore Jr., A. Rachev, T.P.C. Kane, J.-J. Meister, Experimental Investigation of the Distribution of Residual Strains in the Artery Wall, Journal of Biomechanical Engineering. 119 (1997) 438–444. https://doi.org/10.1115/1.2798291.

[23] P.J. Zeller, T.C. Skalak, Contribution of Individual Structural Components in Determining the Zero-Stress State in Small Arteries, J Vasc Res. 35 (1998) 8–17. https://doi.org/10.1159/000025560.

[24] T. Matsumoto, M. Tsuchida, M. Sato, Change in intramural strain distribution in rat aorta due to smooth muscle contraction and relaxation, American Journal of Physiology-Heart and Circulatory Physiology. 271 (1996) H1711–H1716. https://doi.org/10.1152/ajpheart.1996.271.4.H1711.

[25] X. Guo, Y. Lanir, G.S. Kassab, Effect of osmolarity on the zero-stress state and mechanical properties of aorta, American Journal of Physiology-Heart and Circulatory Physiology. 293 (2007) H2328–H2334. https://doi.org/10.1152/ajpheart.00402.2007.

[26] E.U. Azeloglu, M.B. Albro, V.A. Thimmappa, G.A. Ateshian, K.D. Costa, Heterogeneous transmural proteoglycan distribution provides a mechanism for regulating residual stresses in the aorta, American Journal of Physiology-Heart and Circulatory Physiology. 294 (2008) H1197–H1205. https://doi.org/10.1152/ajpheart.01027.2007.

[27] N. Ghadie, J.-P. St-Pierre, M.R. Labrosse, Intramural Glycosaminoglycans Distribution vs. Residual Stress in Porcine Ascending Aorta: a Computational Study*, in: 2020 42nd Annual International Conference of the IEEE Engineering in Medicine Biology Society (EMBC), 2020: pp. 2816–2819. https://doi.org/10.1109/EMBC44109.2020.9176381.

[28] J.-W.M. Beenakker, B.A. Ashcroft, J.H.N. Lindeman, T.H. Oosterkamp, Mechanical Properties of the Extracellular Matrix of the Aorta Studied by Enzymatic Treatments, Biophysical Journal. 102 (2012) 1731–1737. https://doi.org/10.1016/j.bpj.2012.03.041.

[29] W.M. Lai, J.S. Hou, V.C. Mow, A Triphasic Theory for the Swelling and Deformation Behaviors of Articular Cartilage, Journal of Biomechanical Engineering. 113 (1991) 245–258. https://doi.org/10.1115/1.2894880.

[30] Y. Lanir, Osmotic swelling and residual stress in cardiovascular tissues, Journal of Biomechanics. 45 (2012) 780–789. https://doi.org/10.1016/j.jbiomech.2011.11.018.

[31] H. Hillman, Limitations of clinical and biological histology, Medical Hypotheses. 54 (2000) 553–564. https://doi.org/10.1054/mehy.1999.0894.

[32] K.L. Camplejohn, S.A. Allard, Limitations of safranin ‘O’ staining in proteoglycan-depleted cartilage demonstrated with monoclonal antibodies, Histochemistry. 89 (1988) 185–188. https://doi.org/10.1007/BF00489922.

[33] H.J. Safi, C.C. Miller, C. Carr, D.C. Iliopoulos, D.A. Dorsay, J.C. Baldwin, Importance of intercostal artery reattachment during thoracoabdominal aortic aneurysm repair, Journal of Vascular Surgery. 27 (1998) 58–68. https://doi.org/10.1016/S0741-5214(98)70292-7.

[34] M.R. Labrosse, E.R. Gerson, J.P. Veinot, C.J. Beller, Mechanical characterization of human aortas from pressurization testing and a paradigm shift for circumferential residual stress, Journal of the Mechanical Behavior of Biomedical Materials. 17 (2013) 44–55. https://doi.org/10.1016/j.jmbbm.2012.08.004.

[35] J.D. Humphrey, Cardiovascular Solid Mechanics: Cells, Tissues, and Organs, Springer Science & Business Media, 2002.

[36] C. Zheng, M.E. Levenston, Fact versus artifact: Avoiding erroneous estimates of sulfated glycosaminoglycan content using the dimethylmethylene blue colorimetric assay for tissue-engineered constructs, Eur Cell Mater. 29 (2015) 224–236.

[37] G. Kesava Reddy, C.S. Enwemeka, A simplified method for the analysis of hydroxyproline in biological tissues, Clinical Biochemistry. 29 (1996) 225–229. https://doi.org/10.1016/0009-9120(96)00003-6.

[38] A. Hazra, N. Gogtay, Biostatistics series module 6: Correlation and linear regression, Indian Journal of Dermatology. 61 (2016) 593. https://doi.org/10.4103/0019-5154.193662.

[39] J.M. Mattson, R. Turcotte, Y. Zhang, Glycosaminoglycans contribute to extracellular matrix fiber recruitment and arterial wall mechanics, Biomech Model Mechanobiol. 16 (2017) 213–225. https://doi.org/10.1007/s10237-016-0811-4.

[40] N. Ghadie, J.-P. St-Pierre, M. Labrosse, The Contribution of Glycosaminoglycans/Proteoglycans to Aortic Mechanics in Health and Disease: A Critical Review, IEEE Transactions on Biomedical Engineering. (2021) 1–1. https://doi.org/10.1109/TBME.2021.3074053.

[41] P. Panpho, B. Geraghty, Y.H. Chim, H.A. Davies, M.L. Field, J. Madine, R. Akhtar, Macro- and Micro-mechanical Properties of the Ovine Aorta: Correlation with Regional Variations in Collagen, Elastin and Glycosaminoglycan Levels:, ARTRES. 25 (2019) 27. https://doi.org/10.2991/artres.k.191114.003.

[42] J.-W.M. Beenakker, B.A. Ashcroft, J.H.N. Lindeman, T.H. Oosterkamp, Mechanical Properties of the Extracellular Matrix of the Aorta Studied by Enzymatic Treatments, Biophysical Journal. 102 (2012) 1731–1737. https://doi.org/10.1016/j.bpj.2012.03.041.

[43] G.A. Holzapfel, T.C. Gasser, R.W. Ogden, A new Constitutive Framework for Arterial Wall Mechanics and a Comparative Study of Material Models, in: S.C. Cowin, J.D. Humphrey (Eds.), Cardiovascular Soft Tissue Mechanics, Kluwer Academic Publishers, Dordrecht, 2004: pp. 1–48. https://doi.org/10.1007/0-306-48389-0_1.

[44] M. Jadidi, S.A. Razian, M. Habibnezhad, E. Anttila, A. Kamenskiy, Mechanical, structural, and physiologic differences in human elastic and muscular arteries of different ages: Comparison of the descending thoracic aorta to the superficial femoral artery, Acta Biomaterialia. 119 (2021) 268–283. https://doi.org/10.1016/j.actbio.2020.10.035.

[45] G. Martufi, T.C. Gasser, A constitutive model for vascular tissue that integrates fibril, fiber and continuum levels with application to the isotropic and passive properties of the infrarenal aorta, Journal of Biomechanics. 44 (2011) 2544–2550. https://doi.org/10.1016/j.jbiomech.2011.07.015.

[46] J.E. Scott, Elasticity in extracellular matrix ‘shape modules’ of tendon, cartilage, etc. A sliding proteoglycan-filament model, The Journal of Physiology. 553 (2003) 335–343. https://doi.org/10.1113/jphysiol.2003.050179.

[47] S. Zeinali-Davarani, M.-J. Chow, R. Turcotte, Y. Zhang, Characterization of Biaxial Mechanical Behavior of Porcine Aorta under Gradual Elastin Degradation, Ann Biomed Eng. 41 (2013) 1528–1538. https://doi.org/10.1007/s10439-012-0733-y.

[48] A. Saini, C. Berry, S. Greenwald, Effect of Age and Sex on Residual Stress in the Aorta, JVR. 32 (1995) 398–405. https://doi.org/10.1159/000159115.

## 5.8 SUPPLEMENTARY INFORMATION

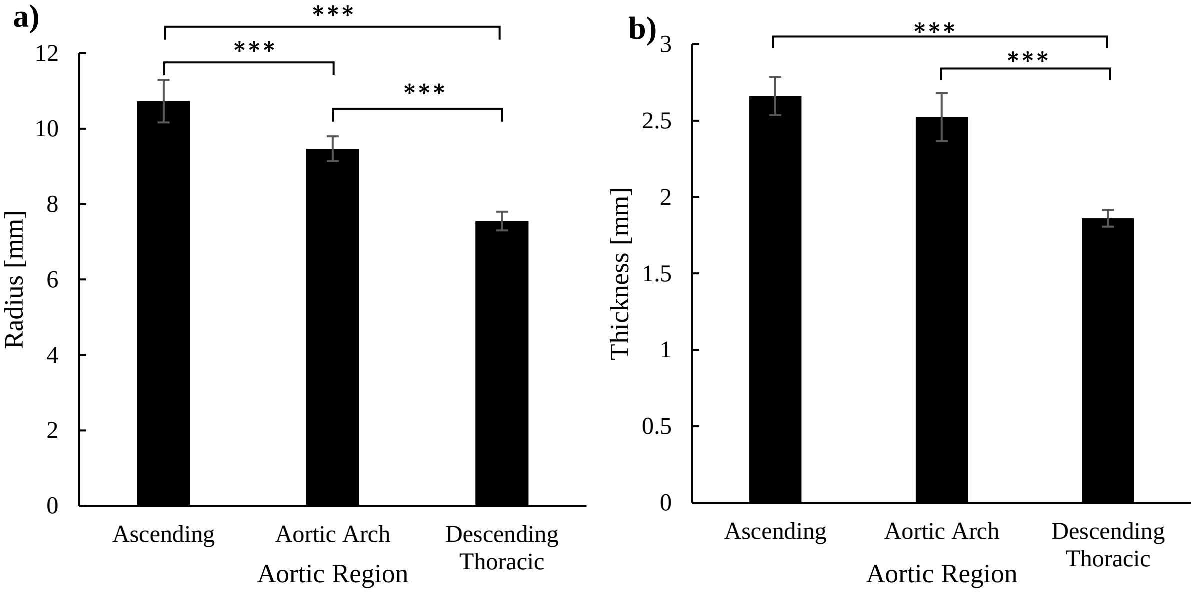

*Figure S5.1: (a) Radius and (b) thickness of aortic rings obtained from different anatomical regions presented as mean ± SEM (n=17 rings per region obtained from 7 animals, 3 anatomical regions per animal). ** p < 0.01 and *** p < 0.001 (Welch with Games-Howell Post-Hoc test). The radius and thickness are measured in the load-free configuration.*

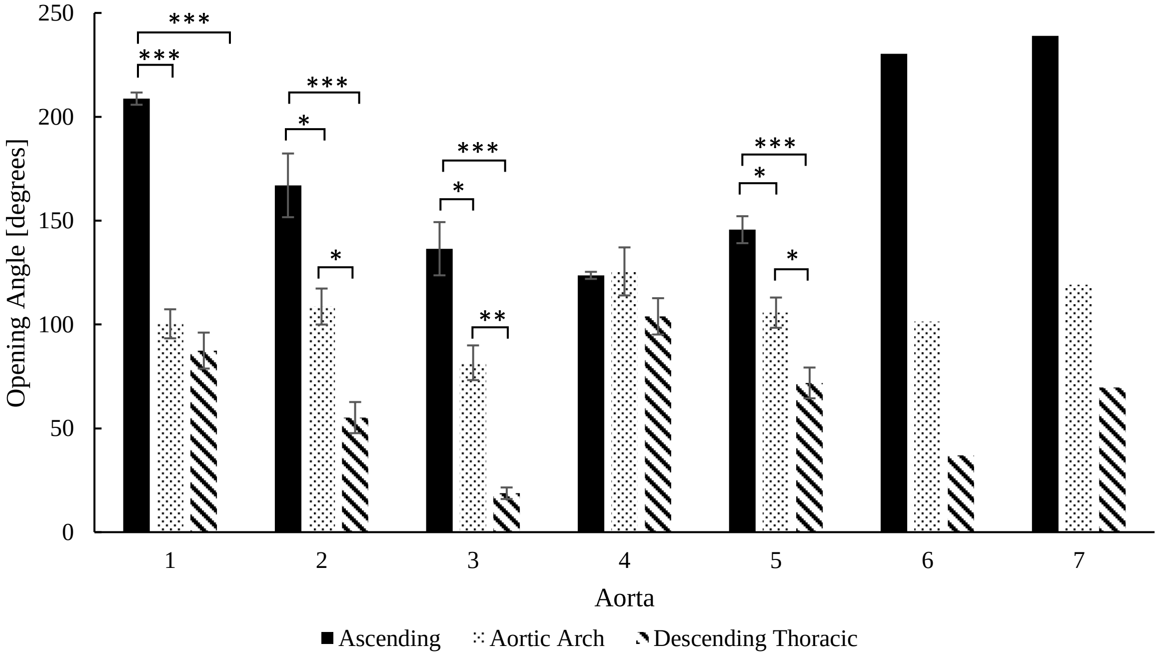

*Figure S5.2: Opening angle of aortic rings obtained from different anatomical regions in 7 aortas presented as mean ± SEM (n=3 rings per region for aortas 1-5, n=1 ring per region for aortas 6 and 7, 3 anatomical regions per animal). * indicates p < 0.05, ** p < 0.01 and *** p < 0.001. (ANOVA with Tukey's HSD Post-Hoc test)*

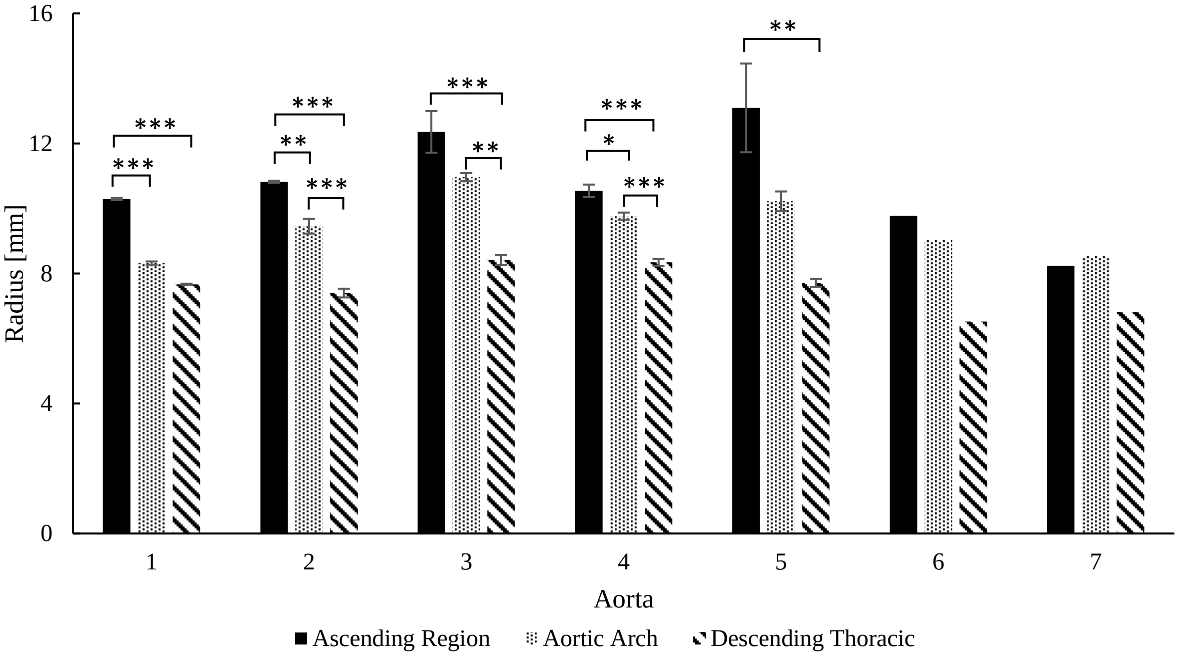

*Figure S5.3: Radius of aortic rings, measured in the load-free configuration, and obtained from different anatomical regions in 7 aortas presented as mean ± SEM (n=3 rings per region for aortas 1-5, n=1 ring per region for aortas 6 and 7, 3 anatomical regions per animal). * indicates p < 0.05, ** p < 0.01 and *** p < 0.001. (ANOVA with Tukey's HSD Post-Hoc test).*

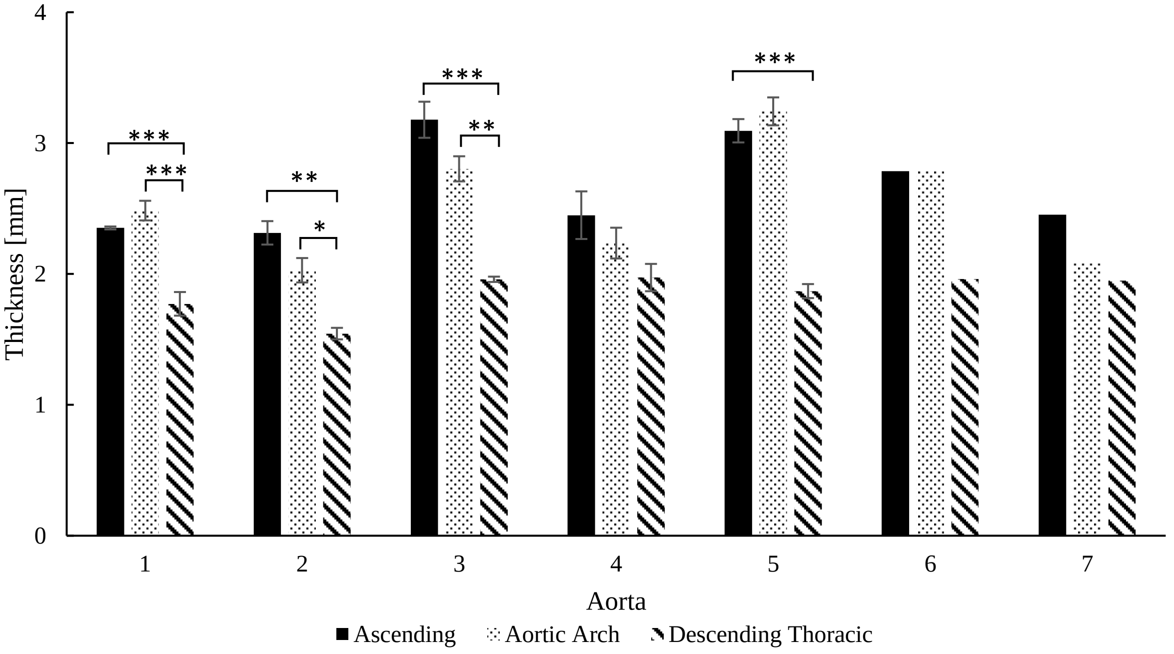

*Figure S5.4: Thickness of aortic rings, measured in the load-free configuration, and obtained from different anatomical regions in 7 aortas presented as mean ± SEM (n=3 rings per region for aortas 1-5, n=1 ring per region for aortas 6 and 7, 3 anatomical regions per animal). * indicates p < 0.05, ** p < 0.01 and *** p < 0.001. (ANOVA with Tukey's HSD Post-Hoc test).*

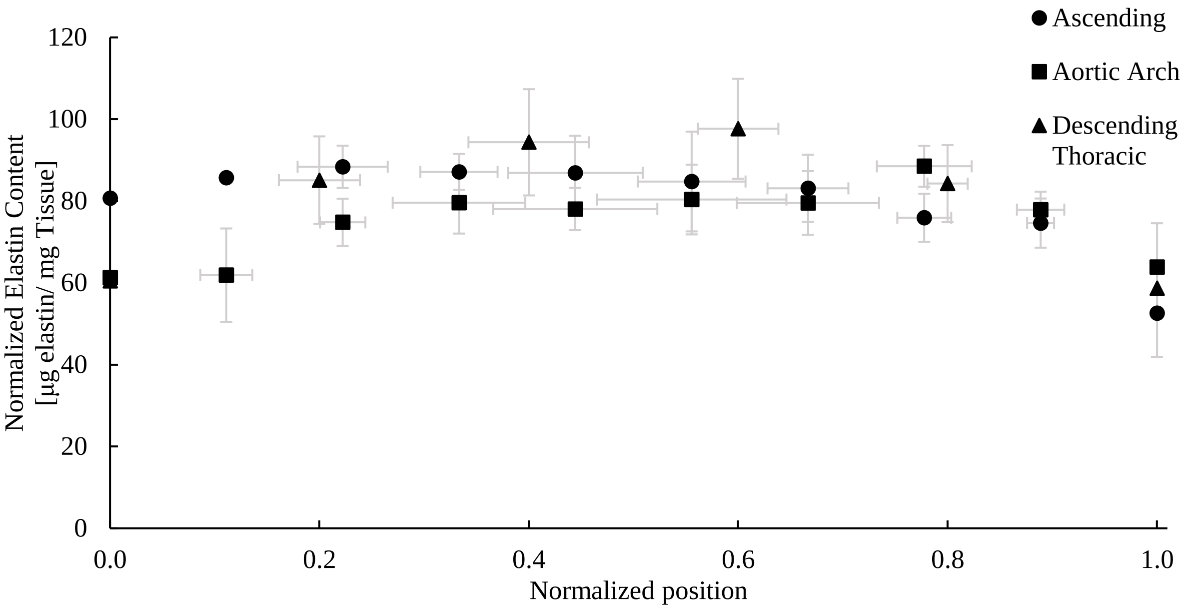

*Figure S5.5: Intramural Distribution of Elastin (n=5 from 5 animals) in the Ascending, Aortic Arch and Descending Thoracic Regions of Porcine Aortas 3-7 presented as mean ± SEM. Position 0.0 along the x-axis refers to the intima while position 1.0 refers to the adventitia. Error bars along x-axis represent the SEM for section position to account for the fact that samples produced different numbers of sections because of variations in thicknesses.*

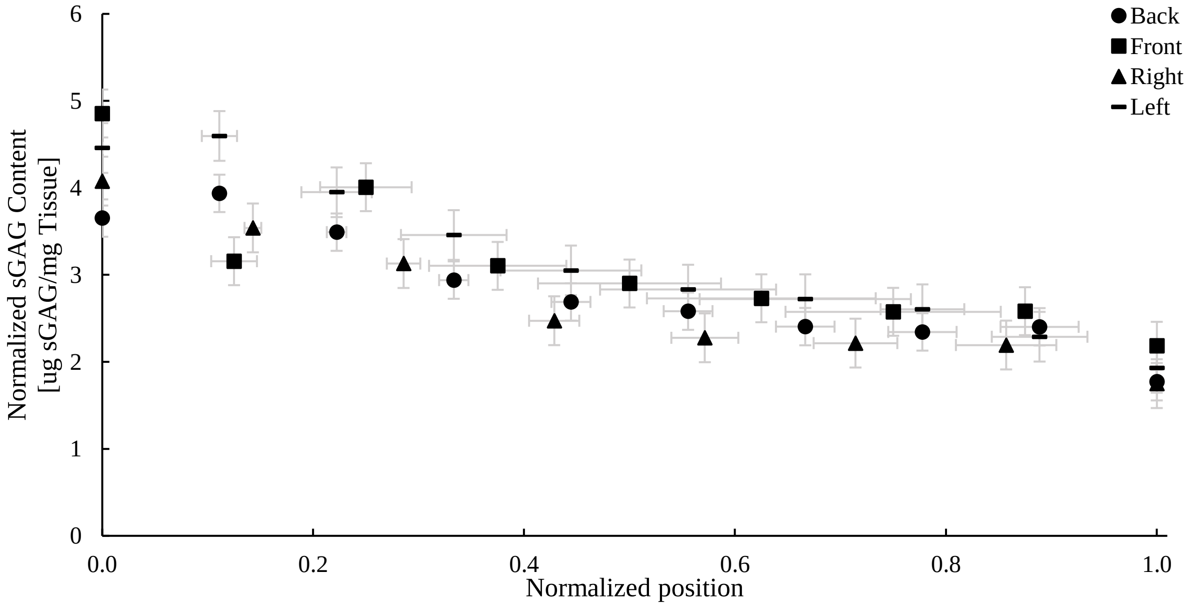

*Figure S5.6: sGAG intramural distribution in the back, front, right and left quadrants from 3 rings the ascending region of aorta 1 presented as mean ± SEM (n=3 rings from 1 animal). Position 0.0 along the x-axis refers to the intima while position 1.0 refers to the adventitia. Error bars along x-axis represent the SEM for section position to account for the fact that samples produced different numbers of sections because of variations in thicknesses.*

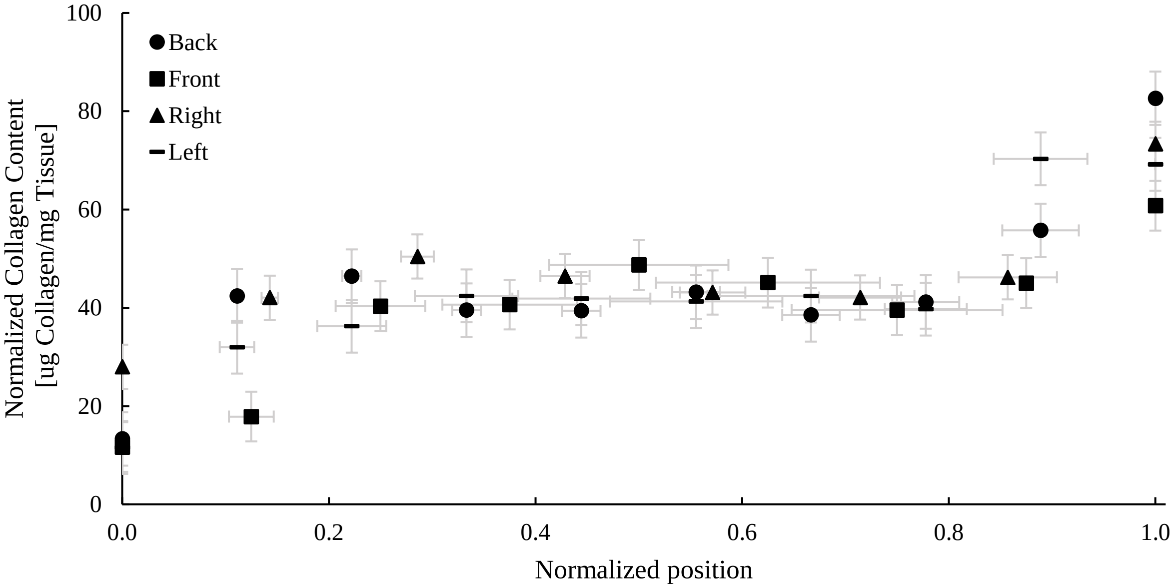

*Figure S5.7: Collagen intramural distribution in the back, front, right and left quadrants from 3 rings the ascending region of aorta 1 presented as mean ± SEM (n=3 rings from 1 animal). Position 0.0 along the x-axis refers to the innermost intima while position 1.0 refers to the outermost adventitia. Error bars along x-axis represent the SEM for section position to account for the fact that samples produced different numbers of sections because of variations in thicknesses.*

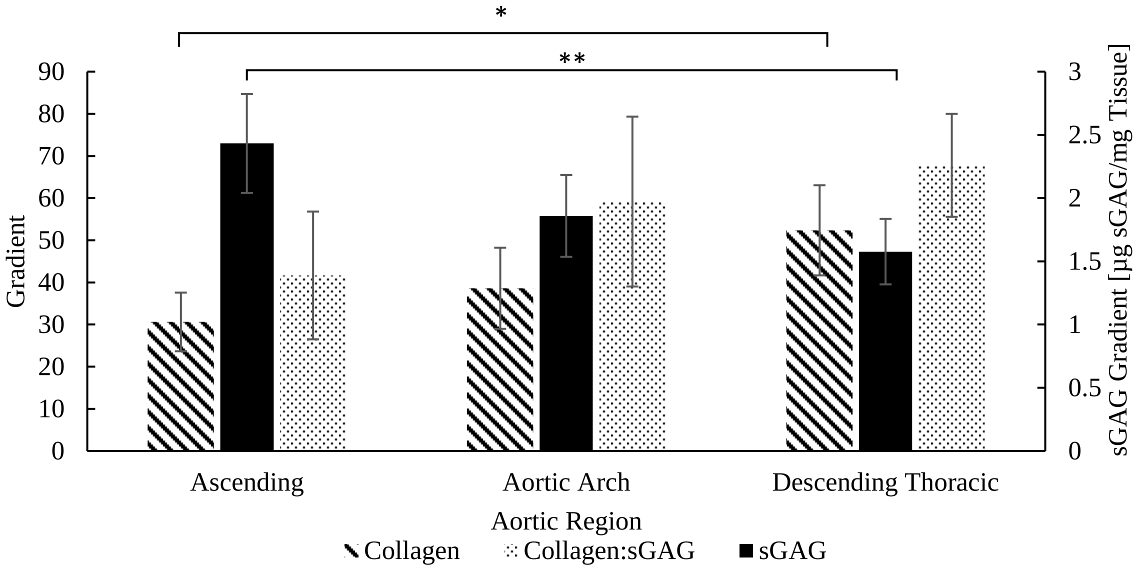

*Figure S5.8: Gradients of sGAG (N=15 from 5 animals), collagen (N=15 from 5 animals), and collagen:sGAG (N=15 from 5 animals) normalized by wet weight in the ascending, aortic arch and descending thoracic regions of porcine aortas (mean ± SEM). * indicates $p < 0.05$, ** $p < 0.01$ (ANOVA with Tukey HSD Post-Hoc test). Units for the collagen and collagen:sGAG gradients are respectively µg collagen/mg Tissue and µg Collagen/ug sGAG.*

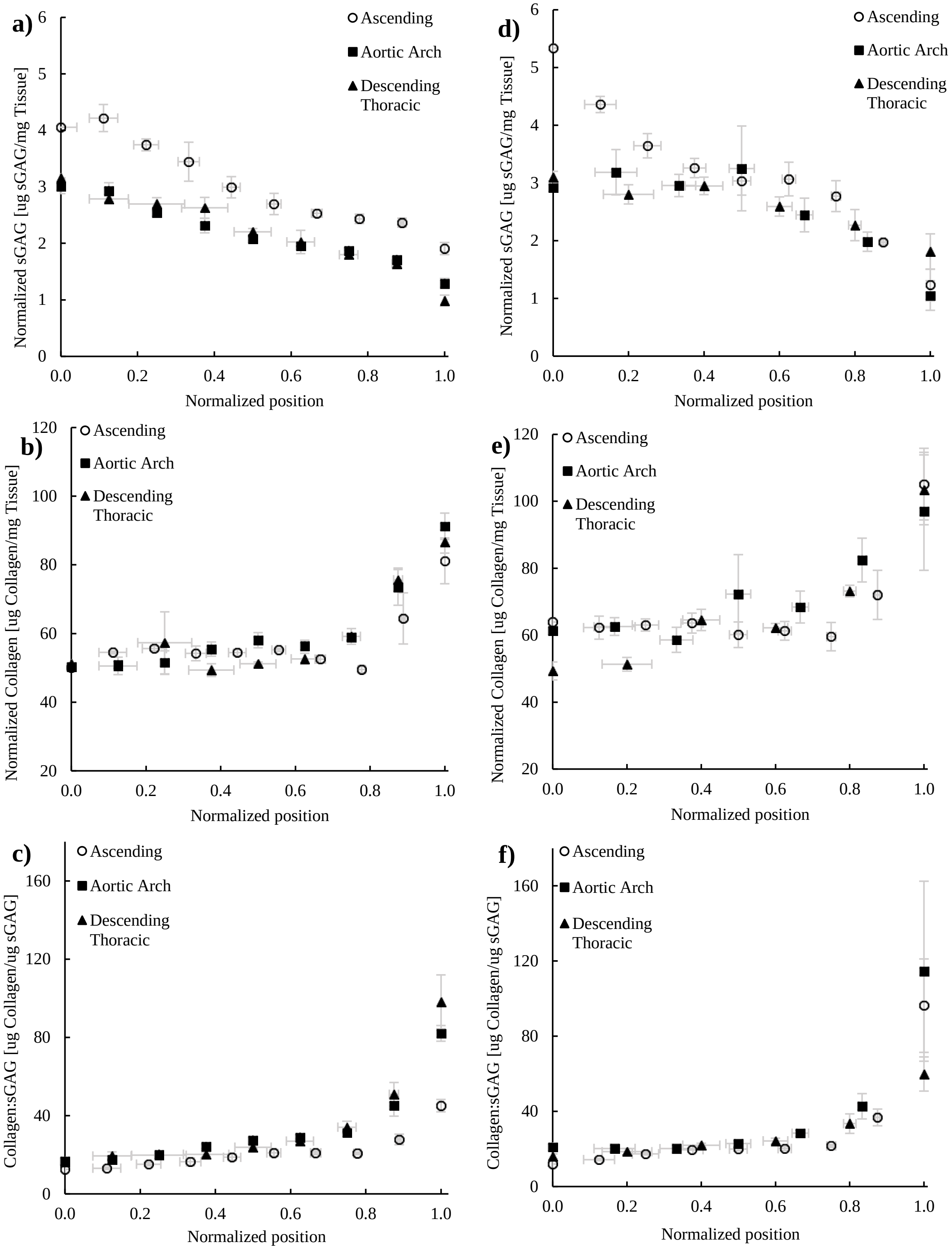

*Figure S5.9: Intramural Distribution of (a) sGAG (N=3), (b) collagen (N=3), and (c) collagen:GAG (N=3) in the Ascending, Aortic Arch and Descending Thoracic Regions of Porcine Aorta 2; (d) sulfated GAG (N=3), (e) collagen (N=3), and (f) collagen:GAG (N=3) in the Ascending, Aortic Arch and Descending Thoracic Regions of Porcine Aorta 4. Position 0.0 along the x-axis refers to the innermost intima while position 1.0 refers to the outermost adventitia. Error bars along x-axis represent the SEM for section position to account for the fact that samples produced different numbers of sections because of variations in thicknesses.*

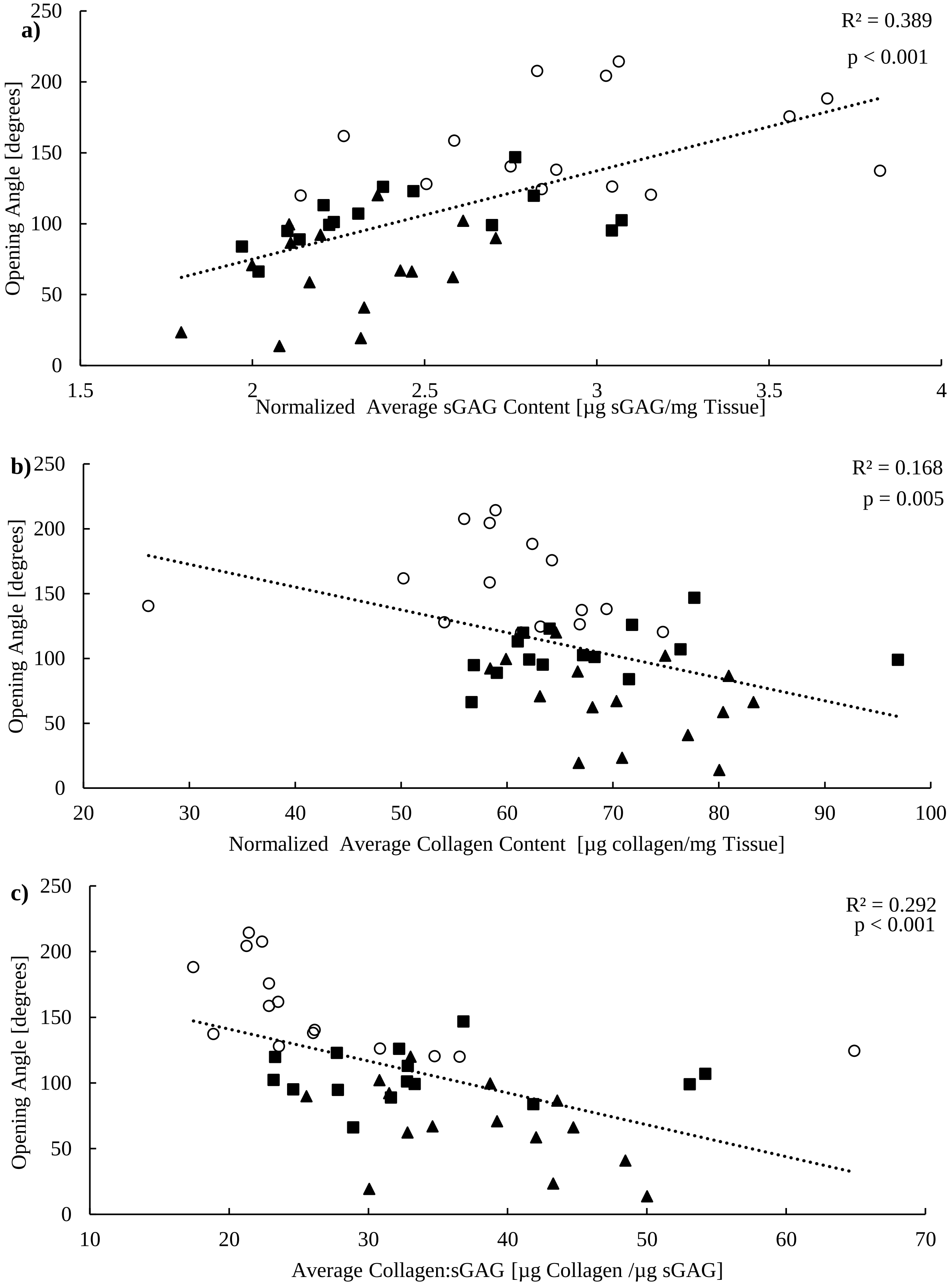

*Figure S5.10: Variation of the average (a) sGAG content (r=0.623;N=45), (b) Collagen content (r=-0.410;N=45), and (c) Collagen:GAG (r=-0.540;N=45) in the aortic wall with respect to the opening angle. The ascending region is presented with a hallow circle, the aortic arch region with a full square and the descending thoracic region with a full triangle.*

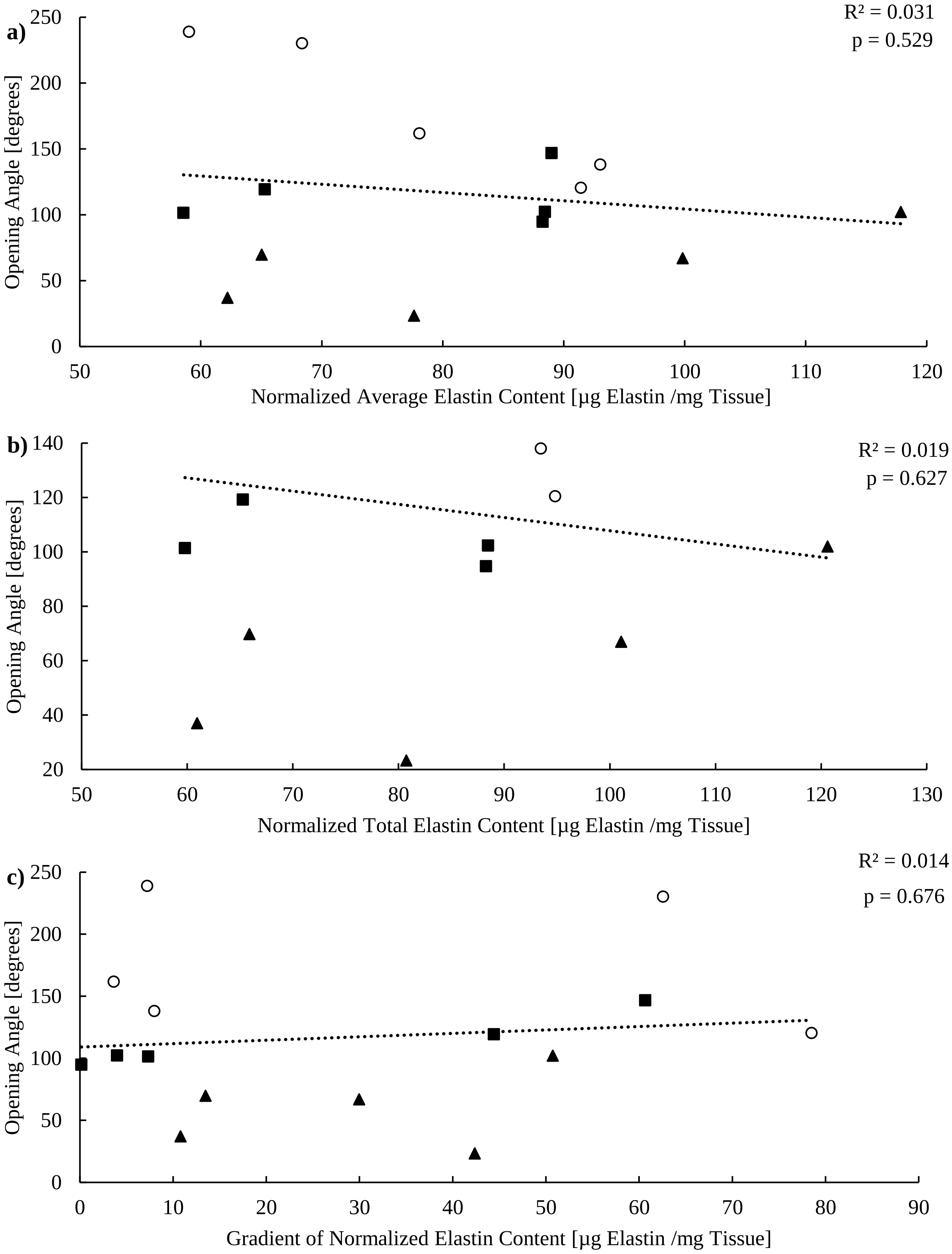

*Figure S5.11: Variation of the (a) Average Elastin (r=-0.180;N=15), (b) Total Elastin Amounts (r=-0.137;N=15) and, (c) the Elastin Gradient (r=0.118;N=15) in the aortic wall with respect to the opening angle. Correlations are not significant (p>0.05). The ascending region is presented with a hallow circle, the aortic arch region with a full square and the descending thoracic region with a full triangle.*

### 5.8.1 Opening Angle Measurement

Opening angles were measured using a previously published custom-written MATLAB code [34]. Consider the unloaded and unstressed configurations of an aortic ring as shown in the figure below.

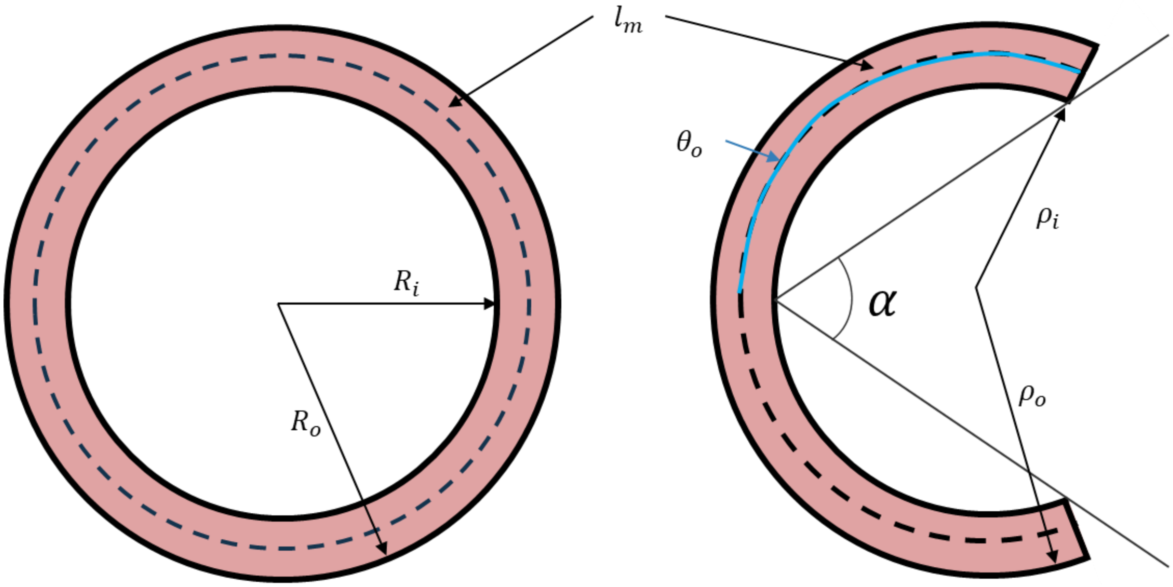

*Figure S5.12: Annotated aortic ring in the unloaded (left) and unstressed (right) configurations.*

The midline arc length $l_m$ is assumed to be equivalent in both unloaded and unstressed configurations, and can be respectively written as:

$$l_m = 2\pi \left[\frac{1}{2}(R_o + R_i)\right]$$

$$l_m = 2\theta_o \left[\frac{1}{2}(\rho_o + \rho_i)\right]$$

This leads to expressing $\theta_o$ as follows:

$$\theta_o = \frac{\pi(R_o + R_i)}{\rho_o + \rho_i}$$

Given the unstressed configuration, angle $\alpha$ and $\theta_o$ relate as follows:

$$\alpha + \theta_o = \pi$$

Assuming no change in the sample thickness after opening aortic ring ($R_o - R_i = \rho_o - \rho_i$), the opening angle $\alpha$ can be finally calculated as follows:

$$\alpha = \pi - \theta_o$$

$$\alpha = \pi - \frac{\pi(R_o + R_i)}{\rho_o + \rho_i} \times \frac{R_o - R_i}{\rho_o - \rho_i}$$

$$\alpha = \pi - \pi\frac{(R_o^2 - R_i^2)}{\rho_o^2 - \rho_i^2}.$$

# 6

# GLYCOSAMINOGLYCANS MODULATE COMPRESSIVE STIFFNESS AND CIRCUMFERENTIAL RESIDUAL STRESS IN THE PORCINE THORACIC AORTA

Noor Ghadie[a], Michel R. Labrosse[a,b], Jean-Philippe St-Pierre[c*]

[a]Mechanical Engineering Department, University of Ottawa, Ottawa, ON. Canada K1N6N5

[b]Department of Cardiac Surgery, University of Ottawa Heart Institute, Ottawa, ON. Canada K1Y4W7

[c]Chemical and Biological Engineering Department, University of Ottawa, Ottawa, ON. Canada K1N6N5

Content of this chapter accepted by Acta Biomaterialia | August 2023

## 6.1 FOREWORD

Chapters 4 and 5 provided evidence of the contribution of glycosaminoglycans (GAG) to residual stress through their content, gradient and intramural distribution. However, the extent of contribution of GAG to the opening angle remains poorly understood, which we aimed to uncover in this chapter through enzymatic GAG depletion. In this chapter, we also intended to gain an all-encompassing understanding of the mechanical roles of GAG in the aorta by understanding their effect on the compressive properties of the aorta. We further aimed to investigate the mechanisms through which GAG modulate the mechanical properties of the aorta by evaluating the water content in the tissue and their contribution to circumferential prestretch. Additionally, advanced glycation end products also deposit within the extracellular matrix, but their effect on residual stress was not evaluated in Chapter 5, and we aimed to address this gap in the present study.

## 6.2 ABSTRACT

The mechanical properties of the aorta are influenced by the extracellular matrix, a network mainly comprised of fibers and glycosaminoglycans (GAG). In this work, we demonstrate that GAG contribute to the opening angle (a marker of circumferential residual stresses) in intact and glycated aortic tissue. Enzymatic GAG depletion was associated with a decrease in the opening angle, by approximately 25% (p=0.009) in the ascending (AS) region, 32% (p=0.003) in the aortic arch (AR), and 42% (p=0.001) in the lower descending thoracic (LDT) region. A similar effect of GAG depletion on aortic ring opening angle was also observed in previously glycated tissues. Using indentation testing, we found that the radial compressive stiffness significantly increased in the AS region following GAG depletion, compared to fresh (p=0.006) and control samples (p=0.021), and that the compressive properties are heterogeneous along the aortic tree.

A small loss of water content was also detected after GAG depletion, which was most prominent under hypotonic conditions. Finally, the AS region was also associated with a significant loss of compressive deformation (circumferential stretch that is $< 1$) in the inner layer of the aorta following GAG depletion, suggesting that GAG interact with ECM fibers in their effect on aortic mechanics. The importance of this work lies in its identification of the role of GAG in modulating the mechanical properties of the aorta, namely the circumferential residual stresses and the radial compressive stiffness, as well as contributing to the swelling state and the level of circumferential prestretch in the tissue.

**Keywords:** Aorta, Glycosaminoglycans, Residual Stress, Stiffness, Prestretch

## 6.3 INTRODUCTION

The extracellular matrix (ECM) of the aorta is a complex three-dimensional network of biomolecules mainly comprised of elastin, collagen and ground substance such as glycosaminoglycans (GAG). Changes in its composition and organization impact the mechanical properties of the aorta [1–4]. In turn, alterations in the biomechanical properties of the aorta are implicated in several medical conditions, such as hypertension [5], atherosclerosis [6], aneurysm and dissection [7], leading in many cases to tissue failures and deadly ruptures. When evaluating the mechanical function of the aorta, one must account for the residual stresses present in the tissue. Residual stresses are those existing in the unloaded configuration of the aorta. Their circumferential component can be assessed *ex vivo* by measuring the opening angle following a radial cut through an unloaded aortic ring, which leads to an open, approximately stress-free, portion of a circular arc [8]. Circumferential residual stresses have been attributed to various levels of circumferential prestretch, whereby the inner layers of the aortic wall are under residual compression, while the outer layers are under residual tension [8,9]. Understanding the origin of residual stresses is paramount because they significantly affect the magnitude of *in vivo* mechanical stresses, which, when in excess of the aortic strength, result in aortic ruptures. Residual stresses are also believed to contribute to maintaining the mechanical stresses relatively homogenous throughout the thickness of the aorta [8,10]. In addition, residual stresses may affect aortic stiffness [10,11], an important clinical marker in vascular disease. The stiffness of the aorta dictates its ability to expand and recoil, providing the vessel with a cushioning effect that is essential to accommodate the deformations caused by the pulsatile pumping of blood [12].

The roles of elastic and collagen fibers in impacting the mechanical properties and functions of the aorta have been studied extensively [13–15]; while the contribution of GAG in aortic biomechanics has recently garnered increased interest [3,16–18]. GAG are negatively charged polysaccharides that contribute to the swelling state of the tissue, and have been found to undergo alterations in vascular disease such as thoracic and abdominal aortic aneurysm [19]. While they represent a minor portion of dry weight of aortic ECM, they are thought to contribute to residual stresses through their quantities, local distributions and intramural gradients [16,17]; however, the extent of the contribution of GAG to residual stresses remains poorly characterized. Moreover, although GAG may also contribute to the local stiffness of the aorta, results reported to date remain conflicting on that matter [13,20,21].

In addition to ECM compositional changes, aging and pathologies are also associated with the deposition of advanced glycation end products (AGEs) [2,22–24]. The accumulation of AGEs, which are the product of a reaction between sugar molecules and lipids or proteins, leads to the creation of crosslinks in aortic tissue [25]. The effect of glycation crosslinks on aortic stiffness has been thoroughly studied, and crosslink accumulation has been shown to cause a loss of compliance [26,27]; however, to our knowledge, in the aorta, although increased stiffness is expected to reduce the opening angle [16], the direct contribution of glycation crosslinks to circumferential residual stresses has not yet been investigated.

In this study, we evaluate the effects of GAG in explanted porcine aortic tissue directly and after initiating the formation of glycation crosslinks. To do so, we measure the effect of GAG removal by enzymatic digestion on circumferential residual stresses in the aorta, using the opening angle method. We also study the effect of GAG removal on the radial compressive stiffness of the aorta using indentation. Finally, we investigate potential underlying mechanisms by which GAG impact the mechanical properties of the aorta, notably by evaluating the response of aortic rings to variations in external bath osmolarity, as well as the swelling state of the tissues, and the distribution of circumferential prestretch, before and after GAG depletion.

## 6.4 METHODS

### 6.4.1 Tissue Harvesting

Porcine thoracic aortas (5-6 months animals; 90-100 kg) were acquired from a local slaughterhouse and cleaned from adjacent fatty and connective tissue. A series of experiments was carried out using samples (strips or rings) isolated from the ascending (AS) region, the aortic arch (AR) region, the upper descending thoracic (UDT) (above the 1st intercostal artery), and the lower descending thoracic (LDT) (between the 3rd and 5th intercostal arteries) regions of thoracic aortas.

### 6.4.2 Enzymatic GAG Depletion and Glycation Treatments

The GAG in aortic strips and rings were enzymatically removed by treating samples with 0.075U/mL chondroitinase ABC, 15U/mL hyaluronidase, 0.75U/mL heparinase (Sigma-Aldrich; C3667, H3506 and H3917, respectively) in 100 mM ammonium acetate buffer (pH 7.0) (Sigma-Aldrich) for 48 hours at 37°C. Control samples were incubated in the buffer only, and fresh samples were maintained in PBS at 4°C and evaluated within 48 hours after death. Before further testing, samples were washed 3 times in phosphate buffered saline (PBS), for 5 min each.

Aortic tissue glycation was achieved by treatment with 700 mM ribose (Sigma-Aldrich) in 100 mM ammonium acetate buffer (pH 7.0) for 48 hours at 37ºC, in order to simulate AGE crosslinks *in vitro*. Control samples were incubated in the buffer alone. Samples were washed 3 times in PBS, for 5 min each, after which they underwent a subsequent incubation for GAG treatment, according to the enzymatic GAG digestion protocol detailed above.

### 6.4.3 Opening Angle

Measuring the opening angle $\alpha$, shown in Figure 6.1, is a simple indirect approach to evaluate circumferential residual stresses in blood vessels. To study the effect of GAG depletion on the opening angle, five porcine aortas ($N_1 = 5$ animals) were harvested, from which sets of two adjacent rings were excised from each of the AS, AR and LDT regions. One ring served as a control, and the second ring underwent enzymatic GAG depletion, as described in Section 2.2. A subsequent experiment was carried out to study the contribution of GAG to the opening angle in glycated tissue. Here, sets of four adjacent aortic rings were excised from the UDT region in 9 porcine aortas ($N_2 = 9$ animals). In this test, the UDT region was harvested instead of the AS, AR, and/or LDT given the additional space it provides, making it possible to extract four adjacent rings, which were required for the glycation experiment. Of note, ten aortas were initially tested, but one was detected as an outlier based on Tukey's method for finding outliers in SPSS Statistics, and removed from the data set. One ring served as a control, while a second ring underwent enzymatic GAG depletion alone, the third underwent glycation alone, and the fourth ring underwent a combination of glycation, followed by enzymatic GAG depletion. The positions of the ring treatments were randomized to prevent bias with respect to the anatomical locations. Fresh aortic rings were also evaluated to verify that the incubation in buffers alone did not yield any significant differences in the opening angle results, as shown in Supplemental Figure S6.1. Following incubation, and after 3 PBS washes, rings were left to float in Petri dishes containing 300 mosM of PBS, under which a calibration grid was positioned. Rings were then radially cut and left to equilibrate for 20 min [28]. The unloaded (closed) and approximately unstressed (cut) configurations of the rings were imaged from which the corresponding inner and outer radii, thicknesses and opening angles were measured using a previously published MATLAB image processing code as detailed in [28]. Briefly, digital images for load-free and stress-free configurations were acquired, from which inner and outer arc lengths were measured. The opening angle was then calculated via the assumption that the mid-line length in the load-free and stress-free configurations is identical. Of note, and as can be deduced from Figure 6.1, the opening angle $\alpha$ would equal 180 deg when the ring opens up into a straight line.

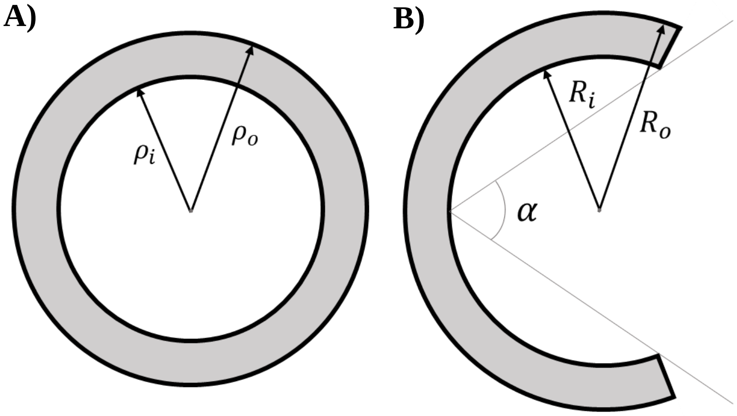

*Figure 6.1: Parameters to describe the opening angle $\alpha$, and the inner and outer radii, in the (A) unloaded, and (B) unstressed configurations.*

In addition, using a separate set of porcine thoracic aortas ($N_3$ = 3 animals), the opening angle response to different external bath osmolarities of intact and GAG-depleted rings was evaluated. The opening angles were measured in solutions of different concentrations: hypotonic (0 mosM NaCl), isotonic (300 mosM NaCl), and hypertonic (3000 mosM NaCl). Rings were first radially cut in isotonic baths and were left to equilibrate for 30 min. The ring was then transferred to a bath of hypotonic (or hypertonic) osmolarity and left for 30 min, then back into an isotonic bath for 30 min, and finally to a hypertonic (or hypotonic) bath for 30 min. The sequence of bath osmolarities (hypotonic and hypertonic) was randomized to prevent bias. A digital image was taken at 0 min, 10 min, 20 min and 30 min in each solution for the opening angle measurements, confirming that 20 min is sufficient to allow the opening angle to plateau. This method was adopted from [16]. To validate our methods against the published work performed by Azeloglu on rodent tissue [16], 11 rings were acquired from the thoracic aortas of two 4-months old rats ($N_4$ = 2 animals) and the opening angles of aortic rings were measured immediately after their death. Procedures were approved by the institutional animal care committee at the University of Ottawa (Protocol #3997) and were performed in accordance with the ARRIVE guidelines.

### 6.4.4 Indentation Mechanical Testing

Three aortic strip samples of approximately 2.5 x 2.5 cm were excised from each of the AS, AR, and LDT regions of 5 porcine aortas ($N_5$ = 5 animals). One sample was tested in a fresh state (within 24 hours of harvesting; kept at $4^oC$ until testing), the second sample served as a control that was incubated in the buffer used for GAG depletion without enzymes, and the third sample underwent enzymatic GAG depletion. Indentation tests were carried out using a Biomomentum Mach-1 mechanical tester (Biomentum Inc., Laval, QC, Canada) with a 150-gf load cell and a 1 mm-diameter flat cylindrical indenter, with samples being immersed in PBS. The choice of the indenter was made to address the difficulties stemming from the non-uniform thickness and curvature of the aortic samples. A total of 40 preconditioning cycles were applied. The initial thickness at the start of the preconditioning test was detected by a protocol that involved localizing the support and sample surfaces through changes in the force measured. After preconditioning, samples were indented radially from the intimal layer, to 20% of their thickness, in a timespan of 5s. For the compression test, the initial position was selected as the initial thickness measured before preconditioning and care was taken to examine the generated force-displacement data and determine the new thickness of the sample following preconditioning ($t_o$), as the thickness corresponding to the onset of the loading cycle and the initiation point of the stress-strain curve. The onset of each loading cycle was established as the point when the force transitioned from 0 to a quantifiable value. The force-displacement data were then used to calculate the corresponding first Piola-Kirchhoff compressive stress ($\frac{force}{indenter\ cross\ sectional\ area}$) and Green-Lagrange strain ($\frac{1}{2}\left(\left(\frac{t}{t_o}\right)^2 - 1\right)$) where $t$ is the sample thickness at each loading point, which enabled to generate compressive stress-strain curves. Each sample was subjected to a series of 5 indentation tests across 5 different locations of its intimal surface.

### 6.4.5 Water content

To evaluate the swelling state of tissues before and after GAG depletion, 9 samples were procured from each of the AS, AR, and LDT regions per porcine aorta for a total of 8 aortas ($N_6$ = 8 animals). Similar to the other experiments carried out in this study, 3 states were evaluated (fresh, control, and GAG-depleted) and 3 samples were considered for each state: one incubated in a hypotonic solution, the second in an isotonic solution, and the third sample in a hypertonic bath for at least 1 hour before weighing. Wet weights were obtained after gentle dabbing to remove excess water. Samples were stored at -80°C, and then lyophilized to obtain their respective dry weights, from which the corresponding water content was calculated, whereby the weight of water was calculated as the difference between wet and dry weights and expressed as a percentage of wet weight.

### 6.4.6 Circumferential Prestretch

Considering the unloaded and the approximate stress-free configurations shown in Figure 6.1, and assuming that the opening angle $\alpha$ is the same across the thickness of the ring, the circumferential prestretch (i.e. the circumferential stretch present in the unloaded aorta) can be expressed as $\Lambda_\theta = \frac{\pi\rho}{(\pi-\alpha)R}$, where $\rho$ is the radius in the closed (unloaded) configuration ($\rho_i \leq \rho \leq \rho_o$), $R$ is the radius in the open configuration ($R_i \leq R \leq R_o$), and index *i* refers to the inner radius, while index *o* refers to the outer radius ([29], p. 290). For given inner radii acquired as described in Section 2.3, intermediate $\rho$ and $R$ are related by equation $\rho^2 = \rho_i^2 + \frac{(\pi-\alpha)}{\pi}(R^2 - R_i^2)$. To investigate the effect of GAG depletion, the circumferential prestretch was evaluated in 8 positions throughout the aortic wall of control and GAG-depleted rings. Given the definition of the circumferential prestretch, a value less than 1 describes a compressive deformation, a value of 1 describes no deformation, and a value greater than 1 describes a tensile deformation. Furthermore, a prestretch getting closer to, while staying below 1, describes a reduction in the compressive local deformation associated with the closing of the opening angle. Conversely, a prestretch getting farther from, while staying above 1, describes an increase in the tensile local deformation associated with the closing of the opening angle.

### 6.4.7 Biochemical Analysis of Tissue Composition

The sulfated GAG (sGAG), collagen, and general AGE contents were quantified from papain digests of aortic tissues. After measuring the wet and/or dry weights of aortic tissues, the samples were incubated for 48 hours at 60°C in at least 40 µg/ml papain from papaya latex, in papain digestion buffer containing 5 mM of cysteine and 5 mM of ethylenediaminetetraacetic acid (EDTA). The sGAG content of papain digests was determined using a dimethylmethylene blue (DMMB) spectrophotometric assay as described in [17]. Color changes were evaluated spectrophotometrically at a wavelength ratio of 525 nm/590 nm, and the standard curve was generated using chondroitin sulfate A sodium salt. General AGEs were obtained from fluorescence readings at 360 nm excitation and 440 nm emission, and were compared against a quinine standard [30,31], and normalized to both wet weight and collagen content. The collagen content was estimated from the hydroxyproline content after hydrolysing papain digest in 6N HCl for 18 hours at 110$^{o}$C, as detailed in [17,32]. Hydroxyproline content was quantified by usage of chloramine-T/Ehrlich’s reagent and measurement of absorbance at 560 nm. L-hydroxyproline was used as a standard.

### 6.4.8 Histology

Aortic tissue samples were fixed in 10% formalin for 72 hours, then transferred to 70% ethanol. Samples were embedded in paraffin, then cut into 4 µm-thick sections and stained with Alcian blue to highlight GAG within the aortic tissue in blue and Verhoeff - van Gieson elastic stain to highlight elastic fibers in black and visualized by light microscopy.

### 6.4.9 Statistical Analysis

Statistical analyses were carried out using IBM SPSS Statistics version 28.0.1.1. A paired sample t-test was used to evaluate the differences between the before and after treatments groups (GAG depletion, glycation). To evaluate the significance between groups (e.g. regions), a one-way ANOVA was used. When Levene’s test was not significant, a Tukey HSD post-hoc test was used, otherwise a Welch test was used along with a Games-Howell post-hoc. Significance was accepted at $p < 0.05$ (2-tailed). For compositional data (GAG, collagen, AGE, as well as water content) statistical methods were performed on log-ratio transformed data. An additive log-ratio approach was employed for the GAG, collagen and water contents with ratios calculated using the amalgamation of all tissue components, while a pairwise log-ratio was used for the AGE content with ratios calculated using the collagen content. Results are presented as mean±standard deviation (SD), or standard error of the mean (SEM) as indicated in figure captions.

## 6.5 RESULTS

### 6.5.1 Confirmation of tissue treatments

Using enzymatic digestion, the GAG content of aortic tissues was successfully decreased by 94 ± 2% in fresh tissues and by 93 ± 3% in glycated tissues, as shown in Figure 6.2A. The successful GAG removal for other experiments is also shown in Supplemental Figure S6.2. This was also confirmed by histological sections stained with Alcian blue, with the hallmark blue stain absent in GAG-depleted samples (Figures 6.2C,D).

The efficacy of the glycation step was also evaluated by quantifying general AGEs, which were found to be between 1.7 and 2.0 times higher in the samples incubated with ribose compared to controls (Figure 6.2B and Supplemental Figure S6.3A). General AGEs and collagen contents were not altered following GAG depletion, as shown in Figure 6.2B and in Supplemental Figure S6.3B, respectively.

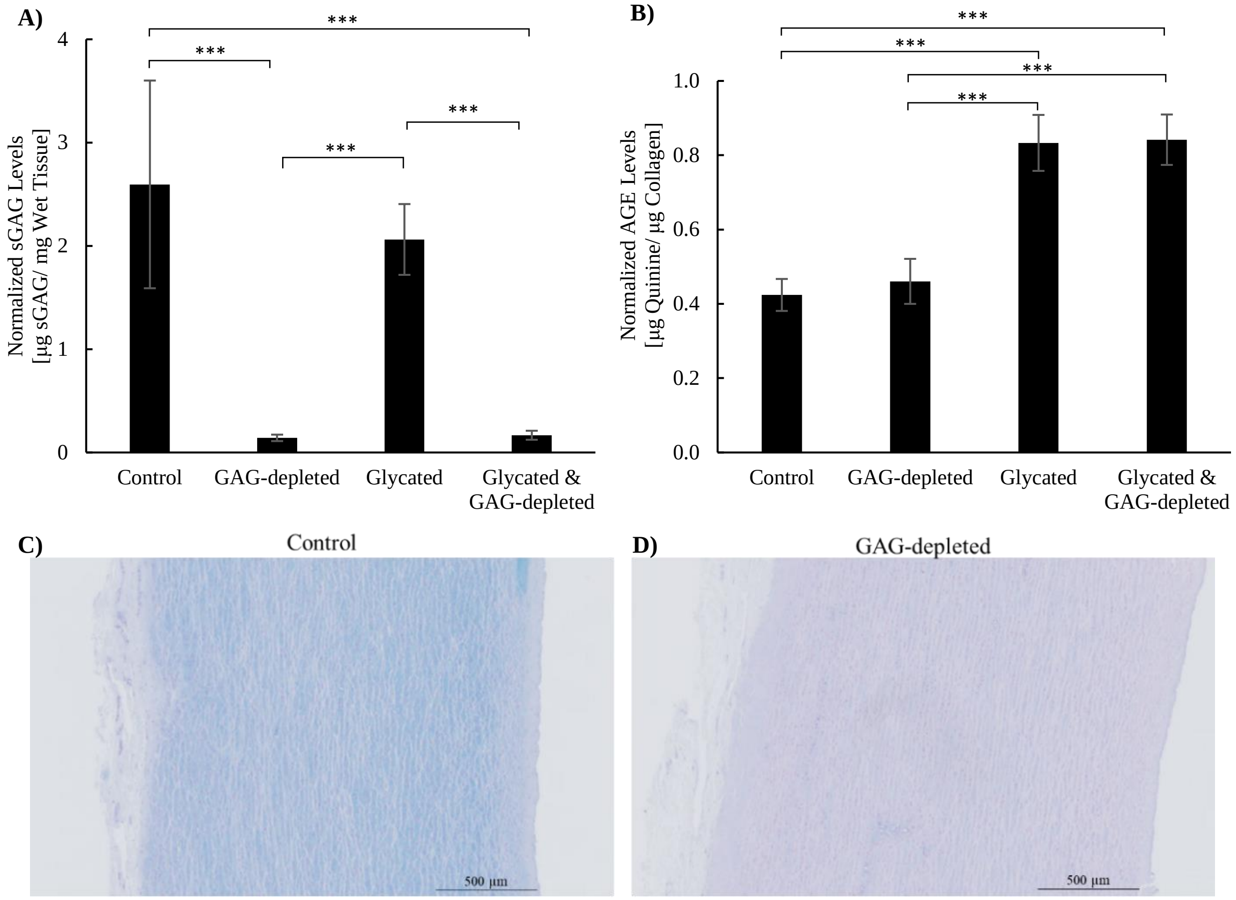

*Figure 6.2: (A) sGAG content normalized to tissue wet weight and (B) general AGEs normalized to collagen content for control, GAG-depleted, glycated and, glycated and GAG-depleted aortic rings excised from the UDT region. Results are expressed as mean ± SD ($N_2$=9 animals). *** indicates p<0.001 (paired sample t-test). (C) Representative histological sections from control and (D) GAG-depleted aortic samples excised from the AS region.*

### 6.5.2 Effects of treatments on aortic ring opening angles

Following GAG depletion, the opening angle significantly decreased from 114 ± 17 deg to 85 ± 18 deg in the AS region (p=0.009), from 61 ± 27 deg to 41 ± 24 deg in the AR region (p=0.003), and from 31 ± 9 deg to 18 ± 7 deg in the LDT region (p=0.001), as illustrated in Figure 6.3A. Detailed results for all samples are presented in Supplemental Figure S6.4, illustrating the relative decrease in the opening angle within each pair of control and GAG-depleted rings excised from the same aorta. In evaluating the combined effect of glycation followed by GAG-depletion in aortic samples from the UDT region, it was observed that the opening angle significantly decreased from 45 ± 7 deg to 30 ± 9 deg following GAG depletion alone (p<0.001), to 39 ± 9 deg following glycation alone (p<0.001) and to 25 ± 9 deg following combined glycation and GAG-depletion ($p<0.001$), as shown in Figure 6.3B. Of note, the opening angles of GAG-depleted ($p=0.002$) rings, and rings that underwent a combination of glycation and GAG-depletion treatments ($p=0.002$) were significantly smaller than the opening angle of samples that underwent glycation only. We also confirmed that incubation in the buffer alone (without enzymes) did not affect the opening angle, as shown in Supplemental Figure S6.1.

To further probe the influence of GAG on the opening angle, a complementary study was conducted to investigate the effect of solution osmolarity on the opening angle of aortic rings according to a protocol adapted from [16]. As shown in Figure 6.3C the opening angles under hypertonic conditions were not significantly different from those in isotonic solutions. Similarly, incubation in hypotonic solution did not elicit a change in opening angle, with the exception of the AS region for which the opening angle of 131 ± 20 deg, was significantly higher than the opening angle in isotonic solution, at 115 ± 23 deg ($p=0.032$). This was not the case for GAG-depleted tissue, where no significance was found between the opening angles in any of the 3 solutions as shown in Figure 6.3D. These results contrast with those obtained by [16] in rodents. To validate our methods in light of these results, we repeated the experiment with rodent aortic rings (Supplemental Figure S6.5). The opening angle of rodent rings from the AS region for hypotonic solution was 144 ± 34 deg, significantly higher than the opening angles in isotonic solution, which was 93 ± 47 deg ($p=0.016$), and in hypertonic solution, which was 97 ± 52 deg. Similarly, the opening angle of rodent rings from the UDT region in hypotonic solution was 127 ± 57 deg, significantly higher than the opening angles in isotonic ($p<0.001$) and hypertonic ($p=0.037$) solutions, which were 100 ± 61 deg and 87 ± 74 deg, respectively. These results are comparable to those in [16], which validate the adopted protocol, and support the validity of the different response obtained in porcine tissue.

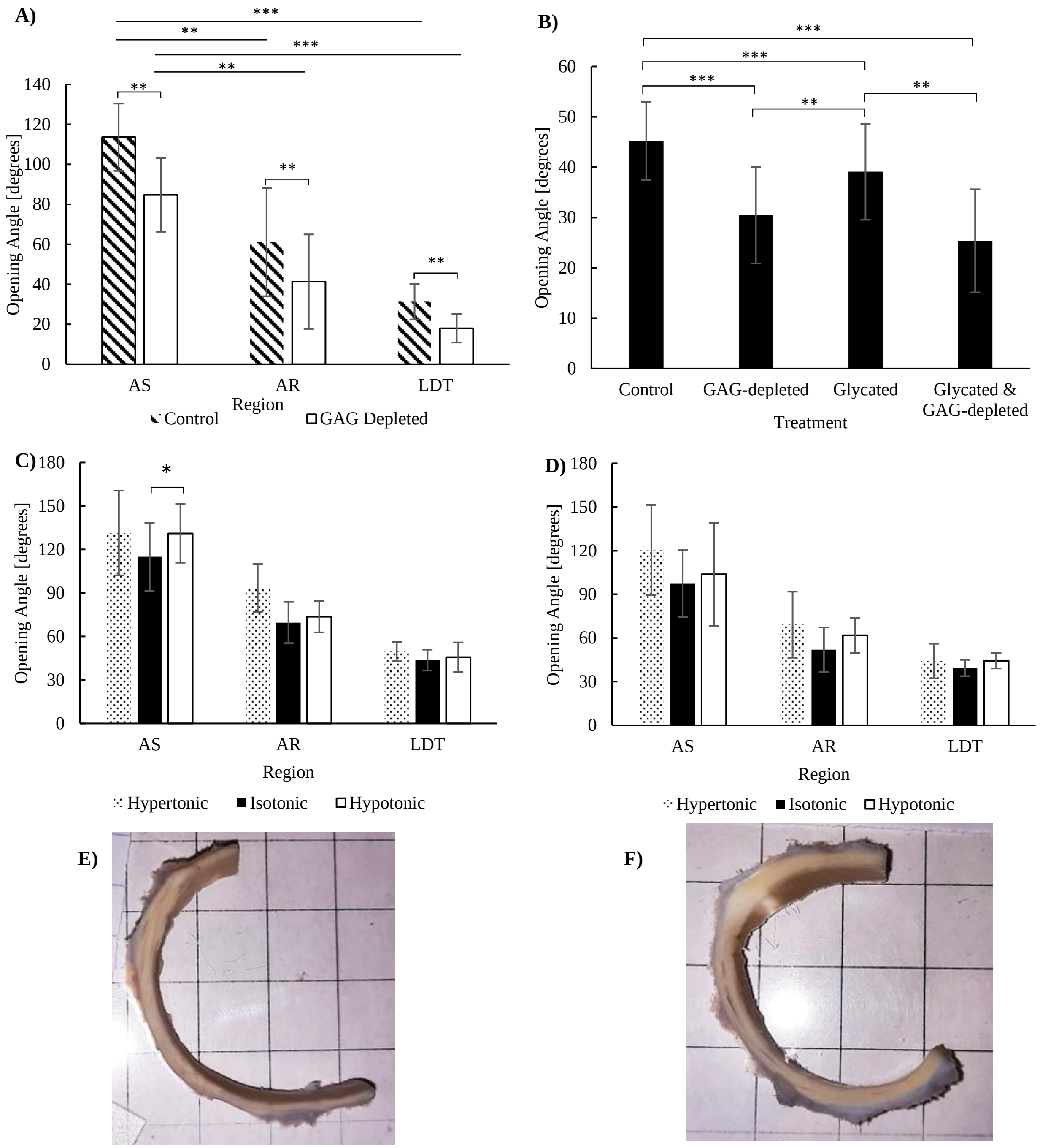

*Figure 6.3: Opening angles of (A) control and GAG-depleted aortic rings from the AS, AR, and LDT regions ($N_1$=5 animals); (B) GAG-depleted, glycated, and glycated in combination with GAG-depleted aortic rings excised from the UDT regions ($N_2$=9 animals); (C) control rings at equilibrium under hypertonic, isotonic, and hypotonic osmolarities in the AS, AR, LDT regions ($N_3$=3 animals); (D) GAG-depleted rings at equilibrium under hypertonic, isotonic, and hypotonic osmolarities in the AS, AR, LDT regions ($N_3$=3 animals). Results are expressed as mean ± SD; *** indicates $p<0.001$, ** indicates $p<0.01$, * indicates $p<0.05$. Horizontal bracket symbols refer to statistical results from the paired sample t-test while straight lines are from ANOVA with Tukey-HSD Post-Hoc test. (E) Representative illustrations of radially cut control and (F) GAG-depleted aortic rings from the AS region.*

### 6.5.3 Indentation

Radial indentation was carried out on fresh, control, and GAG-depleted samples from each of the AS, AR and LDT regions to analyse the effect of GAG on the radial compressive stiffness. Figure 6.4 summarizes the first Piola-Kirchhoff stress at 10% Green-Lagrange strain for a force applied onto the intimal layer. In the AS region, the first Piola-Kirchhoff stress in GAG-depleted samples was significantly higher than in fresh ($p=0.006$) and control samples ($p=0.021$). In the AR and LDT regions, GAG depletion did not generate any alterations in the stress measurements. Furthermore, the first Piola-Kirchhoff stresses in fresh, control and GAG-depleted samples in the AS region were 17 ± 4 kPa, 14 ± 4 kPa and 19 ± 5 kPa, respectively, and were significantly higher than in the AR region, where they were 9 ± 2 kPa ($p=0.002$), 7 ± 2 kPa ($p<0.001$) and 10 ± 2 kPa ($p<0.001$), respectively, and as well as significantly higher than in the LDT region, where they were 10 ± 3 kPa ($p=0.023$), 12 ± 2 kPa ($p <0.001$) and 10 ± 1 kPa ($p<0.001$), respectively. Detailed results for all samples are presented in Supplemental Figure S6.6.

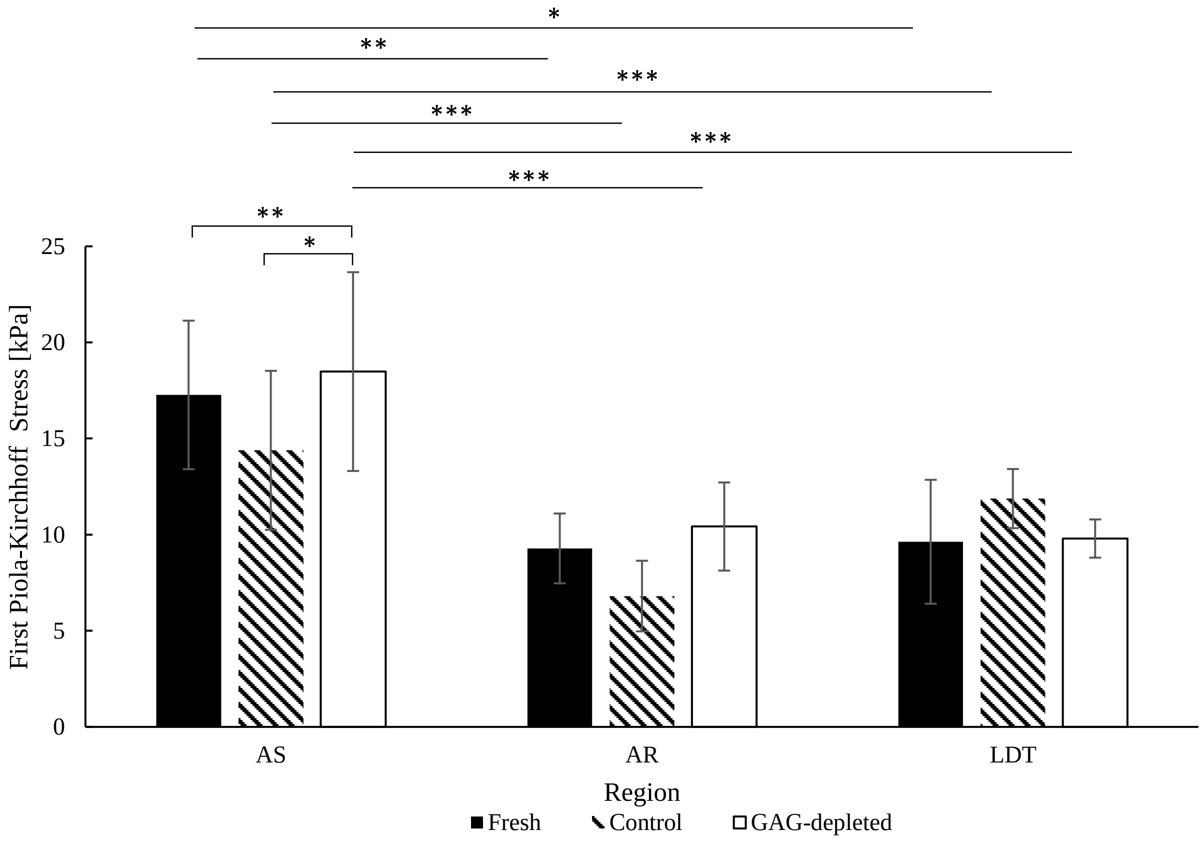

*Figure 6.4: First Piola-Kirchhoff stress in kPa at 10% strain (in the radial direction) of fresh, control and GAG-depleted aortic samples from the AS, AR, and DT regions (n=25 tests from $N_4$=5 animals). Results are presented as mean ± SEM. *** indicates p<0.001, ** indicates p<0.01, * indicates p<0.05. Horizontal bracket symbols indicate results from the paired sample t-test, while straight lines are from Welch with Games-Howell Post-Hoc test.*

### 6.5.4 Swelling

To gain insight into the mechanisms at play in the changes to mechanical properties due to GAG depletion, we first investigated if swelling, a fundamental behavior of GAG in tissues, was affected. GAG depletion was associated with a water content loss, which was mostly detectable in hypotonic conditions as shown in Figure 6.5A. Under hypotonic conditions, the water content in the AS, AR, and LDT regions was respectively 75 ± 1%, 71 ± 5%, and 75 ± 2% in GAG-depleted tissue, showing a significant decrease from 81 ± 1% (p<0.001) in the AS, 82 ± 2% (p=0.002) in the AR and 79 ± 3% (p=0.008) in the LDT regions of fresh samples, and from 76 ± 4%, 80 ± 5% (p=0.028), 78 ± 1% (p<0.001) in control samples. The water loss was also observed under isotonic and hypertonic conditions, however, it was not always significant. For instance, in isotonic solutions, the water content in the AS, AR, and LDT regions was respectively 69 ± 4%, 71 ± 4%, and 70 ± 4% in GAG-depleted tissue, showing a decrease from 74 ± 5% in the AS, 76 ± 3% (p=0.039) in the AR and 75 ± 1% (p=0.016) in the LDT regions of fresh samples, and from 72 ± 3%, 74 ± 3%, 73 ± 2% in control samples.

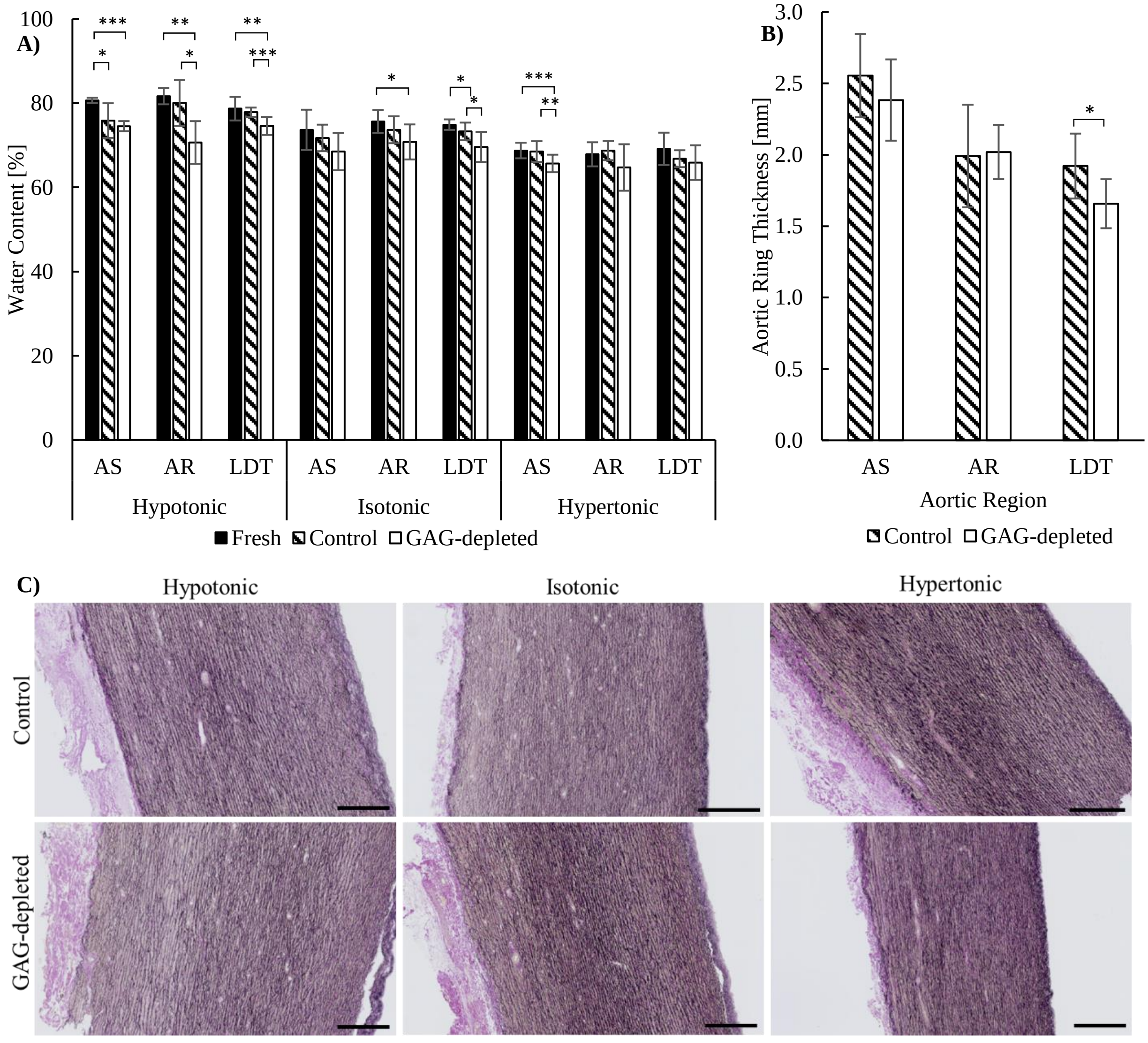

*Figure 6.5: (A) Water content of fresh, control and GAG-depleted aortic rings under hypotonic, isotonic, and hypertonic conditions, n=8 samples per region ($N_5$=8 animals). (B) Aortic ring thickness of control and GAG-depleted aortic rings, 5 rings per region ($N_1$=5 animals). Results are presented as mean ± SD. *** indicates p<0.001, ** indicates p<0.01, * indicates p<0.05 (paired sample t-test). (C) representative histological sections from control (top) and GAG-depleted (bottom) aortic samples excised from the AS region, under hypotonic, isotonic, and hypertonic conditions. Scale bar length = 500 µm.*

The data also confirmed that swelling was greatest under hypotonic conditions, less in isotonic, and least in hypertonic solutions, as represented in Figure 6.5 and in Supplemental Figure S6.7. Figure S6.7 also shows that, although water content decreased after GAG-depletion, the tissue still responded with the same swelling trend under the different bath concentrations. This was also confirmed using histological sections stained with Verhoeff's -VanGieson as shown in Figure 6.5C, where, for both control and GAG-depleted tissue, the spacing between the elastin fibers was found to decrease from hypotonic, to isotonic, to hypertonic conditions. As shown in Figure 6.5B, the effect of GAG depletion on water content was only accompanied by a significant decrease in the thickness of the aortic rings in the LDT region (p=0.01). There were no statistical differences between thickness values in the AR region nor the AS region before and after GAG depletion.

### 6.5.5 Circumferential Prestretch

Another factor that underlies the opening angle and could explain the changes following GAG depletion is the circumferential prestretch $\Lambda_\theta$ . The circumferential prestretch increased significantly following GAG depletion in the AS region as shown in Figure 6.6A; however, no statistically significant differences were found in the AR region (Supplemental Figure S6.8), or the LDT region (Figure 6.6B). In the AS region, the loss of compressive local deformation was prominent in the inner layers. Mainly, a significant loss of compressive local deformation was found in the inner half of the of the aortic wall, at positions 0.0 (p=0.002), 0.125 (p=0.007), 0.25 (p=0.01), and position 0.375 (p=0.025).

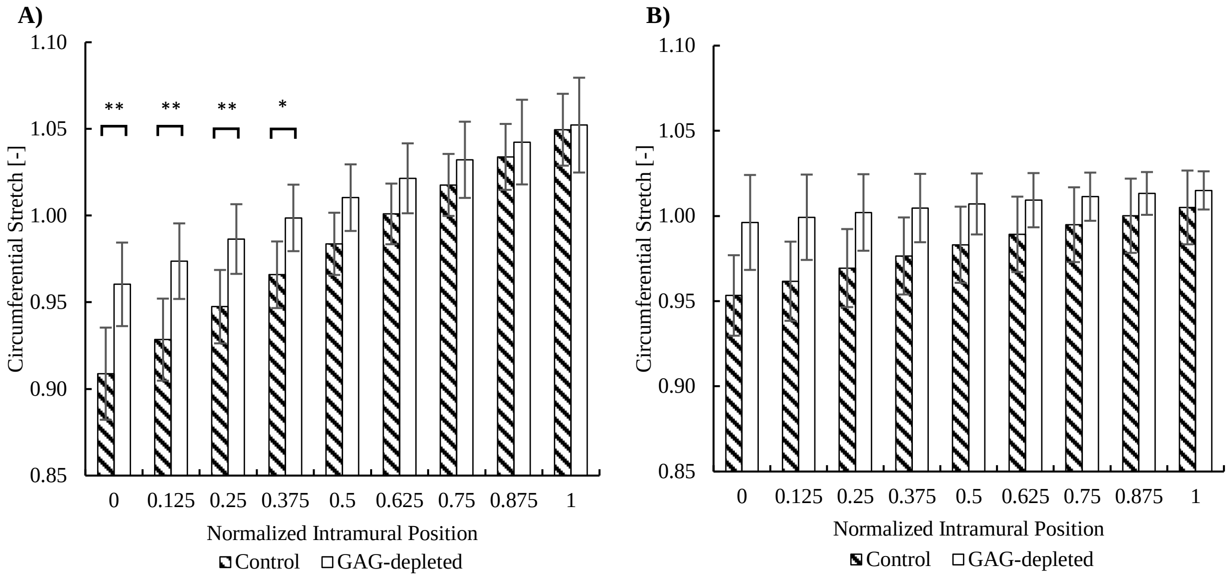

*Figure 6.6: Circumferential stretch from the unstressed to the unloaded configuration at 8 positions of the aortic wall of control and GAG-depleted aortic rings of the (A) AS and (B) LDT regions. Position 0.0 along the x-axis refers to the innermost intima and position 1.0 refers to the outermost adventitia, Results are presented as mean ± SD ($N_1$=5 animals). ** indicates $p<0.01$, * indicates $p<0.05$ (paired sample t-test).*

## 6.6 DISCUSSION

Recently, GAG have been suggested as potential important regulators of residual stresses in aortic tissues [16], and our previous efforts demonstrated that a correlation exists between the GAG content and the opening angle of porcine aortic rings [17]. However, to date, the extent of the contribution of GAG to the opening angle is still unknown. To answer this question, we subjected porcine rings to enzymatic GAG depletion. This resulted in a significant decrease in the opening angle. On average, the opening angle decreased by approximately 33%, with a decrease by 25% in the AS region, by 32% in the AR, by 42% in the LDT region, and by 33% in the UDT region. We previously showed that the sulfated GAG content is approximately 1.03 ± 0.04%dw in the ascending aorta of animals in the same age range as those investigated in this study, higher than amounts found in the aortic arch and descending thoracic regions, at 0.83 ± 0.03%dw and 0.78 ± 0.02%dw, respectively [17]. It is worthwhile to emphasize the fact that a relatively minor component of the ECM, sGAG, only occupying ~1% of the dry weight of the aorta in pigs, was found herein to contribute to approximately 30% of the opening angle. Hence the pressing need to more thoroughly understand the relationship between the two.

In addition, because glycated crosslinks play major roles in aging and disease, and since their impact on biomechanics has only been studied in the context of stiffness, we also assessed the changes in the opening angle following glycation, as well as the contribution of GAG to the opening angle in glycated tissue. Our experiments showed that after almost doubling (1.7-2.0) the amount of general AGEs in the tissue, the opening angle significantly decreased by approximately 13%. Since the tissue stiffness is expected to increase in crosslinked tissue [26,27], these findings are in line with the numerical evaluations that suggest that the opening angle decreases with increased stiffness [16]. In glycated tissue, GAG still played a similar role, and the opening angle decreased by 36% after GAG depletion, or by 44% compared to intact tissue. Hence, in this work, GAG played a more important role than AGEs in regulating the opening angle, at the glycation levels achieved.

Previous reports have shown that osmolarity affects the opening angle in rodent and porcine aortas, where a decrease in osmolarity was associated with an increase in the opening angle [16,33]. We therefore evaluated the opening angle of intact and GAG-depleted porcine rings in different external bath osmolarities, and found that in control rings, the opening angle in hypotonic solution was significantly higher than isotonic solution in the AS region only. This was in line with the observations in [16,33], and with our Supplemental study on rodent aortas. However, in contrast to [16,33], the opening angle under hypertonic solution was not the smallest, and no significant differences in the opening angle between solutions were found in the AR and LDT regions. We suggest two possible interpretations for these observations. Firstly, while Azeloglu et al. attributed the change in opening angle due to variation in osmolarity to the swelling capability of GAG only [16], Guo et al. related it to the swelling of cells, given their permeability to water [33]. Therefore, an alternative hypothesis would be that both GAG and cells contribute to the swelling state of the tissue, possibly confounding the opening angle variation due to change in osmolarity. Secondly, the porcine aortic tissue used by Guo et al [33] were excised from animals weighing 32-35 kg, whereas ours weighed 90-100 kg, suggesting significantly different sizes and/or maturity. Furthermore, we also performed the osmolarity challenge on GAG-depleted samples, and the overall response was like that in control samples. However, the opening angle in hypotonic solution was no longer significantly higher than that in isotonic conditions in the AS region. Taken together, these results support that GAG is one of the contributors to the swelling state of the tissue and may therefore contribute to regulating the opening angle response to osmolarity.

Indeed, it has previously been shown that the fixed charge density of the negatively charged GAG present in the ECM produce an osmotic swelling in the tissue [34]. It was therefore of interest to investigate if such a fundamental behaviour of GAG was present in our samples. We evaluated the tissue’s swelling state following GAG depletion and found an overall loss of water content, which was accompanied with a decrease in the tissue thickness that was significant in the LDT region. This confirmed the fundamental behavior of GAG [16,34], which may partially explain the loss in opening angle caused by GAG depletion. However, after GAG depletion, the tissue still responded to the external bath osmolarity variation in the same manner as non-GAG-depleted tissue. Namely, the water content remained highest under hypotonic solution and lowest in hypertonic solution even after GAG were removed, suggesting that GAG may not be the only regulators of water content and swelling in the aorta as speculated earlier in the discussion, and that swelling may not be the only underlying mechanism through which GAG contribute to the opening angle.

The existence of residual stresses has been primarily attributed to the presence of prestretch in the ECM [8], which is thought to be caused by the fibrous components, elastin and collagen. Elastic fibers undergo extensive deformation during growth due to change in the size and shape of the aorta, given that elastin is deposited during the perinatal period and then does not turnover substantially during the lifespan of an individual [35]. Conversely, collagen turns over continuously and is assumed to be deposited at a given prestretch [36,37]. In our first efforts to understand the contribution of the ECM constituents to the residual stresses, we found that the strongest correlation existed between the opening angle and the ratio between collagen and GAG. This led us to hypothesize that GAG may influence the prestretch level of collagen and elastin, which in turn may influence residual stresses [17]. Focussing specifically on the circumferential direction of the aorta, we showed that GAG depletion causes a loss of compressive local deformation in the inner layers of the aortic wall in the AS region, which is consistent with our previous findings and suggests that fiber prestretch in the aorta may be influenced by GAG, which in turn may affect residual stresses. We previously showed that higher amounts of GAG exist in the AS region compared to other regions of the thoracic tree, and in the inner layers of the aortic wall compared to the outer layers [17]. This is noteworthy here since these regions experienced higher significance in loss of compressive local deformation, as well as an increase in radial compressive stiffness – as discussed later – after GAG depletion.

It is important to note a limitation in our calculations of the circumferential stretch, which is that we assumed that the opening angle is the same throughout the aortic wall thickness, whereas it is likely layer-dependent due to the heterogeneous nature of the aortic wall [38]. This assumption may impact the estimates of stretch values at each mural location, and lead to different stretch distributions across the wall of the aorta. However, given that the stretch values were compared at consistent mural positions between the control and GAG-depleted rings, this assumption would not change our conclusion that GAG influence circumferential prestretch. In addition, in control samples, $\Lambda_\theta$ was 0.91 ± 0.02, 0.97 ± 0.02, 0.95 ± 0.03 in the innermost position of the AS, AR, and LDT regions, and 1.05 ± 0.03, 1.04 ± 0.03, and 1.01 ± 0.01 in the outermost position of the aortic wall, respectively. These are similar to results in [9] which were 0.93 ± 0.01 in the intima and 1.04 ± 0.00 in the adventitia of porcine thoracic aortas. In the rabbit aorta, Chuong and Fung showed that the circumferential stretch was around 0.86 in the innermost layer and 1.14 in the outermost adventitia [8].

Interestingly, the interaction between GAG and ECM fibers has previously been found to affect the mechanical behavior of the aorta. For instance, in aneurysmal aortas, GAG have been found to be associated positively with local collagen fiber dispersion, and negatively with the ultimate strength in the circumferential direction [39]. Additionally, the collagen fibers' waviness in excised square samples of healthy porcine aortas was reduced after GAG depletion, and both elastic and collagen fiber were recruited at lower strains [20]. This work done by Mattson et al. also showed that GAG influences the aortic stiffness, whereas earlier, but not absolute, stiffening was found in the tensile stress-strain response of tissues subjected to GAG depletion [20]. In an earlier study, Gandley et al. found an absolute loss of tensile compliance after removal of chondroitin sulfate, an abundant sulfated-GAG found in the aorta [21]. However, Beenakker et al. [13] reported a decrease in the compressive stiffness of the medial and adventitial layers of porcine aortic samples that underwent depletion of GAG using atomic force microscopy (AFM). In our study, the radial compressive stiffness of the aorta was evaluated using indentation. Our result suggested that, in the AS region only, GAG depletion induced an increase in radial compressive stiffness (measured by stress at 10% strain, applied from the intimal layer) following GAG depletion. This is conforming to findings on tensile stiffness [20,21], but seems to contradict findings from AFM [13]. However, these, in addition to our findings, confirm that GAG influence the stiffness of the aorta. Still, more work is needed to understand at what levels GAG begin to influence stiffness, as well as their actual effect on compressive stiffness. Also noteworthy is that indentation and AFM enable the analysis of local properties only, and therefore testing the tissue under macroscopic compression may better confirm these observations.

Through indentation, we were also able to confirm the heterogeneous nature of the aortic tree, given that our findings suggest that the AS region, under 10% radial strain (applied from the intima), is stiffer than the AR and LDT regions. Heterogeneity throughout the aortic wall, as well as through the aortic tree has been extensively evaluated [38,40–44]. Since the aorta is mainly subjected to tensile deformation under physiological pressure, the focus has been on evaluating the tensile response of the aorta, and it is well established that the tensile stiffness (evaluated through uniaxial and biaxial tensile testing) increases from the proximal to distal samples in the descending thoracic aorta [38,42–44]. Evaluating the compressive properties has garnered less attention than those in tension, but nanoindentation previously showed an increase in radial stiffness in the most distal regions of the descending thoracic aorta [40,41]. Although we did not evaluate the properties through as many positions in the descending thoracic aorta, our results revealed no differences in radial compressive stiffness between the AR and LDT regions. However, our findings suggest that, under 10% radial strain (applied from the intima), the compressive stiffness in the AS region is significantly higher than that of the AR and LDT regions, which may seem to contradict findings in [41]. Nevertheless, it is important to note that the indenter is this study was 1 mm in diameter, i.e. larger than the indenter used in [40,41] by several orders of magnitude. In addition, given that the mechanical properties of the layers in the aortic wall are heterogeneous under tension [38], it is expected that the compressive properties also differ throughout the aortic wall. Our analysis was also conducted at an indentation depth of 10% of the tissue thickness from the intimal layer, while the depth in [41] was set to 60 µm. These differences in the tissue mechanical response at different testing scales highlight the complexity of the aortic tissue in its mechanical response. Indeed, the aorta is a soft hyperelastic nonlinear tissue, highly heterogeneous and is characterised by its sensitivity to loading conditions, which stems from its viscoelastic properties. Under tension, the sensitivity of the tissue to loading conditions has been discussed in the literature, and for instance, the aorta possesses distinct mechanical responses that depend on the type of test employed (ex. Displacement-controlled versus force-controlled tests) [45]. As the literature develops a foundation for evaluating the aorta's response to compression, it will become important to investigate the tissue's sensitivity across various testing scales.

Another important aspect that requires discussion is the effect of GAG depletion on the structure and composition of the tissue. GAG depletion is expected to cause alterations in the ECM structure, given that GAG are closely associated with collagen and elastin fibers [20,46]. However, in this work, the contents of collagen and general AGEs were quantified following GAG depletion and no differences were found. Additionally, histological observations did not reveal any apparent differences in the elastin arrangement in the unstressed configuration. It has been previously shown that GAG depletion alters the waviness of collagen fibers, but no evident effects on the structure of elastin was detected [20]. This is therefore an area that warrants further investigation, in order to elucidate other possible effects of GAG removal on the structure of the tissue, including ECM fibers, crosslinks, as well as cells structures. Additionally, it is important to note the elevated ribose concentration used to induce AGE crosslinks *in vitro* in this study. It is possible that this leads to additional structural changes in the tissue beyond the accumulation of AGE crosslinks. For example, it has been reported that high glucose concentrations can lead to deteriorate the endothelial glycocalyx [47]. Such potential tissue changes were not investigated here. Another study limitation that needs stating is the use of a low number of animals for some of the tests. For the opening angle and indentation tests, five porcine aortas were sufficient to provide key information and statistical significance. For the osmolarity test however, after running experiments on samples from three porcine aortas, it became clear that adding more samples would not lead to changes in the conclusions. To ensure the robustness of our experimental methods for the osmolarity test, we carried out the same investigation using the rat aortas, from which we were able to reproduce previously published data [16]. In this test, only two animals were used. Finally, given the possible variations between species, investigations into human tissue are necessary in future work.

To summarize, it has been previously been speculated that GAG regulate the opening angle via established correlations and numerical simulations, however the extent of contribution of GAG to the opening angle remains poorly understood. In this work, and for the first time, we showed through enzymatic GAG-depletion that GAG contribute to 25-42% of the opening angle in 5-6 months old porcine aortas. We also showed that the accumulation of AGE crosslinks causes a reduction in the opening angle. In addition, we deciphered potential underlying mechanisms causing the reduction in opening angle after GAG loss, which in this work was attributed not only to the fundamental swelling of GAG, but also to their ability to interact with the ECM fibers and hence impact circumferential prestretch. Remarkably, we show that GAG depletion contributed to a loss of compressive deformation in the inner layers of the aortic wall, mainly in the AS region, which contains the highest levels of GAG in our animals. In addition, it was confirmed that the compressive properties of the aorta vary throughout its tree, and that GAG, at certain levels, cause significant alterations to the compressive mechanical response of the aorta. Indeed, we found a significant increase in radial compressive stiffness under indentation in the AS region following GAG depletion. Given the contradicting results with the literature, understanding how GAG contribute to compressive stiffness requires a deeper evaluation, which should include comparisons between different mechanical testing methods.

## 6.7 REFERENCES

[1] A. Brüel, H. Oxlund, Changes in biomechanical properties, composition of collagen and elastin, and advanced glycation endproducts of the rat aorta in relation to age, Atherosclerosis. 127 (1996) 155–165. https://doi.org/10.1016/S0021-9150(96)05947-3.

[2] K. Prasad, A. Sarkar, M.A. Zafar, A. Shoker, H.E. Moselhi, M. Tranquilli, B.A. Ziganshin, J.A. Elefteriades, Advanced Glycation End Products and its Soluble Receptors in the Pathogenesis of Thoracic Aortic Aneurysm, Aorta (Stamford). 04 (2016) 1–10. https://doi.org/10.12945/j.aorta.2015.15.018.

[3] F.S. Cikach, C.D. Koch, T.J. Mead, J. Galatioto, B.B. Willard, K.B. Emerton, M.J. Eagleton, E.H. Blackstone, F. Ramirez, E.E. Roselli, S.S. Apte, Massive aggrecan and versican accumulation in thoracic aortic aneurysm and dissection, JCI Insight. 3 (2018). https://doi.org/10.1172/jci.insight.97167.

[4] M.R. Roach, A.C. Burton, The reason for the shape of the distensibility curves of arteries, Can. J. Biochem. Physiol. 35 (1957) 681–690. https://doi.org/10.1139/o57-080.

[5] Y. Zhang, P. Lacolley, A.D. Protogerou, M.E. Safar, Arterial Stiffness in Hypertension and Function of Large Arteries, American Journal of Hypertension. 33 (2020) 291–296. https://doi.org/10.1093/ajh/hpz193.

[6] B.R. Kwak, M. Bäck, M.-L. Bochaton-Piallat, G. Caligiuri, M.J.A.P. Daemen, P.F. Davies, I.E. Hoefer, P. Holvoet, H. Jo, R. Krams, S. Lehoux, C. Monaco, S. Steffens, R. Virmani, C. Weber, J.J. Wentzel, P.C. Evans, Biomechanical factors in atherosclerosis:

mechanisms and clinical implications†, European Heart Journal. 35 (2014) 3013–3020. https://doi.org/10.1093/eurheartj/ehu353.

[7] S. Sherifova, G.A. Holzapfel, Biomechanics of aortic wall failure with a focus on dissection and aneurysm: A review, Acta Biomaterialia. 99 (2019) 1–17. https://doi.org/10.1016/j.actbio.2019.08.017.

[8] C.J. Chuong, Y.C. Fung, On Residual Stresses in Arteries, Journal of Biomechanical Engineering. 108 (1986) 189–192. https://doi.org/10.1115/1.3138600.

[9] A. Giudici, B. Spronck, The Role of Layer-Specific Residual Stresses in Arterial Mechanics: Analysis via a Novel Modelling Framework, Artery Res. 28 (2022) 41–54. https://doi.org/10.1007/s44200-022-00013-1.

[10] Y. Lanir, Mechanisms of Residual Stress in Soft Tissues, Journal of Biomechanical Engineering. 131 (2009) 044506. https://doi.org/10.1115/1.3049863.

[11] M. Zhang, H. Liu, Z. Cai, C. Sun, W. Sun, An improved analytical method to estimate three-dimensional residual stresses of the aorta, Applied Mathematical Modelling. 90 (2021) 351–365. https://doi.org/10.1016/j.apm.2020.08.063.

[12] G.L. Pierce, T.A. Coutinho, L.E. DuBose, A.J. Donato, Is It Good to Have a Stiff Aorta with Aging? Causes and Consequences, Physiology. 37 (2022) 154–173. https://doi.org/10.1152/physiol.00035.2021.

[13] J.-W.M. Beenakker, B.A. Ashcroft, J.H.N. Lindeman, T.H. Oosterkamp, Mechanical Properties of the Extracellular Matrix of the Aorta Studied by Enzymatic Treatments, Biophysical Journal. 102 (2012) 1731–1737. https://doi.org/10.1016/j.bpj.2012.03.041.

[14] E. Fonck, G. Prod'hom, S. Roy, L. Augsburger, D.A. Rüfenacht, N. Stergiopulos, Effect of elastin degradation on carotid wall mechanics as assessed by a constituent-based biomechanical model, American Journal of Physiology-Heart and Circulatory Physiology. 292 (2007) H2754–H2763. https://doi.org/10.1152/ajpheart.01108.2006.

[15] S.E. Greenwald, J.E. Moore Jr., A. Rachev, T.P.C. Kane, J.-J. Meister, Experimental Investigation of the Distribution of Residual Strains in the Artery Wall, Journal of Biomechanical Engineering. 119 (1997) 438–444. https://doi.org/10.1115/1.2798291.

[16] E.U. Azeloglu, M.B. Albro, V.A. Thimmappa, G.A. Ateshian, K.D. Costa, Heterogeneous transmural proteoglycan distribution provides a mechanism for regulating residual stresses in the aorta, American Journal of Physiology-Heart and Circulatory Physiology. 294 (2008) H1197–H1205. https://doi.org/10.1152/ajpheart.01027.2007.

[17] N.M. Ghadie, J.-P. St-Pierre, M.R. Labrosse, Intramural Distributions of GAGs and Collagen vs. Opening Angle of the Intact Porcine Aortic Wall, Ann Biomed Eng. 50 (2022) 157–168. https://doi.org/10.1007/s10439-022-02901-8.

[18] S. Roccabianca, C. Bellini, J.D. Humphrey, Computational modelling suggests good, bad and ugly roles of glycosaminoglycans in arterial wall mechanics and mechanobiology, J R Soc Interface. 11 (2014). https://doi.org/10.1098/rsif.2014.0397.

[19] N. Ghadie, J.-P. St-Pierre, M. Labrosse, The Contribution of Glycosaminoglycans/Proteoglycans to Aortic Mechanics in Health and Disease: A Critical Review, IEEE Transactions on Biomedical Engineering. (2021) 1–1. https://doi.org/10.1109/TBME.2021.3074053.

[20] J.M. Mattson, R. Turcotte, Y. Zhang, Glycosaminoglycans contribute to extracellular matrix fiber recruitment and arterial wall mechanics, Biomech Model Mechanobiol. 16 (2017) 213–225. https://doi.org/10.1007/s10237-016-0811-4.

[21] R.E. Gandley, M.K. McLaughlin, T.J. Koob, S.A. Little, L.J. McGuffee, Contribution of chondroitin-dermatan sulfate-containing proteoglycans to the function of rat mesenteric arteries, American Journal of Physiology-Heart and Circulatory Physiology. 273 (1997) H952–H960. https://doi.org/10.1152/ajpheart.1997.273.2.H952.

[22] A. Prasad, P. Bekker, S. Tsimikas, Advanced Glycation End Products and Diabetic Cardiovascular Disease, Cardiology in Review. 20 (2012) 177–183. https://doi.org/10.1097/CRD.0b013e318244e57c.

[23] M. McNulty, A. Mahmud, J. Feely, Advanced Glycation End-Products and Arterial Stiffness in Hypertension*:, American Journal of Hypertension. 20 (2007) 242–247. https://doi.org/10.1016/j.amjhyper.2006.08.009.

[24] R. Bucala, Lipoprotein Modification by Advanced Glycosylation Endproducts (AGEs): Role in Atherosclerosis, Trends in Cardiovascular Medicine. 7 (1997) 39–47. https://doi.org/10.1016/S1050-1738(96)00137-5.

[25] R. Singh, A. Barden, T. Mori, L. Beilin, Advanced glycation end-products: a review, Diabetologia. 44 (2001) 129–146. https://doi.org/10.1007/s001250051591.

[26] A. Brüel, G. Ørtoft, H. Oxlund, Inhibition of cross-links in collagen is associated with reduced stiffness of the aorta in young rats, Atherosclerosis. 140 (1998) 135–145. https://doi.org/10.1016/S0021-9150(98)00130-0.

[27] T.J. Sims, L.M. Rasmussen, H. Oxlund, A.J. Bailey, The role of glycation cross-links in diabetic vascular stiffening, Diabetologia. 39 (1996) 946–951. https://doi.org/10.1007/BF00403914.

[28] M.R. Labrosse, E.R. Gerson, J.P. Veinot, C.J. Beller, Mechanical characterization of human aortas from pressurization testing and a paradigm shift for circumferential residual stress, Journal of the Mechanical Behavior of Biomedical Materials. 17 (2013) 44–55. https://doi.org/10.1016/j.jmbbm.2012.08.004.

[29] J.D. Humphrey, Cardiovascular Solid Mechanics: Cells, Tissues, and Organs, Springer Science & Business Media, 2002.

[30] G. Fessel, Y. Li, V. Diederich, M. Guizar-Sicairos, P. Schneider, D.R. Sell, V.M. Monnier, J.G. Snedeker, Advanced Glycation End-Products Reduce Collagen Molecular Sliding to Affect Collagen Fibril Damage Mechanisms but Not Stiffness, PLOS ONE. 9 (2014) e110948. https://doi.org/10.1371/journal.pone.0110948.

[31] A.G. Gouldin, J.L. Puetzer, An Inducible Model for Unraveling the Effects of Advanced Glycation End-Products in Collagen with Age and Diabetes, (2020) 18.

[32] J.-P. St-Pierre, Q. Wang, S.Q. Li, R.M. Pilliar, R.A. Kandel, Inorganic Polyphosphate Stimulates Cartilage Tissue Formation, Tissue Engineering Part A. 18 (2012) 1282–1292. https://doi.org/10.1089/ten.tea.2011.0356.

[33] X. Guo, Y. Lanir, G.S. Kassab, Effect of osmolarity on the zero-stress state and mechanical properties of aorta, American Journal of Physiology-Heart and Circulatory Physiology. 293 (2007) H2328–H2334. https://doi.org/10.1152/ajpheart.00402.2007.

[34] W.M. Lai, J.S. Hou, V.C. Mow, A Triphasic Theory for the Swelling and Deformation Behaviors of Articular Cartilage, Journal of Biomechanical Engineering. 113 (1991) 245–258. https://doi.org/10.1115/1.2894880.

[35] E.C. Davis, Elastic lamina growth in the developing mouse aorta., J Histochem Cytochem. 43 (1995) 1115–1123. https://doi.org/10.1177/43.11.7560894.

[36] J.D. Humphrey, K.R. Rajagopal, A constrained mixture model for growth and remodeling of soft tissues, Math. Models Methods Appl. Sci. 12 (2002) 407–430. https://doi.org/10.1142/S0218202502001714.

[37] L. Cardamone, A. Valentín, J.F. Eberth, J.D. Humphrey, Origin of axial prestretch and residual stress in arteries, Biomech Model Mechanobiol. 8 (2009) 431. https://doi.org/10.1007/s10237-008-0146-x.

[38] J.A. Peña, M.A. Martínez, E. Peña, Layer-specific residual deformations and uniaxial and biaxial mechanical properties of thoracic porcine aorta, Journal of the Mechanical Behavior of Biomedical Materials. 50 (2015) 55–69. https://doi.org/10.1016/j.jmbbm.2015.05.024.

[39] A. Tokgoz, S. Wang, P. Sastry, C. Sun, N.L. Figg, Y. Huang, M.R. Bennett, S. Sinha, J.H. Gillard, M.P.F. Sutcliffe, Z. Teng, Association of Collagen, Elastin, Glycosaminoglycans, and Macrophages With Tissue Ultimate Material Strength and Stretch in Human Thoracic Aortic Aneurysms: A Uniaxial Tension Study, Journal of Biomechanical Engineering. 144 (2022). https://doi.org/10.1115/1.4054060.

[40] A. Hemmasizadeh, M. Autieri, K. Darvish, Multilayer material properties of aorta determined from nanoindentation tests, Journal of the Mechanical Behavior of Biomedical Materials. 15 (2012) 199–207. https://doi.org/10.1016/j.jmbbm.2012.06.008.

[41] G. Kermani, A. Hemmasizadeh, S. Assari, M. Autieri, K. Darvish, Investigation of inhomogeneous and anisotropic material behavior of porcine thoracic aorta using nano-

indentation tests, Journal of the Mechanical Behavior of Biomedical Materials. 69 (2017) 50–56. https://doi.org/10.1016/j.jmbbm.2016.12.022.

[42] P.P. Purslow, Positional variations in fracture toughness, stiffness and strength of descending thoracic pig aorta, Journal of Biomechanics. 16 (1983) 947–953. https://doi.org/10.1016/0021-9290(83)90058-1.

[43] D.P. Sokolis, H. Boudoulas, P.E. Karayannacos, Segmental Differences of Aortic Function and Composition: Clinical Implications, Hellenic Journal of Cardiology : HJC = Hellēnikē Kardiologikē Epitheōrēsē. 49 (2008) 145–54.

[44] S. Zeinali-Davarani, Y. Wang, M.-J. Chow, R. Turcotte, Y. Zhang, Contribution of Collagen Fiber Undulation to Regional Biomechanical Properties Along Porcine Thoracic Aorta, Journal of Biomechanical Engineering. 137 (2015) 051001. https://doi.org/10.1115/1.4029637.

[45] T. Sigaeva, S. Polzer, R. Vitásek, E.S. Di Martino, Effect of testing conditions on the mechanical response of aortic tissues from planar biaxial experiments: Loading protocol and specimen side, Journal of the Mechanical Behavior of Biomedical Materials. 111 (2020) 103882. https://doi.org/10.1016/j.jmbbm.2020.103882.

[46] M.-J. Chow, R. Turcotte, C.P. Lin, Y. Zhang, Arterial Extracellular Matrix: A Mechanobiological Study of the Contributions and Interactions of Elastin and Collagen, Biophysical Journal. 106 (2014) 2684–2692. https://doi.org/10.1016/j.bpj.2014.05.014.

[47] A. Singh, V. Fridén, I. Dasgupta, R.R. Foster, G.I. Welsh, J.E. Tooke, B. Haraldsson, P.W. Mathieson, S.C. Satchell, High glucose causes dysfunction of the human glomerular endothelial glycocalyx, American Journal of Physiology-Renal Physiology. 300 (2011) F40–F48. https://doi.org/10.1152/ajprenal.00103.2010.

## 6.8 SUPPLEMENTARY INFORMATION

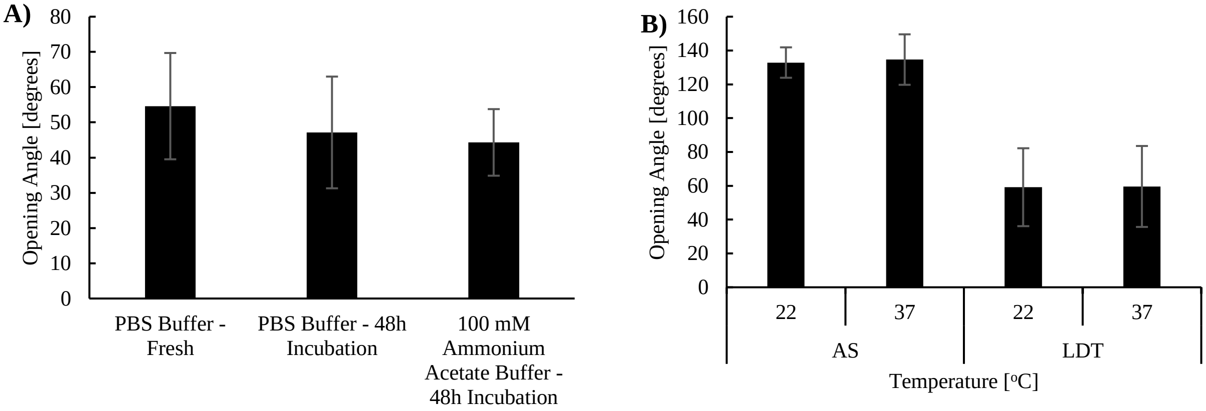

*Figure S6.1: Opening angles (mean ± SD) of aortic rings evaluated (A) at room temperature in PBS buffer when fresh, in PBS after 48h incubation at 37$^{o}$C, and in 100 mM ammonium acetate buffer after 48h incubation at 37$^{o}$C (n=5 rings from 5 animals) (B) at room temperature and 37$^{o}$C from the AS and LDT regions*

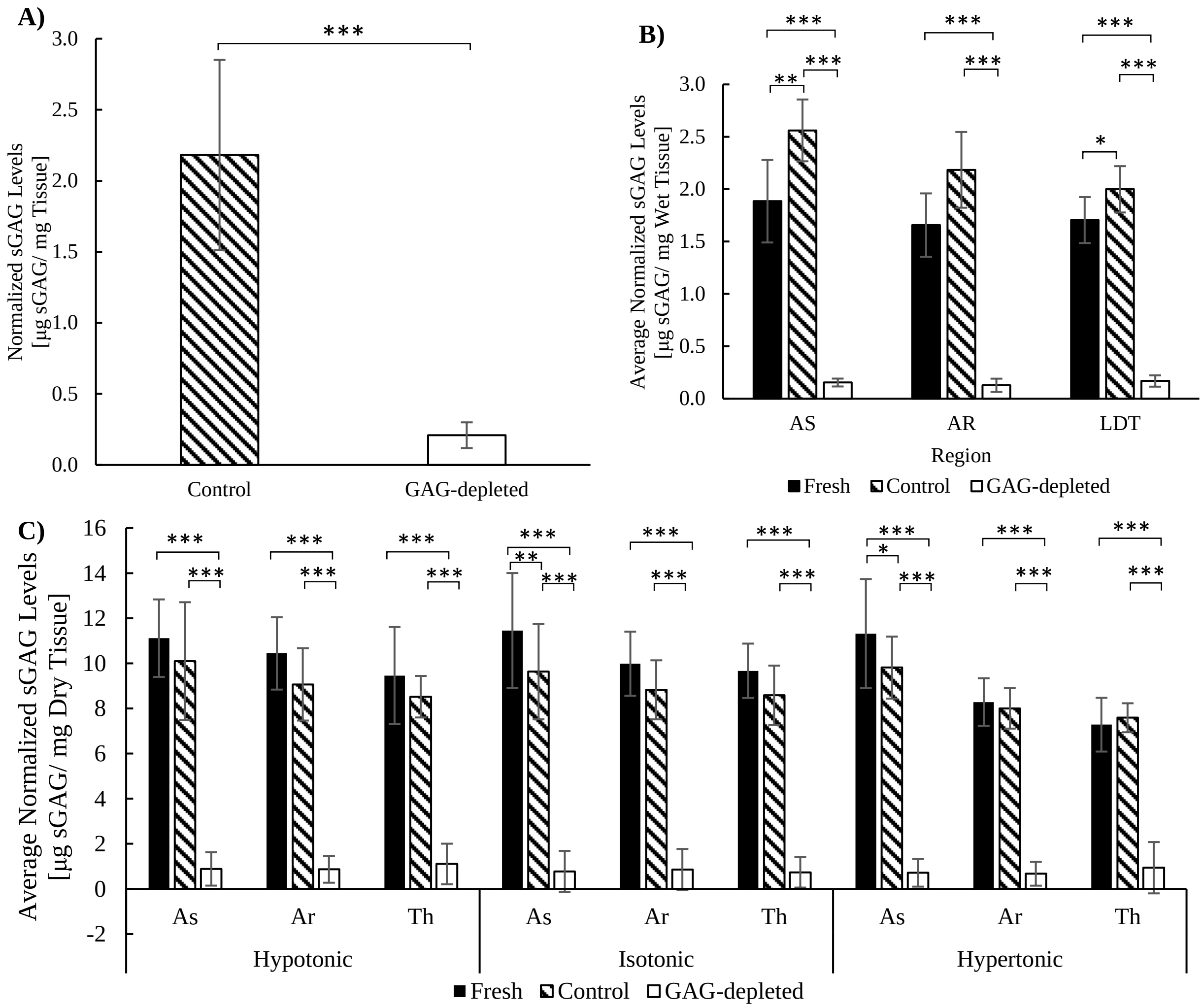

*Figure S6.2: Normalized sGAG levels (mean ± SD) of fresh, control and GAG-depleted aortic samples that underwent (A) opening angle tests, n = 24 rings from 8 animals ($N_1$=5 animals, $N_3$=3 animals) (B) indentation ($N_5$=5 animals) and (C) water content measurement ($N_6$=8 animals). *** indicates p<0.001, ** indicates p<0.01, * indicates p<0.05 (paired sample t-test).*

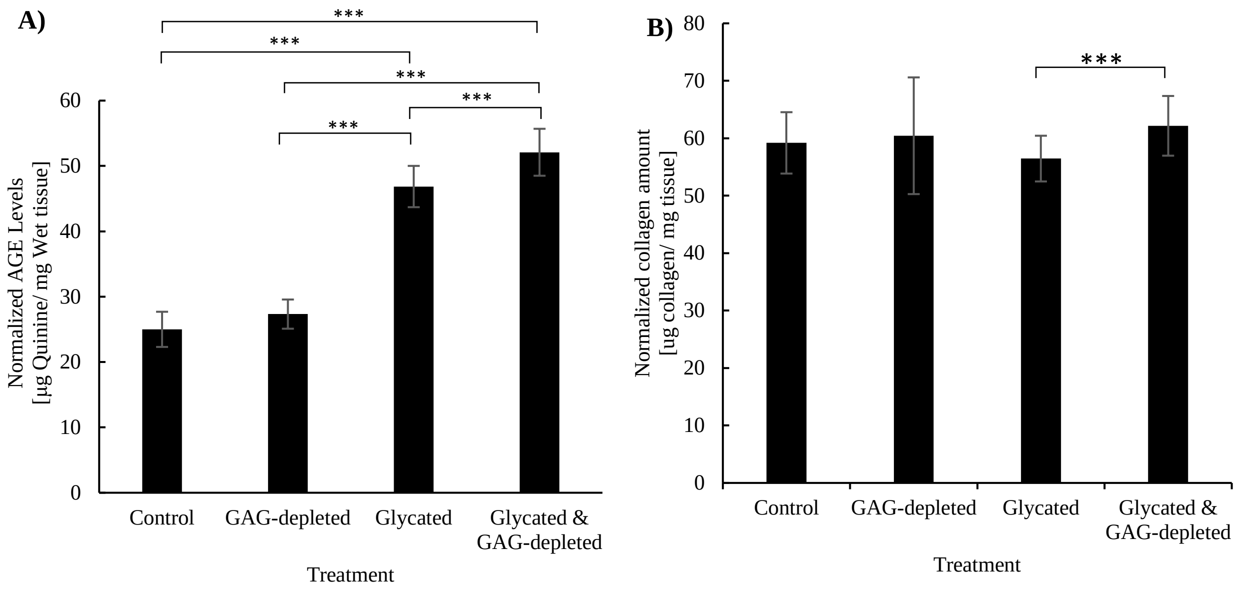

*Figure S6.3: (A) General AGEs (B) and collagen content, normalized by wet weights (mean ± SD) of control, GAG-depleted, glycated, and glycated in combination with GAG-depleted aortic rings excised from the UDT region ($N_2$=9 animals). *** indicates p<0.001 (paired sample t-test).*

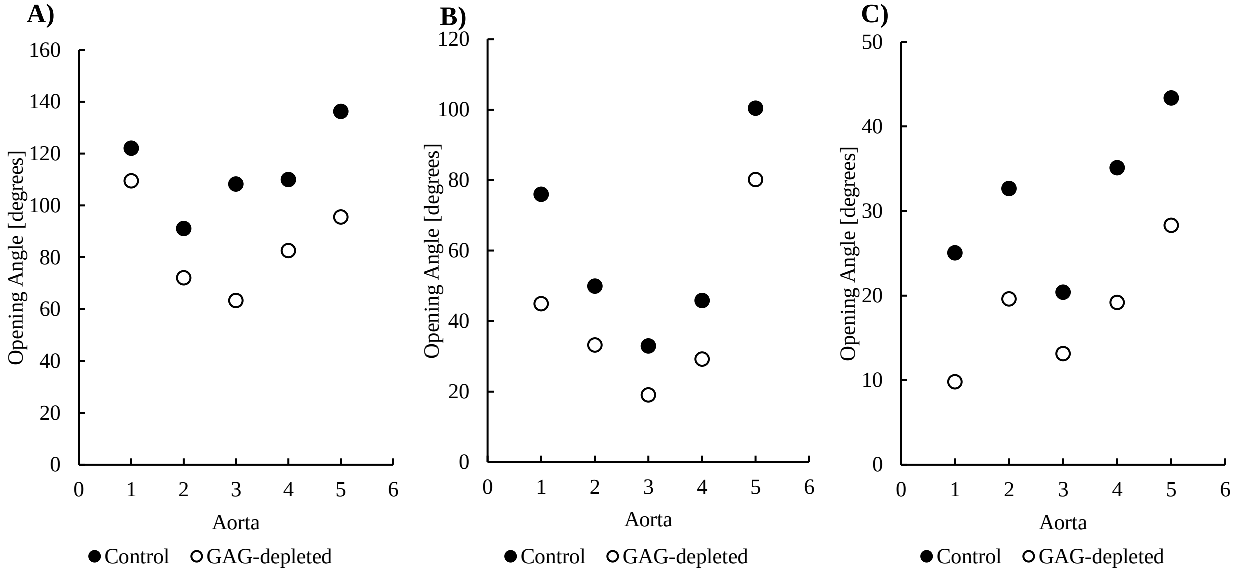

*Figure S6.4: Detailed opening angles results of control and GAG-depleted aortic rings from the (A) AS, (B) AR, and (C) LDT regions. This figure represents the detailed data of Figure 3A, in which the data is presented as mean ± SD.*

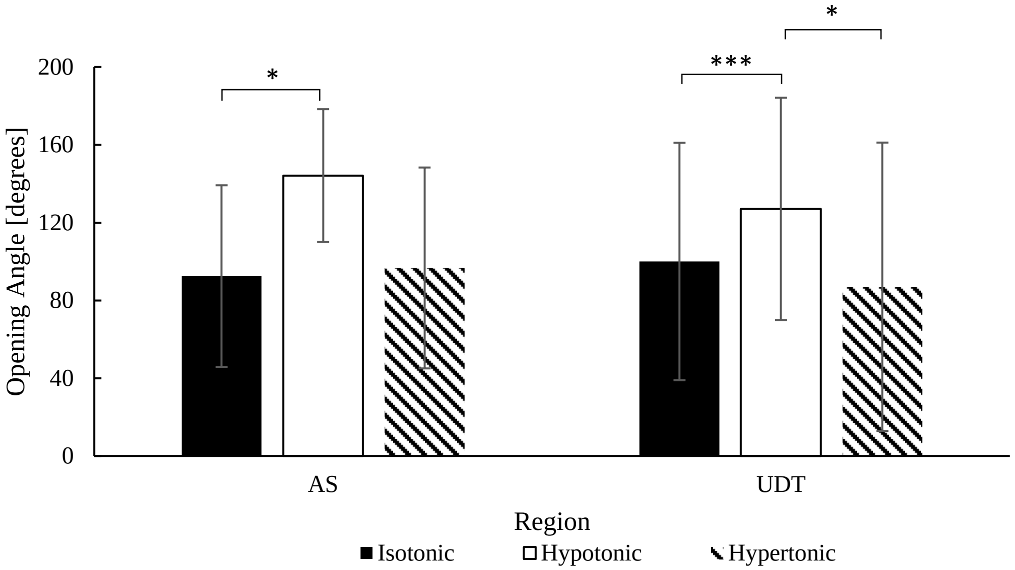

*Figure S6.5: Opening angle (mean ± SD) of rings extracted from the AS and UDT regions of rat aortas ($N_4$=2 animals), under isotonic, hypotonic and hypertonic osmolarities. *** indicates p<0.001, * indicates p<0.05 (paired sample t-test).*

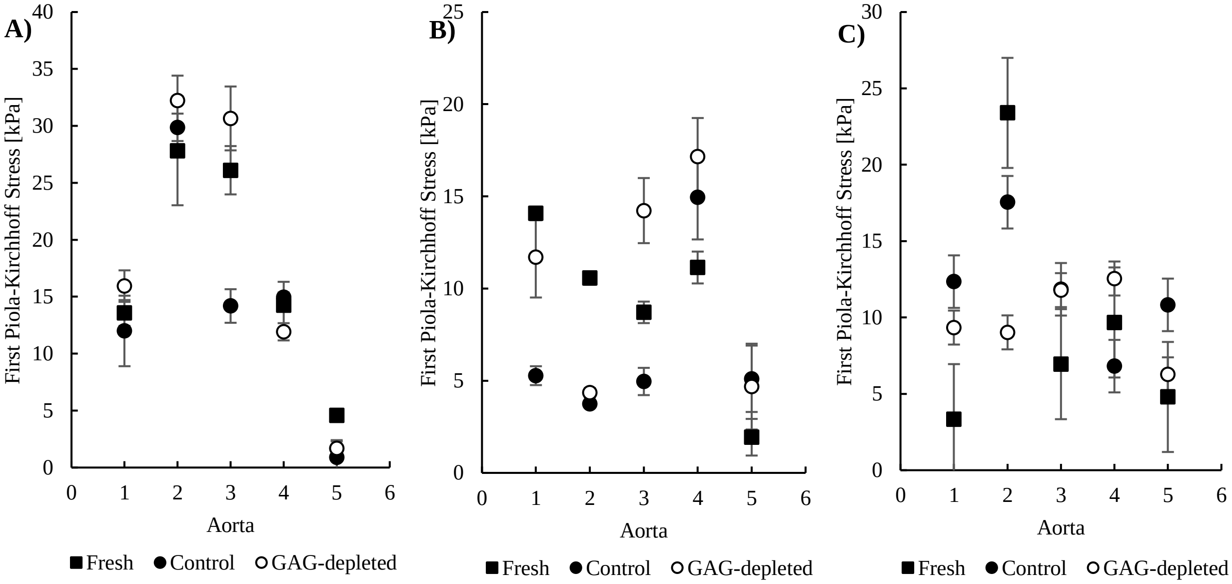

*Figure S6.6: First Piola-Kirchhoff stress in kPa at 10% strain of fresh, control and GAG-depleted aortic samples from the (A) AS, (B) AR, and (C) DT regions. Results are presented as mean ± SD (n=5 tests from $N_4$=5 animals). This figure represents the detailed data of Figure 4, in which the data is presented as mean ± SEM.*

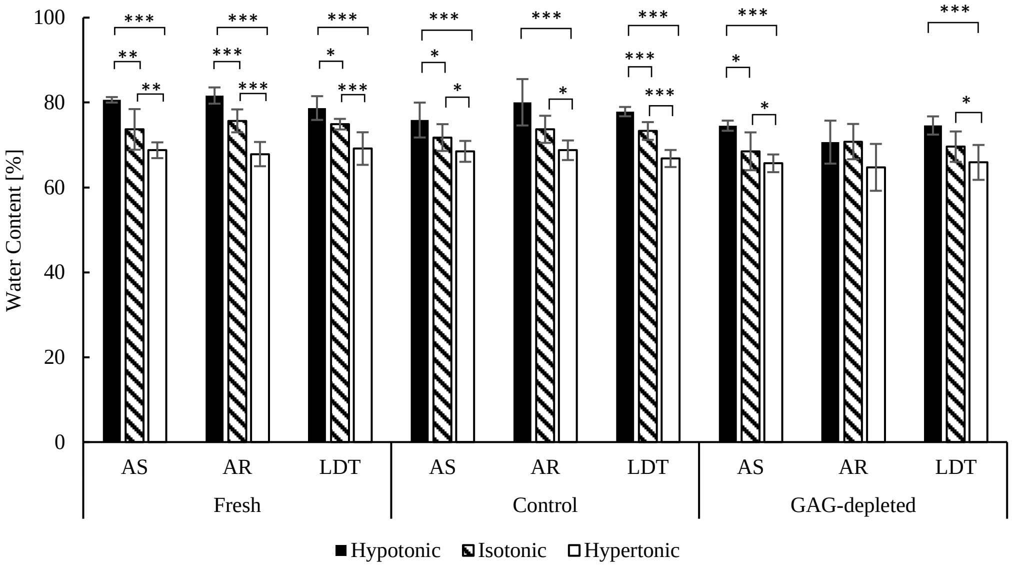

*Figure S6.7: Water content (mean ± SD) of fresh, control and GAG-depleted aortic rings, presented to visualize differences between the external bath osmolarity from each of the AS, AR and LDT regions; n=8 samples per region ($N_5$=8 animals). *** indicates p<0.001, ** indicates p<0.01, * indicates p<0.05 (ANOVA with Tukey Post-hoc test). Note: the data in this figure is identical to Figure 5A in the manuscript, but organized differently to allow us to present significance bars between osmolarities in a clear manner.*

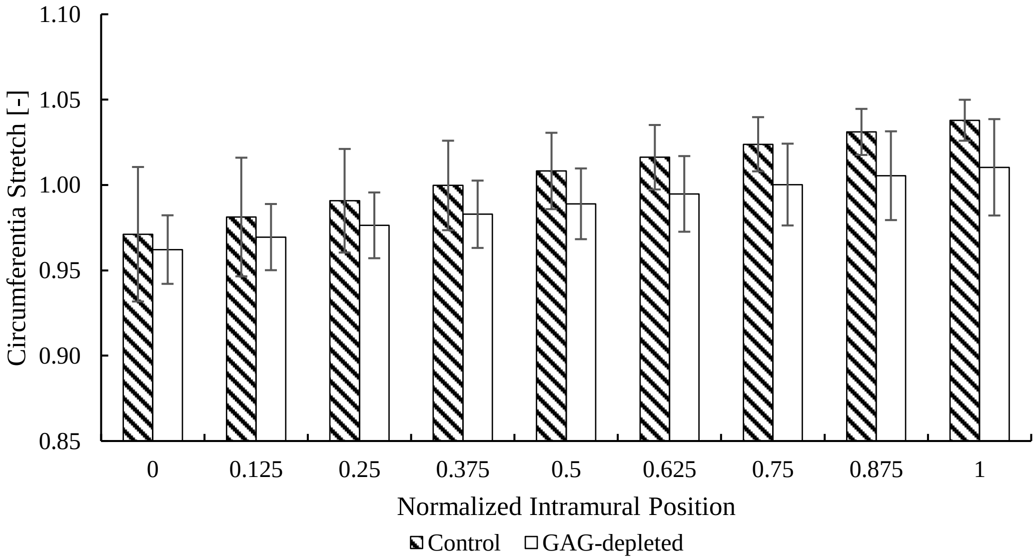

*Figure S6.8: Circumferential stretch from the unstressed to the unloaded configuration at 8 positions of the aortic wall of control and GAG-depleted aortic rings of the AR region. Position 0.0 along the x-axis refers to the innermost intima and position 1.0 refers to the outermost adventitia, Results are presented as mean ± SD ($N_1$=5 animals).*

# 7

# HOW MUCH OPENING ANGLE DOES THE SWELLING OF GAG CONTRIBUTE IN PORCINE AORTAS? FINITE ELEMENT ANALYSES BASED ON EXPERIMENTAL DATA

Noor Ghadie [a], Jean-Philippe St-Pierre [b], Michel R. Labrosse [a,c]

[a] Mechanical Engineering Department, University of Ottawa, Ottawa, ON. Canada K1N6N5

[b] Chemical and Biological Engineering Department, University of Ottawa, Ottawa, ON. Canada K1N6N5

[c] Department of Cardiac Surgery, University of Ottawa Heart Institute, Ottawa, ON. Canada K1Y4W7

Content of this chapter prepared for submission

## 7.1 FOREWORD

With the computational framework established in Chapter 4, and the experimental data collected throughout Chapters 5 and 6, we strengthened the foundations for constructing a more reliable computer model and overcome the limitations that were associated with the initial simulations. This will enable us to rigorously assess the model's accuracy in reproducing experimental results. The framework established in Chapter 4 will be used to establish computer aortic rings from the three main regions (ascending, arch, and descending thoracic) investigated in Chapters 5 and 6. We are better positioned to use the respective geometries and intramural GAG distributions acquired from the experimental tests, and evaluate the output by comparing the simulated opening angle to the experimental observations. However, another challenge is modelling the solid matrix. To address this, we will also focus on implementing a relevant constitutive model, which entails employing optimization techniques to determine material constants specific to each of the regions. Nevertheless, the aortic wall is made of several layers which are believed to possess distinct mechanical behavior, which we aim to account for by modeling the solid matrix as two layers, representing the intima-media and the adventitia. Additionally, we will also assess the distinct mechanical behaviors of the intima-media and adventitia considering the scarcity and conflicting nature of information available in the literature.

## 7.2 ABSTRACT

Recent studies have identified an effect of glycosaminoglycans (GAG) on residual stress in the aorta, underscoring the need to better understand their biomechanical roles. In this work, three aortic rings models for each of the ascending, arch and descending thoracic regions of the porcine thoracic aorta were modelled using FEBio, using a framework that combines the Donnan

osmotic swelling in a solid matrix of hydrated charged tissue. The fixed charge densities (FCDs) were prescribed as they were calculated from experimentally quantified sulfated GAG mural distributions. A Holmes-Mow constitutive law was used for the solid matrix, for which material parameters were optimized using data from biaxial tensile tests. In addition to modelling the solid matrix as one layer, two layers were considered to capture the differences between the intima-media and the adventitia, for which various stiffness ratios were explored. The simulated opening angles of rings charged with GAG FCDs were respectively 37 deg, 17 deg, and 10 deg for the ascending, arch and descending thoracic regions when using one layer for the solid matrix, with respective errors of 28%, 15% and 23% compared to the experimental contribution of GAG to the opening angle. When using two layers for the solid matrix, the smallest errors in the ascending and arch regions were 21% and 5% when the intima-media was modelled as 10 times stiffer, and as twice stiffer than the adventitia, respectively, and 23% in the descending thoracic regions when the intima-media and adventitia shared similar properties.

## 7.3 INTRODUCTION

The existence of circumferential residual stresses in blood vessels was revealed in the 1980's, when Vaishnav and Vossoughi [1], and Chuong and Fung [2] showed that a radial cut through the vessel's wall in the unloaded state causes it to spring open. The open state of a tubular shaped aortic segment can be characterized by the opening angle. In the case of the aorta, knowledge of residual stresses is important for several reasons. First, their relief, such as approximated by a radial cut, provides an unloaded reference geometry from which the mechanical stresses and strains can be calculated [2], [3]. Secondly, residual stresses are thought to ensure a homogeneous distribution of the *in vivo* mechanical stresses across the aortic wall [2], [4]. Finally, understanding the mechanisms causing alterations in residual stresses is of prime interest as it may provide insights into aortic pathogenesis [5], [6]. It is therefore widely accepted that inclusion of residual stresses in computational models is of paramount importance to obtain an accurate assessment of the *in vivo* mechanical stress field of the tissue.

The development of computational models also requires the use of constitutive equations to describe the mechanical response of the tissue to loading. *In silico* models may consider one or multiple layers of the aortic wall [7]–[9], whereby using multiple layers allows one to account for the distinct mechanical properties that the different layers of the aortic wall may exhibit [10], [11]. The main layers of the aortic wall are the intima (the innermost layer from the lumen), the media (the middle layer) and the adventitia (the outermost layer). These layers occupy different proportions of the aortic wall at different locations along its tree [12], and contain a mixture of cells along with a well organized extracellular matrix (ECM). The ECM of the aortic wall is mainly comprised of elastin, collagen and glycosaminoglycans (GAG). The content and organization of the ECM components vary throughout the aortic wall thickness. For instance, while the collagen content increases from the intima to the adventitia and the GAG content decreases, elastin exists in its highest levels in the media [13]. In addition, these ECM constituents influence the mechanical properties of the aorta, such as stiffness [14]–[16], and residual stresses [4], [17].

Different methods for incorporating residual stresses in computational models have been established. The most common methods have focused on either setting a known opening angle [7], [18], [19], or incorporating ad-hoc local prestretches [20]–[22]. On the one hand, knowledge of the opening angle allows one to determine the residual stress field by putting the opened sector back into a closed tubular shape, or in other words, by mapping the open unstressed configuration to the closed unloaded state. On the other hand, the residual stress field can be created via the inclusion of *in situ* prestretches, which have been associated to the fibrous components on the ECM, elastin and collagen. However, recent evidence shows that it may be possible to recover the opening angle computationally via the inclusion of fixed charge densities (FCDs) to model the Donnan swelling of GAG [23]. Due to the lack of comprehensive data on one single type and age of a given animal, this previous study was limited to incorporating composite information from different sources. In addition, no recent efforts have been made to evaluate the feasibility of using Donnan swelling to recover the unloaded, but residually stressed configuration of an aortic ring.

We recently demonstrated that GAG content and gradient in the aorta strongly correlate with its opening angle [13], and that enzymatic removal of GAG yields a significant reduction in the opening angle of the porcine aorta in the ascending, arch, and descending thoracic regions (*Chapter 6*). Specifically, in *Chapter 6* we demonstrated that GAG contribute to approximately 25%, 32%, and 42% in the ascending, aortic arch, and lower descending thoracic regions respectively. Therefore, it is expected that the simulated opening angles would better recover the experimental contribution of GAG to the opening angle (corresponding to the difference in opening angle – which will be referred to as "Delta" in this document – before and after GAG depletion in *Chapter 6*), rather than recover the full opening angle. In addition, we characterized the mural distribution of sulfated GAG (sGAG) in these 3 regions of the aorta [13], and performed biaxial tests on samples excised from the same regions [16]. Using these previously published experimental parameters obtained from the porcine animals by our team, our aims, in the present study, were to (1) corroborate our prior experimental findings on the contribution of GAG to residual stress through *in silico* modelling, (2) evaluate the reliability of using the Donnan osmotic swelling mathematical law to illustrate the contribution of GAG to the opening angle computationally, and (3) evaluate the opening angle response in models using one layer for the solid matrix versus two layers, in order to illustrate the possible impact of differences in mechanical properties between the intima bundled with the media, and the adventitia.

## 7.4 METHODS

### 7.4.1 General framework

In this work, we used a mixture-based finite element model using FEBioStudio Version 1.7 [24] (https://febio.org/). The mixture combined a porous solid matrix and a Donnan equilibrium swelling material with a fluid phase which describes the presence of fixed-charge densities (FCDs), illustrating the negative charges of GAG. The Cauchy stress tensor $\boldsymbol{\sigma}$ associated with the Donnan equilibrium swelling material is given in [23]:

$$\boldsymbol{\sigma} = -\pi \boldsymbol{I}$$

where $I$ is the identity tensor, and the osmotic pressure $\pi$ is:

$$\pi = RT\Phi\left(\sqrt{(c^F)^2 + (\bar{c}^*)^2} - \bar{c}^*\right)$$

In the latter equation, $R$ is the universal gas constant, $T$ is the temperature, $\Phi$ is the osmotic coefficient and is equal to 1 for ideal Donnan law, $\bar{c}^*$ is the external bath osmolarity, and $c^F$ is the proteoglycan FCD in the current configuration and relates to the reference configuration via the equation below:

$$c^F = \frac{\varphi_0^\omega}{J - 1 + \varphi_0^\omega} c_0^F$$

where $J$ is the relative volume and $\varphi_0^\omega$ and $c_0^F$ are the fluid volume fraction and FCD in the reference configuration respectively.

This approach was used to model aortic rings from the ascending, aortic arch and descending thoracic regions of porcine aortas from 5- to 6-months old animals harvested in our lab in previous studies (cf. [13], *Chapter 6*). The approach was directly adapted from [23], in which residual stresses in rodent tissue were studied, and by comparison with which we previously validated our model in [25]. The rings were assumed to be bathing in a solution at physiological osmolarity of 300 mosM. They were meshed using 20-node quadratic hexahedral elements, with 8 elements across the aortic wall thickness, 40 elements along the circumference of the ring, and 8 elements along the ring height (i.e. aortic slice thickness). Only one-quarter of a ring was modelled, with appropriate boundary conditions to represent symmetry, and the radial cut on one side, as shown in Figure 7.1. Convergence of solutions was verified using a classical mesh sensitivity analysis. Parameters for geometry, FCD distributions and mechanical behaviour of the solid matrix for each of the ascending, aortic arch, and descending thoracic (from in between the 3rd and 5th intercostal arteries) rings were acquired from previous experiments carried out in our lab [13], [16], as described next.

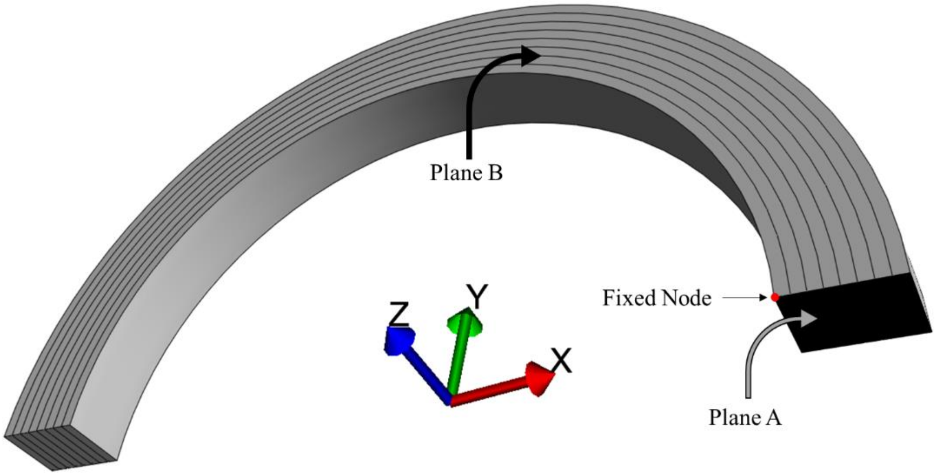

*Figure 7.1: Representative quarter aortic ring geometry (for symmetry) from the ascending region displaying boundary conditions. Plane A is fixed in the y-direction, plane B is fixed along the z-direction, and the fixed node is constrained in all directions.*

### 7.4.2 Geometry

The model parameters described in this section were averaged from a total of 15 rings per region from 5 porcine aortas that we investigated in [13]. The outer diameters and thicknesses of the computer ring models for each of the ascending, aortic arch and descending thoracic regions are summarized in Table 7.1, and a ring height of 4.5 mm was used for all 3 models.

*Table 7.1: Outer diameter and thickness (mm) used in the computer models of rings from the ascending, arch and descending thoracic regions averaged from 15 porcine aortic rings in [13].*

| **Region** | **Outer Diameter (mm)** | **Mural Thickness (mm)** |
|---|---|---|
| Ascending | 25.5 | 2.68 |
| Arch | 22.0 | 2.56 |
| Descending Thoracic | 17.6 | 1.82 |

### 7.4.3 FCD Distribution

The average sGAG masses were interpolated across 8 equally sized domains through the wall thickness (corresponding to as many elements in the computer model) using quantitative normalized sGAG measurements published in [13] (cf. Figure 3b), where the intramural sGAG distribution in the ascending, aortic arch, and descending thoracic regions of porcine aorta was measured using a DMMB spectrophotometric assay on slices cryo-sectioned from the aortic wall. This allowed us to compute the FCD distributions in each of the ascending, aortic arch, and descending thoracic regions (see Table 7.2) using the formula [23]:

$$c^F = \frac{GAG\ charge\ number}{GAG\ molecular\ weight} \times \frac{GAG\ mass}{water\ volume}$$

Consistent with [23], each chondroitin sulfate isomer was assumed to have a molecular weight of 513 g/mol with two negative charges. The water content was assumed to be 70%.

*Table 7.2: Fixed charge densities [mEq/L] in aortic wall domains for each of the ascending, arch, and descending thoracic ring models.*

| Mural Position | Ascending | Arch | Descending Thoracic |
|---|---|---|---|
| 1 | -35.3 | -25.3 | -19.4 |
| 2 | -32.1 | -20.5 | -16.8 |
| 3 | -29.6 | -17.4 | -17.8 |
| 4 | -25.8 | -16.2 | -17.9 |
| 5 | -21.7 | -14.9 | -15.7 |
| 6 | -19.9 | -14.2 | -14.3 |
| 7 | -18.1 | -12.9 | -12.7 |
| 8 | -15.0 | -9.7 | -9.0 |

### 7.4.4 Aortic Layers

The proportions of the intima-media and adventitia in each of the investigated anatomical regions were obtained from samples procured from 4 porcine aortas. Samples were excised from each of the ascending, arch, and descending thoracic regions and were fixed in 10% formalin solution for 72 hours, then transferred to 70% ethanol. Samples then underwent a series of dehydration in water-ethanol, after which they were cleared with xylene and infiltrated with molten paraffin wax. Samples were then cut into 4 $\mu$m-thick sections and stained with a Verhoeff's-VanGieson elastic stain. Scanned slices (Figure 7.2) were then viewed with Zen 3.3 (blue edition), from which input images with calibration scale bars were generated and processed using Matlab R2020a, to obtain the respective intima-media proportion. The media was found to occupy 90 ± 3%, 76 ± 7%, and 66 ± 6% of the aortic wall thickness in the ascending, aortic arch, and descending thoracic regions, respectively (Table 7.3). Therefore, to represent the thickness of the intima-media in our computer models, we used 7 elements in the ascending region (88% of the aortic wall), 6 elements in the aortic arch region (75% of the aortic wall), and 5 elements (63% of the aortic wall) in the descending thoracic region.

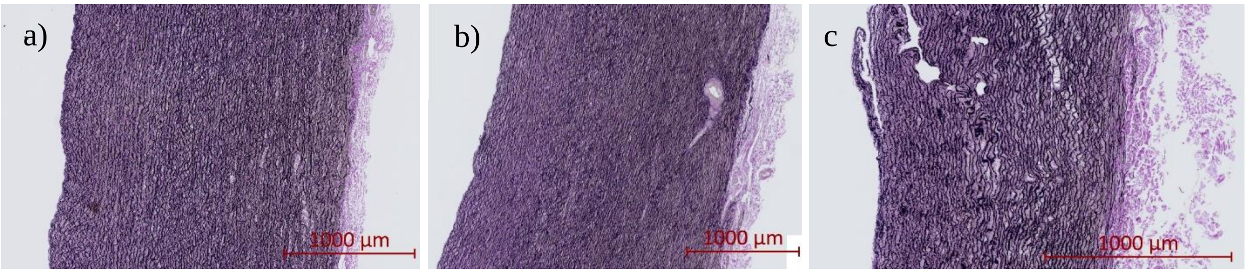

*Figure 7.2: Representative histology sections of aortic tissues from (a) the ascending, (b) aortic arch, and (c) descending thoracic aorta, stained with Verhoeff's-VanGieson's. Intimal layers are aligned with the left side of each panel.*

*Table 7.3: Intima-media proportion measured from 4 porcine aortas.*

| Aorta | Intima-Media Proportion [%] | | |
|---|---|---|---|
| | Ascending | Arch | Descending Thoracic |
| 1 | 90 | 67 | 64 |
| 2 | 86 | 77 | 60 |
| 3 | 90 | 85 | 70 |
| 4 | 93 | 76 | 72 |
| Average | 90 | 76 | 66 |
| Standard Deviation | 3 | 7 | 6 |

### 7.4.5 Solid Matrix

#### *7.4.5.1 Constitutive Modeling*

Experimental 2nd P-K membrane tension vs. Green strain curves obtained from planar biaxial tensile tests performed in another independent study on similar tissues in [16] were used to fit constitutive models to describe the solid matrix. A total of 9 samples per region acquired from 9 animals were used. One sample from each of the ascending and descending thoracic regions did not display appropriate stress-stretch curves and was eliminated from the curve-fitting process. A total of 9 equibiaxial and non-equibiaxial stretching protocols were used, as detailed previously in [26]. A Holmes-Mow [27] constitutive law was used to model the solid matrix and is given by:

$$W = \frac{1}{2}c(e^{Q} - 1)$$

$$c = \frac{\lambda + 2\mu}{2\beta}$$

$$Q = \frac{\beta}{\lambda + 2\mu}[(2\mu - \lambda)(I_1 - 3) + \lambda(I_2 - 3) - (\lambda + 2\mu)\ln J^2]$$

In these equations, $I_1$ and $I_2$ are the first and second invariants of the right Cauchy-Green tensor, $\lambda$ and $\mu$ are the Lamé parameters, $\beta$ is an exponential stiffening coefficient, and $J$ is the determinant of the deformation gradient. Since the modeling framework consists of a fluid phase is addition to a solid phase, we imposed $\lambda = 0$ to ensure a Poisson's ratio of zero [28]. However, given the equivalence between the response of an incompressible material and that of a biphasic material under short time loading [28], we also imposed $J = 1$. This equivalence between a short time biphasic response and an incompressible elastic material was introduced by Ateshian et al. [28]: upon sudden loading, except at the boundaries, the pores change in shape, not volume, as the interstitial fluid does not have time to leave the tissue. Under such conditions, the divergence of the fluid flux is null and the equations for the Cauchy stress tensor, conservation of mass and conservation of linear momentum become identical for both biphasic and incompressible elastic responses, as well as the boundary condition except for the pressure at the boundaries. This assumption was possible in this context, as the phenomenon we were evaluating was quasi-instantaneous, both numerically and physically.

The equations therefore reduced to $W = \frac{\mu}{2\beta}(e^Q - 1)$, where $Q = \beta(I_1 - 3)$. Therefore, two material constants, $\mu$>0 and $\beta$>0, were fitted according to the protocol outlined in [26]. Briefly, the objective function $\left\| |T^S_{11\_exp} - T^S_{11\_theo}| + |T^S_{22\_exp} - T^S_{22\_theo}| + |T^S_{12\_exp} - T^S_{12\_theo}| \right\|$ was minimized, where $T^S$ represents the 2nd P-K membrane tension from experimentally ($\_exp$) and theoretically ($\_theo$) derived membrane tensions, via tensor

$$\overline{\overline{\boldsymbol{T^S}}} = \begin{bmatrix} \partial w/\partial E_{11} & \partial w/\partial E_{12} & 0 \\ \partial w/\partial E_{21} & \partial w/\partial E_{22} & 0 \\ 0 & 0 & 0 \end{bmatrix}$$

In this expression, $w = H\widehat{W}$, where H is the undeformed thickness, and $\widehat{W}$ is a reduced function of $W$ as follows. Given that the shear strains are minimal, and using the incompressibility assumption $J = \det F = 1$, which makes it possible to express $E_{33}$ in terms of $E_{11}$ and $E_{22}$, we can indeed introduce a reduced strain energy density function such that $\widehat{W} = \widehat{W}(E_{11}, E_{22}) = W(E_{11}, E_{22}, E_{12}, E_{33})$. This allowed us to express the Holmes-Mow constitutive model as a function of $E_{11}$, and $E_{22}$ only, such that $\widehat{W} = \frac{\mu}{2\beta}(e^{Q} - 1)$, where $Q = 2\beta\left(E_{11} + E_{22} + \frac{1}{2}\left[\frac{1}{\Delta} - 1\right]\right)$ and $\Delta = (2E_{11} + 1)(2E_{22} + 1)$. Therefore, the theoretical 2nd P-K membrane tensions were derived as:

$$T^{S}_{11\_theo} = \mu\left[1 - \frac{1}{\Delta(2E_{11} + 1)}\right]e^{Q}$$

$$T^{S}_{22\_theo} = \mu\left[1 - \frac{1}{\Delta(2E_{22} + 1)}\right]e^{Q}$$

$$T^{S}_{12\_theo} = 0.$$

Of note, $E_{11}$ is along the fiber (circumferential) direction, and $E_{22}$ is along the cross fiber (longitudinal) direction.

#### *7.4.5.2 Two-layer material modelling*

In addition to modelling the aortic wall as one layer, we also implemented a two-layered model for the solid matrix to represent the distinct mechanical behaviors of the media-intima (inner layers) and the adventitia (outer layer) of the aorta. This was carried out in the framework developed in [26], which was used for material parameter optimization as described in Section 7.4.5.1. Consider the two intimal-medial $(M)$ and adventitial $(A)$ layers with undeformed thicknesses $H_M$ and $H_A$ in the reference configurations, such that $H = H_M + H_A$. Herein, four positive material parameters $\mu_M$, $\beta_M$, $\mu_A$,and $\beta_A$ were considered, such that $\widehat{W_M} = \frac{\mu_M}{2\beta_M}(e^{Q_M} - 1)$

and $\widehat{W_A} = \frac{\mu_A}{2\beta_A}(e^{Q_A} - 1)$ , with $Q_M = 2\beta_M\left(E_{11} + E_{22} + \frac{1}{2}\left[\frac{1}{\Delta} - 1\right]\right)$ , $Q_A = 2\beta_A\left(E_{11} + E_{22} + \frac{1}{2}\left[\frac{1}{\Delta} - 1\right]\right)$ and $\Delta = (2E_{11} + 1)(2E_{22} + 1)$.

The four constants were optimized by minimizing the objective function introduced in Section 7.4.5.1. The experimental 2nd P-K membrane tensions were

$$T^S_{11\_\exp\_A} = \frac{H_A}{H} T^S_{11\_\exp}$$

$$T^S_{22\_\exp\_A} = \frac{H_A}{H} T^S_{22\_\exp}$$

$$T^S_{12\_\exp\_A} = \frac{H_A}{H} T^S_{12\_\exp}$$

such that

$$T^S_{11\_\exp\_A} + T^S_{11\_\exp\_M} = \frac{H_A}{H} T^S_{11\_\exp} + \frac{1 - H_A}{H} T^S_{11\_\exp} = T^S_{11\_\exp}$$

$$T^S_{22\_\exp\_A} + T^S_{22\_\exp\_M} = T^S_{22\_\exp}$$

$$T^S_{12\_\exp\_A} + T^S_{12\_\exp\_M} = T^S_{12\_\exp}$$

The theoretical 2nd P-K membrane tensions can be derived from the respective strain energy density functions of layers $M$ and $A$ , $w_M = H_M\widehat{W_M}$ and $w_A = H_A\widehat{W_A}$ , such that $\overline{\overline{\boldsymbol{T^S}}} = \partial w/\partial E$ , and $w = w_M + w_A$ . The values for $H_M$ and $H_A$ for computing the required material parameters for FEBio were calculated from the total thicknesses of the 9 aortas that underwent biaxial tensile testing, which were approximately 2.00 mm, 1.96 mm and 1.40 mm in the ascending, arch, and thoracic regions, respectively. However, since the behaviors of the 2 layers may differ even if they possess equal thicknesses, a factor $r = \frac{\mu_A}{\mu_M}$ was introduced to scale the stiffness of the adventitia with respect to that of the media. The fixed relationship between $\mu_A$ and $\mu_M$ was used as a constraint during the material constant identification process. Given that conflicting results have been reported with respect to the behavior of the media and adventitia [9]–[11], [29]–[31], we explored $r$ ratios of 0.1, 0.2, 0.5, 1, 2, 5 and 10.

### 7.4.6 Statistical analysis

Results are reported as mean ± standard deviation. The material parameters were determined in MATLAB using nonlinear multivariate optimization, at the 95% (2-tailed) confidence interval (CI) with their Pearson correlation coefficient.

### 7.4.7 Model evaluation

The computer models were evaluated by comparing simulated opening angles to experimental ones in [13] and *Chapter 6*, as detailed in the discussion.

## 7.5 RESULTS

### 7.5.1 Material Constants

#### *7.5.1.1 One-Layer Matrix*

The material constants obtained from use of all 9 stretching protocols for a one-layer solid matrix are summarized in Table 7.4. The Pearson's correlation coefficients for a one-layered model were all above 0.93 in all directions and for all the aortic regions considered, reflecting an overall good match between the experimental and predicted theoretical data. Representative graphs are provided in Supplemental Figures S7.1-S7.5.

*Table 7.4: Holmes-Mow material parameters (mean ± standard deviation) derived from all protocols for a one-layer solid matrix. $R^2$-FD and $R^2$-XD are the Pearson correlation coefficients between the experimental and predicted membrane tensions in the fiber direction and cross-fiber directions respectively.*

| Region | Ascending | Aortic Arch | Descending Thoracic |
|---|---|---|---|
| $\mu$ [N/m] | 61.31 ± 1.45 | 65.99 ± 1.63 | 58.90 ± 1.46 |
| $\beta$ [-] | 2.09 ± 0.06 | 2.56 ± 0.08 | 2.37 ± 0.07 |
| $R^2$-FD | 0.94 | 0.94 | 0.93 |
| $R^2$-XD | 0.94 | 0.94 | 0.95 |

#### *7.5.1.2 Two-Layer Matrix*

Material parameters for the intima-media and adventitia were also obtained using a two-layer model and are summarized in Tables 7.5-7.7 for each of the ascending, aortic arch, and descending thoracic regions. Not all ratios $r$ between the stiffness of the adventitia and media yielded acceptable curve fits. In the ascending region (Table 7.5), the best curve fits between the experimental and theoretical curves were achieved when $r$ was 0.1, 0.2, and 0.5, with Pearson's correlation coefficients 0.93 or above. The worst curve fits between experimental and theoretical curves were achieved when $r$ was 2, 5, and 10, with Pearson's correlation coefficients in the range of 0.76-0.87. In the aortic arch region, the best curve fits were achieved when $r$ was 0.1, 0.2, 0.5 and 1, with Pearson's correlation coefficients 0.93 or above, and the worst curve fits were observed when $r$ was 5 and 10. Finally, in the descending thoracic region, the best curve fits were achieved when $r$ was 0.2, 0.5, 1 and 2, with Pearson's correlation coefficients 0.94 or above.

*Table 7.5: Holmes-Mow material parameters derived from all protocols for the media and adventitia of a two-layer solid matrix in the ascending region, where the media occupied 88% of the aortic wall. $R^2$-FD and $R^2$-XD are the Pearson correlation coefficients between the experimental and predicted membrane tensions in the fiber direction and cross-fiber directions respectively.*

| $r$ | Media | | Adventitia | $R^2$-FD | $R^2$-XD |
|---|---|---|---|---|---|
| | $\mu_M$ [N/m] | $\beta_M$ [-] | $\beta_A$ [-] | | |
| **0.1** | **55.65 ± 1.29** | **2.00 ± 0.06** | **2.77 ± 0.08** | **0.94** | **0.94** |
| **0.2** | **50.88 ± 1.25** | **2.20 ± 0.06** | **1.49 ± 0.06** | **0.94** | **0.94** |
| **0.5** | **38.99 ± 1.24** | **2.75 ± 0.08** | **0.00 ± 0.10** | **0.93** | **0.94** |
| 1 | 23.85 ± 1.23 | 3.85 ± 0.11 | 0.00 ± 0.12 | 0.90 | 0.91 |
| 2 | 11.92 ± 1.07 | 5.27 ± 0.19 | 0.00 ± 0.12 | 0.86 | 0.87 |
| 5 | 4.20 ± 0.71 | 7.17 ± 0.33 | 0.00 ± 0.10 | 0.80 | 0.80 |
| 10 | 1.95 ± 0.47 | 8.50 ± 0.46 | 0.00 ± 0.10 | 0.76 | 0.76 |

*Table 7.6: Holmes-Mow material parameters derived from all protocols for the media and adventitia of a two-layer solid matrix in the aortic arch region, where the media occupied 75% of the aortic wall. $R^2$-FD and $R^2$-XD are the Pearson correlation coefficients between the experimental and predicted membrane tensions in the fiber direction and cross-fiber directions respectively.*

| $r$ | Media | | Adventitia | $R^2$-FD | $R^2$-XD |
|---|---|---|---|---|---|
| | $\mu_M$ [N/m] | $\beta_M$ [-] | $\beta_A$ [-] | | |
| **0.1** | **57.36 ± 1.35** | **2.14 ± 0.07** | **5.40 ± 0.16** | **0.93** | **0.93** |
| **0.2** | **54.44 ± 1.30** | **2.28 ± 0.07** | **3.64 ± 0.10** | **0.94** | **0.94** |
| **0.5** | **43.30 ± 1.18** | **2.90 ± 0.08** | **1.82 ± 0.07** | **0.94** | **0.94** |
| **1** | **33.79 ± 1.19** | **3.49 ± 0.10** | **0.34 ± 0.11** | **0.93** | **0.94** |
| 2 | 19.88 ± 1.16 | 4.88 ± 0.16 | 0.00 ± 0.12 | 0.91 | 0.92 |
| 5 | 7.80 ± 0.90 | 7.12 ± 0.28 | 0.00 ± 0.12 | 0.86 | 0.86 |
| 10 | 3.75 ± 0.66 | 8.71 ± 0.41 | 0.00 ± 0.12 | 0.82 | 0.83 |

*Table 7.7: Holmes-Mow material parameters derived from all protocols for the media and adventitia of a two-layer solid matrix in the descending thoracic region, where the media occupied 63% of the aortic wall. $R^2$-FD and $R^2$-XD are the Pearson correlation coefficients between the experimental and predicted membrane tensions in the fiber direction and cross-fiber directions respectively.*

| $r$ | Media | | Adventitia | $R^2$-FD | $R^2$-XD |
|---|---|---|---|---|---|
| | $\mu_M$ [N/m] | $\beta_M$ [-] | $\beta_A$ [-] | | |
| 0.1 | 45.75 ± 1.06 | 1.86 ± 0.07 | 6.06 ± 0.21 | 0.90 | 0.93 |
| **0.2** | **45.98 ± 1.06** | **1.85 ± 0.07** | **4.51 ± 0.13** | **0.92** | **0.94** |
| **0.5** | **39.33 ± 0.95** | **2.18 ± 0.07** | **2.68 ± 0.07** | **0.93** | **0.95** |
| **1** | **28.60 ± 0.86** | **2.98 ± 0.08** | **1.78 ± 0.07** | **0.93** | **0.95** |
| **2** | **19.05 ± 0.87** | **3.92 ± 0.11** | **0.98 ± 0.08** | **0.92** | **0.94** |
| 5 | 8.45 ± 0.76 | 5.71 ± 0.20 | 0.62 ± 0.09 | 0.89 | 0.91 |
| 10 | 3.55 ± 0.54 | 7.47 ± 0.32 | 1.17 ± 0.08 | 0.85 | 0.87 |

### 7.5.2 Opening Angle

#### *7.5.2.1 One-Layer Matrix*

Open ring models for each of the ascending, aortic arch, and descending thoracic regions using one layer for the solid matrix are shown in Figure 7.3, and the corresponding simulated opening angles are summarized in Table 7.8.

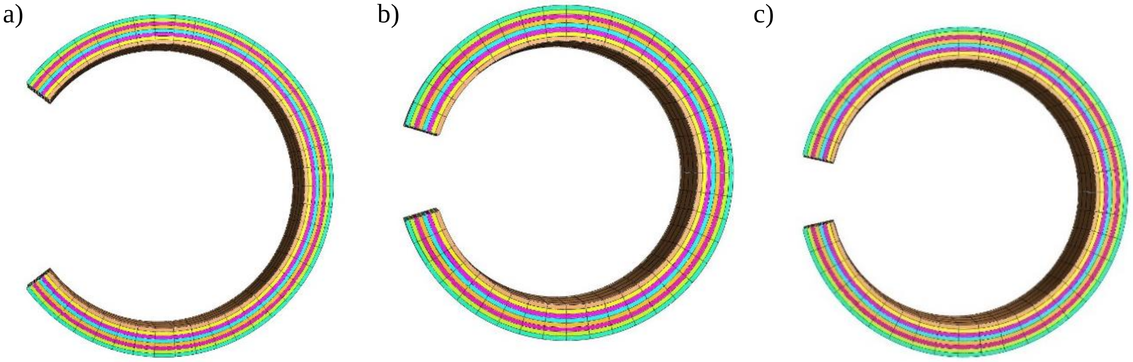

*Figure 7.3: Open aortic rings (1/2 model) of the (a) ascending, (b) aortic arch, and (c) descending thoracic regions.*

*Table 7.8: Simulated opening angle results in the ascending, aortic arch, and descending thoracic regions, using a one-layer solid matrix.*

| Region | Ascending | Aortic Arch | Descending Thoracic |
|---|---|---|---|
| Opening Angle [degrees] | 37 | 17 | 10 |

#### *7.5.2.2 Two-Layer Matrix*

The simulated opening angles in each of the ascending, arch, and descending thoracic two-layered matrix models, for each of the respective stiffness ratios $r$ that were tested are summarized in Table 7.9. As shown, the opening angle increases with r in all regions.

*Table 7.9: Simulated opening angle results in the ascending, aortic arch, and descending thoracic regions, using a two-layer solid matrix. The opening angles for r ratios that generated curve fits with Pearson's correlation coefficients above 0.93 are bolded, whereas the others are in italics.*

| $r$ | Opening angle [degrees] | | |
|---|---|---|---|
| | Ascending | Arch | Descending Thoracic |
| 0.1 | **35** | **10** | *-7* |
| 0.2 | **40** | **13** | **-1** |
| 0.5 | **54** | **21** | **8** |
| 1 | *76* | **28** | **16** |
| 2 | *105* | *43* | **27** |
| 5 | *141* | *75* | *52* |
| 10 | *160* | *99* | *82* |

## 7.6 DISCUSSION

In this study, animal-specific rings from the ascending, aortic arch, and descending thoracic regions of porcine aortas were modelled as solid matrices with embedded FCDs to simulate the effect of GAG on the opening angle. Parameters for ring dimensions, FCDs, and the solid matrix were consistently obtained from experimental testing of porcine thoracic aortas from animals aged 5-6 months and weighing approximately 90-100 kg. It is important to note that the FCDs in these models, due to limitations in our experimental techniques, only account for the swelling effect of sulfated GAG. The FCDs were prescribed in 8 equally sized domains through the aortic wall, and were calculated using previously experimentally quantified GAG distributions [32]. Overall, the FCD distribution in all investigated regions of the aortic tree decreased from the inner layers to the outer layers. The rings' responses were evaluated in one- and two-layered solid matrices to simulate the difference in mechanical behavior between the intima-media and the adventitia of the aortic wall. The proportion of the intima-media with respect to the aortic thickness was obtained using histological sections from each of the ascending, arch, and descending thoracic regions, and was found to occupy approximately 90%, 76%, and 66%, respectively. These are similar to results reported by Sokolis [12] who measured the mean thickness of the intima-media at different anatomical locations of the aortic tree (cf. Figure 5A in [12]), where, however, the intima-media occupied a smaller proportion in the ascending region compared to our animals. Specifically, the intima-media occupied approximately ~78% in the ascending, ~70-88% in the arch, and ~50-80% in the thoracic region, as estimated from the original graphs. The mid-thoracic region in [12], in which the intima-media occupied about 70% of the aortic wall, best aligned with the descending thoracic region described in our study. The intima-media proportions were also evaluated in the thoracic region by other researchers, with Peña et al. [11] reporting that the intima and media occupy approximately 73% and 64% in the upper (end of arch to 4th intercostal artery) and lower descending thoracic regions, respectively, and Guidici and Spronck [8] reporting that the intima and media occupy around 69% of the wall thickness of the porcine thoracic aorta, which are also in line with our findings.

In addition to having different proportions in the aortic wall along the aortic tree, the intima-media and adventitia also possess different elastic properties [9]–[11], [29]–[31]. However, it remains unclear whether the adventitia is stiffer or more compliant than the intima-media in tension, and whether differences are consistent along the aortic tree. Previous numerical calculations have been based on the assumption that the media is approximately 10 times stiffer than the adventitia [9], which is associated with experimental observations in [29]–[31]. Yu et al. [31] showed that the intima-media of the porcine aorta is stiffer than the adventitia by one order of a magnitude, and Xie et al. [30] found that the intima-media of blood vessels is 3 to 4 times stiffer than the adventitia. Our results are in line with these findings in that, in most cases, better curve fits were obtained when the intima-media was stiffer than the adventitia, except in the descending thoracic region, where both stiffer and softer behaviors provided satisfactory results. Specifically, our model optimization suggested that in the ascending region, the adventitia was more compliant than the intima-media, given that best curve fits were obtained when $r$ was 0.1, 0.2, and 0.5. Similar findings were obtained in the arch region, which however, also displayed good curve fits when $r$ was 1, suggesting that the adventitia could be more compliant than the intima-media, or share similar elastic properties. In the descending thoracic region, best curve fits were observed when $r$ ranged from 0.2 and 0.5 to 1 and 2, indicating that both stiffer and softer behaviors were plausible. Recent biaxial tensile testing performed by Peña et al. [11] and Amabili et al. [10] in the descending thoracic aorta of porcine and human aortas, respectively, suggested that the adventitia is stiffer than the media. Our curve fits in the descending thoracic region reflected both findings in [29]–[31] and [10], [11], suggesting that either both behaviors of the intima-media versus the adventitia are possible, or that more work is needed to settle this issue.

The opening angle simulated in both one- and two-layered solid matrices was found to decrease from the ascending to the descending thoracic region, which is in line with experimental observations [12], [13]. The model results were evaluated by comparing the simulated opening angles to experimental opening angles evaluated in two previous studies [13], *Chapter 6*. Figure 7.4 summarizes the opening angle results obtained using the one-layered solid matrix with experimental results from [13], and *Chapter 6*. From [13], we considered 15 fresh rings per region from the porcine animals that were studied. The experimental opening angles in each of the ascending, aortic arch, and descending thoracic regions were approximately 156 ± 33 deg, 104 ± 19 deg, and 67 ± 31 deg, respectively (denoted as "Exp1" in Figure 7.4). Herein, the simulated opening angles of models using one layer for the solid matrix were 37 deg, 17 deg, and 10 deg in the ascending, arch, and descending thoracic regions, respectively (denoted as "Sim1" in Figure 7.4), accounting for 24%, 16%, and 15% of the experimental opening angles ("Exp1").

In contrast to conclusions in [23], simulated values did not readily yield values in the range of the experimental opening angles.

In another study (*Chapter 6*), we evaluated 5 sets of adjacent rings per region from 5 porcine animals. In each set, one ring was a control and did not undergo any alterations in the ECM, while the second ring was subjected to enzymatic GAG depletion. The experimental opening angles of the control rings were 114 ± 17 deg, 61 ± 27 deg, 31 ± 9 deg in the ascending, arch, and descending thoracic regions, respectively (denoted as "Exp2" in Figure 7.4) and the simulated opening angles of the one-layer models accounted for 32%, 28%, and 32% of the experimental opening angles for control rings in *Chapter 6*. Herein, these errors suggest that GAG are not the only regulators of the opening angle, in line with our previous experimental findings (*Chapter 6*).

As mentioned in the introduction, in this previous study, we captured the contribution of GAG to the opening angle via the enzymatic digestion experiments. After GAG removal, the experimental opening angles decreased by 29 ± 12 deg, 20 ± 6 deg, and 13 ± 3 deg (denoted as "Delta" in Figure 7.4). We believe it is the opposite of this relative decrease in the opening angle following GAG depletion that is captured by the simulation of GAG done in the present study, and may be the best reference for comparison of our simulated results. Indeed, "Delta" represents the decrease in opening angle caused the removal of GAG from the ECM, which is therefore expected to directly reflect the effect of GAG on the opening angle. To wit, our simulated results accounted for 128%, 85%, and 77% of the experimental decrease "Delta" in opening angle following GAG removal, demonstrating relatively small percent errors between the experimental and simulated results (namely: 28%, 15%, and 23% in the ascending, arch and descending thoracic regions, respectively).

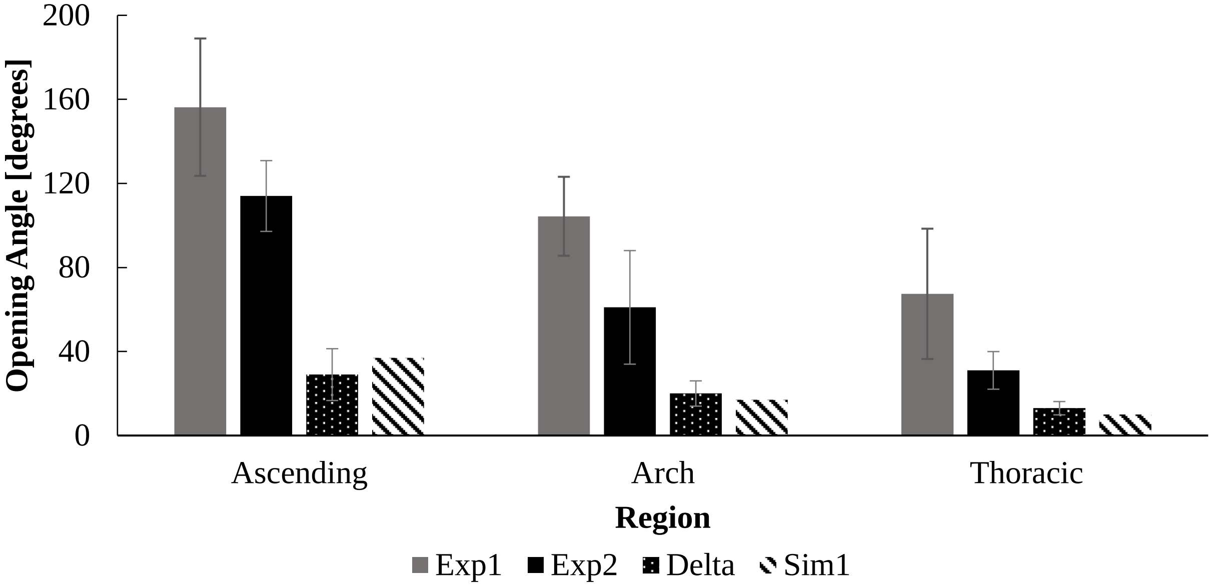

*Figure 7.4: Simulated opening angles (Sim) vs experimental opening angles from 15 fresh rings (N=5 animals, 3 rings per region) (Exp1) cf. [13], vs experimental opening angles from 5 control rings, and vs the difference in opening angle following GAG removal (Delta) (N=5 animals, 1 ring per regions) cf. Chapter 6.*

Another line of interesting findings comes from the difference in simulated opening angles using a one-layered (Table 7.8) vs. a two-layered solid matrix (Table 7.9). The respective percent errors of the simulated opening angles with respect to the experimental contribution of GAG to the opening angle ("Delta") are summarized in Table 7.10. Again, "Delta" is used as a reference to evaluate the simulated opening angles herein, as it reflects the experimental effect of GAG on the opening angle. In the ascending region, the smallest error of 21% was when the FCDs were embedded in a two-layered solid matrix, with the intima-media 10 times stiffer than the adventitia ($r = 0.1$). In the arch region, the smallest error of 5% was obtained when the solid matrix was modelled as 2 layers with the media twice stiffer than the adventitia ($r = 0.5$). In the descending thoracic region, the smallest error of 23% was when the solid matrix was considered as one layer or when the intima-media and adventitia shared similar properties in a two-layer matrix ($r$ = 1), and very large errors were found when two layers were used for the solid matrix when $r$ was 2. Unfortunately, it is not possible to report comparisons with findings from other research groups, due to the lack of literature data on this topic.

*Table 7.10: Percent errors of simulated opening angles in rings using one and two layers for the solid matrix, with respect to the experimental decrease in the opening angle caused by GAG removal "Delta". The smallest errors are bolded.*

| Solid Matrix Number of Layers | $r$ | Error [%] | | |
|---|---|---|---|---|
| | | Ascending | Arch | Descending Thoracic |
| 1 | - | 28 | 15 | **23** |
| 2 | 0.1 | **21** | 50 | - |
| 2 | 0.2 | 38 | 35 | - |
| 2 | 0.5 | 86 | **5** | 38 |
| 2 | 1 | - | 40 | **23** |
| 2 | 2 | - | - | 108 |
| 2 | 5 | - | - | - |
| 2 | 10 | - | - | - |

The discrepancies between the simulated opening angle and the experimental decrease caused by GAG removal suggest that GAG do not contribute to the opening angle solely through their Donnan swelling capacity, which was the only factor considered in this work. This is in line with our previous suggestions that, in addition to their fundamental swelling behavior, GAG may contribute to the opening angle through their interaction with the ECM fibers [13], (*Chapter 6)*. For instance, in addition to loss of swelling, GAG removal was also associated with a loss of circumferential prestretch in *Chapter 6*, a known fundamental contributor to residual stress [2]. Consistently, Mattson et al. showed that GAG also contribute to collagen fiber recruitments, which they also implemented in a constitutive modelling framework [15].

Another interesting observation is this study is the increase in opening angle with increased ratio r, suggesting that, as the intima-media becomes relatively more compliant compared to the adventitia, the opening angle increases. One reasonable explanation for this observation is that, as a material becomes more compliant, it exhibits greater flexibility and becomes less resistant to deformation. In fact, the intima-media contains higher amounts of GAG compared to the adventitia [13], [23]. Higher osmotic pressures are therefore expected to be experienced by the intima-media, and as it becomes more compliant, the deformation is amplified leading to a larger opening angle.

For the porcine samples of 5- to 6-month-old animals used in our studies, the biaxial behavior of the intact samples compared to the tissue samples that underwent GAG depletion was comparable as can be determined by visual inspection from Figure 23 in [16]. Similarly to the young porcine samples herein, no major differences in the overall biaxial behavior were detected in descending thoracic porcine aortas acquired from older animals aging 12-24 months, although indications of earlier stiffening were apparent [34]. As such, if one intends to perform a similar study using a mixture of GAG FCDs in a solid matrix, care should be taken to first verify that the biaxial behavior of the tissue does not differ when GAG are removed. Indeed, for 11-15 week old female Sprague-Dawley rats, an absolute leftward shift in the mechanical stress-strain curve has been reported for samples treated with chondroitinase ABC [35].

Some study limitations need stating. The effect of hyaluronic acid, which is also present in the aortic wall, but in small proportions compared to sGAG [36], was excluded. Although the mechanical separation of the media from the adventitia has been achieved by other groups [10], [11], in our hands, despite our best efforts on the tissues considered, it was not possible to do so without arbitrarily deciding where the separation lay between both layers, which defeated the purpose of the effort. This is why scaling ratio $r$ was introduced in the model instead. In addition, given the expected minimal contribution of the intima in the mechanical behavior of the healthy aorta, the intima and media were modelled as one layer. Finally, while constitutive equations other than Holmes-Mow's could have been used, such as the Holzapfel-Gasser-Ogden model among many others, it was the only one that was readily implemented in FEBioStudio for combination with Donnan swelling, and afforded satisfactory curve-fits (Supplemental Figures S7.1-S7.4).

In conclusion, the majority of studies in the literature have focused on modelling circumferential residual stresses via either the implementation of prestretch in the aortic wall [8] or consideration of FCDs [23]. The findings in this work corroborate our previous experimental studies [13], (*Chapter 6*) and suggest that although a significant portion of the opening angle is regulated by GAG, they are not the only contributors. We therefore submit that both circumferential prestretch and swelling of GAG should be considered when modelling the opening angle in the aorta. In addition, given the coupling effect between GAG and other ECM fiber, efforts may be warranted to elucidate the interaction between the two.

## 7.7 REFERENCES

[1] R. N. Vaishnav and J. Vossoughi, “Residual stress and strain in aortic segments,” *Journal of Biomechanics*, vol. 20, no. 3, pp. 235–239, Jan. 1987, doi: 10.1016/0021-9290(87)90290-9.

[2] C. J. Chuong and Y. C. Fung, “On Residual Stresses in Arteries,” *Journal of Biomechanical Engineering*, vol. 108, no. 2, pp. 189–192, May 1986, doi: 10.1115/1.3138600.

[3] Y. Lanir, “Mechanisms of Residual Stress in Soft Tissues,” *Journal of Biomechanical Engineering*, vol. 131, no. 4, Feb. 2009, doi: 10.1115/1.3049863.

[4] S. E. Greenwald, J. E. Moore Jr., A. Rachev, T. P. C. Kane, and J.-J. Meister, “Experimental Investigation of the Distribution of Residual Strains in the Artery Wall,” *Journal of Biomechanical Engineering*, vol. 119, no. 4, pp. 438–444, Nov. 1997, doi: 10.1115/1.2798291.

[5] L. A. Taber, “Biomechanics of Growth, Remodeling, and Morphogenesis,” *Applied Mechanics Reviews*, vol. 48, no. 8, pp. 487–545, Aug. 1995, doi: 10.1115/1.3005109.

[6] X. Lu, J. B. Zhao, G. R. Wang, H. Gregersen, and G. S. Kassab, “Remodeling of the zero-stress state of femoral arteries in response to flow overload,” *American Journal of Physiology-Heart and Circulatory Physiology*, vol. 280, no. 4, pp. H1547–H1559, Apr. 2001, doi: 10.1152/ajpheart.2001.280.4.H1547.

[7] V. Alastrué, E. Peña, M. Á. Martínez, and M. Doblaré, “Assessing the Use of the ‘Opening Angle Method’ to Enforce Residual Stresses in Patient-Specific Arteries,” *Ann Biomed Eng*, vol. 35, no. 10, pp. 1821–1837, Oct. 2007, doi: 10.1007/s10439-007-9352-4.

[8] A. Giudici and B. Spronck, “The Role of Layer-Specific Residual Stresses in Arterial Mechanics: Analysis via a Novel Modelling Framework,” *Artery Res*, vol. 28, no. 2, Art. no. 2, Jun. 2022, doi: 10.1007/s44200-022-00013-1.

[9] G. A. Holzapfel, T. C. Gasser, and R. W. Ogden, “A New Constitutive Framework for Arterial Wall Mechanics and a Comparative Study of Material Models,” *Journal of Elasticity*, vol. 61, no. 1, pp. 1–48, Jul. 2000, doi: 10.1023/A:1010835316564.

[10] M. Amabili, P. Balasubramanian, I. Bozzo, I. D. Breslavsky, and G. Ferrari, “Layer-specific hyperelastic and viscoelastic characterization of human descending thoracic aortas,” *Journal of the Mechanical Behavior of Biomedical Materials*, vol. 99, pp. 27–46, Nov. 2019, doi: 10.1016/j.jmbbm.2019.07.008.

[11] J. A. Peña, M. A. Martínez, and E. Peña, “Layer-specific residual deformations and uniaxial and biaxial mechanical properties of thoracic porcine aorta,” *Journal of the Mechanical Behavior of Biomedical Materials*, vol. 50, pp. 55–69, Oct. 2015, doi: 10.1016/j.jmbbm.2015.05.024.

[12] D. P. Sokolis, “Regional distribution of layer-specific circumferential residual deformations and opening angles in the porcine aorta,” *Journal of Biomechanics*, vol. 96, p. 109335, Nov. 2019, doi: 10.1016/j.jbiomech.2019.109335.

[13] N. M. Ghadie, J.-P. St-Pierre, and M. R. Labrosse, “Intramural Distributions of GAGs and Collagen vs. Opening Angle of the Intact Porcine Aortic Wall,” *Ann Biomed Eng*, vol. 50, no. 2, pp. 157–168, Feb. 2022, doi: 10.1007/s10439-022-02901-8.

[14] J.-W. M. Beenakker, B. A. Ashcroft, J. H. N. Lindeman, and T. H. Oosterkamp, “Mechanical Properties of the Extracellular Matrix of the Aorta Studied by Enzymatic Treatments,” *Biophysical Journal*, vol. 102, no. 8, pp. 1731–1737, Apr. 2012, doi: 10.1016/j.bpj.2012.03.041.

[15] J. M. Mattson, Y. Wang, and Y. Zhang, “Contributions of Glycosaminoglycans to Collagen Fiber Recruitment in Constitutive Modeling of Arterial Mechanics,” *Journal of Biomechanics*, vol. 82, pp. 211–219, Jan. 2019, doi: 10.1016/j.jbiomech.2018.10.031.

[16] D. Zunder, “Biaxial Mechanical Testing of Native and Glycosaminoglycan-Depleted Porcine Aortic Wall,” Thesis, Université d’Ottawa / University of Ottawa, 2021. doi: 10.20381/ruor-27121.

[17] P. J. Zeller and T. C. Skalak, “Contribution of Individual Structural Components in Determining the Zero-Stress State in Small Arteries,” *J Vasc Res*, vol. 35, no. 1, pp. 8–17, 1998, doi: 10.1159/000025560.

[18] M. L. Raghavan, S. Trivedi, A. Nagaraj, D. D. McPherson, and K. B. Chandran, “Three-Dimensional Finite Element Analysis of Residual Stress in Arteries,” *Annals of Biomedical Engineering*, vol. 32, no. 2, pp. 257–263, Feb. 2004, doi: 10.1023/B:ABME.0000012745.05794.32.

[19] C. Díaz, J. A. Peña, M. A. Martínez, and E. Peña, “Unraveling the multilayer mechanical response of aorta using layer-specific residual stresses and experimental properties,” *Journal of the Mechanical Behavior of Biomedical Materials*, vol. 113, p. 104070, Jan. 2021, doi: 10.1016/j.jmbbm.2020.104070.

[20] G. A. Holzapfel and R. W. Ogden, “Modelling the layer-specific three-dimensional residual stresses in arteries, with an application to the human aorta,” *J. R. Soc. Interface.*, vol. 7, no. 46, pp. 787–799, May 2010, doi: 10.1098/rsif.2009.0357.

[21] C. Bellini, J. Ferruzzi, S. Roccabianca, E. S. Di Martino, and J. D. Humphrey, “A Microstructurally Motivated Model of Arterial Wall Mechanics with Mechanobiological Implications,” *Ann Biomed Eng*, vol. 42, no. 3, pp. 488–502, Mar. 2014, doi: 10.1007/s10439-013-0928-x.

[22] A. Rachev and T. Shazly, “A structure-based constitutive model of arterial tissue considering individual natural configurations of elastin and collagen,” *Journal of the Mechanical Behavior of Biomedical Materials*, vol. 90, pp. 61–72, Feb. 2019, doi: 10.1016/j.jmbbm.2018.09.047.

[23] E. U. Azeloglu, M. B. Albro, V. A. Thimmappa, G. A. Ateshian, and K. D. Costa, “Heterogeneous transmural proteoglycan distribution provides a mechanism for regulating residual stresses in the aorta,” *American Journal of Physiology-Heart and Circulatory Physiology*, vol. 294, no. 3, pp. H1197–H1205, Mar. 2008, doi: 10.1152/ajpheart.01027.2007.

[24] S. A. Maas, B. J. Ellis, G. A. Ateshian, and J. A. Weiss, “FEBio: Finite Elements for Biomechanics,” *J Biomech Eng*, vol. 134, no. 1, pp. 11005-NaN, Jan. 2012, doi: 10.1115/1.4005694.

[25] N. Ghadie, J.-P. St-Pierre, and M. R. Labrosse, “Intramural Glycosaminoglycans Distribution vs. Residual Stress in Porcine Ascending Aorta: a Computational Study*,” in *2020 42nd Annual International Conference of the IEEE Engineering in Medicine Biology Society (EMBC)*, Jul. 2020, pp. 2816–2819. doi: 10.1109/EMBC44109.2020.9176381.

[26] M. R. Labrosse, R. Jafar, J. Ngu, and M. Boodhwani, “Planar biaxial testing of heart valve cusp replacement biomaterials: Experiments, theory and material constants,” *Acta Biomaterialia*, vol. 45, pp. 303–320, Nov. 2016, doi: 10.1016/j.actbio.2016.08.036.

[27] M. H. Holmes and V. C. Mow, “The nonlinear characteristics of soft gels and hydrated connective tissues in ultrafiltration,” *Journal of Biomechanics*, vol. 23, no. 11, pp. 1145–1156, Jan. 1990, doi: 10.1016/0021-9290(90)90007-P.

[28] G. A. Ateshian, B. J. Ellis, and J. A. Weiss, “Equivalence Between Short-Time Biphasic and Incompressible Elastic Material Responses,” *Journal of Biomechanical Engineering*, vol. 129, no. 3, pp. 405–412, Jun. 2007, doi: 10.1115/1.2720918.

[29] W. W. von Maltzahn, R. G. Warriyar, and W. F. Keitzer, “Experimental measurements of elastic properties of media and adventitia of bovine carotid arteries,” *Journal of Biomechanics*, vol. 17, no. 11, pp. 839–847, Jan. 1984, doi: 10.1016/0021-9290(84)90142-8.

[30] J. Xie, J. Zhou, and Y. C. Fung, “Bending of Blood Vessel Wall: Stress-Strain Laws of the Intima-Media and Adventitial Layers,” *Journal of Biomechanical Engineering*, vol. 117, no. 1, pp. 136–145, Feb. 1995, doi: 10.1115/1.2792261.

[31] Q. Yu, J. Zhou, and Y. C. Fung, “Neutral axis location in bending and Young’s modulus of different layers of arterial wall,” *American Journal of Physiology-Heart and Circulatory Physiology*, vol. 265, no. 1, pp. H52–H60, Jul. 1993, doi: 10.1152/ajpheart.1993.265.1.H52.

[32] N. M. Ghadie, J.-P. St-Pierre, and M. R. Labrosse, “Intramural Distributions of GAGs and Collagen vs. Opening Angle of the Intact Porcine Aortic Wall,” *Ann Biomed Eng*, vol. 50, no. 2, pp. 157–168, Feb. 2022, doi: 10.1007/s10439-022-02901-8.

[33] X. Guo, Y. Lanir, and G. S. Kassab, “Effect of osmolarity on the zero-stress state and mechanical properties of aorta,” *American Journal of Physiology-Heart and Circulatory Physiology*, vol. 293, no. 4, pp. H2328–H2334, Oct. 2007, doi: 10.1152/ajpheart.00402.2007.

[34] J. M. Mattson, R. Turcotte, and Y. Zhang, “Glycosaminoglycans contribute to extracellular matrix fiber recruitment and arterial wall mechanics,” *Biomech Model Mechanobiol*, vol. 16, no. 1, pp. 213–225, Feb. 2017, doi: 10.1007/s10237-016-0811-4.

[35] R. E. Gandley, M. K. McLaughlin, T. J. Koob, S. A. Little, and L. J. McGuffee, “Contribution of chondroitin-dermatan sulfate-containing proteoglycans to the function of rat mesenteric arteries,” *American Journal of Physiology-Heart and Circulatory Physiology*, vol. 273, no. 2, pp. H952–H960, Aug. 1997, doi: 10.1152/ajpheart.1997.273.2.H952.

[36] B. G. Salisbury and W. D. Wagner, “Isolation and preliminary characterization of proteoglycans dissociatively extracted from human aorta.,” *J. Biol. Chem.*, vol. 256, no. 15, pp. 8050–8057, Aug. 1981.

## 7.8 SUPPLEMENTARY INFORMATION

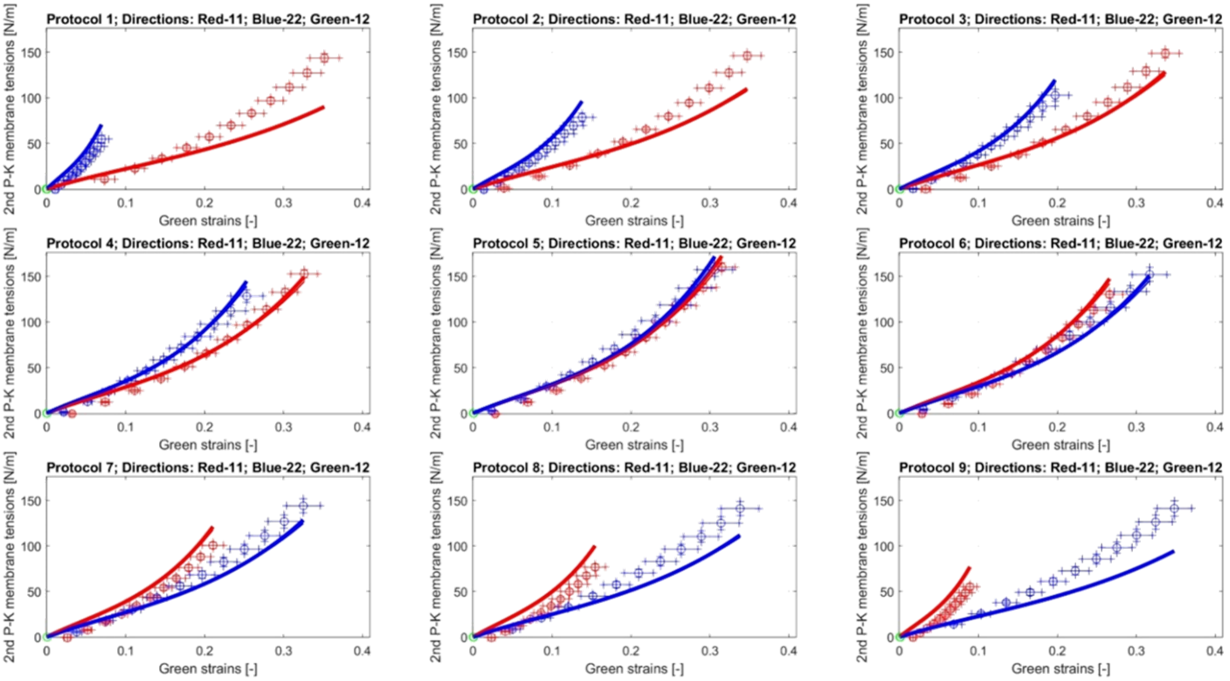

*Figure S7.1: Experimental data and model fit membrane tensions vs. green strains for the ascending region using one layer for the aortic wall. $R^2$-FD = 0.94 and $R^2$-XD = 0.94.*

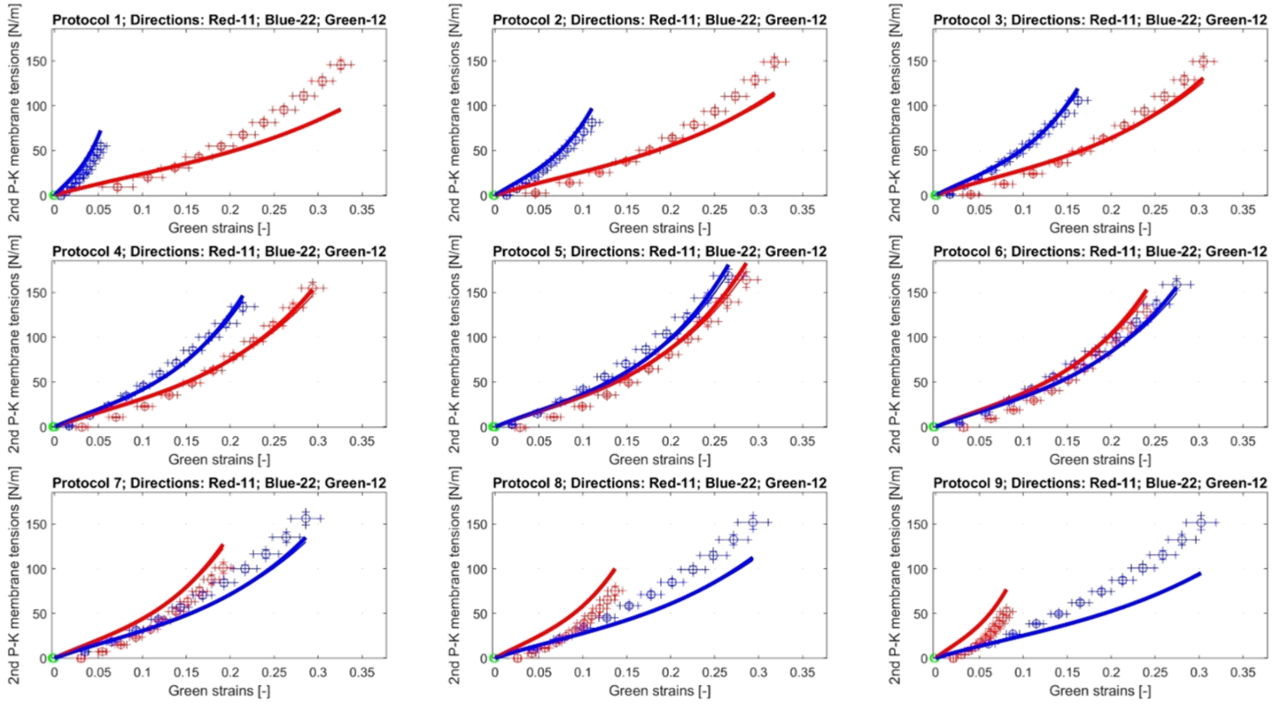

*Figure S7.2: Experimental data and model fit membrane tensions vs. green strains for the arch region using one layer for the aortic wall. $R^2$-FD = 0.94 and $R^2$-XD = 0.94.*

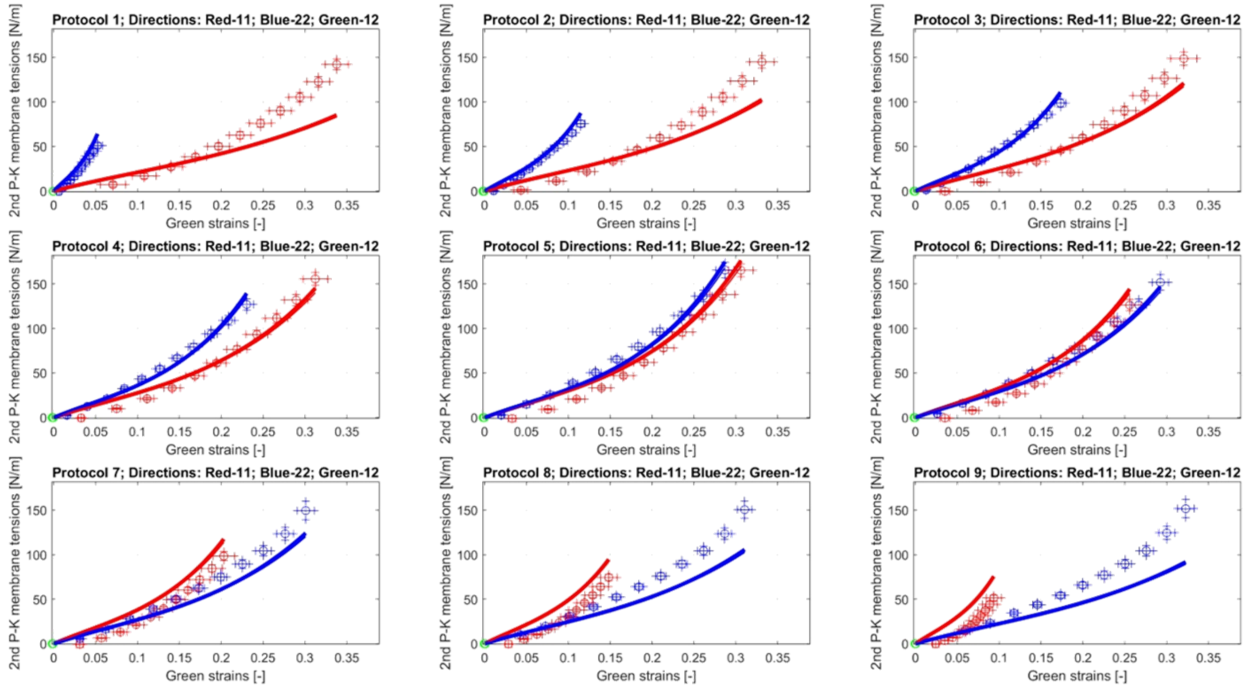

*Figure S7.3: Experimental data and model fit membrane tensions vs. green strains for the descending thoracic region using one layer for the aortic wall. $R^2$-FD = 0.93 and $R^2$-XD = 0.95.*

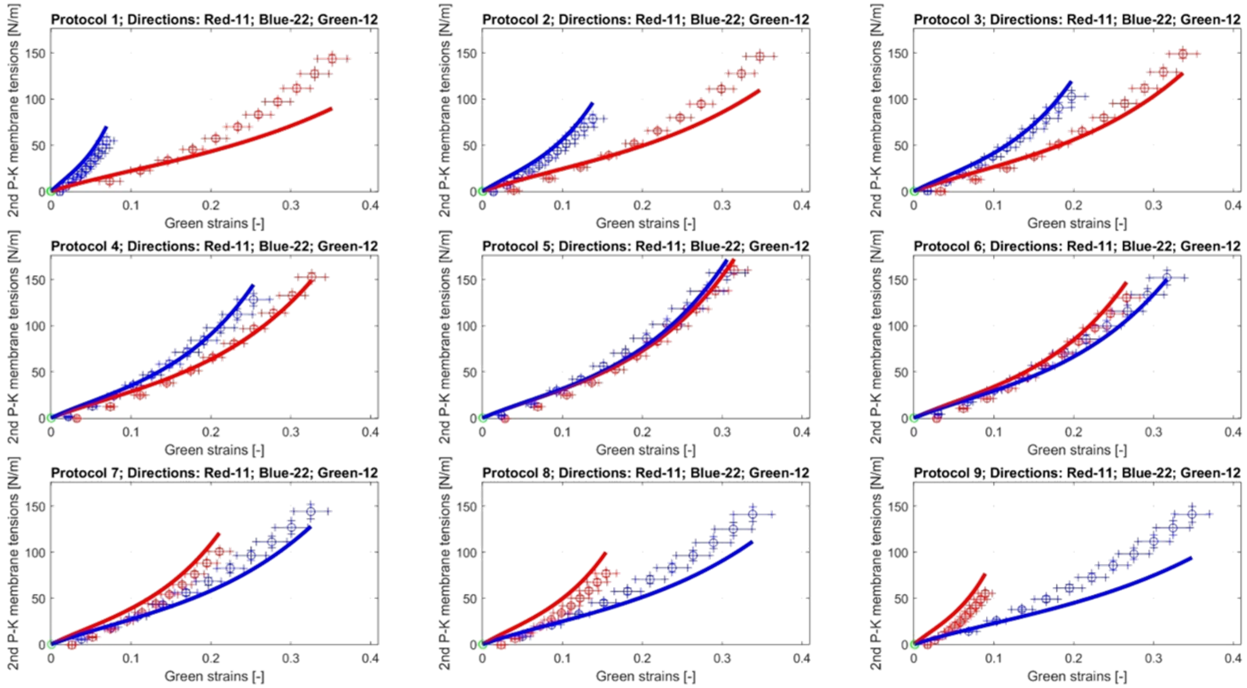

*Figure S7.4: Experimental data and model fit membrane tensions vs. green strains for the ascending region using two layers for the aortic wall, with r = 0.1. $R^2$-FD = 0.94 and $R^2$-XD = 0.94. This is representative of curve fits that were considered acceptable for finite element modelling.*

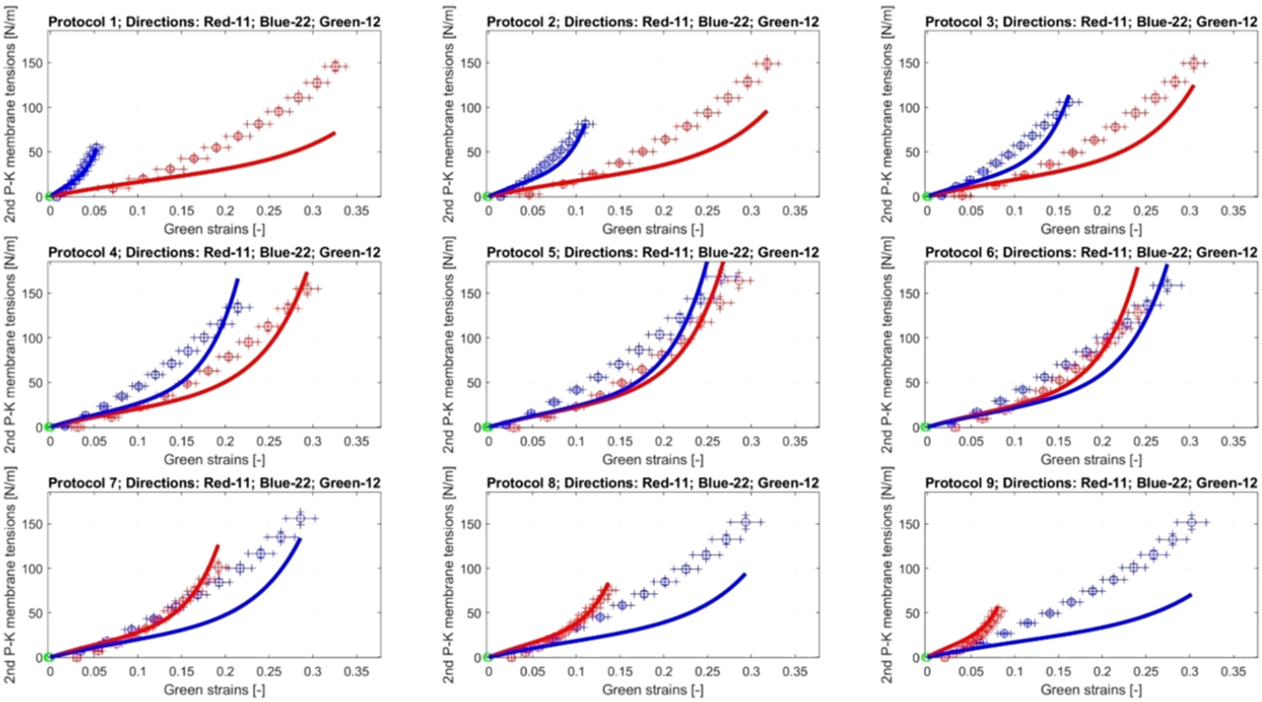

*Figure S7.5: Experimental data and model fit membrane tensions vs. green strains for the arch region using two layers for the aortic wall, with r = 5. $R^2$-FD = 0.86 and $R^2$-XD = 0.86. This is representative of curve fits that were considered not acceptable for finite element modelling.*

## 7.9 SUPPLEMENTARY INFORMATION 2

### 7.9.1 First and Second Partial Derivatives

Through the information in this Supplemental material section, we first provide more details into the derivations the constitutive formulation and the considerations in the optimization process. The Holmes-Mow constitutive law can be written as,

$$W = \frac{1}{2}c(e^{Q} - 1)$$

$$c = \frac{\lambda + 2\mu}{2\beta}$$

$$Q = \frac{\beta}{\lambda + 2\mu}[(2\mu - \lambda)(I_1 - 3) + \lambda(I_2 - 3) - (\lambda + 2\mu)\ln J^2]$$

By imposing $J = 1$ (incomressibility) and $\lambda = 0$ (biphasic medium), the expression becomes:

$$W = \frac{1}{2}c(e^{Q} - 1)$$

$$c = \frac{2\mu}{2\beta}$$

$$Q = \frac{\beta}{2\mu}[(2\mu)(I_1 - 3)]$$

$$Q = \beta(I_1 - 3)$$

Therefore,

$$W = \frac{1}{2}\frac{2\mu}{2\beta}(e^{Q} - 1)$$

$$W = \frac{\mu}{2\beta}(e^{Q} - 1)$$

with

$$Q = \beta(I_1 - 3)$$

$$I_1 = 2(E_{11} + E_{22} + E_{33}) + 3$$

$$Q = \beta(2(E_{11} + E_{22} + E_{33}) + 3 - 3)$$

$$Q = \beta\big(2(E_{11} + E_{22} + E_{33})\big)$$

$$Q = 2\beta(E_{11} + E_{22} + E_{33})$$

The incompressibility assumption was achieved by imposing $\det \bar{\bar{\bar{F}}} = 1$ (Chapter 2, Section 2.5.1), and will allow us to express $E_{33}$ as a function of $E_{11}$ and $E_{22}$. Under no shear conditions:

$$\bar{\bar{F}} = \begin{bmatrix} \lambda_1 & 0 & 0 \\ 0 & \lambda_2 & 0 \\ 0 & 0 & \lambda_3 \end{bmatrix}$$

$$\det \bar{\bar{F}} = \lambda_1 \lambda_2 \lambda_3 = 1$$

$$(\lambda_1 \lambda_2 \lambda_3)^2 = 1$$

With $\lambda_1^2 = 2E_{11} + 1$, $\lambda_2^2 = 2E_{22} + 1$, $\lambda_3^2 = 2E_{33} + 1$ (Refer to Chapter 3.4 in J. D. Humphrey, *Cardiovascular Solid Mechanics: Cells, Tissues, and Organs*. Springer Science & Business Media, 2002.), the equation becomes:

$$(2E_{11} + 1)(2E_{22} + 1)(2E_{33} + 1) = 1$$

$$(2E_{33} + 1) = \frac{1}{(2E_{11} + 1)(2E_{22} + 1)}$$

$$E_{33} = \frac{1}{2}\left[\frac{1}{(2E_{11} + 1)(2E_{22} + 1)} - 1\right] = \frac{1}{2}\left[\frac{1}{\Delta} - 1\right]$$

The first partial ($\bar{\bar{S}} = \frac{dW}{d\bar{\bar{E}}}$) derivatives can therefore be derived as:

- $\frac{\partial W}{\partial E_{11}} = \frac{\partial}{\partial E_{11}}\left[\frac{\mu}{2\beta}(e^Q - 1)\right] = \frac{\mu}{2\beta}\frac{\partial Q}{\partial E_{11}} e^Q$

$$\frac{\partial Q}{\partial E_{11}} = 2\beta\left[1 + \frac{-2.2(2E_{22} + 1)}{4(2E_{11} + 1)^2(2E_{22} + 1)^2}\right] = 2\beta\left[1 - \frac{1}{(2E_{11} + 1)^2(2E_{22} + 1)}\right]$$
$$= 2\beta\left[1 - \frac{1}{\Delta(2E_{11} + 1)}\right]$$

$$\frac{\partial W}{\partial E_{11}} = \frac{\partial}{\partial E_{11}}\left[\frac{\mu}{2\beta}(e^Q - 1)\right] = \frac{\mu}{2\beta} 2\beta\left[1 - \frac{1}{\Delta(2E_{11} + 1)}\right] e^Q = \mu\left[1 - \frac{1}{\Delta(2E_{11} + 1)}\right] e^Q$$

- $\frac{\partial W}{\partial E_{22}} = \frac{\partial}{\partial E_{22}}\left[\frac{\mu}{2\beta}(e^Q - 1)\right] = \frac{\mu}{2\beta}\frac{\partial Q}{\partial E_{22}} e^Q$

$$\frac{\partial Q}{\partial E_{22}} = 2\beta\left[1 + \frac{-2.2(2E_{11}+1)}{4(2E_{11}+1)^2(2E_{22}+1)^2}\right] = 2\beta\left[1 - \frac{1}{(2E_{22}+1)^2(2E_{11}+1)}\right]$$
$$= 2\beta\left[1 - \frac{1}{\Delta(2E_{22}+1)}\right]$$

$$\frac{\partial W}{\partial E_{22}} = \frac{\mu}{2\beta}\frac{\partial Q}{\partial E_{22}}e^Q = \frac{\mu}{2\beta}2\beta\left[1 - \frac{1}{\Delta(2E_{22}+1)}\right]e^Q = \mu\left[1 - \frac{1}{\Delta(2E_{22}+1)}\right]e^Q$$

- $\frac{\partial W}{\partial E_{12}} = 0$

The second partial derivatives ($C_{ijkl} = \frac{\partial^2 W}{\partial E_{ij}\partial E_{kl}}$) are:

- $\frac{\partial^2 W}{\partial^2 E_{11}} = \frac{\partial}{\partial E_{11}}\left[\frac{\partial W}{\partial E_{11}}\right] = \frac{\partial}{\partial E_{11}}\left[\frac{\mu}{2\beta}\frac{\partial Q}{\partial E_{11}}e^Q\right] = \frac{\mu}{2\beta}\left[\frac{\partial^2 Q}{\partial^2 E_{11}}e^Q + \left(\frac{\partial Q}{\partial E_{11}}\right)^2 e^Q\right] = \frac{\mu}{2\beta}e^Q\left[\frac{\partial^2 Q}{\partial^2 E_{11}} + \left(\frac{\partial Q}{\partial E_{11}}\right)^2\right]$

$$\frac{\partial^2 Q}{\partial^2 E_{11}} = \frac{\partial}{\partial E_{11}}\left(2\beta\left[1 - \frac{1}{(2E_{11}+1)^2(2E_{22}+1)}\right]\right) = 2\beta\frac{2.2(2E_{11}+1)(2E_{22}+1)}{(2E_{11}+1)^4(2E_{22}+1)^2}$$
$$= 2\beta\frac{4}{(2E_{11}+1)^3(2E_{22}+1)} = 2\beta\frac{4}{\Delta(2E_{11}+1)^2}$$

$$\frac{\partial^2 W}{\partial^2 E_{11}} = \frac{\mu}{2\beta}e^Q\left[\frac{\partial^2 Q}{\partial^2 E_{11}} + \left(\frac{\partial Q}{\partial E_{11}}\right)^2\right] = \frac{\mu}{2\beta}e^Q\left[2\beta\frac{4}{\Delta(2E_{11}+1)^2} + \left(2\beta\left[1 - \frac{1}{\Delta(2E_{11}+1)}\right]\right)^2\right]$$
$$= \mu e^Q\left[\frac{4}{\Delta(2E_{11}+1)^2} + 2\beta\left[1 - \frac{1}{\Delta(2E_{11}+1)}\right]^2\right]$$

- $\frac{\partial^2 W}{\partial^2 E_{22}} = \frac{\partial}{\partial E_{22}}\left[\frac{\partial W}{\partial E_{22}}\right] = \frac{\partial}{\partial E_{22}}\left[\frac{\mu}{2\beta}\frac{\partial Q}{\partial E_{22}}e^Q\right] = \frac{\mu}{2\beta}\left[\frac{\partial^2 Q}{\partial^2 E_{22}}e^Q + \left(\frac{\partial Q}{\partial E_{22}}\right)^2 e^Q\right] = \frac{\mu}{2\beta}e^Q\left[\frac{\partial^2 Q}{\partial^2 E_{22}} + \left(\frac{\partial Q}{\partial E_{22}}\right)^2\right]$

$$\frac{\partial^2 Q}{\partial^2 E_{22}} = \frac{\partial}{\partial E_{22}}\left(2\beta\left[1 - \frac{1}{(2E_{22}+1)^2(2E_{11}+1)}\right]\right) = 2\beta\frac{2.2(2E_{11}+1)(2E_{22}+1)}{(2E_{11}+1)^2(2E_{22}+1)^4}$$

$$= 2\beta\frac{4}{(2E_{11}+1)(2E_{22}+1)^3} = 2\beta\frac{4}{\Delta(2E_{22}+1)^2}$$

$$\frac{\partial^2 W}{\partial^2 E_{22}} = \frac{\mu}{2\beta}e^Q\left[\frac{\partial^2 Q}{\partial^2 E_{22}} + \left(\frac{\partial Q}{\partial E_{22}}\right)^2\right]$$

$$= \frac{\mu}{2\beta}e^Q\left[2\beta\frac{4}{\Delta(2E_{22}+1)^2} + \left(2\beta\left[1 - \frac{1}{\Delta(2E_{22}+1)}\right]\right)^2\right]$$

$$= \mu e^Q\left[\frac{4}{\Delta(2E_{22}+1)^2} + 2\beta\left[1 - \frac{1}{\Delta(2E_{22}+1)}\right]^2\right]$$

- $\frac{\partial^2 W}{\partial E_{11}\partial E_{22}} = \frac{\partial}{\partial E_{11}}\left[\frac{\partial W}{\partial E_{22}}\right] = \frac{\partial}{\partial E_{11}}\left[\frac{\mu}{2\beta}\frac{\partial Q}{\partial E_{22}}e^Q\right] = \frac{\mu}{2\beta}\left[\frac{\partial^2 Q}{\partial E_{11}\partial E_{22}}e^Q + \frac{\partial Q}{\partial E_{22}}\frac{\partial Q}{\partial E_{22}}e^Q\right] =$

$\frac{\mu}{2\beta}e^Q\left[\frac{\partial^2 Q}{\partial E_{11}\partial E_{22}} + \frac{\partial Q}{\partial E_{11}}\frac{\partial Q}{\partial E_{22}}\right]$

$$\frac{\partial^2 Q}{\partial E_{11}\partial E_{22}} = \frac{\partial}{\partial E_{11}}\left[\frac{\partial Q}{\partial E_{22}}\right] = \frac{\partial}{\partial E_{11}}\left(2\beta\left[1 - \frac{1}{(2E_{22}+1)^2(2E_{11}+1)}\right]\right)$$

$$= 2\beta\frac{2(2E_{22}+1)^2}{(2E_{22}+1)^4(2E_{11}+1)^2} = 2\beta\frac{2}{(2E_{22}+1)^2(2E_{11}+1)^2} = \frac{4\beta}{\Delta^2}$$

$$\frac{\partial^2 W}{\partial E_{11}\partial E_{22}} = \frac{\mu}{2\beta}e^Q\left[\frac{4\beta}{\Delta^2} + 2\beta\left[1 - \frac{1}{\Delta(2E_{11}+1)}\right]2\beta\left[1 - \frac{1}{\Delta(2E_{22}+1)}\right]\right]$$

$$= 2\beta\mu e^Q\left[\frac{1}{\Delta^2} + \left[1 - \frac{1}{\Delta(2E_{11}+1)}\right]\left[1 - \frac{1}{\Delta(2E_{22}+1)}\right]\right]$$

### 7.9.2 Convexity of Strain Energy Function

It is also essential to verify the convexity of the strain energy function, as it is required for the stability of the finite element analysis. Convexity of the strain energy function requires its

Hessian (square matrix of second order partial derivatives of a scalar function) to be positive definite. The Hessian of $W$ is the elasticity tensor. Recall from Chapter 2 Section 2.5.4 that the second Piola-Kirchhoff stress tensors can be expressed as $\bar{\bar{S}} = \frac{dW}{d\bar{\bar{E}}}$, and the stiffness (or tangent modulus) is $\bar{\bar{\bar{\bar{\mathbb{C}}}}} = \frac{d\bar{\bar{S}}}{d\bar{\bar{E}}}$. Therefore, $\bar{\bar{\bar{\bar{\mathbb{C}}}}} = \frac{d\bar{\bar{S}}}{d\bar{\bar{E}}} = \frac{d^2W}{d^2\bar{\bar{E}}}$.

$$C_{ijkl} = \frac{\partial^2 W}{\partial E_{ij} \partial E_{kl}}$$

Knowing that in 2D (in-plane), the tangent modulus can be represented as:

$$\bar{\bar{\bar{\bar{\mathbb{C}}}}}_{2D} = \begin{bmatrix} C_{11} & C_{12} & C_{14} \\ C_{12} & C_{22} & C_{24} \\ C_{14} & C_{24} & C_{44} \end{bmatrix}$$

we have

$$C_{11} = \frac{\partial^2 W}{\partial E_{11} \partial E_{11}} \quad C_{22} = \frac{\partial^2 W}{\partial E_{22} \partial E_{22}} \quad C_{12} = \frac{\partial^2 W}{\partial E_{11} \partial E_{22}}$$

$$C_{44} = \frac{\partial^2 W}{\partial E_{12} \partial E_{12}} \quad C_{14} = \frac{\partial^2 W}{\partial E_{11} \partial E_{12}} \quad C_{24} = \frac{\partial^2 W}{\partial E_{22} \partial E_{12}}$$

With no shear:

$$C_{44} = \frac{\partial^2 W}{\partial E_{12} \partial E_{12}} = 0 \quad C_{14} = \frac{\partial^2 W}{\partial E_{11} \partial E_{12}} = 0 \quad C_{24} = \frac{\partial^2 W}{\partial E_{22} \partial E_{12}} = 0$$

The matrix is positive definite if it is symmetric and its eigenvalues are positive. The eigenvalues are the roots of its characteristic equations. The characteristic equation of the tangent modulus is given by:

$$\det\begin{bmatrix} C_{11} & C_{12} & C_{14} \\ C_{12} & C_{22} & C_{24} \\ C_{14} & C_{24} & C_{44} \end{bmatrix} = 0$$

$$\begin{vmatrix} C_{11}-x & C_{12} & C_{14} \\ C_{21} & C_{22}-x & C_{24} \\ C_{14} & C_{24} & C_{44}-x \end{vmatrix} = 0$$

$$(C_{11}-x)[(C_{22}-x)(C_{44}-x)-C_{24}^2]-C_{12}[C_{21}(C_{44}-x)-C_{14}C_{24}]$$
$$+C_{14}[C_{21}C_{24}-C_{14}(C_{22}-x)]=0$$

which becomes

$$x^3-(C_{11}+C_{22}+C_{44})x^2+(C_{11}C_{22}+C_{11}C_{44}+C_{22}C_{44}-C_{24}^2-C_{14}^2-C_{12}^2)x-C_{11}C_{22}C_{44}$$
$$-2C_{14}C_{24}C_{12}+C_{12}^2C_{14}+C_{14}^2C_{22}+C_{11}C_{24}^2=0$$

To get three positive roots, the sign must alternate between the non-zero terms, and therefore the following equations need to be respected.

$$-C_{11}-C_{22}-C_{44}<0$$

$$C_{11}C_{22}+C_{11}C_{44}+C_{22}C_{44}-C_{24}^2-C_{14}^2-C_{12}^2>0$$

$$-C_{11}C_{22}C_{44}-2C_{14}C_{24}C_{12}+C_{12}^2C_{14}+C_{14}^2C_{22}+C_{11}C_{24}^2<0$$

Let us ensure that the constraints on the material constants for the strain energy function are convex at least at the origin. At the zero strain (origin), $E_{11}=E_{22}=E_{33}=0$. Therefore $Q=0$, and

$$e^Q=1$$

$$\frac{\partial Q}{\partial E_{11}}=2\beta\left[1-\frac{1}{(0+1)^2(0+1)}\right]=0$$

$$\frac{\partial Q}{\partial E_{22}} = 0,$$

$$\frac{\partial^2 Q}{\partial^2 E_{11}} = 2\beta \frac{4}{(0+1)^3(0+1)} = 8\beta$$

$$\frac{\partial^2 Q}{\partial^2 E_{22}} = 8\beta$$

$$\frac{\partial^2 Q}{\partial E_{11} \partial E_{22}} = 4\beta$$

Therefore,

- $C_{11} = \frac{\partial^2 W}{\partial^2 E_{11}} = \frac{\mu}{2\beta} 1[8\beta + (0)^2] = 4\mu$
- $C_{22} = \frac{\partial^2 W}{\partial^2 E_{22}} = \frac{\mu}{2\beta} 1[8\beta + (0)^2] = 4\mu$
- $C_{12} = \frac{\mu}{2\beta} 1[4\beta + 0] = 2\mu$

(1) From $-C_{11} - C_{22} - C_{44} < 0$

$$-8\mu < 0 \qquad \mu > 0$$

(2) From $C_{11}C_{22} + C_{11}C_{44} + C_{22}C_{44} - C_{24}^2 - C_{14}^2 - C_{12}^2 > 0,\ 16\mu^2 - 4\mu^2 > 0$

$$12\mu^2 > 0 \qquad always\ true$$

(3) The third equation is always satisfied.

### 7.9.3 Mesh Sensitivity Analysis

*Table S7.1: Mesh sensitivity analysis of ascending aortic ring model. Parameters are provided for quarter model.*

| Number of elements in thickness | Number of elements in length | Number of elements in circumference | Number of elements | Number of nodes | Opening Angle (degrees) |
|---|---|---|---|---|---|
| 7 | 4 | 8 | 256 | 1449 | 36.44 |
| 7 | 4 | 10 | 320 | 1781 | 36.91 |
| 7 | 4 | 12 | 384 | 2113 | 37.03 |
| 7 | 4 | 14 | 448 | 2445 | 37.07 |
| **7** | **4** | **20** | **640** | **3441** | **37.10** |
| 7 | 4 | 25 | 800 | 4271 | 37.11 |
| 7 | 4 | 30 | 960 | 5101 | 37.11 |
| 7 | 6 | 20 | 960 | 4893 | 37.10 |
| 7 | 8 | 20 | 1280 | 6345 | 37.10 |
| 7 | 10 | 20 | 1600 | 7797 | 37.11 |

*Table S7.2: Mesh sensitivity analysis of arch aortic ring model. Parameters are provided for quarter model.*

| Number of elements in thickness | Number of elements in length | Number of elements in circumference | Number of elements | Number of nodes | Opening Angle (degrees) |
|---|---|---|---|---|---|
| 7 | 4 | 8 | 256 | 1449 | 16.58 |
| 7 | 4 | 10 | 320 | 1781 | 16.71 |
| 7 | 4 | 12 | 384 | 2113 | 16.75 |
| 7 | 4 | 14 | 448 | 2445 | 16.76 |
| **7** | **4** | **20** | **640** | **3441** | **16.76** |
| 7 | 4 | 25 | 800 | 4271 | 16.76 |
| 7 | 4 | 30 | 960 | 5101 | 16.76 |
| 7 | 6 | 20 | 960 | 4893 | 16.78 |
| 7 | 8 | 20 | 1280 | 6345 | 16.82 |
| 7 | 10 | 20 | 1600 | 7797 | 16.86 |

*Table S7.3: Mesh sensitivity analysis of thoracic aortic ring model. Parameters are provided for quarter model*.

| Number of elements in thickness | Number of elements in length | Number of elements in circumference | Number of elements | Number of nodes | Opening Angle (degrees) |
|---|---|---|---|---|---|
| 7 | 4 | 8 | 256 | 1449 | 12.90 |
| 7 | 4 | 10 | 320 | 1781 | 13.01 |
| 7 | 4 | 12 | 384 | 2113 | 13.04 |
| 7 | 4 | 14 | 448 | 2445 | 13.05 |
| **7** | **4** | **20** | **640** | **3441** | **13.06** |
| 7 | 4 | 25 | 800 | 4271 | 13.06 |
| 7 | 4 | 30 | 960 | 5101 | 13.06 |
| 7 | 6 | 20 | 960 | 4893 | 13.09 |
| 7 | 8 | 20 | 1280 | 6345 | 13.18 |
| 7 | 10 | 20 | 1600 | 7797 | 13.25 |
| 7 | 20 | 20 | 3200 | 15057 | 13.44 |
| 7 | 40 | 20 | 6400 | 29577 | 13.55 |

# III

# CLOSING

# 8 DISCUSSION

Discussion| Conclusions| Recommendations for Future Work

## 8.1 SUMMARY

To begin, let us provide a recapitulation of this dissertation. Chapter 3 reviewed the current understanding on glycosaminoglycans (GAG) in the normal and diseased aorta, and their roles in regulating the mechanical properties of the aorta. It identified gaps in the literature and suggested avenues for future investigations to expand our current knowledge of the roles of GAG in the aorta. Chapter 4 introduced and validated a finite element model that simulated the effect of GAG in uncut and radially cut aortic rings. The model served to launch an initial *in silico* investigation into the effect of GAG on the opening angle and residual stresses, via a series of parametric studies. To ascertain the observations made based on the computer simulations, Chapter 5 aimed to study the effect of GAG on the opening angle experimentally. Attention was also paid to the extracellular matrix (ECM) fibers, elastin and collagen, to seek a comprehensive understanding of the mechanical roles of the ECM constituents. Chapter 5 investigated the intramural distribution of these components in the three main regions of the aorta: ascending, arch, and descending thoracic regions, and correlated this compositional data with opening angle measurements. Chapter 6 then uncovered the effect of GAG on the opening angle and radial circumferential stiffness via enzymatic GAG depletion. The contribution of glycated crosslinks to the opening angle was also investigated. Additionally, the possible underlying mechanisms through which GAG may play mechanical roles were also examined. Chapter 7 finally established finite element models of aortic rings for each of the ascending, arch, and descending thoracic regions, that depict the experimental effect of GAG swelling on the opening angle with small errors.

## 8.2 GENERAL DISCUSSION

This dissertation employs experimental and computational methodologies, highlighting their synergy as they consistently produced congruent outcomes and mutually reinforced each other with their data and findings. Observations from both *in vitro* and *in silico* experimentations offered robust evidence and new knowledge on the roles of GAG in regulating residual stress. Specifically, finite element modelling suggested that an increase in the fixed charge density (FCD) of GAG would increase the residual stresses in a closed ring, as well as the opening angle of a radially cut aortic ring. In line with these findings, a positive correlation between the GAG content and the opening angle was established, and GAG depletion also resulted in a decrease in the opening angle. Taking these observations together, the accumulation of GAG is therefore expected to cause an increase in circumferential residual stress. Additionally, finite element modelling suggested that the opening angle continuously increased only when the GAG gradient, not just content, increased, as higher GAG content only led to a plateau in the opening angle without further increase. Experimental data also suggested that the GAG gradient correlates with the opening angle of porcine thoracic aortas. Both *in silico* and *in vitro* experimentations therefore suggested that the GAG gradient affects the level of circumferential residual stress present in the aortic wall.

Other roles of GAG in the thoracic aorta were elucidated, such as their contribution to the radial compressive properties of the aorta. The effect of GAG on osmotic swelling was investigated and GAG removal via enzymatic digestion was associated with loss of water content. The findings of this work also shed light on the complexity of the synergy of the ECM constituents in their effect on the mechanical properties of the aorta. The correlation between the ratio of the collagen and GAG contents and the opening angle was one of the strongest, highlighting the interaction between GAG and collagen fibers. Additionally, GAG removal altered the level of circumferential stretch in the aorta and, given that the origin of circumferential stretch has been attributed to the fibrous components of the ECM, this suggests that GAG, in their interaction with the ECM fibers, may influence the level of prestretch present in them.

Furthermore, the mural distribution of the main ECM constituents of the thoracic aorta were characterized quantitatively and histologically, providing new detailed data regarding the distribution of collagen, elastin, and GAG through the aortic wall of different regions of the thoracic aorta of 5- to 6-month-old porcine animals, which sheds light on the heterogeneous nature of the aorta. In addition to changes in the aortic size along its tree, the ECM exhibited regional variations, characterized by decreased levels of GAG and elastin, and increased collagen content in the distal regions. The ECM also exhibited intramural variations, such that GAG content decreased from the intima to the adventitia, collagen content increased, and elastin content was highest towards the media. This work not only expands our understanding on the ECM distribution in the porcine thoracic aorta, but also establishes a robust methodology to quantitatively assess the distributions of these ECM components in other tissues. Such inroads are necessary for our understanding of tissue composition-structure effects on tissue function, and for the development and advancement of mathematical and numerical models that can not only further our knowledge of the physical behaviour of the aorta, but also are promising in predicting lethal ruptures caused by aortic disease such as aneurysm and dissection.

Similarly, the mechanical properties of the aorta exhibited regional variations. The radial compressive stiffness was highest in the ascending region and the opening angle decreased distally, suggesting higher levels of residual stresses in the proximal aorta. Additionally, the layers of the aorta, namely the intima-media and adventitia in this work, were demonstrated to be characterized by distinct elastic properties which also varied throughout the regions of the aorta. This is particularly noteworthy considering the impact of the aorta's heterogeneous nature on its mechanical integrity and function, as well as the potential implications of its heterogeneity in the development of aortic disease. Indeed, this sheds light on 1) the importance of targeted and tailored medical interventions, and 2) the necessity of improving computational models to take into account these compositional and mechanical variations.

The experimental studies conducted within this dissertation provided the essential components (geometry and dimensions including layer dependent information, tissue composition namely GAG content, biaxial data to inform constitutive formulation) required to establish and evaluate finite element models of aortic rings for each of the ascending, arch and descending thoracic regions, which captured the effect of GAG swelling on the opening angle with a relatively small error. To date, numerous efforts have been developed with the aim of incorporating residual stresses in aortic computer models [1]–[3], yet challenges persist. Aside from the limitations associated with the ability to non-invasively measure the opening angle to represent residual stresses, the inclusion of in-situ prestreches or FCDs has thus far relied heavily on substantial assumptions. These efforts are primarily motivated by the impact of residual stresses on the *in vivo* state of mechanical stresses, as well as the importance of including them in finite element models to prevent biased prediction of the mechanical stress distributions. Indeed, computational modeling offers a distinct advantage over the current diameter criterion in predicting aortic ruptures, by leveraging advanced algorithms and patient-specific data, providing clinicians with enhanced decision-making capabilities and thereby paving the way for personalized medical interventions.

Another aspect that requires discussion is the definition of circumferential residual stresses adopted by the scientific community in vascular mechanics, being the stresses in the unloaded configuration of an excised aortic ring. As discussed throughout this dissertation, the swelling pressure caused by the presence of GAG in the aortic wall contribute to a portion of the opening angle, and this leads to an open question on whether this swelling pressure should be distinguished from residual stresses.

This dissertation contributes new data and knowledge to the scientific community's current understanding of the biomechanics of the aorta and lays the foundation for future lines of investigation. Indeed, understanding the biomechanical properties of the aorta is imperative to the community's efforts in preventing deadly ruptures caused by aneurysms and dissection, as these catastrophic events stem from mechanical failures, which occur when mechanical stresses exceed the strength of the wall of the aorta.

## 8.3 CONCLUSIONS

Overall, this dissertation provides new knowledge on the roles that GAG play in the thoracic aorta by modulating its mechanical properties and the circumferential residual stresses present in it, through their fundamental swelling behaviour and interaction with the ECM fibers. It establishes a finite element ring model for each of the ascending, arch, and descending thoracic regions, which through prescription of the FCDs of GAG present in the matrix, demonstrated overall good agreement with the experimental findings. To summarize, the main conclusions of this work are:

1- Through an in-depth review of the scientific literature, it was concluded that overall, GAG accumulate in thoracic aortic aneurysm and diminish in abdominal aortic aneurysm. We also underscored the potential biomechanical roles of GAG in the aorta with regards to their contribution to the aortic stress-strain behavior, stiffness and residual stresses, which remain poorly understood. We highlighted gaps in the literature and recommended future lines of investigations such as the need to (1) accurately characterise the layer-specific GAG quantities in the aorta to overcome current computational limitations that have been based on qualitative assumptions; (2) delineate the relationship between the GAG and swelling distributions; (3) clarify the contribution of GAG to aortic stiffness.

2- Quantitative and histological characterization revealed that the GAG content is significantly higher in the ascending aorta compared to the arch and descending thoracic regions of 5- to 6-month-olds porcine animals, and that the GAG content decreases from the intimal to the adventitial layers of the aortic wall. By contrast, the collagen content was found to increase from the intimal to the adventitial layers, and the elastin content was highest towards the medial layers.

3- Correlations between the opening angle and the content and intramural gradient of the ECM constituents, as well as the ratio between the collagen and sulfated GAG (sGAG) content (collagen:sGAG) were established and classified based on Pearson's correlation "r" as strong, good, moderate and poor. These correlations revealed that residual stresses are significantly modulated by the sGAG through their content and interaction with the collagen fibers, given that strong and good correlations were found between the collagen:sGAG ratio, and the sGAG content with the opening angle, respectively. Additionally, the gradients of sGAG, collagen and the collagen:sGAG ratio correlated moderately with the opening angle.

4- This work not only established correlations between GAG and the opening angle but also delineated the extent of contribution of GAG to circumferential residual stresses in the main regions of the porcine thoracic aorta. GAG were found to contribute to approximately 25%, 32%, and 42% of the opening angle in the ascending, arch, and descending thoracic regions, respectively.

5- This dissertation also shows that the accumulation of advanced glycation end products (AGEs), which create crosslinks in the tissue, contribute to circumferential residual stresses by reducing the opening angle. GAG also played a role in glycated tissue, such that their removal still caused a decrease in the opening angle.

6- GAG were found to affect the radial compressive stiffness of the ascending aorta, which contains the highest amount of GAG (sGAG occupy ~1% dry weight). Specifically, an increase in radial compressive stiffness was detected following removal of GAG from the ECM.

7- Mechanisms by which GAG contribute to the residual stresses and mechanical properties were deciphered. Although this dissertation revealed that GAG may not be the only regulators of the swelling state of the tissue, GAG were found to contribute though their fundamental swelling behaviour given that a small loss of water content was detected after GAG removal. In addition, GAG contribute to the aorta's radial compressive properties and circumferential residual stresses by interacting with ECM fibers and affecting their level of prestress. This stems from the strong correlation established between the ratio between collagen and GAG and the opening angle, and from the discovery that GAG removal caused a loss of compressive deformation in the inner layers of the aortic wall.

8- This work highlights the heterogeneity of the aorta along its tree and its wall. The opening angle and radial compressive stiffness were highest in the ascending region and decreased distally. The ECM composition (collagen, elastin, GAG), as mentioned in Point 2, also varied along the tree of the aorta, and through its wall.

9- The biaxial tensile mechanical behaviour of the ascending, arch and descending thoracic regions of the porcine thoracic aorta were modelled using a Holmes-Mow constitutive formulation, which demonstrated an overall good representation of the tissue's mechanical behavior. The intima-media and adventitial layers were also mathematically simulated to reflect the difference in elastic properties between the two, and the behavior of the adventitia with respect to the intima-media was predicted via optimization. The findings suggested that in the ascending region, the intima-media was stiffer than the adventitia; it was stiffer or just as stiff as the adventitia in the aortic arch; and it was possibly either stiffer or softer than the adventitia in the descending thoracic region.

10- Finite element models were built to capture the effect of GAG on the opening angle, using animal-specific (5- to 6-month-old pig aortas) parameters collected experimentally, including dimensions, material parameters and layer specific intramural GAG FCDs. Simulated opening angles of aortic rings modelled with one layer for the solid matrix were 37 deg, 17 deg and 10 deg in the ascending, arch and descending thoracic regions. The best opening angle prediction capacity of the computer models was achieved when the intima-media was prescribed as 10 times stiffer than the adventitia in the ascending region; in the aortic arch, the best match was when the intima-media was two times stiffer than the adventitia; and for the descending thoracic region, the best match was achieved when using one layer for the solid matrix.

## 8.4 RECOMMENDATIONS FOR FUTURE WORK

This dissertation offers robust findings and comprehensive analyses regarding the mechanical roles of GAG in the aorta, but also lays foundations for future investigations.

- One of the notable revelations from this research is the potential mechanism of interaction between GAG and the ECM fibers. While the correlation between the collagen:GAG ratio and the opening angle (Chapter 5) suggested an interaction mechanism between collagen and GAG in regulating residual stress, our work did not reveal details on how this interaction occurs. This has been a matter of debate within the literature and no conclusive evidence has been established. It is believed that the swelling of GAG puts both collagen and elastic fibers under tension [4]–[6], which is in line with the theorical assumption that collagen fibers do not support compression [7]. However, other studies have demonstrated that collagen [8] and elastin [9], [10] fibers may be under residual compressive stress. Based on a more recent study [11], GAG removal was found to cause a decrease in the collagen waviness, suggesting that the swelling of GAG could either contribute to the collagen waviness, or fill in the existing collagen waviness which could be under compression due to tensile elastin. To address this lack of understanding, future work could include investigating the interaction between the ECM constituents, and specifically whether the swelling of GAG puts the ECM fibers under tension or compression. Characterizing the ECM fibers using more advanced technologies such as multiphoton microscopy [13] may provide further information and details regarding fiber structure and help bridge this gap.
- Chapter 6 allowed us to evaluate the effect of GAG on the circumferential stretch, where we found that GAG depletion reduced the circumferential compressive stretch in the

inner layers of the aortic wall. In line with [12], the inner layers were shown to be under residual compression, while the outer layers were shown to be under residual tension. Although the correlation between the collagen:GAG ratio and the opening angle suggests that GAG puts the collagen fibers under some level of prestretch, the concept of circumferential prestretch remains elusive. Further characterizing the ECM fibers, which are believed to be the origin of circumferential prestretch, may provide a deeper understanding on how fiber prestretch regulates the circumferential prestretch. Similar to the previous recommendation, multiphoton microscopy may also enable to elucidate the relationship between the fiber and circumferential prestretch via an in-depth characterization of the matrix.

- While this dissertation was concerned with understanding the effect of the ECM on the residual stresses and mechanical properties of the aorta, the cellular component may also be implicated, but was not considered. It has been previously shown that destroying smooth muscle cells (SMCs) by freezing does not affect arterial opening angle [14]. Additionally, Azeloglu et al. found no difference in the opening angle of aortic rings treated with cytochalasin D, which eliminates SMC contraction [2]. However, Guo et al. speculated that changes in the opening angle of aortic rings due to change in external bath osmolarity may be due to the swelling of the cellular component of the aortic wall [15]. On the other hand, SMC activation was found to affect the mechanical properties of the thoracic aorta, namely aortic stiffness and its viscoelastic properties [16]. To address these conflicting findings, and bridge the gap in the present dissertation, one recommendation for future work would be to study the effect of SMCs and their activation status on residual stress and the mechanical properties of the aorta.

- In this work, we implemented a mathematical optimization technique to model two layers of the aortic wall. One interesting suggestion for future work would be to validate the effectiveness of this optimization method by comparing its results to experimental findings where intima-media and adventitia have been mechanically separated before testing.
- Since GAG swelling only contributes a portion of the opening angle, in numerical simulations, a model that combines both the effects of GAG and circumferential prestretch could be developed.
- While this work offers a robust framework for studying the GAG roles in the aorta, it is important to note that it was limited to porcine tissue. Therefore, future research should focus on validating and/or investigating these mechanisms in the context of the healthy and diseased human aorta.
- To establish clinical relevance, it would be interesting to develop a methodology for measuring GAG or their FCDs non-invasively. Interestingly, multiple imaging methods are available and widely used to measure the FCD of GAG in cartilage from magnetic resonance images (MRI). Two examples of these methods are known as the Delayed Gadolinium-Enhanced MRI (dGEMRIC) [17]–[20] and the T1rho method [21]–[24]. One suggestion for future work would be to evaluate the feasibility and efficiency of such methods for measuring GAG in the aorta.

## 8.5 REFERENCES

[1] P. Badel, K. Genovese, and S. Avril, “3D Residual Stress Field in Arteries: Novel Inverse Method Based on Optical Full-field Measurements,” *Strain*, vol. 48, no. 6, pp. 528–538, 2012, doi: 10.1111/str.12008.

[2] E. U. Azeloglu, M. B. Albro, V. A. Thimmappa, G. A. Ateshian, and K. D. Costa, “Heterogeneous transmural proteoglycan distribution provides a mechanism for regulating

residual stresses in the aorta," *American Journal of Physiology-Heart and Circulatory Physiology*, vol. 294, no. 3, pp. H1197–H1205, Mar. 2008, doi: 10.1152/ajpheart.01027.2007.

[3] A. Giudici and B. Spronck, "The Role of Layer-Specific Residual Stresses in Arterial Mechanics: Analysis via a Novel Modelling Framework," *Artery Res*, vol. 28, no. 2, Art. no. 2, Jun. 2022, doi: 10.1007/s44200-022-00013-1.

[4] J.-W. M. Beenakker, B. A. Ashcroft, J. H. N. Lindeman, and T. H. Oosterkamp, "Mechanical Properties of the Extracellular Matrix of the Aorta Studied by Enzymatic Treatments," *Biophysical Journal*, vol. 102, no. 8, pp. 1731–1737, Apr. 2012, doi: 10.1016/j.bpj.2012.03.041.

[5] W. M. Lai, J. S. Hou, and V. C. Mow, "A Triphasic Theory for the Swelling and Deformation Behaviors of Articular Cartilage," *J Biomech Eng*, vol. 113, no. 3, pp. 245–258, Aug. 1991, doi: 10.1115/1.2894880.

[6] A. Maroudas, "Balance between swelling pressure and collagen tension in normal and degenerate cartilage," *Nature*, vol. 260, no. 5554, p. 808, Apr. 1976, doi: 10.1038/260808a0.

[7] Y. Lanir, "A structural theory for the homogeneous biaxial stress-strain relationships in flat collagenous tissues," *Journal of Biomechanics*, vol. 12, no. 6, pp. 423–436, Jan. 1979, doi: 10.1016/0021-9290(79)90027-7.

[8] P. J. Zeller and T. C. Skalak, "Contribution of Individual Structural Components in Determining the Zero-Stress State in Small Arteries," *J Vasc Res*, vol. 35, no. 1, pp. 8–17, 1998, doi: 10.1159/000025560.

[9] E. Fonck, G. Prod'hom, S. Roy, L. Augsburger, D. A. Rüfenacht, and N. Stergiopulos, "Effect of elastin degradation on carotid wall mechanics as assessed by a constituent-based biomechanical model," vol. 292, p. 10, 2007.

[10] S. Roy, P. Silacci, and N. Stergiopulos, "Biomechanical proprieties of decellularized porcine common carotid arteries," *American Journal of Physiology-Heart and Circulatory Physiology*, vol. 289, no. 4, pp. H1567–H1576, Oct. 2005, doi: 10.1152/ajpheart.00564.2004.

[11] J. M. Mattson, R. Turcotte, and Y. Zhang, "Glycosaminoglycans Contribute to Extracellular Matrix Fiber Recruitment and Arterial Wall Mechanics," *Biomech Model Mechanobiol*, vol. 16, no. 1, pp. 213–225, Feb. 2017, doi: 10.1007/s10237-016-0811-4.

[12] C. J. Chuong and Y. C. Fung, "On Residual Stresses in Arteries," *Journal of Biomechanical Engineering*, vol. 108, no. 2, pp. 189–192, May 1986, doi: 10.1115/1.3138600.

[13] A. M. Barlow, L. B. Mostaço-Guidolin, E. T. Osei, S. Booth, and T.-L. Hackett, "Super resolution measurement of collagen fibers in biological samples: Validation of a commercial solution for multiphoton microscopy," *PLOS ONE*, vol. 15, no. 2, p. e0229278, Feb. 2020, doi: 10.1371/journal.pone.0229278.

[14] S. E. Greenwald, J. E. Moore, A. Rachev, T. P. C. Kane, and J.-J. Meister, “Experimental Investigation of the Distribution of Residual Strains in the Artery Wall,” *Journal of Biomechanical Engineering*, vol. 119, no. 4, pp. 438–444, Nov. 1997, doi: 10.1115/1.2798291.

[15] X. Guo, Y. Lanir, and G. S. Kassab, “Effect of osmolarity on the zero-stress state and mechanical properties of aorta,” *American Journal of Physiology-Heart and Circulatory Physiology*, vol. 293, no. 4, pp. H2328–H2334, Oct. 2007, doi: 10.1152/ajpheart.00402.2007.

[16] G. Franchini, I. D. Breslavsky, F. Giovanniello, A. Kassab, G. A. Holzapfel, and M. Amabili, “Role of smooth muscle activation in the static and dynamic mechanical characterization of human aortas,” *Proceedings of the National Academy of Sciences*, vol. 119, no. 3, p. e2117232119, Jan. 2022, doi: 10.1073/pnas.2117232119.

[17] C. Zilkens *et al.*, “Delayed Gadolinium-enhanced Magnetic Resonance Imaging of Cartilage in the Long-term Follow-up After Perthes Disease,” *Journal of Pediatric Orthopaedics*, vol. 30, no. 2, p. 147, Mar. 2010, doi: 10.1097/BPO.0b013e3181cf13e6.

[18] A. Williams *et al.*, “Glycosaminoglycan Distribution in Cartilage as Determined by Delayed Gadolinium-Enhanced MRI of Cartilage (dGEMRIC): Potential Clinical Applications,” *American Journal of Roentgenology*, vol. 182, no. 1, pp. 167–172, Jan. 2004, doi: 10.2214/ajr.182.1.1820167.

[19] A. Bashir, M. L. Gray, and D. Burstein, “Gd-DTPA2− as a measure of cartilage degradation,” *Magnetic Resonance in Medicine*, vol. 36, no. 5, pp. 665–673, 1996, doi: 10.1002/mrm.1910360504.

[20] C. E. Jones *et al.*, “Delayed Gadolinium-Enhanced Magnetic Resonance Imaging of Cartilage Values in Hips With Bone Marrow Lesions,” *Arthritis Care & Research*, vol. 74, no. 12, pp. 1997–2004, 2022, doi: 10.1002/acr.24733.

[21] A. T. Collins *et al.*, “Selective Enzymatic Digestion of Proteoglycans and Collagens Alters Cartilage T1rho and T2 Relaxation Times,” *Ann Biomed Eng*, vol. 47, no. 1, pp. 190–201, Jan. 2019, doi: 10.1007/s10439-018-02143-7.

[22] C. E. Jones, K. Mulpuri, T. Teo, D. R. Wilson, and A. G. d’Entremont, “T1ρ and T2 MRI show hip cartilage damage in adolescents with healed Legg-Calvé-Perthes disease,” *Journal of Pediatric Orthopaedics B*, vol. 31, no. 4, p. 344, Jul. 2022, doi: 10.1097/BPB.0000000000000892.

[23] R. R. Regatte, S. V. S. Akella, J. h. Lonner, J. b. Kneeland, and R. Reddy, “T1ρ relaxation mapping in human osteoarthritis (OA) cartilage: Comparison of T1ρ with T2,” *Journal of Magnetic Resonance Imaging*, vol. 23, no. 4, pp. 547–553, 2006, doi: 10.1002/jmri.20536.

[24] A. Borthakur *et al.*, “Three-dimensional T1ρ-weighted MRI at 1.5 Tesla,” *Journal of Magnetic Resonance Imaging*, vol. 17, no. 6, pp. 730–736, 2003, doi: 10.1002/jmri.10296.